Dissertation zur Erlangung des Doktorgrades der Fakultät für Chemie und Pharmazie der Ludwig-Maximilians-Universität München

Molecular mechanisms of endolysosomal nucleic acid processing controlling RNA-sensing Toll-like receptors

Marleen Bérouti

aus

Hermeskeil, Deutschland

2025

Erklärung

Diese Dissertation wurde im Sinne von § 7 der Promotionsordnung vom 28. November 2011 von Herrn Prof. Dr. Veit Hornung betreut.

Eidesstattliche Versicherung

Diese Dissertation wurde eigenständig und ohne unerlaubte Hilfe erarbeitet.

München, 01.09.2025

Marleen Bérouti

Dissertation eingereicht am: 01.09.2025

1. Gutachter: Prof. Dr. Veit Hornung

2. Gutachter: Prof. Dr. Karl-Peter Hopfner

Mündliche Prüfung am: 26.11.2025

Für

Christian, Daniela und Veit.

Table of Contents

1 Introduction

1.1 The immune system

All living organisms encode for a broad array of mechanisms that are meant to protect them from infectious agents, such as viruses, bacteria, fungi, and parasites. This system, commonly referred to immune system, requires the fundamental feature to distinguish self from non-self. Once a potentially harmful agent is recognized as foreign, it mounts a response to eliminate or neutralize the threat. In higher multicellular organisms, the immune system also serves additional, homeostatic roles beyond pathogen defense, which include the elimination of aberrant cells or the facilitation of tissue repair.

Generally, the immune system is divided into the innate and adaptive. The innate immune system is evolutionarily ancient, with innate-like defense mechanisms found across all domains of life. Its molecular components are encoded in the genome and passed down through successive generations (e.g., germ-line encoded), making them broadly conserved and relatively invariant. It forms the first line of defense and acts rapidly, within minutes post infection. Adaptive immunity, as it is present in vertebrates, relies on a large repertoire of rearranging receptors that are created *de novo* and distributed in a clonal fashion. Therefore, and in contrast to the innate immune system, it typically responds in a delayed fashion, but it can provide highly specific, long-lasting protection and generates immunological memory. Although adaptive immunity is traditionally considered restricted to vertebrates, bacteria also possess an adaptive-like defense system in the form of CRISPR-Cas, which allows them to “remember” prior viral infections (Barrangou and Marraffini, 2014; Chaplin, 2010; Murphy and Weaver, 2017). In the following paragraph, I briefly outline the key components of the innate and adaptive immune system, while I focus on vertebrate immunity.

1.1.1 The innate immune system

The primordial function of the innate immune system is to eliminate threats and prevent their spread. It involves both humoral and cell-mediated responses. Traditionally, the

innate immune system is categorized into three layers: physical/chemical barriers, humoral components, and cellular components. Physical and chemical barriers, such as the skin and mucosal surfaces, are considered to be the first layer of the innate immune system. The skin acts as a physical barrier that prevents most pathogens from entering the body, and mucosal surfaces produce antimicrobial proteins and peptides, such as lysozymes, which degrade bacterial cell walls and cause lysis (Murphy and Weaver, 2017; Primo et al., 2018).

The second layer, the humoral component, relies on soluble proteins that are circulating in body fluids, most of which are produced by the liver. A core element is the complement system, consisting of about 30 plasma proteins, which can directly lyse pathogens or opsonize them to enhance phagocyte uptake and elimination. Acute-phase proteins, such as C-reactive protein (CRP) and serum amyloid A (SAA), are also components of the humoral innate immune response that bind to microbial or altered host molecules and promote immune activation, either by triggering complement activation or by recruiting immune cells to the site of infection (Eklund et al., 2012; Mold et al., 1999; Sarma and Ward, 2011). Additionally, the coagulation system bears innate immune-like functions, beyond its role in blood clotting. For instance, complex extracellular networks, formed by the protein fibrin, entrap pathogens, restrict their dissemination, and provide a physical scaffold that mobilizes immune cells (Almskog and Ågren, 2025; Sozmen and Akassoglou, 2021).

The third layer of the innate immune system relies on cells that can carry out effector functions in various ways, such as phagocytosis, mediating cell death, or releasing inflammatory mediators.

Phagocytosis is a key cell-mediated response of the innate immune system that directly eliminates pathogens. Cells of the innate immune system that can engulf and destroy marked pathogens or other pathogen-infected cells primarily arise from the myeloid compartment in the bone marrow. These include blood-circulating monocytes, neutrophils, dendritic cells, and tissue-resident macrophages (Murphy and Weaver, 2017). Destruction by phagocytes is mediated by endolysosomal proteolytic enzymes and the production of antimicrobial chemicals by the phagocyte, such as reactive oxygen species (ROS) and nitric oxide (NO) (Fang, 2004).

In addition to killing microorganisms through phagocytosis, pathogen-infected cells can trigger their own, cell-autonomous death, as this often goes along with eliminating the

invading pathogen. Generally, immune cells can undergo different types of programmed host cell death. These include apoptosis, an immunologically silent form of cell death, as well as pyroptosis and necroptosis, both of which are highly inflammatory forms of lytic cell death (Labbé and Saleh, 2008).

Nevertheless, innate immune responses are not confined to cells that are being infected or detect the infection, but can also spread systemically. By releasing inflammatory mediators such as cytokines and chemokines, innate immune cells also amplify immune responses by recruiting additional cells or effector molecules. Examples of this are the release of the chemotactic cytokines CXCL8 (Cambier et al., 2023) and CXCL10 (Tighe et al., 2011) by macrophages, which recruit neutrophils, a type of blood-circulating phagocyte (Cambier et al., 2023), and natural killer (NK) cells (Lodoen and Lanier, 2006).

NK cells play an important role in eliminating infected cells, as they can, in contrast to the self-driven forms, extrinsically mediate cell death. Their activation is tightly controlled by activating and inhibitory receptors on their cell surface. These receptors are specialized to detect changes in the expression of surface molecules on the target cell. An example of this is the expression of the cell surface molecule MHC, which serves as a marker to inhibit NK cell activation. Because some viruses and other pathogens can induce downregulation of MHC class molecules to avoid recognition by adaptive immune cells (see below), NK cells can sense these changes as a “missing self” signal (Murphy and Weaver, 2017). Upon their activation, NK cells induce apoptosis by releasing a cocktail of apoptosis-inducing cytokines or cytotoxic granules, containing perforins and granzymes (Belizário et al., 2018).

However, while certain infections can be contained by the innate immune system alone, in many cases, it is not sufficient. In such situations, the innate immune system plays a crucial role in activating and shaping the adaptive immune response, with dendritic cells (DCs) serving as the key bridge between the two systems. Although these cells are classified as phagocytes, it is not their primary role to directly kill microorganisms, but to process engulfed peptide antigens and present them to specific lymphocytes, which are part of the adaptive immune system, leading to their activation (Cabeza-Cabrerizo et al., 2021; Ngo et al., 2024).

1.1.2 The adaptive immune system

Cells of the adaptive immune system derive from a common lymphoid progenitor in the bone marrow and include B and T cells. These cells recognize pathogenic molecular structures, known as antigens, through distinct antigen receptors generated by somatic rearrangement of specific gene segments. Upon their activation, B cells mature into plasma cells that secrete antibodies. Antibodies help protect against extracellular pathogens primarily through two mechanisms. First, by directly binding to pathogens or their products, such as bacterial toxins, they can block these agents from entering and infecting host cells. This process is known as neutralization. While neutralization prevents viruses or bacterial toxins from infecting cells, it is generally less effective against whole bacteria. In such cases, antibodies aid in pathogen elimination by opsonizing bacteria and, simultaneously, help to activate the complement system to enhance pathogen recognition by phagocytic cells (Murphy and Weaver, 2017).

T cells recognize peptide antigens that are presented by antigen-presenting cells, such as dendritic cells, in MHC molecules on their cell surface. The delivery of a cognate antigen (signal 1), and the simultaneous provision of co-stimulatory molecules (signal 2) and the presence of specific cytokines (signal 3), provides a crucial link between innate immune recognition and the induction of adaptive immunity, enabling naïve T cells to proliferate and differentiate into different subsets (Sun et al., 2023). These subsets include CD8+ T cells (restricted to MHC I molecules), which kill infected target cells bearing the same antigen on their cell surface, as well as helper T cells (restricted to MHC II molecules) that secrete cytokines and express surface molecules to regulate tailored immune responses. These include, e.g., the activation of macrophages to enhance phagocytosis or the activation of B cells to induce antibody production (Sun et al., 2023). Additionally, regulatory T cells inhibit other lymphocytes, thereby preventing harmful and excessive immune reactions (Vignali et al., 2008). Crucially, certain B and T cells develop into memory cells, establishing immunological memory that enables a rapid response upon re-exposure to the same pathogen (Murphy and Weaver, 2017).

In summary, the immune system uses multiple, finely tuned strategies to defend against infection. These involve an integrated response from innate and adaptive immune systems to efficiently remove foreign threats.

1.2 Paradigms of non-self-sensing by the innate immune system

To recognize non-self, innate immune cells are equipped with germline-encoded pattern recognition receptors (PRRs). These receptors detect microbial signatures, known as pathogen-associated molecular patterns (PAMPs). PAMPs are highly conserved structures, found in many pathogens of a given class, such as lipopolysaccharide (LPS) in Gram-negative bacteria. Because PAMPs are essential for microbial survival, they cannot easily be altered, making them reliable signals for immune recognition (Mogensen, 2009; Takeuchi and Akira, 2010).

Beyond this classical view of pattern-triggered immunity (PTI), another paradigm of non-self-recognition, termed effector-triggered immunity (ETI), has been proposed as a mechanism of innate immune sensing. Unlike PTI, ETI is not triggered by conserved microbial patterns but by activities carried out by the pathogen, while infecting the host. For example, many pathogens release specialized proteins, called effectors or virulence factors, that disrupt host cellular functions to facilitate the replication and spread of the pathogen. The host can sense such activities through various mechanisms, triggering an immune response (Remick et al., 2023).

One example of ETI is the secretion of the HSV-1 protein infected cell protein 0 (ICP0), an E3 ligase that targets many host proteins that restrict viral replication. One of its targets is the protein microrchidia family CW-type zinc finger 3 (MORC3), a repressor of interferon beta 1 (IFNB1). Consequently, when MORC3 is targeted for degradation, the expression of interferon-β is potently induced (Gaidt et al., 2021).

Additionally, the innate immune system also responds to endogenous molecules and signals that are released upon cell stress, cell death, or tissue damage. Often, these signals are referred to as damage-associated molecular patterns (DAMPs) in analogy to the PAMP nomenclature. Examples of DAMPs are ATP, uric acid crystals, or host DNA that act as danger signals to alert the innate immune system, even in the absence of pathogen infection. Nevertheless, recognizing DAMPs is believed to be detrimental to the host rather than protective, as these patterns can trigger or worsen sterile inflammatory diseases (Hornung and Gaidt, 2024; Remick et al., 2023).

1.2.1 Pattern recognition receptors

Upon activation, PRRs initiate signaling cascades that activate transcription factors to induce the expression of numerous genes, including those encoding chemokines, pro-inflammatory cytokines, type I interferons, or antimicrobial proteins. These molecules can recruit additional immune cells to amplify the immune response or trigger downstream pathways that can, e.g., lead to programmed host cell death, metabolic changes to promote the production of reactive oxygen species for pathogen killing, or systemic inflammation such as fever.

Based on structural similarities and localization, PRRs are typically divided into different families. These include the class of membrane-associated Toll-like receptors (TLRs) and C-type lectin receptors (CLRs), as well as the cytosolic sensors retinoic acid-inducible gene (RIG)-I-like receptors (RLRs) and NOD-like receptors (NLRs) (Takeuchi and Akira, 2010), as well as the cGAS-STING axis.

Because TLRs are central to this thesis project, they will be discussed in a dedicated chapter (see Chapter 1.3), while the following paragraph briefly summarizes key components of the remaining receptor classes.

CLRs are characterized by their unique carbohydrate recognition domain that functions to recognize a variety of glycan moieties on pathogens. A classical feature of CLR recognition is its dependence on Ca^{2+} ions. However, some CLRs can bind carbohydrates independently of Ca^{2+} and are called C-type lectin-like receptors (CTLRs) (Chiffoleau, 2018). One example is the receptor Dectin-1 that recognizes β-glucans, carbohydrates found in many cell walls of fungi (Huysamen and Brown, 2009). Activation of CLRs typically leads to the stimulation of a signaling pathway that culminates in the activation of the transcription factor NF-κB (Chiffoleau, 2018).

The family members of RLRs are double-stranded (ds)RNA sensors that comprise three members in humans. These include RIG-I, detecting 5'phosphorylated dsRNA (Hornung et al., 2006; Pichlmair et al., 2006), melanoma differentiation-associated protein 5 (MDA5), sensing long dsRNA (del Toro Duany et al., 2015), and laboratory of genetics and physiology 2 (LGP2). RIG-I and MDA5 signal via binding to the adaptor molecule mitochondrial antiviral-signaling protein (MAVS) to ultimately activate the transcription factors IRF3, IRF7, and NF-κB (Rehwinkel and Gack, 2020). LGP2 lacks

the essential MAVS binding domain, but it has been shown to play a regulatory role for RIG-I and MDA5 activation (Bruns et al., 2014; Rothenfusser et al., 2005).

Nucleotide-binding domain and leucine-rich repeat-containing receptors (NLRs) comprise at least 23 members in the human system. All of these share a central NACHT domain, which mediates oligomerization, and a C-terminal leucine-rich repeat (LRR) domain, often involved in ligand sensing (Sundaram et al., 2024). Activation of NLRs extends beyond classical PAMP-PRR recognition, as some NLRs can also be activated in an indirect fashion. One example is NLRP3, which senses cellular membrane perturbations (Gaidt and Hornung, 2018). In contrast, other NLRs are triggered by direct ligand interactions. As such, NOD1 and NOD2 detect bacterial peptidoglycan fragments (Girardin et al., 2003; Laroui et al., 2011). Upon activation, some NLRs can form large multiprotein complexes known as inflammasomes that induce pyroptosis (Shi et al., 2015). Additionally, some NLRs, like NOD1 and NOD2, also activate NF-κB and MAPK signaling pathways, leading to the release of pro-inflammatory cytokines and chemokines upon their activation (Heim et al., 2019).

In addition to the four classical PRR families, the cGAS/STING axis plays a crucial role in the detection of pathogens that either contain DNA or produce it during their life cycle (Zhang et al., 2020). Specifically, the sensor cyclic GMP-AMP synthase (cGAS) recognizes cytosolic dsDNA. Upon DNA binding, cGAS produces the second messenger cyclic GMP-AMP (cGAMP) from ATP and GTP (Ablasser et al., 2013; Diner et al., 2013), which subsequently binds to Stimulator of interferon genes (STING). STING is a dimeric protein that, under steady state, is located at the endoplasmic reticulum (ER). Upon cGAMP binding to STING, the receptor translocates to the Golgi via endoplasmic reticulum-Golgi intermediate compartment (ERGIC) (Zhang et al., 2020). At the Golgi, STING recruits the kinase TBK1 and IKKε to activate IRF3 and NF-κB (Balka et al., 2020; Murthy et al., 2020).

1.2.2 Consequences of non-self-recognition

As described above, many PRRs activate the transcription factor NF-κB, a central regulator of inflammation that controls the expression of pro-inflammatory cytokines and chemokines that coordinate immune cell recruitment. A key step in NF-κB signaling is the activation of transforming growth factor beta-activated kinase 1 (TAK1). TAK1 associates with two regulatory subunits, TAB1 and TAB2, with TAB2 binding polyubiquitin chains, an essential step for TAK1 activation (Liu et al., 2017). Activated TAK1 then phosphorylates the downstream IκB kinase (IKK) complex, composed of IKKα, IKKβ, and IKKγ (also called NEMO) (Ninomiya-Tsuji et al., 1999; Wang et al., 2001b). Activation of the IKK complex leads to phosphorylation of the NF-κB inhibitory protein IκBα, which is subsequently degraded by the proteasome. The degradation of IκBα allows NF-κB to translocate to the nucleus, where it induces the expression of numerous pro-inflammatory genes (Liu et al., 2017) (see Fig. 1, right panel).

The activation of IRFs, which is essential for producing type I interferon, requires the activity of TANK-binding kinase 1 (TBK1). TBK1 is recruited by the adaptor proteins STING, MAVS, and TRIF downstream of cGAS, RLR, and TLR activation. Each adaptor protein contains a conserved pLxIS motif, which is phosphorylated at a serine residue by TBK1. This phosphorylation creates a binding site for IRF proteins, which TBK1 subsequently phosphorylates. Phosphorylated IRFs dissociate, dimerize, and translocate to the nucleus, where they induce the expression of type I interferons (Liu et al., 2015a). Additionally, STING and MAVS recruit the kinase IKKε, which also phosphorylates both the adaptor proteins and IκBα, thereby promoting the production of pro-inflammatory cytokines downstream of cGAS/STING and RLR signaling (Balka et al., 2020; Rehwinkel and Gack, 2020) (see Fig. 1, left panel).

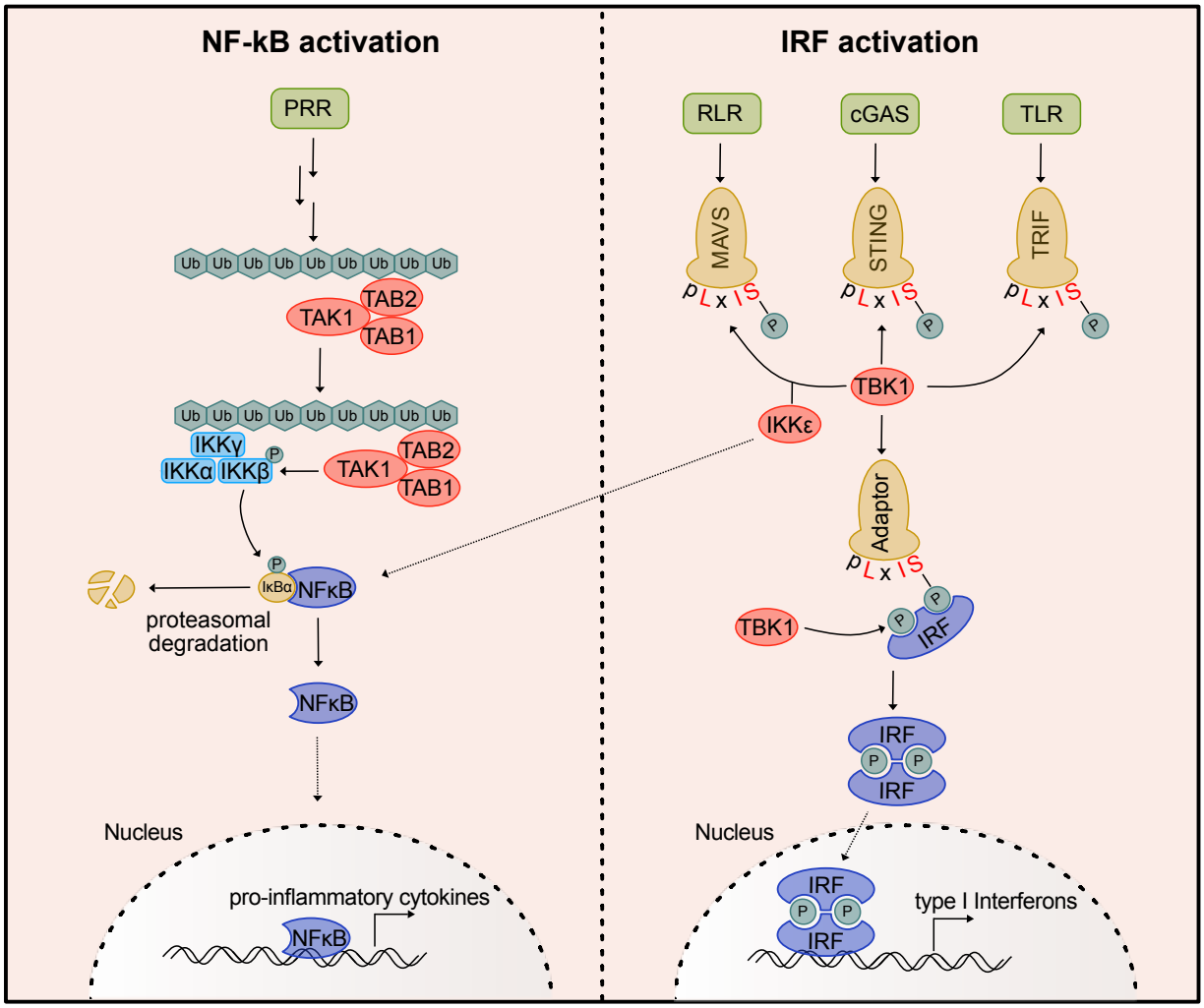

Figure 1 Overview of NF-κB and IRF activation downstream of PRR signaling. PRR signaling converges into activation of TAK1, which subsequently phosphorylates the IKK complex. Activated IKK complex phosphorylates IκBα, leading to its degradation by the proteasome and enabling NF-κB to translocate to the nucleus, where it drives the expression of pro-inflammatory cytokines. TBK1 is recruited by adaptor proteins MAVS, STING, and TRIF to phosphorylate their conserved pLxIS motifs, enabling IRF binding, phosphorylation, dimerization, and nuclear translocation to drive type I interferon expression. In parallel, STING and MAVS recruit IKKε, which phosphorylates the adaptor proteins and IκBα to promote pro-inflammatory cytokine production.

Pro-inflammatory cytokines expressed downstream of NF-κB activation include members of the interleukin (IL) family, such as IL-6, and members of the tumor necrosis factor (TNF) superfamily, like TNF-α, both of which were used as readouts to study TLR activation in this thesis. These cytokines can induce fever. IL-6 additionally promotes the synthesis of acute-phase proteins in the liver and, together with transforming growth factor (TGF)-β, is essential for differentiating Th17 cells from naïve $CD4^+$ T cells (Tanaka et al., 2014). TNF-α further enhances inflammatory signaling and triggers apoptosis or necroptosis (Jang et al., 2021).

The induction of type I interferons (IFN), like IFN-α or IFN-β, is particularly important when it comes to battling virus infections (Cabeza-Cabrerizo et al., 2021; Ngo et al., 2024). By promoting the expression of many interferon-stimulated genes (ISGs) such as the enzyme oligoadenylate synthase (OAS) or the double-stranded (ds)RNA-dependent protein kinase (PKR), IFNs are critical to inhibit viral replication (Yang and Li, 2020). Specifically, OAS proteins are cytosolic sensors that are activated by viral dsRNA. Upon their activation, these enzymes synthesize 2'-5'-linked oligomers from ATP. Binding of 2'-5'-oligoadenylates to the endoribonuclease RNase L promotes its dimerization and activation. RNase L degrades viral RNA and cellular ribosomal RNA, decreasing viral replication (Drappier and Michiels, 2015). PKR, a serine-threonine kinase, phosphorylates the alpha subunit of the eukaryotic initiation factor 2 (eIF2a), thereby suppressing protein translation and contributing to the inhibition of viral replication (Saelens et al., 2001). Additionally, PKR activation triggers apoptosis (Balachandran et al., 1998).

1.3 Toll-like receptors

Toll-like receptors (TLRs) were the first PRRs to be identified. Initially discovered in 1996 in *Drosophila melanogaster* (Lemaitre et al., 1996), the human homologue TLR4 was characterized shortly thereafter as the first member of the TLR family in humans (Medzhitov et al., 1997). Subsequently, TLR4 was reported to recognize LPS, a component of the outer membrane of Gram-negative bacteria (Poltorak et al., 1998).
All TLRs are type I transmembrane proteins that share a similar domain architecture. An N-terminal ectodomain with a horseshoe-shaped structure for ligand binding, consisting of leucine-rich repeats (LRR), followed by a transmembrane domain and a C-terminal cytosolic Toll/interleukin-1(TIR) domain. In humans, the TLR family consists of 10 members (TLR1-TLR10), while mice express 12 members. Based on their localization and ligand sensing, TLRs can be roughly divided into two major subgroups (Fitzgerald and Kagan, 2020). TLR1, TLR2, TLR4, TLR5, TLR6, and TLR10 are plasma membrane-associated TLRs that sense microbial membrane components. TLR2 forms heterodimers with either TLR1 or TLR6 to sense bacterial lipoproteins and lipopeptides (Farhat et al., 2008; Kang et al., 2009), TLR4 recognizes LPS with the help of the protein MD-2 (Poltorak *et al.*, 1998; Shimazu et al., 1999), and TLR5 senses

bacterial flagellin (Hayashi et al., 2001). TLR10 is considered an orphan receptor for which the exact ligand is still unknown (Fitzgerald and Kagan, 2020). The second subgroup includes the endosomal TLRs, TLR3, TLR7, TLR8, and TLR9, which recognize nucleic acids. Specifically, TLR3 senses viral dsRNA (Alexopoulou et al., 2001), TLR7 and TLR8 detect single-stranded (ss)RNA (Diebold et al., 2004; Heil et al., 2004), and TLR9 is activated by unmethylated CpG-motif-containing ssDNA (Hemmi et al., 2000).

TLRs are synthesized and folded in the endoplasmic reticulum (ER) and are subsequently targeted to the plasma or endosomal membrane (Fitzgerald and Kagan, 2020; Randow and Seed, 2001). Trafficking of TLR1, TLR2, TLR4, TLR7, and TLR9 is regulated by the protein associated with TLR4 (PRAT4A) (Takahashi et al., 2007; Wakabayashi et al., 2006), and except for TLR3, folding of all TLRs depends on the chaperone gp96 (Yang et al., 2007). Transport of endosomal TLR3, TLR7, TLR8, and TLR9 and cell surface TLR5 additionally requires the chaperone Unc93B1 (Huh et al., 2014; Kim et al., 2008). Once these TLRs are folded, Unc93B1 stays associated to maintain their stability (Pelka et al., 2018) and further promotes their incorporation into COPII-coated vesicles to leave the ER. While TLR3, TLR7, and TLR8 are directly transported to the endosome, TLR9 is first delivered to the plasma membrane and later endocytosed in an AP-2-dependent manner (Lee et al., 2013).

Upon ligand sensing, TLRs homo- or heterodimerize and initiate the activation of downstream signaling pathways that result in the activation of transcription factors like NF-κBs and IRFs, leading to the production of pro-inflammatory cytokines and type I interferons (Fitzgerald and Kagan, 2020). TLR signaling is enabled by the recruitment of a large assembly of cytosolic proteins, leading to the formation of two distinct signaling hubs: the myddosome (Lin et al., 2010; Motshwene et al., 2009) and the triffosome (Fitzgerald and Kagan, 2020). Signaling hubs are not present in resting cells but are rapidly induced after TLR dimerization (Bonham et al., 2014). Myddosome formation is mediated by the recruitment of the adaptor molecule MyD88 to the cytosolic TLR TIR domains. Except for TLR3, MyD88 is recruited to all TLRs upon their engagement (Kawai and Akira, 2006). TLR2, TLR4, TLR7, and TLR9 additionally require the adaptor molecule TIRAP/MAL to recruit MyD88 (Bonham et al., 2014; Fitzgerald et al., 2001; Horng et al., 2001; Nagpal et al., 2009; Piao et al., 2015). Once MyD88 is associated with the TLR TIR domain, it recruits IRAK kinases via its death

domain (Cao et al., 1996a). By solving the structure of the myddosome complex, it was discovered that the myddosome is a helical oligomer composed of six MyD88, four IRAK4, and four IRAK2 molecules. Myddosome assembly brings the IRAK kinase domains into close proximity, leading to their phosphorylation and auto-activation (Lin et al., 2010). Activation of IRAK kinases further results in the recruitment of the E3 RING ligase TNF receptor-associated factor 6 (TRAF6) (Cao et al., 1996b). TRAF6, along with the ubiquitin-conjugation enzymes UBC13 and UEV1A, facilitates its own ubiquitin-K63 linkage, thereby creating a scaffold for TAK1 (Deng et al., 2000; Wang et al., 2001a). TAK1 in complex with the adaptor proteins TAB1/TAB2 or TAB1/TAB3 further activates two distinct pathways (Cheung et al., 2004; Shibuya et al., 1996; Takaesu et al., 2000). The first involves activation of the IKK complex, leading to NF-κB activation and the induction of pro-inflammatory cytokines as described in detail above (see Fig. 1). Additionally, TAK1 can activate MAPK members such as ERK1/2, p38, and JNK, leading to the activation of the transcription factor AP-1 (Fitzgerald and Kagan, 2020) (see Fig. 2).

The second signaling hub that can be formed downstream of TLR3 and TLR4 is the triffosome. Here, the adaptor molecule TRIF is directly recruited to TLR3 and indirectly recruited to TLR4 via the adaptor molecule TRAM (Fitzgerald et al., 2003b; Yamamoto et al., 2003). Like MyD88, TRIF can recruit the E3 ligase TRAF6, which in turn recruits the kinase receptor-interacting serine/threonine-protein kinase 1 (RIPK1). RIPK1 then phosphorylates and activates the kinase TAK1, activating the NF-κB and MAPK signaling pathway (Kawasaki and Kawai, 2014) (see Fig. 2).

Additionally, TRIF can activate an alternative signaling pathway that leads to IRF3 activation, ultimately inducing the expression of type I interferons downstream of TLR3 and TLR4 activations. Upon binding to the TIR domain, TRIF recruits the E3 ligase TRAF3 and maybe other TRAFs, which, upon activation, undergo self-ubiquitination. This creates a scaffold for the recruitment of TBK1, which in turn phosphorylates the pLxIS motif of TRIF, resulting in the activation of IRF3 as described earlier (see Fig. 1) (Fitzgerald et al., 2003a; Liu et al., 2015b).

Signaling of TLR7, TLR8, and TLR9 also leads to the expression of type I interferons, but independent of TRIF. These TLRs signal via the adaptor protein “TLR adaptor interacting with SLC15A4 on the lysosome” (TASL), which interacts with the endolysosomal transporter SLC15A4, a lysosomal transmembrane protein known to

shuttle oligopeptides across the lysosomal membrane. TASL contains the same pLxIS motif as TRIF, MAVS, and STING, which enables the activation of IRF5 (Heinz et al., 2020) (see Fig. 2).

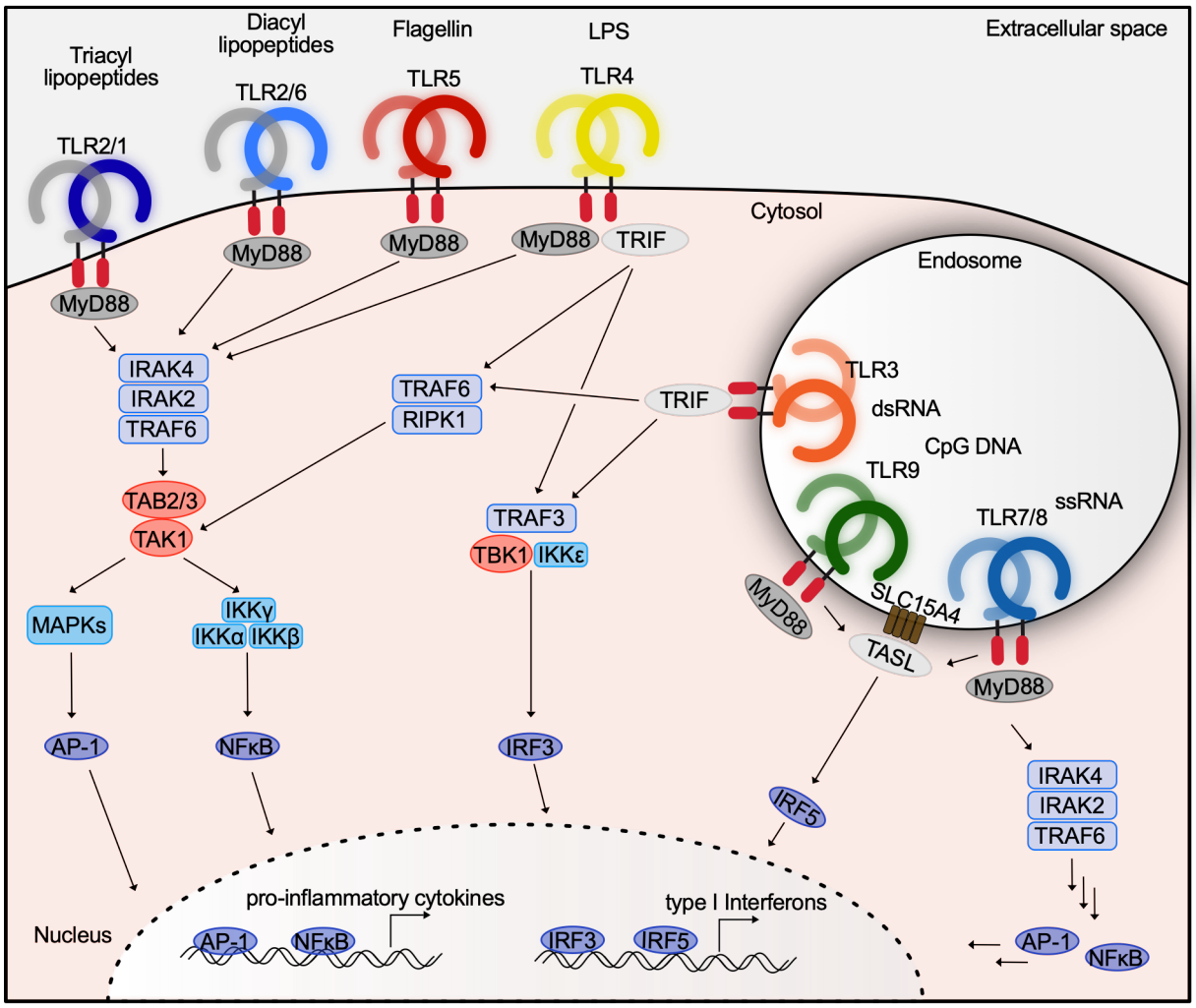

Figure 2 Toll-like receptor signaling pathways: The TLR family is divided into plasma membrane-resident TLRs that sense microbial membrane components and endosomal nucleic acid-sensing TLRs. Except for TLR3, the adaptor molecule MyD88 is recruited to all TLRs upon ligand binding. MyD88 recruitment initiates a signaling cascade that ultimately leads to NF-κB and AP-1 activation and consequently the expression of pro-inflammatory cytokines. TLR4 and TLR3 further recruit the adaptor molecule TRIF, leading to IRF3 activation and the expression of type I interferons. TLR7, TLR8, and TLR9 additionally signal via the adaptor molecule TASL, thereby activating the transcription factor IRF5.

1.3.1 Nucleic acid recognition by TLR7, TLR8 and TLR9

TLR7, TLR8, and TLR9 differ in their expression profile. While high levels of TLR7 and TLR9 are predominantly found in plasmacytoid dendritic cells and B cells, TLR8 is not found in pDCs but is highly abundant in monocytes, macrophages, and monocyte-derived DCs (mDCs) (Hornung et al., 2002).

In addition to the common TLR architecture, these receptors contain a Z loop in their LRR domain. Cleavage of the Z loop is essential to obtain mature and functional receptors (Maeda and Akira, 2016; Ohto et al., 2015; Tanji et al., 2015; Zhang et al., 2016) and is mediated by cathepsins or asparagine endopeptidase (Ewald et al., 2011). Upon cleavage of the Z loop, the two LRR domains stay non covalently associated and form a functional unit that senses nucleic acids (Ohto et al., 2015; Tanji et al., 2015; Zhang et al., 2016). The crystal structure of the TLR9 ectodomain revealed that the immune receptor senses two types of ssDNA using two distinct binding pockets. Pocket 1 recognizes a 5'-xCx motif, with x indicating any nucleoside, and pocket 2 engages unmethylated CpG DNA motifs. Moreover, it was found that occupation of both binding sites is required to promote receptor dimerization and activation (Ohto et al., 2018; Ohto et al., 2015). Fragments for TLR9 are generated by the enzyme DNase II in the lysosomal compartment by cutting 20-mer DNA fragments into smaller 11-12-mers (Chan et al., 2015). TLR9-dependent DNA responses were further demonstrated to be regulated by the lysosomal exonucleases PLD3 and PLD4, which are discussed in more detail below (see Chapter 1.6) (Gavin et al., 2018).

TLR7 and TLR8 are closely related TLRs that both sense guanosine and uridine-rich ssRNA (Heil et al., 2004) derived from a wide range of pathogens, e.g., influenza A virus (Wang et al., 2008). Similar to TLR9, crystal structure analysis of TLR7 and TLR8 ectodomains showed that these receptors also contain two distinct ligand-binding pockets to sense degradation products of ssRNA. The structure of hTLR8 ectodomain was solved first, revealing that the nucleoside uridine engages the first binding pocket of TLR8, located at the dimerization interface. The second pocket, located at the concave surface of TLR8, shows high affinity for UG-terminated short oligonucleotides (Tanji et al., 2015). TLR7 also senses a single nucleoside in its first pocket, recognizing guanosine instead of uridine, while its second pocket binds short uridine-containing fragments (Zhang et al., 2016). A follow-up study examining the exact binding site

fragments revealed that a specific phosphorylation at the ribose of guanosine, namely 2',3'-cyclic guanosine monophosphate (2',3'-cGMP), is favored over unphosphorylated guanosine (see Fig. 3, right).

Both ligands engage TLR7 through partly the same non-covalent interactions, whereas the cyclic phosphate of 2',3'-cGMP forms three additional hydrogen bonds in the first binding pocket. Specifically, hydrogen bonds are formed with the main-chain and side-chain nitrogen atoms of amino acid Q354 and with the side-chain OH-group of amino acid Y264 (see Fig. 3, left). Consistent with this observation, isothermal titration calorimetry (ITC) binding assays revealed that 2′,3′-cGMP binds with approximately sixfold higher affinity to TLR7 than guanosine. Additionally, 2',3'-cGMP induced stronger TLR7 activation in cells compared to guanosine. Consequently, it was proposed that 2',3'-cGMP serves as the endogenous ligand of TLR7 pocket 1 (Zhang et al., 2018).

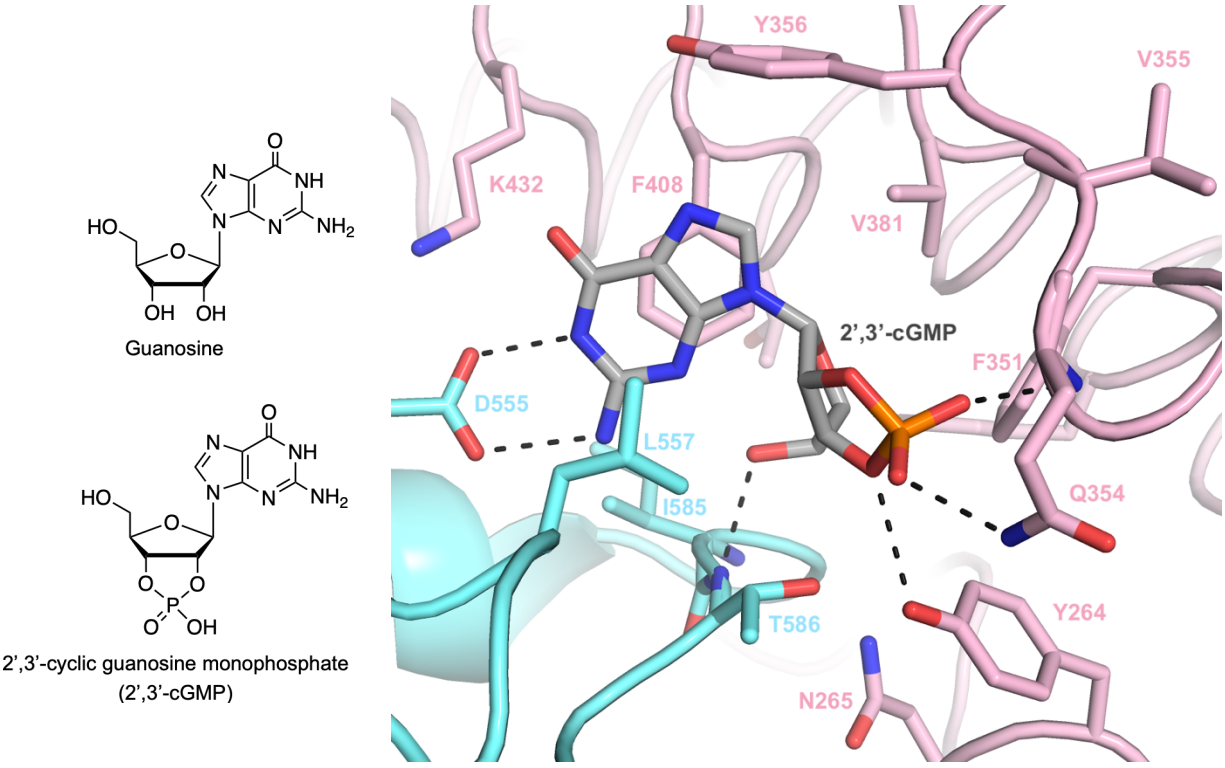

Figure 3 2‘,3‘-cGMP binding to TLR7 pocket 1: Chemical structures of guanosine and 2‘,3‘-cyclic guanosine monophosphate (2',3'-cGMP) (left) and 2‘,3‘-cGMP binding to TLR7 pocket 1 (right) are depicted. Nitrogen atoms are marked in blue and oxygen atoms are marked in red. 2',3'-cGMP forms hydrogen bonds (black dashed lines) with amino acids D555, T586, Y264, and Q354 in TLR7 pocket 1(PDB: 6IF5 (Zhang et al., 2018), image generated with PyMOL).

In the absence of ligands, TLR7 exists as a monomeric protein. Engagement of a short oligonucleotide in pocket 2 leads to structural changes in the receptor, thereby enhancing the binding affinity of the first pocket ligand, resulting in its dimerization and activation (Zhang et al., 2016). TLR8, on the other hand, is proposed to exist as a preformed inactive dimer after Z loop cleavage that transforms into an active dimer upon agonist binding (Tanji et al., 2016; Tanji et al., 2013; Tanji et al., 2015).

Although endolysosomal TLRs have evolved to detect viral and microbial nucleic acids from diverse sources, their aberrant activation by self-nucleic acids can contribute to the development of autoimmune diseases such as systemic lupus erythematosus (SLE) (Celhar et al., 2012; Pelka et al., 2016). Over the past decades, several hypotheses have emerged to explain why intracellular TLRs do not recognize self-nucleic acids under healthy conditions. Among many, it was proposed that the localization of TLR7, TLR8, and TLR9 in the endolysosome shields them from self-RNA and self-DNA that is released from dead or dying cells. By engineering TLR9 expression to the cell surface instead of the lysosomal compartment, it was demonstrated that cell surface TLR9 indeed displayed responses to endogenous DNA, which was added to the culture medium. In contrast, lysosomal TLR9 remained unresponsive to such DNA (Barton et al., 2006). Although not shown for TLR7 and TLR8, it is conceivable that a similar scenario applies for these two receptors. Second, it is hypothesized that lysosomal TLRs can tolerate a certain amount of RNA and DNA being present without being activated and that a definite immunostimulatory threshold - in terms of quantity - must be reached to trigger dimerization and signaling of these receptors (Roers et al., 2016). This would explain that pathological conditions associated with increased release or supply of endogenous nucleic acids can lead to TLR-dependent inflammatory responses. Third, similar to a quantity threshold for RNA and DNA, it was demonstrated that the expression of TLRs and their delivery into endosomes also regulate their activation. As such, duplication of the TLR7 gene locus was shown to exacerbate a lupus-like disease phenotype in mice (Deane et al., 2007), and similarly, mice engineered to express high amounts of human TLR8 were demonstrated to suffer from multi-organ inflammatory syndrome that mainly arises from activation of myeloid cells (Guiducci et al., 2013). Additionally, increased trafficking of TLRs into endosomes also enhances their potential to sense endogenous nucleic acids. In this context, it was shown that TLR7, TLR8, and TLR9 compete for

the chaperone Unc93B1 to reach the endosomal compartment (Fukui et al., 2009) and in the absence of TLR8 and TLR9, higher levels of TLR7 are found within endosomes, leading to enhanced or even spontaneous TLR7-driven autoimmunity (Christensen et al., 2006). Lastly, modifications found in endogenous nucleic acids have been proposed to help distinguish between self and non-self. A prominent example is the case of TLR9, which has been shown to ignore methylated CG dinucleotides, as it is commonly the case in endogenous DNA (Lamphier et al., 2006). Further, in vertebrates, endogenous RNAs are post-transcriptionally modified at their nucleobase, ribose, or phosphate, and more than 170 of such nucleoside modifications exist (Cappannini et al., 2024; Rozenski et al., 1999). In this regard, a pioneer study from Katalin Karikó in 2005 demonstrated that certain RNA modifications, like pseudouridine, 5-methylcytosine (m5C), 6-methyladenosine (m6A), 5-methyluridine (m5U), or 2-thiouridine (s2U) that are present in self-RNA lack immune-stimulatory potential for TLR3, TLR7, and TLR8 (Kariko et al., 2005). Additionally, a recent study proposed that 2'O-methyl guanosine, which is naturally found in ribosomal RNA, can act as a natural inhibitor for TLR7 and TLR8 by occupying a newly identified third binding pocket of the receptors, thereby keeping the receptors in an inactive open form state (Alharbi et al., 2024).

1.4 Pseudouridine

Pseudouridine (Ψ), first identified in 1951 (Cohn and Volkin, 1951), is the most abundant mammalian RNA modification that makes up 9% of the total uridine pool in human RNA. It is found in all subtypes of human RNA, including messenger RNA (mRNA), transfer RNA (tRNA), ribosomal RNA (rRNA), or small nuclear RNA (snRNA) (Borchardt et al., 2020). This nucleobase modification is not exclusively found in humans; however, eukaryotes possess four to eight times more pseudouridine than bacteria (Ofengand, 2002). Chemically, pseudouridine is an isomer of uridine, in which the β-D-ribose is attached to a carbon atom of the uracil base, introducing a carbon-carbon glycosidic bond (C-C) instead of the conventional nitrogen-carbon (N-C) glycosidic bond (see Fig. 4).

This small change, introducing an additional hydrogen bond donor on the non-Watson-Crick edge, has been shown to significantly enhance RNA stability when incorporated (Kierzek et al., 2014).

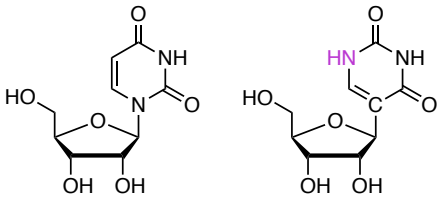

Figure 4 Chemical structures of Uridine (left) and Pseudouridine (right).

In human cells, two distinct mechanisms introduce pseudouridine into RNA post-transcriptionally. One is carried out by a family of stand-alone enzymes known as pseudouridine synthases (PUS). In eukaryotes, this family comprises ten members, which are localized in the nucleus, the cytoplasm, or the mitochondria, where they pseudouridylate a wide range of RNA substrates. These enzymes either recognize a defined nucleotide sequence or a structural RNA motif containing the target uridine (Rintala-Dempsey and Kothe, 2017). Examples of this are PUS7, which has been shown to specifically pseudouridylate the second uridine within a UGUAR sequence motif, and PUS1, which pseudouridylates RU motifs (R for purine base) (Carlile et al., 2014). Mechanistically, their catalysis is initiated by the deprotonation of the ribose sugar, leading to the cleavage of the N–C glycosidic bond, followed by rotation of the uracil ring and its reattachment to the ribose (Veerareddygari et al., 2016). In addition to the 10 PUS enzymes, Dyskerin (DKC1) catalyzes pseudouridylation in an RNA-guided manner. Together with non-histone protein 2 (NHP2), nucleolar protein 10 (NOP10), and glycine-arginine-rich protein 1 (GAR1), DKC1 assembles into ribonucleoprotein complexes with small non-coding RNAs that guide the complex to specific target sites. In association with box H/ACA small nucleolar RNAs (snoRNAs), the complex installs Ψ residues in rRNA, whereas in association with small Cajal body-specific RNAs (scaRNAs), it modifies small nuclear RNAs (snRNAs).

The natural incorporation of pseudouridine into endogenous RNA impacts multiple cellular processes such as protein translation, protein-RNA interactions, and mRNA splicing, and mutations in pseudouridine synthases have been associated with many diseases, including cancer (Cerneckis et al., 2022).

Beyond its natural occurrence, substituting uridine with pseudouridine in synthetic and *in vitro* transcribed mRNAs has been shown to modulate the activation of several innate immune sensors. Specifically, it was demonstrated that incorporating pseudouridine into synthetic RNAs reduces their immune-stimulatory potential for the endosomal receptor TLR3 and completely abolishes activation of TLR7 and TLR8 (Kariko et al., 2005). In addition, it also eliminates RIG-I-dependent IFN-α production in human monocytes and primary plasmacytoid dendritic cells (Hornung et al., 2006). While pseudouridine-modified RNA can bind to RIG-I, it does not induce the necessary conformational changes required for RIG-I activation (Durbin et al., 2016). Apart from the lack of immune stimulation, follow-up studies investigating translational capacities of pseudouridine mRNA found that protein translation is also dramatically enhanced when uridine in the mRNA is substituted with pseudouridine (Karikó et al., 2008). Mechanistically, this could be explained by the observation that *in vitro* transcribed mRNA containing pseudouridine binds to and activates RNA-dependent protein kinase R (PKR) less efficiently than uridine-containing mRNA. Since PKR phosphorylates and activates the translation initiation factor eIF-2α, leading to inhibition of translation, reduced PKR activation results in higher translation of pseudouridine-modified mRNA (Anderson et al., 2010). Additionally, pseudouridine-substituted mRNA was found to limit the activation of 2'-5'-oligoadenylate synthase (OAS) and was suggested to enhance resistance to the enzyme RNase L (Anderson et al., 2011). The evidence that RNA modifications improve protein translation has prompted a plethora of studies investigating different modifications or combinations thereof to further enhance protein output from synthetic mRNAs. Thus, it was discovered that N1-methylpseudouridine (see Fig. 5), a rare modification with one occurrence in human 18S rRNA at position 3797 (Taoka et al., 2018), further increases protein synthesis when incorporated into mRNA compared to pseudouridine mRNA (Andries et al., 2015). This observation was partly attributed to the fact that it reduces immune-stimulatory potential for TLR3 compared to pseudouridine in several cell models and mice (Andries et al., 2015). Additionally, using cell-free translation systems, it was demonstrated that N1-methylpseudouridine enhances ribosome pausing and increases ribosome density on the transcript, ultimately leading to elevated protein expression levels (Svitkin et al., 2017). The findings that

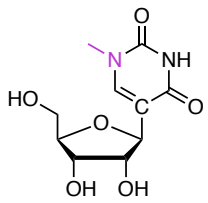

Figure 5 Chemical structure of N1-methylpseudo-uridine

pseudouridine and N1-methylpseudouridine synthetic RNAs reduce immunogenicity and, at the same time, increase protein translation were key to the successful development of mRNA therapeutics such as the COVID-19 vaccines by Pfizer-BioNTech (BNT162b2) and Moderna (mRNA-1273). Here, the spike protein encoding mRNA was fully substituted with N1-methylpseudouridine (Nance and Meier, 2021). In light of the success and lifesaving impact, the discoveries leading to this application were consequently awarded the Nobel Prize in Physiology and Medicine in 2023 to Katalin Karikó and Drew Weissman. Although it has been well established that pseudouridine or N1-methylpseudouridine RNA lacks immune-stimulatory potential for TLR7 and TLR8, the molecular mechanism of this immune evasion remained unknown.

1.5 Lysosomal nucleases upstream of Toll-like receptors 7 and 8

Ribonucleases (RNases) are enzymes that catalyze RNA degradation by hydrolytic cleavage of the phosphodiester bond (Berg et al., 2012). They are present across all domains of life - archaea, bacteria, and eukaryotes - and participate in essential cellular processes like DNA replication (Nishino and Morikawa, 2002), regulation of gene expression (Ohyama et al., 2014), or the defense against pathogens (MacIntosh, 2011). In eukaryotes, RNases are distributed across several cellular compartments. They are present in the cytosol and the secretory pathway, from which they can be directed either to the extracellular space or endosomal/lysosomal compartments.

Within the endosome, only a limited number of RNases have been reported. These include human RNase T2, belonging to the RNase Rh/T2/S acidic hydrolase subfamily, and members of the RNase A family, including RNase 1, RNase 2, and RNase 6 (Lübke et al., 2009). By degrading RNA within the endolysosomal compartment, RNase T2 has been shown to play a non-redundant, positive regulatory role upstream of TLR8. Specifically, RNase T2 cleaves ssRNA between a purine base and uridine, thereby generating 2',3'-cyclic purine-terminated fragments that bind to the second binding pocket of TLR8 (Greulich et al., 2019). In conjunction with RNase 2, another study reported that RNase T2 also contributes to the release of free uridine for the first binding pocket of TLR8 (Ostendorf et al., 2020). Additionally, TLR8 activation by

bacterial RNA has been demonstrated to depend on the enzyme RNase 6 (Nunes et al., 2024).

Although genetic deletion studies of RNase T2 and RNase 6 in primary cells implicated a role for these nucleases upstream of TLR7, their mechanistic role in modulating TLR7 activation has remained unknown (Liu et al., 2021; Tong et al., 2024). Additionally, the exonuclease activity of PLD3 and PLD4 was proposed to function upstream of TLR7 (Gavin et al., 2021), which will be discussed in more detail below (see Chapter 1.6).

1.5.1 RNA cleavage by RNase T2 and RNase A enzymes

Enzymes from the RNase T2 family are transferase-type endoribonucleases that generate oligonucleotides with a terminal 3' phosphate via a 2',3'-cyclic intermediate. Except for archaea, members of the RNase T2 family are present in all other living organisms, including bacteria, fungi, plants, and animals. In eukaryotes, RNase T2 is particularly well conserved, with at least one gene copy found in every genome, indicating that these enzymes carry out essential biological functions that are maintained throughout evolution (MacIntosh, 2011).

Solving the structure of human RNase T2 has revealed that this enzyme crystallizes as a monomeric protein. Similar to other T2 family members, the structure of human RNase T2 is composed of seven α-helices and eight β-strands, featuring two conserved regions crucial for substrate binding, known as the CASI (conserved active site segment or B1) and CASII (B2) pockets. Comparison with other RNase T2 homologs identified the amino acids H65, H113, Q114, K117, and H118 as part of the active site. Interestingly, a potential zinc binding site was identified for RNase T2. However, the addition of zinc or copper ions inhibited the activity of human RNase T2 (Thorn et al., 2012). Although the structure of human RNase T2 in complex with a ligand has not been solved to date to investigate base specificity, structural investigation of the RNase T2 ortholog ribonuclease MC1 of *Momordica charantia* in complex with uridine monophosphate demonstrated a clear substrate preference for uridine in the B2 pocket (Suzuki et al., 2000). Additionally, biochemical assays showed that human RNase T2 exhibits a base preference for cleaving ssRNA between a purine base and uridine, thereby generating 2',3'-cyclic purine-terminated fragments (Greulich et al., 2019). Another study, however, reported a more relaxed substrate specificity

with additional cleavage observed between two uridine nucleotides (Ostendorf et al., 2020).

The cleavage mechanism of RNase T2 enzymes has mainly been studied in plants and fungi (Kawata et al., 1990; Parry et al., 1997). However, based on the similarity of the active center (geometry and conserved amino acid residues), these findings can most likely be extrapolated to human RNase T2. For RNA cleavage by RNase Rhizopus niveus, two histidines, H46 and H109 (correlating to H65 and H113 for human RNase T2), are crucial for its activity and act in a two-step acid-base-catalyzed mechanism (see Fig. 6). In the first step, H109 acts as the general base to deprotonate the 2'-OH group of the ribose. H46 acts as the general acid, providing a proton to the cleaved 5'-OH group, resulting in a 2',3'-cyclophosphate oligonucleotide (see Fig. 6) (MacIntosh, 2011; Ohgi et al., 1992).

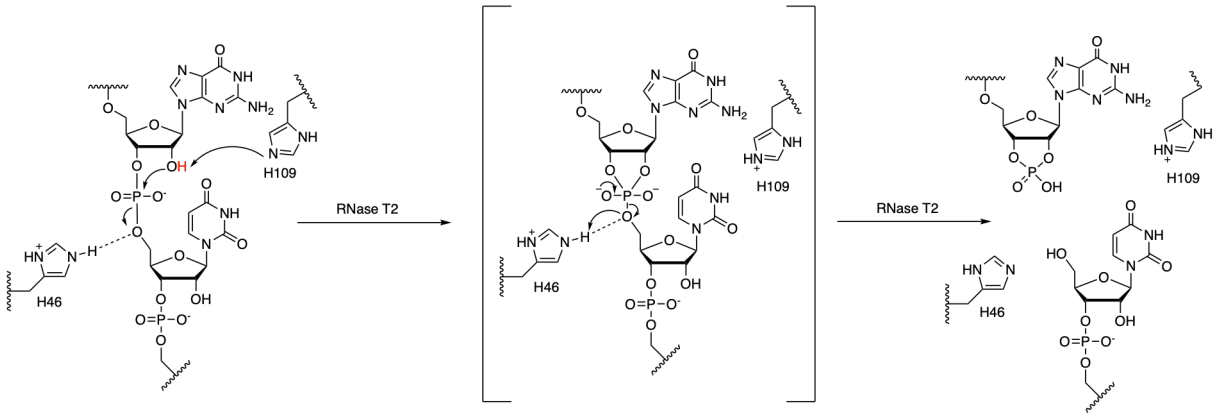

Figure 6 Mechanism of acid-base catalysis by RNase T2: H109 acts as a general base, abstracting a proton from the 2'-hydroxyl group of the ribose in guanosine, thereby facilitating nucleophilic attack. Simultaneously, H46 functions as a general acid by donating a proton to the leaving 5'-hydroxyl group, leading to the formation of a 2',3'-cyclic phosphate-terminated oligonucleotide.

In a subsequent step, reported for other family members of the RNase T2 family, the 2',3'-cyclic phosphate intermediate is further hydrolyzed into 3'-phosphate oligonucleotides (MacIntosh, 2011). However, this step is most likely not carried out by human RNase T2 within the lysosomal compartment, as stable 2',3'-cyclic phosphate-terminated oligonucleotides are detected by LC-MS following RNase T2-mediated cleavage (Greulich et al., 2019). Deprotonation of the 2'-OH group is essential to initiate cleavage of RNA by RNase T2. Therefore, it is not surprising that substitution

of the 2'-OH group with a 2'-OMe group blunts cleavage by human RNase T2 (Ostendorf et al., 2020; Tong et al., 2024).

In contrast to RNase T2, which is present in nearly all living organisms, RNase A family enzymes are restricted to vertebrates. These enzymes are believed to have originated from a RNase 5-like gene that expanded in mammals in response to functional demand (Cho et al., 2005). Nevertheless, recent evidence indicates that RNase A-like enzymes may also exist in some bacteria (Cuthbert et al., 2018).

In humans, the RNase A family comprises 13 members, all located on chromosome 14. The family members are divided into canonical RNases 1-8 and non-canonical RNases 9-13. While canonical RNases possess ribonuclease activity, non-canonical RNases do not (Cho et al., 2005). Like for RNase T2, a catalytic triad consisting of one lysine and two histidine residues accounts for the endoribonuclease activity of canonical RNases. RNase A family members hydrolyze RNA in a similar transphosphorylation and hydrolysis fashion as RNase T2, resulting in 2',3'-cyclic phosphate-terminated RNA fragments (Raines, 1998). However, these enzymes exhibit a different base specificity than human RNase T2, cleaving RNA specifically between a pyrimidine base and any other nucleobase. This specificity arises from a conserved threonine residue in their active site, which mediates hydrogen bonding with cytidine or uracil bases (Kelemen et al., 2000) (see Fig. 7).

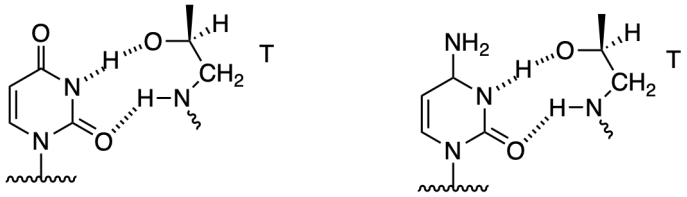

Figure 7: Hydrogen bonds formed between threonine (T) in the active site of RNase A enzymes with uracil (left) and cytidine (right).

1.6 Phospholipase D3 and Phospholipase D4

In addition to endoribonucleases, two exonucleases have been reported to be found inside the lysosomal compartment of a eukaryotic cell, namely Phospholipase D3 (PLD3) and Phospholipase D4 (PLD4) (Gonzalez et al., 2018; Lübke et al., 2009; Otani et al., 2011). Generally, exonucleases do not produce short oligonucleotides like an

endonuclease but cut RNA or DNA from the 3’ or 5’ end into single nucleotides (Berg et al., 2012).

PLD3 and PLD4 are members of the Phospholipase D (PLD) protein family, which includes six members in mammals characterized by conserved domain structures: PLD1 through PLD6. All proteins in this family share a conserved catalytic site signature known as the “HKD” motif (HxxKxxxxD, where "x" represents any amino acid). Among them, PLD1 and PLD2 are the best characterized enzymes, converting phosphatidylcholine into choline and phosphatidic acid (McDermott et al., 2020). Hence, the protein family was dubbed phospholipase D, because these enzymes cleave the phospholipid between the phosphate and the headgroup (R3). Nevertheless, apart from PLD3 and PLD4 – in detail discussed below – PLD5 appears to lack phospholipase activity (McDermott et al., 2020). PLD6, on the other hand, has been shown to exhibit phospholipase activity (Huang et al., 2011) and ssRNA endonuclease activity, producing 5′-monophosphate oligoribonucleotides (Ipsaro et al., 2012; Nishimasu et al., 2012).

PLD3 and PLD4 are glycosylated type II transmembrane proteins that, as mentioned above, localize to the endosomal compartment of the cell (Gonzalez et al., 2018; Lübke et al., 2009; Otani et al., 2011). Proteolytic cleavage of the transmembrane domain after endosomal transport, resulting in a soluble form of the protein, has been reported for PLD3 (Gonzalez et al., 2018). Although this has not been experimentally confirmed for PLD4, a similar processing mechanism likely also occurs for PLD4. Unlike the other PLD family members, PLD3 and PLD4 contain a conserved glutamate to aspartate substitution in the second HxKxxxD motif, resulting in one HKD and one HKE motif. While PLD3 is broadly expressed across various tissues, PLD4 shows high expression exclusively in myeloid and dendritic cells, with low levels in B cells (information taken from the human protein atlas). Although studies linked PLD4 polymorphism to rheumatoid arthritis (Chen et al., 2017), systemic sclerosis (Terao et al., 2013), and systemic lupus erythematosus (SLE) (Akizuki et al., 2019), and PLD3 polymorphism to Alzheimer’s disease (Cruchaga et al., 2014), their function and role remained largely unknown.

In 2018, purification of soluble PLD3 and PLD4 revealed that these proteins exhibit 5’ exonuclease activity toward ssDNA, resulting in 3’ phosphorylated mononucleotides. The authors further demonstrated that PLD3 and PLD4 require unphosphorylated 5’

ends and are most active at an acidic pH, matching their localization in the endosomal compartment. Interestingly, the biochemical properties matched those previously attributed to spleen acid exonuclease. Purification of the active fractions from the commercially available preparation, followed by peptide mass spectrometry, confirmed that spleen acid exonuclease is, in fact, PLD3. In addition to the biochemical characterization of PLD3 and PLD4, the characterization of PLD4-deficient mice revealed that these animals develop an inflammatory disease and splenomegaly in a TLR9-dependent manner. Similarly, macrophages from PLD3-deficient mice displayed increased sensitivity to TLR9 ligands, suggesting that both PLD3 and PLD4 act as negative regulators of TLR9 activation by degrading its ligands. Mice lacking both enzymes developed a lethal hepatic autoinflammatory condition and failed to survive past weaning. Notably, bone marrow-derived macrophages expressing both PLD3 and PLD4 exhibited heightened responsiveness to TLR9 ligands only when both enzymes were absent, but not when either alone was deleted, indicating functional redundancy between the two proteins (Gavin et al., 2018). Based on the complete rescue of the PLD4-deficient phenotype by TLR9 deletion and the proposed functional redundancy between PLD3 and PLD4, a subsequent study investigated whether TLR9 ablation could rescue the phenotype of mice lacking both enzymes. Interestingly, while TLR9 ablation was sufficient to rescue survival of the *Pld3*$^{-/-}$x*Pld4*$^{-/-}$ mice, these animals continued to exhibit pronounced abnormalities, including splenomegaly, anemia, and thrombocytopenia. This observation led to the hypothesis that additional endosomal nucleic acid-sensing pathways might contribute to the phenotype observed. Subsequently, introducing an UNC93B1 mutation (Unc93b1$^{3d/3d}$), which blocks TLR transport to endosomes, thereby preventing sensing through all endosomal TLRs such as TLR3, TLR7, TLR9, TLR11, TLR12 and TLR13, mostly normalized the phenotypes compared to the *Tlr9*$^{CpG11/CpG11}$ x *Pld3*$^{-/-}$ x *Pld4*$^{-/-}$ mice. These results indicated that endosomal TLR sensing of ssRNA plays a role in the pathology associated with PLD3 and PLD4 deficiency, implying that these enzymes also target ssRNA for degradation. Supporting this, PLD3 and PLD4 were shown to degrade not only ssDNA but also ssRNA, exhibiting similar biochemical characteristics in both cases, including an acidic pH optimum, 5' to 3' exonuclease activity, and a preference for unphosphorylated 5' ends (Gavin et al., 2021).

While the absence of PLD3 and PLD4 enhanced TLR9 responses (Gavin et al., 2018), TLR7 stimulation in dendritic cells from *Tlr9*$^{CpG11/CpG11}$ x *Pld3*$^{-/-}$ x *Pld4*$^{-/-}$ mice yielded highly variable outcomes depending on the RNA ligand used. Specifically, some RNA sequences increased TLR7 sensitivity in the absence of PLD3 and PLD4, whereas others resulted in reduced activation or no change. These findings suggested that PLD3 and PLD4 generally act as negative regulators of TLR7, similar to their role with TLR9. However, it was concluded that these proteins also positively regulate TLR7 in certain contexts, depending on the RNA sequence. Notably, dendritic cells from *Tlr9*$^{CpG11/CpG11}$x*Pld3*$^{-/-}$x*Pld4*$^{-/-}$ mice further exhibited increased sensitivity toward the TLR13 ligand Sa19, suggesting that PLD3 and PLD4 also negatively regulate this receptor in mice.

Since *Unc93b1*$^{3d/3d}$ x*Pld3*$^{-/-}$x*Pld4*$^{-/-}$ animals still displayed an elevated type I interferon signature, the involvement of the cytoplasmic STING pathway was assessed. To this end, STING-deficient quadrupole mutant mice (*Tmem173*$^{gt/gt}$x*Unc93b1*$^{3d/3d}$x*Pld3*$^{-/-}$ x*Pld4*$^{-/-}$) were generated. In these animals, serum cytokine levels were fully normalized, supporting the hypothesis that, in the absence of PLD3 and PLD4, lysosomal ssDNA accumulates and leaks into the cytoplasm, where it activates the cGAS/STING signaling axis (Gavin et al., 2021). Another study, using SH-SY5Y neuroblastoma cells, also reported that PLD3 ablation activates the cGAS/STING signaling pathway through lysosomal leakage of unprocessed mitochondrial DNA into the cytoplasm (Van Acker et al., 2023). In conclusion, by degrading both ssDNA and ssRNA, PLD3 and PLD4 are crucial in regulating multiple innate immune sensors, including endosomal TLRs and the cytoplasmic cGAS/STING pathway (see Fig. 8).

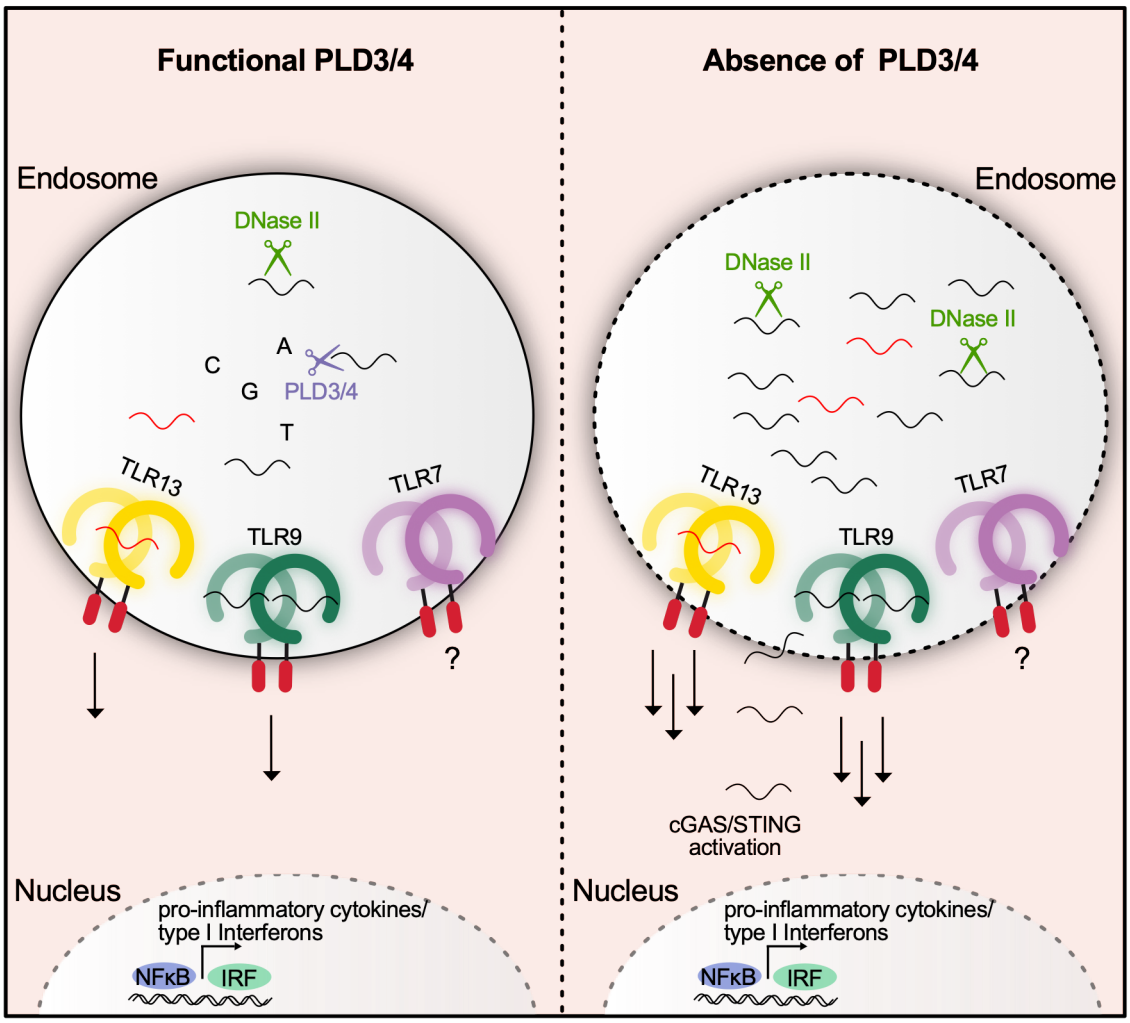

Figure 8: Consequences of non-functional PLD3 and PLD4 in cells: In the presence of PLD3 and PLD4 (left side), the enzymes degrade ssDNA (black) that is processed by the enzyme DNase II. Thereby, PLD enzymes negatively regulate TLR9 by destroying its ligands. PLD3 and PLD4 also degrade ssRNA (red), thus controlling the activation of the immune receptor TLR13. In the absence of PLD3 and PLD4 (right side), ssDNA and ssRNA accumulate in the endosome, leading to hyperactivation of TLR9 and TLR13. Accumulated endosomal DNA further leaks into the cytosol, where it activates the cGAS/STING pathway in the absence of PLD enzymes. How PLD3 and PLD4 influence TLR7 signaling is unclear.

In the course of our project, structural studies revealed that PLD3 and PLD4 form homodimers (Roske et al., 2023; Yuan et al., 2024). In contrast to other PLD family members, such as Nuc from S. typhimurium, whose dimerization results in a single active site (Stuckey and Dixon, 1999), PLD3 and PLD4 homodimers exhibit two active sites, each formed by two HKD/E motifs from a single monomer, positioned on opposing sides of the dimer interface. Since the dimerization interfaces of PLD3 and PLD4 are largely conserved, the potential for heterodimerization of the two proteins has been suggested, although this hypothesis has not been experimentally confirmed (Roske et al., 2023). Co-crystallization of PLD3 with a short ssDNA substrate suggests

a DNA cleavage mechanism similar to the endoribonuclease Zucchini, the *Drosophila* homolog of PLD6. Specifically, H428 in PLD4 and H416 in PLD3, located within the second HKE motif, are proposed to function as a nucleophile to attack the phosphodiester bond of the DNA or RNA, leading to a phospho-histidine intermediate. Subsequently, H214 (PLD4) and H201 (PLD3), from the first HKD motif, serve as general acids to protonate the 5'-OH leaving group, thereby facilitating cleavage (Roske et al., 2023; Yuan et al., 2024).

Because capturing PLD enzymes bound to 5'-OH ssDNA remains challenging, one study aimed to co-crystallize PLD4 with a 5′-phosphorylated (5'-Pi) DNA substrate, as such substrates were previously reported not to be cleaved by PLD3 and PLD4 (Gavin et al., 2018). Interestingly, the structure revealed that the second histidine of PLD4 (H428) was phosphorylated, suggesting that the 5'-phosphate group of the DNA substrate had been cleaved, thereby explaining the inhibitory effect of this DNA molecule. Subsequent biochemical assays confirmed phosphatase activity for PLD3 and PLD4, yet with >10.000 fold slower kinetics compared to their nuclease activity (Yuan et al., 2024).

Further expanding on their functional repertoire, it was recently shown that PLD3 and PLD4 also catalyze the stereoinversion of S,S-BMP (Bis(monoacylglycerol)phosphate) from R, S-BMP, a crucial component required for the degradation of lipids, in particular gangliosides, in the lysosome. Changes in BMP levels are associated with neurodegenerative diseases marked by gangliosidosis and lysosomal abnormalities. Consequently, PLD3 and PLD4 are believed to play a role in maintaining brain health (Singh et al., 2024). These recent findings suggest that PLD3 and PLD4 are involved in both phospholipid metabolism and nucleic acid degradation. However, how they distinguish between these two functions remains to be elucidated in future studies.

2 Summary

2.1 RNA processing upstream of Toll-like receptor 7

TLR7 is an innate immune receptor that plays a critical role in initiating an immune response upon viral infections. It contains two ligand-binding pockets that sense degradation products of ssRNA. Specifically, TLR7 recognizes 2',3'-cyclic guanosine monophosphate (2',3'-cGMP) in its first binding pocket and short pyrimidine-rich oligoribonucleotides (ORNs) in its second binding pocket (Zhang et al., 2018). Previous studies on related endosomal nucleic acid-sensing TLRs, such as TLR8 and TLR9, have demonstrated that nucleases act upstream of these receptors to generate specific RNA or DNA stimulatory fragments necessary for their activation (Chan et al., 2015; Greulich et al., 2019; Ostendorf et al., 2020). Although genetic deletion studies have implicated a role of the endonuclease RNase T2 and the exonucleases PLD3 and PLD4 upstream of TLR7 (Gavin et al., 2021; Liu et al., 2021), their precise roles in modulating TLR7 activation have remained unclear. Using cell-based and *in vitro* assays with recombinant enzymes, we demonstrate that RNase T2 and PLD exonucleases act cooperatively to release 2',3'-cGMP for binding to TLR7 pocket 1. Specifically, RNase T2 precuts the RNA to generate 2',3'-cGMP-terminated fragments that are degraded in a subsequent step to the single-nucleotide level by PLDs, ultimately leading to the release of single 2',3'-cGMP (see Fig. 9).

Interestingly and unexpectedly, while the TLR7 response in RNase T2-deficient cells could be rescued by stimulation with only 2',3'-cGMP, TLR7 in PLD knockout cells remained unresponsive to such stimulations. This pointed towards an additional regulatory role for PLD enzymes in generating pocket 2 ligands. Studying RNA degradation by PLD3 and PLD4 under undercutting conditions revealed that these enzymes primarily stall at cytidines. This suggests that not all RNA substrates are cleaved to the single-nucleotide level, leaving short fragments for pocket 2 behind (see Fig. 9). Consequently, co-stimulation of a short oligoribonucleotide with 2',3'-cGMP finally rescued PLD deficiency.

Lastly, purification of recombinant PLD3 and PLD4 and subsequent structural analysis revealed that these proteins form stable dimers with two active sites on

opposite sides of the dimer. Dimerization was required for the catalytic activity and to bind to long RNA substrates, and disease-associated mutants failed to form stable dimers *in vitro*.

In summary, this work provides the first mechanistic explanation of how RNA fragments for TLR7 activation are generated in cells.

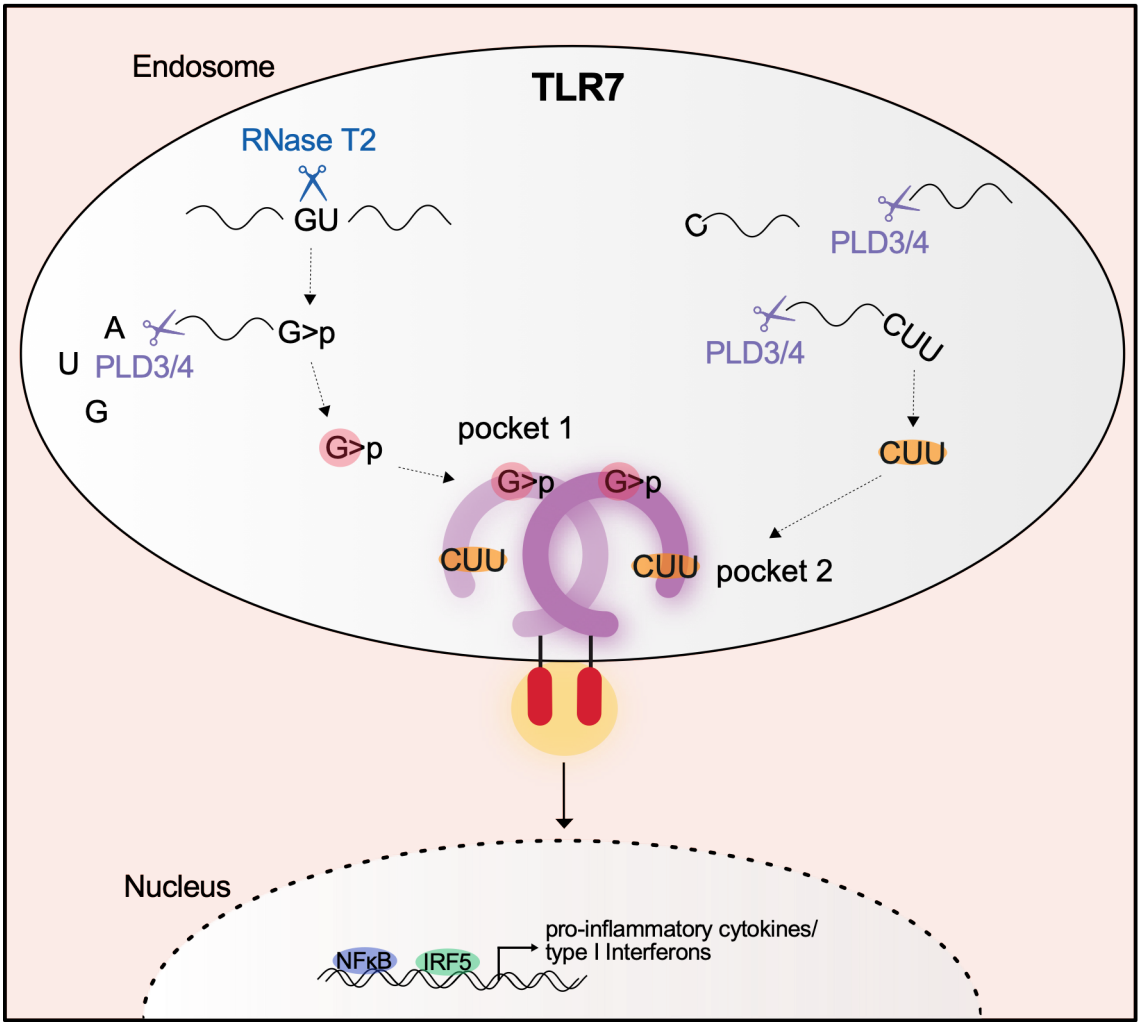

Figure 9: RNA processing upstream of Toll-like receptor 7: RNase T2 and PLD exonucleases cooperatively generate 2‘,3‘-cGMP, the endogenous pocket 1 ligand of TLR7. PLD exonucleases further contribute to the generation of TLR7’s pocket 2 ligands. PLD3 and PLD4 stall at cytidines when encountering them at the 5‘end of the RNA, thereby short fragments for pocket 2 remain.

2.2 Molecular mechanism by which pseudouridine RNA evades detection by Toll-like receptor 7 and 8

Endolysosomal Toll-like receptors 7 and 8 are innate immune sensors that trigger rapid immune responses to bacterial and viral infections. These receptors recognize exogenous, non-self RNA from pathogens while remaining tolerant to self-RNA (Roers et al., 2016). Using two distinct ligand-binding pockets, TLR7 and TLR8 sense RNA degradation products, generated by lysosomal nucleases (Berouti et al., 2024; Greulich et al., 2019; Ostendorf et al., 2020). Specifically, TLR7 senses 2',3'-cGMP and short uridine-containing oligonucleotides, while TLR8 engages uridine and purine-terminated fragments (Tanji et al., 2015; Zhang et al., 2018).

Pseudouridine (Ψ) and N1-methylpseudouridine ($m^1\Psi$)-substituted RNA has been shown to lack immune-stimulatory potential for both TLR7 and TLR8 (Kariko et al., 2005), a finding that was crucial for the successful development of RNA-based drugs. Yet, the mechanism by which these RNAs evade detection remained unknown. Given the essential role of nucleases acting upstream of both TLR7 and TLR8, we hypothesized that pseudouridine-substituted RNA might lack immune-stimulatory potential for two reasons: either because endolysosomal nucleases involved in generating TLR agonists are unable to cleave the modified RNA into stimulatory fragments, or because pseudouridine itself does not function as an agonistic ligand for TLR7 pocket 2 and TLR8 pocket 1.

Studying RNA degradation by all lysosomal nucleases revealed that RNase T2 and PLD exonucleases poorly digest RNA when uridine is replaced by Ψ or m1Ψ, leading to reduced TLR8 ligand generation and complete loss of 2',3'-cGMP release, the endogenous TLR7 pocket 1 ligand. In contrast, RNase A family enzymes, including RNase 1, RNase 2, and RNase 6, degrade modified RNA nearly as efficiently as unmodified RNA.

Biochemical assays using the TLR8 ligand-binding domain and cell-based assays studying TLR7 activation further revealed that Ψ is a weak ligand for TLR8 pocket 1 and that Ψ-RNA is not recognized as a pocket 2 ligand by TLR7. Interestingly, m1Ψ, which escapes cleavage by RNase T2 and PLD exonucleases, could bind and activate TLR8, suggesting that m1Ψ-substituted RNA primarily evades TLR8 detection

because lysosomal nucleases do not process it to the single-nucleotide level (see Fig. 10).

In summary, our study provides the first molecular explanation for how pseudouridine-modified RNA escapes recognition by lysosomal TLRs.

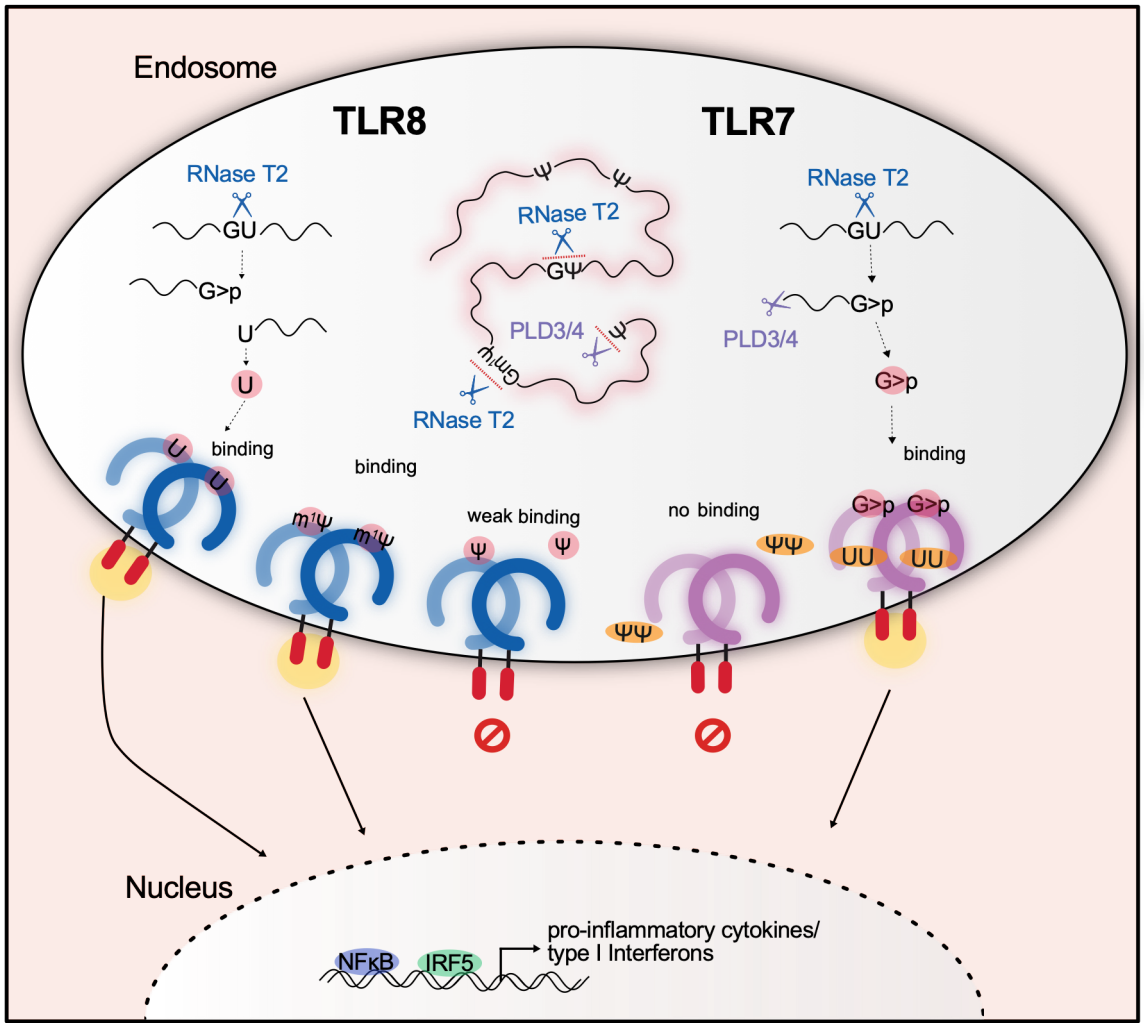

Figure 10 Pseudouridine RNA escapes recognition by Toll-like receptors 7 and 8: RNase T2 and PLD exonucleases generate TLR agonistic ligands from exogenous unmodified RNA. When the RNA is modified, RNase T2 and PLD fail to generate those ligands. Additionally, Ψ and Ψ-containing RNA fail to engage distinct binding pockets of TLR7 and TLR8, while m1Ψ could bind to TLR8 if released from ssRNA.

3 Zusammenfassung

3.1 RNA-Prozessierung für die Aktivierung von Toll-like Rezeptor 7

TLR7 ist ein Rezeptor des angeborenen Immunsystems, der eine wichtige Rolle bei der Erkennung von Virusinfektionen spielt. Er besitzt zwei Ligandenbindetaschen, die Abbauprodukte von Einzelstrang-RNA erkennen. Spezifisch bindet TLR7 in seiner ersten Bindungstasche 2',3'-zyklisches Guanosinmonophosphat (2',3'-cGMP) und in der zweiten Bindungstasche kurze pyrimidinreiche Oligoribonukleotide. Studien an verwandten endosomalen TLRs, wie TLR8 und TLR9, haben gezeigt, dass Nukleasen spezifische RNA- oder DNA-Fragmente erzeugen, die für ihre Aktivierung notwendig sind. Obwohl genetische Deletionsstudien eine regulatorische Rolle der Endonuklease RNase T2 sowie der Exonukleasen PLD3 und PLD4 für TLR7 Aktivierung nahegelegt haben, blieb deren genaue Funktion bei der Modulation der TLR7-Aktivierung bisher unklar.

Mit Hilfe von zellbasierten und *in vitro* Experimenten konnten wir hier zeigen, dass RNase T2 und die PLD-Exonukleasen kooperativ 2',3'-cGMP für TLR7-Bindungstasche 1 freisetzen. Zuerst schneidet RNase T2 die RNA vor, um 2',3'-cGMP-terminierte Fragmente zu erzeugen, die anschließend von PLDs zu Einzelnukleotiden abgebaut werden, was letztlich zur Freisetzung von 2',3'-cGMP führt.

Während die TLR7 Aktivierung in RNase T2-defizienten Zellen durch Stimulation mit 2',3'-cGMP vollständig wiederhergestellt werden konnte, blieb der Rezeptor in PLD-Knockout-Zellen unerwarteterweise weiterhin inaktiv. Dies deutete auf eine zusätzliche regulatorische Rolle der PLD-Enzyme bei der Generierung von Liganden für die zweite Bindungstasche. Die detaillierte Untersuchung des RNA-Abbaus durch PLD3 und PLD4 ergab, dass diese Enzyme eine Präferenz nur für bestimmte Nukleotide aufweisen, was darauf hindeutet, dass nicht alle RNA-Substrate zu Einzelnukleotiden abgebaut werden. Dadurch verbleiben kurze Fragmente, die als Liganden für Bindungstasche 2 fungieren können. Letztlich konnte die gleichzeitige Stimulation mit einem kurzen Oligoribonukleotid und 2',3'-cGMP die PLD-Defizienz kompensieren.

Die Aufreinigung von PLD3 und PLD4 und anschließende strukturelle Analysen zeigen, dass diese Proteine Dimere mit zwei aktiven Zentren an gegenüberliegenden

Seiten bilden. Die Dimerisierung ist sowohl für die katalytische Aktivität als auch für die Bindung an lange RNA-Substrate essenziell. Krankheitsassoziierte PLD-Mutanten hingegen konnten *in vitro* keine stabilen Dimere bilden. Zusammenfassend bildet diese Arbeit die erste mechanistische Erklärung wie RNA-Fragmente für die TLR7 Aktivierung in Zellen hergestellt werden.

3.2 Molekularer Mechanismus durch den pseudouridinhaltige RNA der Erkennung von Toll-like-Rezeptoren 7 und 8 entgeht

Endolysosomale Toll-like Rezeptoren (TLR) 7 und 8 sind Bestandteile des angeborenen Immunsystems, die eine schnelle Immunreaktion auf bakterielle und virale Infektionen auslösen. Diese Rezeptoren unterscheiden zwischen körperfremder RNA von Krankheitserregern und körpereigener RNA, gegenüber der sie tolerant sind. Über zwei Ligandenbindetaschen erkennen TLR7 und TLR8 RNA-Abbauprodukte, die von lysosomalen Nukleasen generiert werden. Spezifisch erkennt TLR7 2‘,3‘-cGMP und kurze Uridin-haltige Oligoribonukleotide. TLR8 hingegen wird von Uridin, sowie purin-terminierten Fragmenten aktiviert.

RNA, bei der Uridin durch Pseudouridine (Ψ) oder N1-Methylpseudouridin (m1Ψ) ersetzt wurde, zeigt keine immunstimulatorische Aktivität gegenüber TLR7 und TLR8. Obwohl diese Erkenntnis entscheidend bei der erfolgreichen Entwicklung von mRNA-Medikamenten war, blieb bislang unklar, wie Pseudouridin- und N1-Methylpseudouridin-RNA der TLR7 und TLR8 Erkennung entkommen. Angesichts der entscheidenden Rolle von Nukleasen bei der RNA Prozessierung stellten wir die Hypothese auf, dass pseudouridin-modifizierte RNA aus zwei Gründen nicht von TLRs erkannt werden könnte: Entweder, weil endolysosomale Nukleasen nicht in der Lage sind diese RNA in TLR-stimulierende Fragmente zu schneiden, oder weil Pseudouridin und pseudouridin-enthaltende Fragmente keine Liganden für die erste Bindetasche von TLR8 oder die zweite Bindetasche von TLR7 darstellen.

Untersuchungen zur RNA-Degradation durch lysosomale Nukleasen zeigten, dass RNase T2 und PLD-Exonukleasen Ψ- und m1Ψ-modifizierte RNA nur unzureichend abbauen. Dies führte zu einer verminderten Bildung TLR8-agonistischer Liganden,

sowie zum vollständigen Ausbleiben der Freisetzung von 2',3'-cGMP, dem endogenen Liganden für TLR7 Tasche 1. Die Endonukleasen RNase 1, RNase 2 und RNase 6 hingegen prozessierten die modifizierte RNA vergleichbar gut wie unmodifizierte RNA. Biochemische Tests mit der Ligandenbindedomäne von TLR8, sowie zellbasierte Studien zur TLR7-Aktivierung zeigten darüber hinaus, dass Ψ ein schwacher Ligand für die erste Bindetasche von TLR8 ist und das Ψ enthaltende Fragmente nicht als Liganden der zweiten Bindetasche von TLR7 erkannt werden. Interessanterweise konnte m1Ψ, welches dem Abbau durch RNase T2 und PLD-Exonukleasen entgeht, an TLR8 binden und aktivieren. Das deutet darauf hin, dass m1Ψ-modifizierte RNA der TLR8-Erkennung vor allem deshalb entgeht, weil sie nicht bis auf die Ebene einzelner Nukleotide durch lysosomale Nukleasen abgebaut wird.

Zusammenfassend liefert unsere Studie erstmals eine molekulare Erklärung dafür, wie pseudouridinmodifizierte RNA der Erkennung durch lysosomale TLRs entgeht.

4 Publications

4.1 Lysosomal endonuclease RNase T2 and PLD exonucleases cooperatively generate RNA ligands for TLR7 activation

The following research article was published in *Immunity*, 2024:

Marleen Bérouti,[1] Katja Lammens,[1] Matthias Heiss,[2] Larissa Hansbauer,[1] Stefan Bauernfried,[1] Jan Stöckl,[1] Francesca Pinci,[1] Ignazio Piseddu,[1,3] Wilhelm Greulich,[1] Meiyue Wang,[1] Christophe Jung,[1] Thomas Fröhlich,[1] Thomas Carell,[2] Karl-Peter Hopfner,[1] and Veit Hornung[1,4,*]

[1]Gene Center and Department of Biochemistry, Ludwig-Maximilians-Universität, Munich, Germany
[2]Department of Chemistry, Ludwig-Maximilians-Universität, Munich, Germany
[3]Department of Medicine II, University Hospital Munich, Munich, Germany
[4]Lead contact
*Correspondence: hornung@genzentrum.lmu.de
https://doi.org/10.1016/j.immuni.2024.04.010

Article

Immunity

Lysosomal endonuclease RNase T2 and PLD exonucleases cooperatively generate RNA ligands for TLR7 activation

Graphical abstract

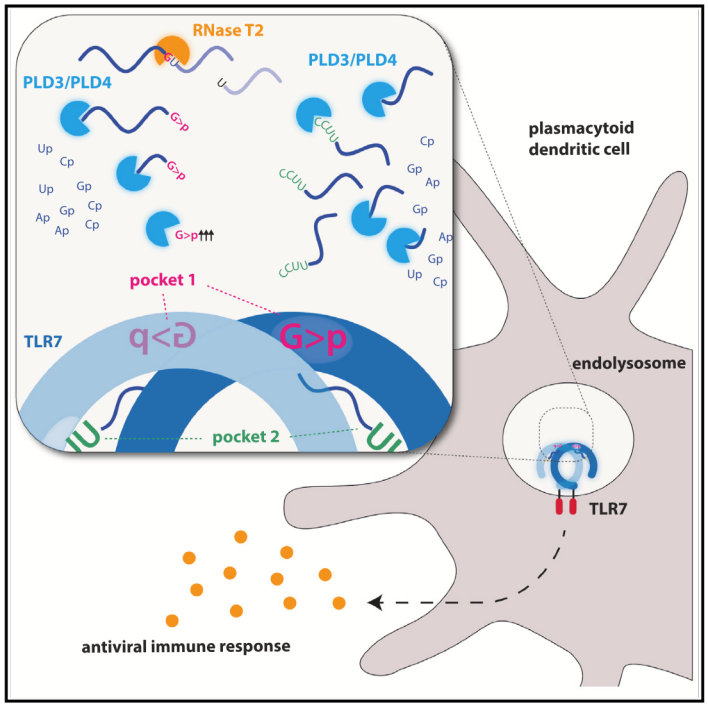

Highlights

- RNase T2 and PLD exonucleases process RNA upstream of TLR7
- PLD exonucleases release terminal 2′,3′-cyclic GMPs to engage TLR7 pocket 1
- PLD enzymes are also critical to generate RNA fragments for TLR7 pocket 2
- PLDs dimer formation is needed for RNA substrate processing

Authors

Marleen Bérouti, Katja Lammens, Matthias Heiss, ..., Thomas Carell, Karl-Peter Hopfner, Veit Hornung

Correspondence

hornung@genzentrum.lmu.de

In brief

TLR7 is critical for recognizing RNA virus infection and initiating antiviral responses. Bérouti et al. demonstrate how RNase T2 and PLD exonucleases generate RNA fragments for TLR7 activation, thus providing insights into immune recognition of exogenous RNAs, with potential therapeutic implications.

Bérouti et al., 2024, Immunity 57, 1–15
July 9, 2024
https://doi.org/10.1016/j.immuni.2024.04.010

CellPress

Please cite this article in press as: Bérouti et al., Lysosomal endonuclease RNase T2 and PLD exonucleases cooperatively generate RNA ligands for TLR7 activation, Immunity (2024), https://doi.org/10.1016/j.immuni.2024.04.010

Immunity

CellPress
OPEN ACCESS

Article

Lysosomal endonuclease RNase T2 and PLD exonucleases cooperatively generate RNA ligands for TLR7 activation

Marleen Bérouti,[1] Katja Lammens,[1] Matthias Heiss,[2] Larissa Hansbauer,[1] Stefan Bauernfried,[1] Jan Stöckl,[1] Francesca Pinci,[1] Ignazio Piseddu,[1,3] Wilhelm Greulich,[1] Meiyue Wang,[1] Christophe Jung,[1] Thomas Fröhlich,[1] Thomas Carell,[2] Karl-Peter Hopfner,[1] and Veit Hornung[1,4,*]

[1]Gene Center and Department of Biochemistry, Ludwig-Maximilians-Universität, Munich, Germany
[2]Department of Chemistry, Ludwig-Maximilians-Universität, Munich, Germany
[3]Department of Medicine II, University Hospital Munich, Munich, Germany
[4]Lead contact
*Correspondence: hornung@genzentrum.lmu.de
https://doi.org/10.1016/j.immuni.2024.04.010

SUMMARY

Toll-like receptor 7 (TLR7) is essential for recognition of RNA viruses and initiation of antiviral immunity. TLR7 contains two ligand-binding pockets that recognize different RNA degradation products: pocket 1 recognizes guanosine, while pocket 2 coordinates pyrimidine-rich RNA fragments. We found that the endonuclease RNase T2, along with 5′ exonucleases PLD3 and PLD4, collaboratively generate the ligands for TLR7. Specifically, RNase T2 generated guanosine 2′,3′-cyclic monophosphate-terminated RNA fragments. PLD exonuclease activity further released the terminal 2′,3′-cyclic guanosine monophosphate (2′,3′-cGMP) to engage pocket 1 and was also needed to generate RNA fragments for pocket 2. Loss-of-function studies in cell lines and primary cells confirmed the critical requirement for PLD activity. Biochemical and structural studies showed that PLD enzymes form homodimers with two ligand-binding sites important for activity. Previously identified disease-associated PLD mutants failed to form stable dimers. Together, our data provide a mechanistic basis for the detection of RNA fragments by TLR7.

INTRODUCTION

Toll-like receptor 7 (TLR7) is a key sentinel of the innate immune system that plays a critical role in detecting non-self RNA,[1,2] primarily from viral sources.[3,4] At the same time, TLR7 can also be erroneously activated by endogenous RNA, which has been implicated in the pathogenesis of several autoimmune diseases.[5] Indeed, TLR7 activation must be tightly balanced, and much progress has been made in understanding the regulation of TLR7 responses at the level of the receptor and also its subcellular compartment, which plays an important role in regulating its activity.[6,7] However, the exact process by which RNA is made "visible" to TLR7 remains unclear. TLR7 is highly expressed in plasmacytoid dendritic cells (pDCs), positioning these cells as central players in RNA-mediated immune surveillance and response.[8] TLR7 and its homolog TLR8 are positioned as homodimers in the endolysosomal compartment according to a rotational symmetry axis, while their leucine-rich repeat (LRR) ligand-binding domains face the lumen. Structural studies have identified two distinct bindings pockets that engage with distinct types of RNA molecules. TLR7 binds to guanosine with its first binding pocket, whereas the second binding pocket engages with pyrimidine-rich oligoribonucleotides (ORNs) that preferably contain two consecutive uridine nucleotides.[9,10] TLR8, on the other hand, binds to uridine with the first binding pocket, yet detects purine-terminated ORN fragments with the second binding pocket.[11] The engagement of the second binding pocket allosterically increases the affinity of the first binding pocket toward its ligand. The first binding pocket lies within the dimerization interface of these TLRs, and agonistic ligands within this pocket bridge the two TLR molecules. In the case of TLR7, this event results in the stable dimerization of this receptor and thereby results in the formation of a signaling-competent state. Interestingly, biochemical studies have shown that guanosine 2′,3′-cyclic monophosphate (2′,3′-cGMP) is a high-affinity ligand for the first pocket of TLR7,[10] suggesting that it may be an endogenous agonist for TLR7.

We and others have found that the endolysosomal nuclease RNase T2 is indispensable for TLR8 activation.[12,13] RNase T2 cleaves single-stranded RNA (ssRNA) with a preference for purine-uridine motifs, thereby generating fragments that are terminated with a purine 2′,3′-cyclic phosphate and initiated with a 5′ hydroxyl uridine. Thereby, RNase T2 activity contributes to two critical steps: on the one hand, RNase T2 generates purine 2′,3′-cyclic phosphate-terminated fragments that engage pocket 2 and on the other hand it results in the increase of

Please cite this article in press as: Bérouti et al., Lysosomal endonuclease RNase T2 and PLD exonucleases cooperatively generate RNA ligands for TLR7 activation, Immunity (2024), https://doi.org/10.1016/j.immuni.2024.04.010

uridine, while the latter mechanism is not fully explored. Interestingly, loss-of-function studies have shown that RNase T2 also plays a role upstream of TLR7.[14] However, despite its genetically proven involvement, the precise mechanistic role of RNase T2 in relation to TLR7 remains unclear, which prompted the initiation of this study.

RESULTS

RNase T2 is required for TLR7 activation

To study TLR7 signaling in a physiologically relevant setting, we used the CAL-1 cell line, a human pDC line derived from a male patient with a blastic plasmacytoid DC neoplasm.[15] CAL-1 cells express a similar repertoire of PRRs as primary pDCs, in particular TLR7 and TLR9, and respond to ssRNA and CpG DNA with the production of antiviral and pro-inflammatory cytokines. We stimulated wild-type (WT) or *TLR7*$^{-/y}$ CAL-1 cells with the RNA-based TLR7 agonists RNA40[2] and RNA9.2s.[16] RNA40 was delivered as a phosphodiester version (RNA40^{O}) as well as a stabilized phosphorothioate version (RNA40^{S}) (Figures 1A and 1B). The small molecule TLR7 agonists, R848 and 2′,3′-cGMP, and CpG DNA—either phosphodiester (CpG^{O}) or phosphorothioate (PTO)-stabilized (CpG^{S}) engaging TLR9—were used as controls. The ORNs triggered a robust type I interferon (IFN) response, albeit at a lower magnitude compared with R848, 2′,3′-cGMP, and CpG DNA (Figure 1A). At the concentration tested, the phosphorothioate-stabilized version RNA40^{S} was completely inactive in CAL-1 cells. As expected, ablation of TLR7 resulted in a complete loss of cytokine production for ORNs as well as for the small molecule TLR7 agonists. CpG DNA triggered IFN responses in both WT and TLR7-deficient CAL-1 cells, yet only when the phosphorothioate-stabilized ODNs were used (Figure 1A). Similar results were obtained in primary pDCs that responded to phosphodiester RNA40 as well as RNA9.2s, but not to the phosphorothioate-stabilized version of RNA40. R848 and 2′,3′-cGMP also triggered TLR7 activation, with R848 being a more potent activator compared with 2′,3′-cGMP (Figure 1C). Addressing the role of RNase T2 in this context revealed that the ORNs were indeed completely dependent on this enzyme for their immune-stimulatory activity, while its requirement could be bypassed by using R848 or 2′,3′-cGMP as direct pocket 1 agonists (Figure 1D). In light of the notion that RNase T2 generates 2′,3′-cGMP-terminated RNAs and the fact that 2′,3′-cGMP levels are strongly decreased in *RNASET2*$^{-/-}$ cells (Greulich et al.[12] and below), we addressed whether RNase T2 could liberate 2′,3′-cGMP from ssRNA *in vitro*. To address this, we designed an ORN in which an RNase T2 cleavage site (GU) was positioned directly at the 5′ end, while we also generated ORNs in which this dinucleotide motif was stepwise moved to the 3′ end of the ORN (Figure 1E). Testing these ORNs using recombinant RNase T2 revealed that RNase T2 required at least two nucleotides 5′ to its recognition motif to cleave. These results suggested that RNase T2 on its own was not able to release 2′,3′-cGMP within the endolysosomal compartment, but rather additional enzyme activities were required for this.

A role for PLD exonuclease activity upstream of TLR7

Because RNase T2 was unable to release the TLR7 first binding pocket ligand by itself, we therefore turned our attention to possible exonucleases of the secretory pathway. Here, phospholipase 3 and 4 (PLD3 and PLD4) operate within the lysosomal compartment.[17,18] Mining publicly available bulk (Figure 2A) and single-cell RNA sequencing (RNA-seq) datasets (Figure 2B) indicated that PLD3 was broadly expressed in myeloid cells, whereas PLD4 was largely confined to pDCs. In the absence of suitable antibodies to detect PLD3 or PLD4 protein expression at the endogenous level, we used quantitative mass spectrometry to study the expression of PLD3 and PLD4 in CAL-1 cells, pDCs, and CD14^{+} monocytes. Both enzymes were detected, yet PLD4 was far more abundant than PLD3 in both pDCs and CAL-1 cells. As such, PLD4 levels exceeded PLD3 levels in primary pDC by 78-fold and about 20-fold in CAL-1 cells. Monocytes, on the other hand, displayed intermediate expression levels for both enzymes (Figure 2C). Ablating PLD3 and PLD4 revealed that CAL-1 cells deficient for both enzymes displayed a completely blunted response toward RNA oligonucleotides, similar to RNase T2-deficient cells. Conversely, CpG-DNA-mediated activation of CAL-1 cells was dramatically enhanced for phosphodiester DNA,[17] while backbone-stabilized PTO ODNs even showed a reduced response in these cells (Figure 2D). When we studied CAL-1 cells deficient in either PLD3 or PLD4, we observed that PLD3 deficiency on its own dramatically boosted responses toward phosphodiester CpG DNA, while this was not observed when knocking out PLD4 (Figure S1A). On the other hand, *PLD4*$^{-/-}$ cell clones showed a greatly blunted RNA response yet showed the same low response toward CpG DNA as WT cells. These results suggest that PLD3 primarily degraded DNA, thereby preventing TLR9 activation, whereas PLD4-mediated degradation of RNA played a positive regulatory role upstream of TLR7. However, screening a larger panel of several PLD4-deficient clones also recovered some *PLD4*$^{-/-}$ CAL-1 cells that were still responding to ssRNA (Figure S1A). In light of the reported redundancy of PLD3 and PLD4 processing DNA and RNA ([17,18] and see below), we ascribe the phenotype in these *PLD4*$^{-/-}$ cell clones to a compensatory increase in PLD3 activity. Indeed, reconstituting *PLD3*$^{-/-}$ × *PLD4*$^{-/-}$ cells with PLD3 (Figure S1B) partially recovered the RNA response, indicating that PLD3 can compensate for the pro-TLR7 activity in the absence of PLD4 (Figure S1C). To avoid such redundancies, we therefore conducted all subsequent experiments addressing the functional relevance of PLD3 and PLD4 in *PLD3*$^{-/-}$ × *PLD4*$^{-/-}$ CAL-1 cells.

To further corroborate the role of PLDs upstream of TLR7, we additionally ablated PLD3 or PLD3 and PLD4 in primary human monocytes using CRISPR/Cas ribonucleoprotein particles and differentiated these cells into macrophages. After 8 days, we stimulated those cells with ssRNA40^{O} in the presence of the selective TLR8 inhibitor CU-CPT9a[21] to monitor solely TLR7 activation. R848 and lipopolysaccharide (LPS) were further used as controls. Like in CAL-1 cells, we observed a largely blunted TLR7 response in the absence of PLD3 and PLD4 upon stimulation with ssRNA. Lack of PLD3 alone already attenuated TLR7 activation in these primary macrophages, indicating that PLD3 constitutes the functionally predominant PLD exonuclease in these cells (Figure 2E). Lastly, we made use of the myeloid cell line BLaER1, which is similar to primary human

Please cite this article in press as: Bérouti et al., Lysosomal endonuclease RNase T2 and PLD exonucleases cooperatively generate RNA ligands for TLR7 activation, Immunity (2024), https://doi.org/10.1016/j.immuni.2024.04.010

CellPress
OPEN ACCESS

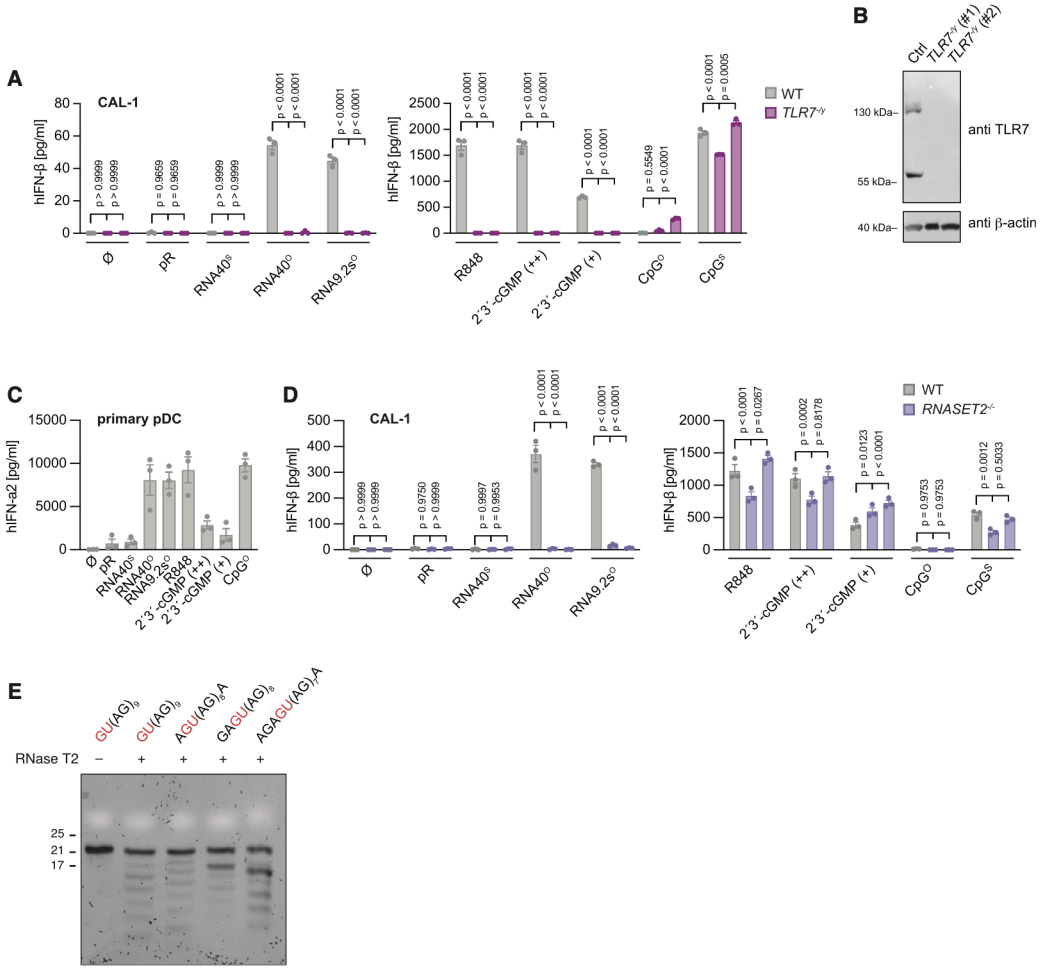

Figure 1. RNase T2 acts upstream of TLR7

(A) Unmodified CAL-1 cells (WT) or two independent *TLR7*$^{-/y}$ CAL-1 clones were unstimulated or stimulated with pR, RNA40^{S}, RNA40^{O}, RNA9.2s^{O}, R848, 2′,3′-cGMP (++ = 1 mM, + = 0.5 mM), CpG^{O}, or CpG^{S}. After 16 h, IFN-β release was measured by enzyme-linked immunosorbent assay (ELISA). Data are depicted as mean ± SEM of *n* = 3 independent experiments. Statistical analysis was conducted by two-way ANOVA with Dunnett's multiple comparison tests.

(B) TLR7 expression in CAL-1 WT and *TLR7*$^{-/y}$ CAL-1 clones by immunoblot. One representative blot of three independent experiments is shown.

(C) Isolated primary plasmacytoid dendritic cells were unstimulated or stimulated with pR, RNA40^{S}, RNA40^{O}, RNA9.2s^{O}, R848, 2′,3′-cGMP (++ = 1 mM, + = 0.5 mM), and CpG^{O}. After 24 h, IFN-α2 release was measured by ELISA. Data are depicted as mean ± SEM of *n* = 3 independent donors.

(D) Unmodified CAL-1 cells (WT) or two independent *RNASET2*$^{-/-}$ CAL-1 clones were stimulated as in (A) and IFN-β release was measured. Data are depicted as mean ± SEM of *n* = 3 independent experiments. Statistical analysis was conducted by two-way ANOVA with Dunnett's multiple comparison tests.

(E) Urea gel of indicated substrates digested with RNase T2 (0.37 nM). One representative gel of three independent experiments is shown.

monocytes functional for both TLR7 and TLR8.[12] BLaER1 cells responded to phosphodiester ORNs with a mixed TLR7 and TLR8 response, with the TLR7 component being more pronounced at high ORN concentrations (Figure S1D). In the absence of TLR8, the TLR7 response triggered by ORNs was completely dependent on PLD3 and PLD4, mirroring the results obtained with CAL-1 cells and primary human macrophages (Figure S1E). Altogether, these results indicated that PLD exonuclease activity negatively regulated the recognition of CpG DNA via TLR9, while it was critically required to process RNA for it to exert TLR7 agonism.

PLD3 and 4 liberate the pocket 1 ligand guanosine 2′,3′-cyclic monophosphate from RNase T2-digested RNA

PLD3 and PLD4 exert 5′ exonuclease activity and primarily release 3′monophosphate nucleosides from their substrates.[17,18] We expressed and purified PLD3 and PLD4 (Figure S2A) and studied their nucleolytic activity toward phosphodiester RNA oligonucleotide substrates that exert a fluorescent signal upon exonucleolytic degradation of the 5′ terminus.[22] In line with previous reports, we found that PLD3 exerted far higher catalytic activity toward RNA (Figures 3A and 3B). As such, the

Please cite this article in press as: Bérouti et al., Lysosomal endonuclease RNase T2 and PLD exonucleases cooperatively generate RNA ligands for TLR7 activation, Immunity (2024), https://doi.org/10.1016/j.immuni.2024.04.010

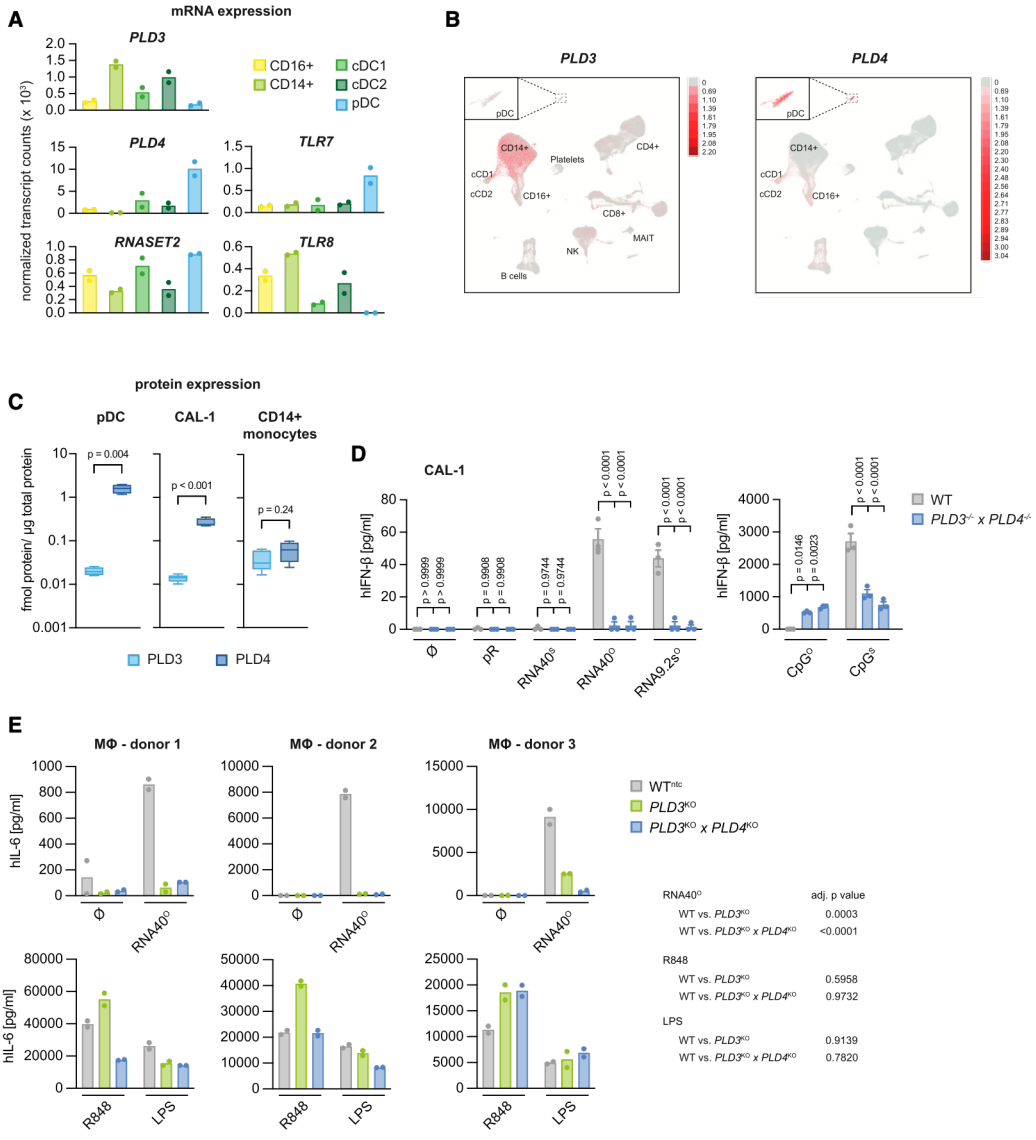

Figure 2. PLD3 and PLD4 act upstream of TLR7

(A) mRNA expression levels of PLD3, PLD4, RNase T2, TLR7, and TLR8 in indicated cell types are plotted.

(B) Single-cell RNA-seq data of human PBMCs from Hao et al.[19] were visualized using the UCSC Cell Browser[20] for the transcripts PLD3 and PLD4. Color coding represents the range of gene expression. The insert in the upper left corner specifically highlights the pDC population. Annotations for relevant cell populations were retrieved as annotated.

(C) Quantification of PLD3 and PLD4 protein expression in CAL-1 cells, primary plasmacytoid dendritic cells, and primary monocytes. Data are presented as box and whiskers of $n = 4–5$ independent experiments, statistics indicate a paired two-tailed Student's t test.

(D) Unmodified CAL-1 cells (WT) or two independent $PLD3^{-/-} \times PLD4^{-/-}$ CAL-1 clones were unstimulated or stimulated with pR, RNA40^S, RNA40^O, RNA9.2s^O, CpG^O, or CpG^S. After 16 h, IFN-β release was measured by ELISA. Data are depicted as mean ± SEM of $n = 3$ independent experiments. Statistical analysis was conducted by two-way ANOVA with Dunnett's multiple comparison tests.

(E) Indicated knockouts of primary human monocytes were unstimulated or stimulated with ssRNA40^O in the presence of CU-CPT9a, R848, and LPS. After 16 h, IL-6 release was measured by ELISA. Each replicate of 3 independent donors is depicted. For statistical analysis, the data of each donor was normalized to WT^{NTC} and two-way ANOVA was conducted on log-transformed data with Dunnett's multiple comparison test.

Please cite this article in press as: Bérouti et al., Lysosomal endonuclease RNase T2 and PLD exonucleases cooperatively generate RNA ligands for TLR7 activation, Immunity (2024), https://doi.org/10.1016/j.immuni.2024.04.010

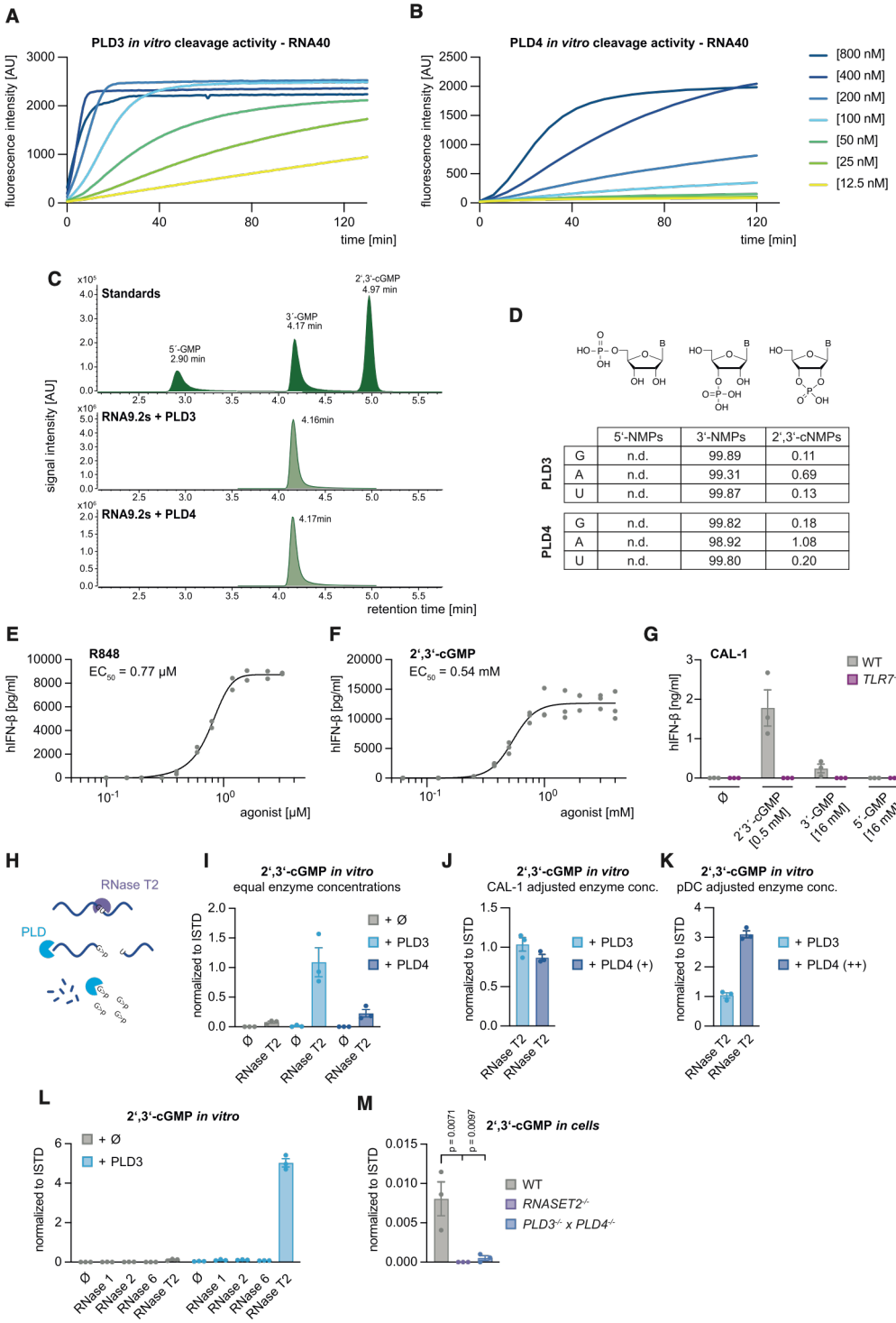

(legend on next page)

Please cite this article in press as: Bérouti et al., Lysosomal endonuclease RNase T2 and PLD exonucleases cooperatively generate RNA ligands for TLR7 activation, Immunity (2024), https://doi.org/10.1016/j.immuni.2024.04.010

calculated specific activity of PLD3 exceeded PLD4 by approximately 17-fold under these conditions. Analyzing RNA degradation at different enzyme concentrations using gel electrophoresis corroborated the notion of PLD3 being more processive than PLD4 (Figures S2B and S2C). Moreover, PLD3 was also far more processive toward a DNA substrate compared with PLD4 (Figure S2D).[17] Studying PLD3 and PLD4 RNA cleavage products using mass spectrometry, we found that both PLD3 and PLD4 released 3′- nucleoside monophosphates (NMPs),[17] while only trace amounts of 2′,3′-cNMP were detected (e.g., for 2′,3′-cGMP 0.1%–0,2% of all guanosines) (Figures 3C, 3D, and S2E). On the other hand, 5′-NMPs were not found at all. Comparing the potency of different guanine nucleotides however revealed that only 2′,3′-cGMP exerted potent TLR7 activation (effective concentration [EC_{50}] = 0.54 mM) with a similar efficacy as R848 (Figures 3E and 3F). 3′-GMP at concentrations 32× higher than the EC_{50} of 2′,3′-cGMP were needed to exert a measurable response, while 5′-GMP was completely inactive in CAL-1 cells (Figure 3G). Similar results were obtained from isolated primary pDCs, showing a robust TLR7 response induced by 2′,3′-cGMP, while 3′-GMP elicited weaker activation and 5′-GMP failed to induce TLR7 activation at all (Figure S2F). Together, these results suggest that 2′,3′-cGMP constitutes the natural pocket 1 ligand for TLR7 and that PLD exonuclease activity toward RNA substrates was not sufficient to generate this agonist. Given the substrate specificity of RNase T2 generating purine 2′,3′-cyclic phosphate-terminated fragments, we hypothesized that the combined activity of PLD exonuclease activity and RNase T2 endonuclease activity might be required for the production of 2′,3′-cGMP (Figure 3H). To address this possibility, we studied the production of 2′,3′-cGMP when processing RNA with PLD3 or PLD4 alone and with or without RNase T2 *in vitro*. Only the combination of PLD3 or PLD4 and RNase T2, but not the single enzymes, were able to generate substantial amounts of 2′,3′-cGMP when processing an ssRNA molecule (Figure 3I). At the same PLD enzyme concentrations, PLD3 released greater levels of 2′,3′-cGMP from ssRNA *in vitro* due to its stronger catalytic activity (Figure 3I). However, we found that PLD4 protein levels exceed those of PLD3 in primary pDCs by 78-fold and by 20-fold in CAL-1 cells (Figure 2C). Therefore, studying 2′,3′-cGMP release under adjusted enzyme concentrations using a 20-fold lower concentration of PLD3 revealed a comparable release of the nucleotide by PLD3 and PLD4, suggesting that both proteins equally contribute to the release of 2′,3′-cGMP in CAL-1 cells (Figure 3J). However, at a concentration 78-fold higher than that of PLD3, mimicking the condition in primary pDCs, PLD4 produced greater levels of 2′,3′-cGMP *in vitro*, implying that PLD4 serves as the main enzyme producing 2′,3′-cGMP in conjunction with RNase T2 in primary pDCs (Figure 3K). We also used recombinantly expressed RNase 1, RNase 2, and RNase 6—RNase A family endonucleases known to cleave after pyrimidines—as controls (Figure 3L). However, none of these enzymes were able to release nearly as much 2′,3′-cGMP as RNase T2 when combined with PLD3. In line with this notion, cells deficient in either RNase T2 or PLD3 and PLD4 displayed absent or strongly reduced 2′,3′-cGMP levels when stimulated with ssRNA (Figure 3M). Altogether, these results showed that PLD activity together with RNase T2 was required to generate the pocket 1 ligand 2′,3′-cGMP for TLR7.

PLD exonucleases are required for pocket 2 ligands

We hypothesized that *PLD3*$^{-/-}$ × *PLD4*$^{-/-}$ cells could be rescued with 2′,3′-cGMP, as it was the case for *RNASET2*$^{-/-}$ cells (Figure 1D). However, when treating *PLD3*$^{-/-}$ × *PLD4*$^{-/-}$ cells with 2′,3′-cGMP, we observed a complete lack of an immune response. R848 also exerted diminished activity in CAL-1 monoclones, CAL-1 *PLD3*^{KO} × *PLD4*^{KO} pool knockout cells, and BLaER1 monocytes (Figures 4A, S3A, and S3B). We also investigated the impact of PLD deficiency on tumor necrosis factor alpha (TNF-α) and interleukin-6 (IL-6) release after stimulation of *PLD3*$^{-/-}$ × *PLD4*$^{-/-}$ monoclones. Similar to the effects seen for IFN-β release, we observed blunted responses upon transfection of ssRNA and upon stimulation with 2′,3′-cGMP. Also, R848 displayed reduced activity in *PLD3*$^{-/-}$ × *PLD4*$^{-/-}$ clones, yet only when using concentrations near or below its EC_{50} value (Figures S3C and S3D). We further generated J774 mouse macrophages lacking PLD3. In line with previous work, we observed diminished TLR7 responses upon stimulation with ssRNA40 (Figure S3E). Stimulation of those cells with

Figure 3. RNase T2 and PLD enzymes release 2′,3′-cyclic GMP

(A and B) Fluorescence intensity signal of FAM-RNA40-BMN-Q530 over time, incubated with indicated concentrations of (A) PLD3 or (B) PLD4. Data are depicted as mean of *n* = 3 independent experiments.

(C) Overlay of extracted ion chromatograms (EIC) of 5′-GMP, 3′-GMP, and 2′,3′-cyclic GMP. Top: standards used as reference. Middle: *in vitro* digests of RNA9.2s with PLD3 (250 nM). Bottom: PLD4 (250 nM).

(D) Normalized signal areas of EIC from released 5′-NMPs, 3′-NMPs, and 2′,3′-cNMPs by PLD3 (250 nM) and PLD4 (250 nM) after degradation of $RNA9.2s^{O}$ in %.

(E and F) CAL-1 WT cells (300,000 cells/well) were stimulated with increasing concentrations of R848 and 2′,3′-cGMP. After 16 h, IFN-β release was determined by ELISA. Each replicate of *n* = 2 (E) or *n* = 3 (F) independent experiments is depicted. A four-parameter dose-response curve was fitted to calculate half-maximal effective concentration (EC_{50}).

(G) CAL-1 cells (300,000 cells/well) of indicated genotypes were unstimulated or stimulated with indicated concentrations of 2′,3′-cGMP and 3′-GMP. Data are depicted as mean ± SEM of three independent experiments.

(H) Schematic view of the *in vitro* digestion assay.

(I) $RNA40^{O}$ was digested with RNase T2 (370 nM), PLD3 (250 nM), and PLD4 (250 nM) or in combinations of RNase T2 (370 nM) with either PLD3 (250 nM) or PLD4 (250 nM) for 20 min, and the release of 2′,3′-cGMP was analyzed by LC-MS.

(J and K) $RNA40^{O}$ was digested with RNase T2 (370 nM) in combination with either PLD3 (+ = 2.5 nM), PLD4 (+ = 50 nM), or with PLD4 (++ = 195 nM) for 20 min, and the release of 2′,3′-cGMP was analyzed by LC-MS.

(L) $RNA40^{O}$ was digested with RNase 1 (5.7 nM), RNase 2 (27 nM), RNase 6 (29 nM), or RNase T2 (37 nM) only or in combination with PLD3 (25 nM) for 30 min, and the release of 2′,3′-cGMP was analyzed by LC-MS. For (I), (J), (K), and (L), data are depicted as mean ± SEM of *n* = 3 independent experiments.

(M) Detection of 2′,3′-cGMP in cell lysates of $RNA40^{O}$-stimulated WT, RNase T2, or *PLD3*$^{-/-}$ × *PLD4*$^{-/-}$ CAL-1 cells by LC-HRMS. Data are depicted as mean ± SEM of *n* = 3 independent experiments. Statistical analysis was conducted by one-way ANOVA with Dunnett's multiple comparison tests.

Please cite this article in press as: Bérouti et al., Lysosomal endonuclease RNase T2 and PLD exonucleases cooperatively generate RNA ligands for TLR7 activation, Immunity (2024), https://doi.org/10.1016/j.immuni.2024.04.010

CellPress
OPEN ACCESS

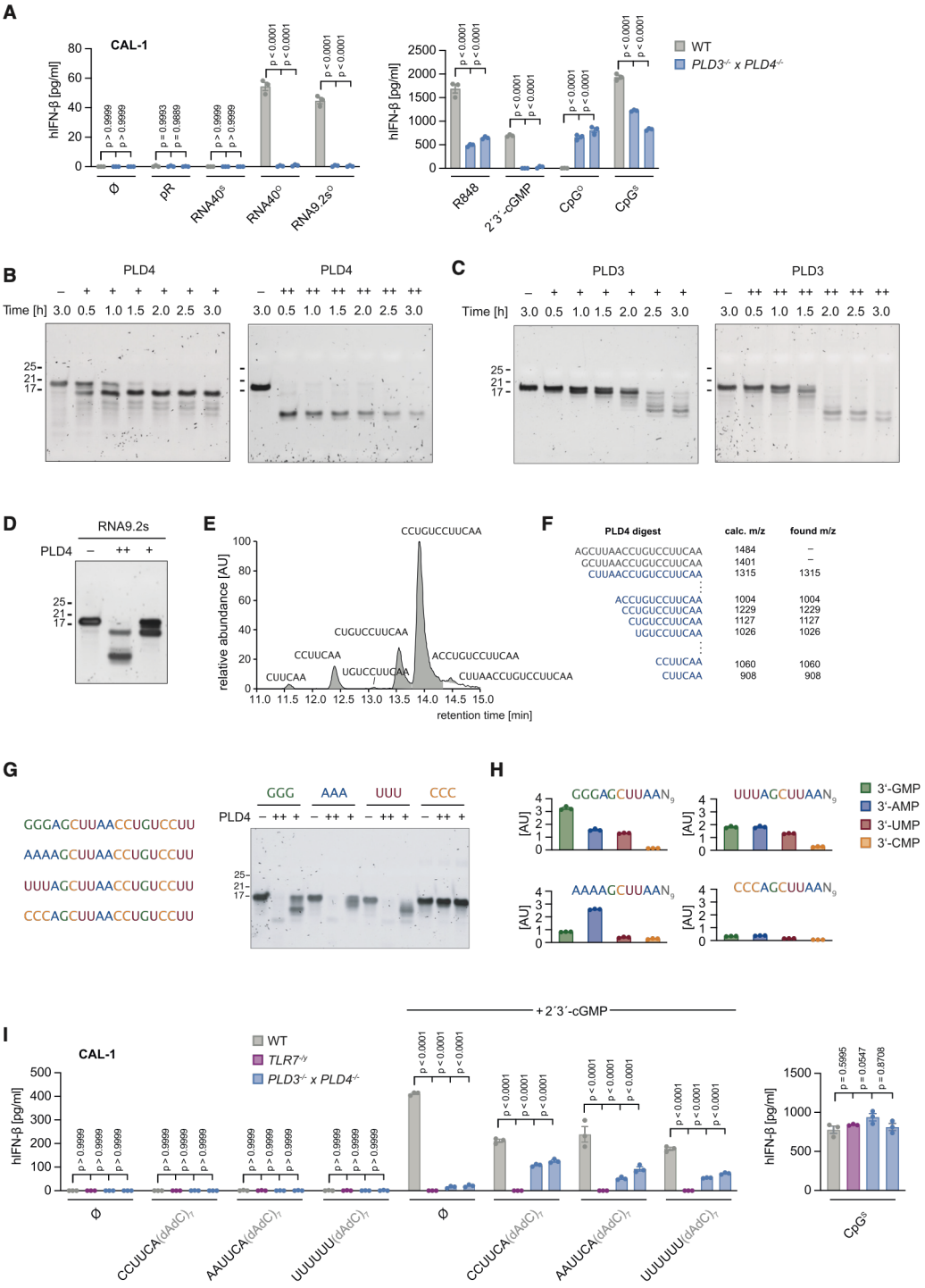

Figure 4. PLD enzymes create TLR7 second binding pocket fragments

(A) CAL-1 cells of indicated genotypes were unstimulated or stimulated with pR, RNA40^{S}, RNA40^{O}, RNA9.2s^{O}, R848, 2′,3′-cGMP (0.5 mM), CpG^{O}, and CpG^{S}. After 16 h, IFN-β release was determined by enzyme-linked immunosorbent assay (ELISA). Data are presented as mean ± SEM of $n = 3$ independent experiments.

(legend continued on next page)

Please cite this article in press as: Bérouti et al., Lysosomal endonuclease RNase T2 and PLD exonucleases cooperatively generate RNA ligands for TLR7 activation, Immunity (2024), https://doi.org/10.1016/j.immuni.2024.04.010

R837 also revealed reduced TLR7 responses when concentrations close to its EC_{50} value were used (EC_{50} = 2.45 μM) (Figures S3E and S3F), mirroring the pattern observed for IL-6 and TNF release in CAL-1 cells. Assessing the whole proteome of *PLD3*$^{-/-}$ × *PLD4*$^{-/-}$ CAL-1 cells excluded the possibility that combined PLD3 and PLD4 deficiency resulted in the secondary perturbation of the proteome, thus potentially affecting TLR7 activity (e.g., lysosomal proteins) (Table S1). Consequently, these results suggested that PLD activity was not only required to generate 2′,3′-cGMP in conjunction with RNase T2 but was also involved in generating ligands to engage the second binding pocket. However, this posed a conundrum, as complete exonucleolytic decay of lysosomal RNA by PLDs should yield mononucleotides, not fragments large enough to occupy the second binding pocket. When we studied RNA degradation by PLD4 at two different enzyme concentrations over a period of 180 min, PLD4 displayed a distinct fragment patterning, indicative of these enzymes "stalling" at certain sites of their substrates (Figure 4B). Similar results were obtained for PLD3 under limiting-enzyme concentrations (Figure 4C). LC-HRMS analysis of PLD4-processed RNA9.2s revealed that largely cytidine-initiated fragments were generated, suggesting that PLD4 preferably disengaged with its substrate when a 5′-C was reached (Figures 4D–4F). To further characterize this phenomenon, we designed substrates with either three consecutive cytidines, uridines, adenosines, or guanosines and subjected these to PLD4 processing. Assessing cleavage of these ORNs indicated that PLD4 showed a preference for degrading substrates that initiated with U, followed by those starting with G and A, with C-initiated substrates being degraded least efficiently (U>G>A>>C) (Figure 4G). LC-HRMS analysis of PLD4-processed RNA oligonucleotides corroborated these findings, with 5′-C substrates being processed poorly (Figure 4H). Altogether, these results suggest that PLD4 and PLD3 may indeed exert differential activity on different types of RNA fragments, sparing certain fragments from exonucleolytic degradation.

We hypothesized that this selective degradation could lead to the accumulation of ORN fragments as potential pocket 2 ligands within the lysosomal compartment. We therefore investigated whether we could bypass the TLR7 activation defect in *PLD3*$^{-/-}$ × *PLD4*$^{-/-}$ cells by co-delivering 2′,3′-cGMP and short ORN fragments. We designed different 6-mer ORN molecules attached to the 5′ end of a 14-mer deoxy oligonucleotide to ensure efficient lysosomal delivery[12] and transfected these oligos into WT, *TLR7*$^{-/y}$, or *PLD3*$^{-/-}$ × *PLD4*$^{-/-}$ cells (Figure 4I). These oligos alone failed to induce immune responses in any of these cell types. However, when delivered together with 2′,3′-cGMP, they induced a measurable immune response in WT cells and this was also observed in *PLD3*$^{-/-}$ × *PLD4*$^{-/-}$ cells. 2′,3′-cGMP, on the other hand, was completely inactive in *PLD3*$^{-/-}$ × *PLD4*$^{-/-}$ cells, while being a potent agonist in WT cells. Collectively, these results indicate that PLDs are not only required to generate pocket 1 ligands in conjunction with RNase T2 but that they also process RNA into fragments suitable for ligand-binding pocket 2, a function for which RNase T2 is not required.

PLD3 and PLD4 form a dimer that forms 2 substrate binding pockets

To obtain a better mechanistic understanding of how exonucleolytic PLDs process nucleic acids, we used cryoelectron microscopy (cryo-EM) to obtain a structural model of the soluble catalytic domain of human PLD3. We mainly focused on PLD3 due to its better expression and purification characteristics. During size exclusion chromatography (SEC) we noted that PLD3 forms a stable dimer (Figure 5A), which was also substantiated by mass photometry analysis (Figure 5B). Analogous results were obtained when expressing PLD4 (Figures 5A and 5B). We recorded datasets of PLD3 as well as PLD3 in complex with ssRNA. Two-dimensional (2D) classifications of the apoenzyme data yielded C2 symmetric dimeric PLD3 classes. Three-dimensional (3D) reconstruction of the dimer using C2 symmetry resulted in a map with a global resolution of 2.87 Å, allowing model building of residues 79–490 (Figures 5C and S4). Although PLD3 is a member of the phospholipase family with two HxKxxxxD/E motifs resulting from internal duplication, it also dimerizes. This dimerization leads to the formation of two active sites on opposite sides of the dimer (Figure 5C). A structural superposition with the catalytic domain of human PLD1 (PDB: 6U8Z[23]) indicated that the typical bi-lobal fold is retained in each protomer and that the conformation of lobe 1 as well as the typical β-sheets are mostly similar (Figure S5A). Conversely, lobe 2 of hPLD1 shows significant structural differences and large insertions (Figure S5B). However, the arrangement of the enzymatically critical HxK motif residues H201 and K203, as well as H416 and K418 in PLD3, are identical to PLD1 and other PLD family members (Figure S5C). This suggests that PLD3 cleaves the single-stranded DNA (ssDNA)/ssRNA substrates utilizing a similar two-step mechanism, as seen by other DNases of the PLD superfamily, by forming a phospho-histidine intermediate.[24] Most likely histidine 416 acts in the reaction as the nucleophile activated by Glu 229, whereas histidine 201 serves as a general acid to protonate

Statistical analysis was conducted by two-way ANOVA with Dunnett's multiple comparison tests. Note that the WT data are identical with the ones shown in Figure 1A.

(B) Urea gels of RNA9.2s^{O} digested with PLD4 (+ = 25 nM, ++ = 250 nM) over time. One representative gel of three independent experiments is shown.

(C) Urea gels of RNA9.2s^{O} digested with PLD3 (+ = 0.39 nM, ++ = 1.56 nM) over time. One representative gel of two independent experiments is shown.

(D) Urea gel of RNA9.2s^{O} (1 μg) incubated with PLD4 (++ = 250 nM, + = 25 nM) for 2 h. One out of three independent experiments is shown.

(E) LC-HRMS total ion current (TIC) chromatogram of RNA9.2s^{O}-derived ORN fragments after digestion with PLD4 (250 nM) for 2 h.

(F) Calculated and found masses (*m/z*) of RNA9.2s-derived ORN fragments after digestion with PLD4 (250 nM) for 2 h.

(G) Urea gel of indicated substrates digested with PLD4 (++ = 250 nM, + =25 nM). One out of two independent experiments is shown.

(H) LC-MS/MS analysis of depicted substrates digested with PLD4 (250 nM) for 20 min. Data were normalized to the amount of the different nucleosides present in the sequence and are depicted as mean ± SEM of *n* = 3 independent experiments.

(I) CAL-1 cells of indicated genotypes were unstimulated or stimulated with 2′,3′-cGMP (0.5 mM), short ORNs, or ORNs in combination with 2′,3′-cGMP (0.5 mM). Data are depicted as mean + SEM of *n* = 3 independent experiments. Statistical analysis was conducted by two-way ANOVA (left panel) or one-way ANOVA (right panel) with Dunnett's multiple comparison tests.

Please cite this article in press as: Bérouti et al., Lysosomal endonuclease RNase T2 and PLD exonucleases cooperatively generate RNA ligands for TLR7 activation, Immunity (2024), https://doi.org/10.1016/j.immuni.2024.04.010

CellPress
OPEN ACCESS

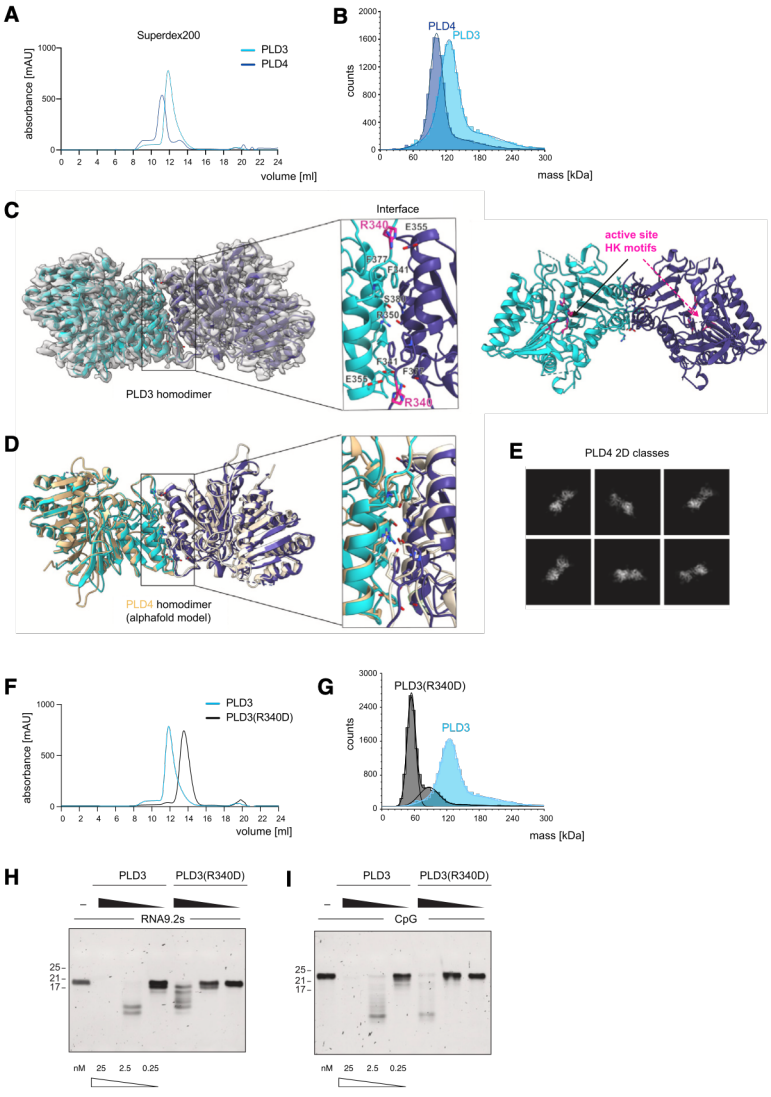

Figure 5. PLD3 and PLD4 form homodimers

(A) Size exclusion chromatography (SEC) run of PLD3 superimposed with the SEC run of PLD4.

(B) Mass distribution of PLD3 and PLD4 observed by mass photometry.

(C) Ribbon representation of the PLD3 dimer shown together with the cryo-EM density map. The inset shows a detailed view of the dimer interface, with the involved residues shown in stick representations. The mutated residue R340 and active site HxK motifs are highlighted in pink.

(D) Structural comparison between the PLD3 cryo-EM structure, colored in turquoise and dark blue, and the PLD4 model predicted by Alphafold, colored in beige. The inset illustrates the comparison of the PLD3/PLD4 dimer interface, with involved residues highlighted using stick representations.

(E) Representative 2D classes of PLD4 particles illustrating the dimeric conformation.

(F) Size exclusion chromatography (SEC) run of PLD3 superimposed with the SEC run of PLD3(R340D). Note that the SEC control run of PLD3 is identical to Figure 5A.

(G) Mass distribution of PLD3 and PLD3(R340D) observed by mass photometry. Note that the mass distribution control of PLD3 is identical to Figure 5B.

(H and I) Urea gels of RNA9.2s^{O} and CpG^{O}-DNA digested with indicated concentrations of PLD3 and PLD3(R340D). One out of two independent experiments is shown.

the oxygen atom of the leaving group.[25] The two adjacent lysine residues, which have been shown to be involved in the coordination of the substrate, extend their ε-amino group into the catalytic center. All four residues are located buried in a cleft formed by mainly hydrophobic and positively charged residues. Apart from the four active site residues, the substrate binding cleft largely differs from human PLD1, which is in agreement with the different substrate types cleaved (Figure S5B). The two PLD3 protomers assemble into a dimer with C2 symmetry, while the dimer interface is formed by hydrophobic interactions (residues F341, F377, and L384)—a salt bridge between residues R340 and E355—as well as hydrogen bonds between R350 and S380, and Y354 and S373, respectively (Figure 5C). A comparison with a PLD4 dimer model calculated by Alphafold[26] suggested that the dimer interface is largely conserved in PLD4 (Figure 5D). To confirm the dimeric PLD4 conformation, a cryo-EM dataset was collected, yielding 2D classes with a structure similar to the PLD3 dimer (Figure 5E). However, the preferred orientation of the particles hindered the reconstruction of a 3D structure.

To prove the structurally determined interface and to analyze the importance of dimerization for the nucleolytic activity of PLD3, we introduced a charge reversal mutation at residue R340 (R340D), thereby preventing the formation of the polar interaction to E355 of the second protomer. The mutant PLD3^{R340D} eluted as a monomer from the size exclusion column and exhibited monomeric behavior in the mass photometry analysis (Figures 5F and 5G). The exonucleolytic activity of the R340D mutant was significantly reduced when using ssRNA9.2s and CpG ssDNA as substrates (Figures 5H and 5I). Because residue R340 is far from the active site HxK motif, we concluded that the dimeric state of PLD3 is important for substrate recognition. PLD3 mutations are linked to susceptibility to Alzheimer's disease[27] (PLD3^{V232M}) and to spinocerebellar ataxia[28] (PLD3^{L308P}), although their exact role in these diseases is not yet understood. Neither V232 nor L308 are localized in close proximity to the catalytic center or to the dimerization interface (Figure S5D). V232 is located in the hydrophobic core of PLD3, and its mutation to methionine might influence the correct folding of PLD3. On the other hand, L308 is situated in a helix that is in the vicinity of the dimer interface. Therefore, a mutation to proline could interrupt the helix formation and influence the folding in this area,

Please cite this article in press as: Bérouti et al., Lysosomal endonuclease RNase T2 and PLD exonucleases cooperatively generate RNA ligands for TLR7 activation, Immunity (2024), https://doi.org/10.1016/j.immuni.2024.04.010

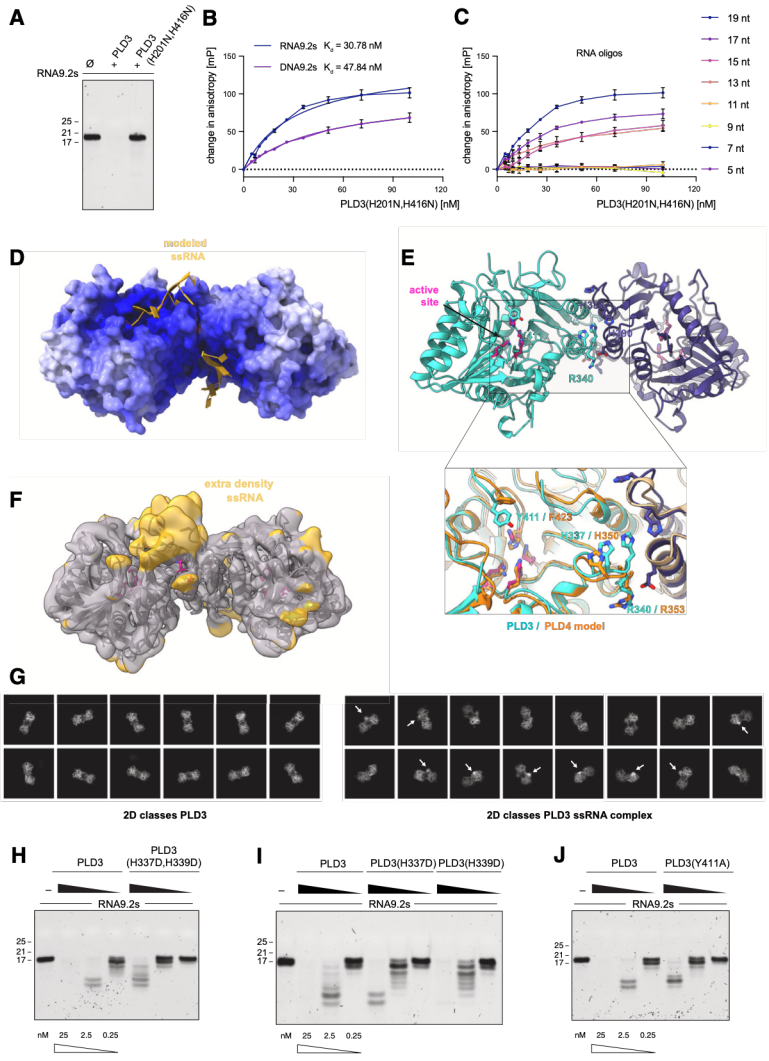

Figure 6. PLD3 shows high-affinity binding to long oligonucleotides

(A) Urea gel of RNA9.2s^{O} incubated with PLD3 (250 nM) and PLD3(H201N, H416N) (250 nM). One out of three independent experiments is shown.

(B and C) Fluorescence anisotropy assays assessing the binding of PLD3(H201N, H416N) at increasing concentrations to indicated substrates. Data are shown as mean ± SEM of n = 3 independent experiments. Note that the 19-nt RNA9.2s binding data are identical in (B) and (C).

(D) The electrostatic surface of the PLD3 dimer, calculated with APBS at pH 5, illustrates the presence of two positively charged areas. The two ssRNA segments, colored in gold, have been modeled using Hdock.

(E) Ribbon representation of PLD3 with highlighted active site HxK motif colored in pink and residues presumably involved in substrate recognition shown as sticks and color coded according to the corresponding protomer, with turquoise or dark blue, respectively. The inset shows a detailed view of the comparison between PLD3 (turquoise) and PLD4 (orange) at the active site cleft, illustrating the conservation of the highlighted residues.

(F) Cryo-EM density map for PLD3 bound to ssRNA highlighting the additional density appearing in gold.

(G) Representative 2D classes of PLD3 particles or PLD3 ssRNA complex particles.

(H–J) Urea gels of RNA9.2s^{O} digested with decreasing concentrations of PLD3 or with decreasing concentrations of depicted PLD3 mutants. For all urea gels, one out of two independent experiments is shown.

including the dimer interface. Expression of these mutants showed that PLD3^{V232M} had, in part, lost its capacity to form a dimer, while it appeared to form multimers in SEC, whereas PLD3^{L308P} was fully monomeric (Figures S5E–SH). Consistent with the relevance of dimer formation, the catalytic activity of PLD3^{L308P} was completely blunted, whereas the activity of PLD3^{V232M} was diminished (Figures S5I and S5K). Altogether, these results indicated that PLD3 and PLD4 form dimeric enzyme complexes and that dimer formation was required to exert catalytic activity.

A model for PLD3 interacting with an RNA substrate

To assess substrate binding in more detail, we generated a PLD3 mutant in which both catalytically relevant histidines were exchanged for asparagines (PLD3^{H201N,H416N}). As expected, recombinant PLD3^{H201N,H416N} was no longer able to process RNA (Figure 6A). To explore nucleic acid binding of this mutant, we conducted fluorescence anisotropy experiments in which we compared a 19-nt DNA and RNA oligonucleotide (Figure 6B). Both DNA and RNA exhibited high-affinity binding, yet with RNA showing slightly higher affinity (Figure 6B). Testing RNA oligonucleotides that were successively shortened by 2-nt each revealed that at least 13 nt were required for binding (Figure 6C). In fact, an 11-nt ORN showed no PLD3 binding. Conducting comparable assays with shortened DNA oligonucleotides confirmed that at least 13 nt were required for binding (Figures S6A and S6B). To pinpoint essential residues involved in nucleic acid substrate recognition, we performed calculations of the electrostatic surface potential of the PLD3 dimer at pH 5. The surface indicated two positively charged areas, one close to the active site cavity and a second area in the dimer interface (Figure 6D). Prediction of ssRNA binding to PLD3 using the Hdock server[29] confirmed the possible involvement of both these areas in nucleic acid recognition (Figure 6D). Closer inspection of the active site cleft and the transition region between both positively charged areas pointed us to two clusters of histidine residues (H337/H339 and H388/H390). In the dimer, H337/H339 from the PLD3$_A$ protomer and H388/H390 from the PLD3$_B$ protomer formed a positively charged patch on each side of the dimerization interface (Figure 6E). A structural overlay of the PLD3 cryo-EM structure with

Please cite this article in press as: Bérouti et al., Lysosomal endonuclease RNase T2 and PLD exonucleases cooperatively generate RNA ligands for TLR7 activation, Immunity (2024), https://doi.org/10.1016/j.immuni.2024.04.010

the PLD4 Alphafold model verified that H337—and also the positively charged residue R340—were conserved and might play a role in nucleic acid binding in both proteins (Figure 6E, inset). Indeed, testing the binding affinity of the corresponding PLD3^{H201N,H416N,H337D} and PLD3^{H201N,H416N,R340D} mutants compared with PLD3^{H201N,H416N} by fluorescence anisotropy revealed diminished binding of the PLD3^{H201N,H416N,H337D} mutant to a 19-nt RNA substrate and nearly abolished binding of the PLD3^{H201N,H416N,R340D} mutant (Figure S6C). To further confirm the predicted binding positions, we collected several cryo-EM datasets of PLD3 with different phosphorothioate-containing substrates, e.g., 20 bases ssRNA and 20 bases ssDNA. Although some of the datasets showed a clear additional signal in the 2D classes (Figures 6F and 6G), the quality of the model was not sufficient to build an atomic model of the ssRNA/-DNA, respectively. However, the cryo-EM density validated the involvement of the positively charged cleft, residue H337, and presumably R340 in substrate recognition (Figure 6F). Indeed, mutation of H337/H339 revealed that this cluster was relevant for the catalytic activity of PLD3, with an approximate 10-fold reduction in enzymatic activity (Figure 6H). Single mutants of either H337 or H339 showed that H337 was especially necessary for the exonucleolytic activity of PLD3 (Figure 6I), which was also in line with its conservation in PLD4 (Figure 6E). Mutagenesis of the second patch (H388/H390) revealed a minor contribution of this site (Figures S6D and S6E), with respective single mutants behaving like the WT enzyme. Moreover, activity assays using DNA as a substrate confirmed these findings (Figures S6F and S6G).

A second site that caught our attention was tyrosine 411 (Y411)—phenylalanine in PLD4 (F423)—that is positioned above the active site (Figure 6E). Because these residues are capable of π-stacking interactions with ssRNA/-DNA, commonly seen in nucleotide binding sites and protein-DNA interactions, we also tested a PLD3 mutant for this residue (PLD3^{Y411A}). Indeed, in line with this hypothesis, PLD3^{Y411A} exerted considerably lower exonucleolytic activity toward RNA (Figure 6J) and DNA (Figure S6H). Taken together, these results indicate that PLD3 requires a minimum footprint of 13 nt for nucleic acid binding, a size that is well in agreement with the proposed nucleotide binding model and the necessity of the PLD3 dimer. In addition, the cryo-EM and biophysical properties were used to identify residues relevant to enzyme function.

DISCUSSION

Here, we showed that RNA recognition via TLR7 required the concerted activity of the endonuclease RNase T2 together with the exonucleases PLD3 and PLD4. In summary our results suggest the following model: complex RNA molecules localized to the endolysosomal compartment are first processed by endonucleases, which then expose new 5′ ends, making these fragments accessible to the 5′ exonucleases PLD3 and PLD4. The critical endonuclease in this context is RNase T2, which generates fragments that are terminated with a 2′,3′-cGMP. The resulting 3′-terminal 2′,3′-cGMP becomes the endogenous pocket 1 ligand for TLR7. The non-redundant role of RNase T2 in this process can be attributed to its unique functionality of cleaving after guanosines, which is not achieved by endonucleases of the RNase A family of enzymes. However, as an endonuclease, RNase T2 cannot process at the termini of an RNA molecule. As such, this process depends on the activity of an exonuclease to release the 3′-terminal 2′,3′-cGMP. In the endolysosomal compartment, this function is performed by the PLD exonucleases. While these enzymes primarily release 3′-NMPs from processed RNA, preprocessing of RNA by lysosomal endonucleases produces the aforementioned 2′,3′-cNMP-terminated RNA fragments, and complete processing of such a fragment releases a 2′,3′-cNMP as the final nucleotide. Consistent with this notion, RNase T2-deficient cells lacked 2′,3′-cGMP upon stimulation and their RNA-sensing defect could be overcome by directly providing 2′,3′-cGMP. PLD-deficient cells also failed to produce 2′,3′-cGMP upon stimulation but, interestingly, they could not be rescued by direct application of 2′,3′-cGMP. This raised the question of how PLD activity might be additionally involved in TLR7 activation and pointed our attention to their role in generating pocket 2 agonistic RNA fragments. Examination of RNA oligonucleotide processing at limiting enzyme concentrations revealed that PLDs stall at specific sites, preferably cytosine-rich RNAs. This implies that PLDs do not necessarily degrade the entire pool of RNA molecules to the single nucleotide level. Consistent with the notion that such fragments are the missing component for TLR7 activation, provision of such RNA molecules in *trans* together with 2′,3′-cGMP complemented the defect of PLD deficiency. R848 activity, as a hyper-physiological pocket 1 agonist, was also diminished in its stimulatory activity when PLDs were absent. It is therefore plausible that PLDs provide a constant level of pocket 2 ligands required for optimal TLR7 activation.

PLD4 is largely restricted to pDCs, whereas PLD3 is more broadly expressed, particularly in the myeloid lineage. Like pDCs, CAL-1 cells also exhibit higher PLD4 expression, but only to the extent that the higher catalytic activity of PLD3 would be balanced. Indeed, when we compared the release of 2′,3′-cGMP at CAL-1-adjusted PLD expression levels, we observed a similar release of this nucleotide by PLD3 or PLD4. Therefore, one would expect that PLD3 and PLD4 are redundantly used in these cells. However, by ablating PLD4 only in CAL-1 cells, we observed a complete loss of TLR7 RNA response in four of several cell clones tested. Interestingly, the remaining PLD3 activity in these cells still suppressed the DNA response, arguing for sufficient DNA exonuclease activity within the lysosome. Although we have not formally compared the exonuclease activity of PLD3 and PLD4 toward DNA, our data suggest that the specific activity of PLD3 toward DNA over RNA is higher than that of PLD4. Moreover, it is plausible that there are additional determinants within the lysosomal compartment that are not captured by the *in vitro* assays (e.g., post-translational modifications or cofactors) that contribute to a "DNA preference" of PLD3. Such a scenario could explain why loss of PLD4 shows a preferential lack of RNA response, while DNA degradation is still maintained. However, we also identified two PLD4-deficient clones that exhibited partial or full RNA response, suggesting that there is a substantial increase in PLD3 activity that functionally compensates for the absence of PLD4. Consistent with this, by overexpressing PLD3 in *PLD3*$^{-/-}$ × *PLD4*$^{-/-}$ cells, we were able to partially restore the RNA response in these cells. In general, it appears that the CAL-1 system operates at the edge where both PLD enzyme

Please cite this article in press as: Bérouti et al., Lysosomal endonuclease RNase T2 and PLD exonucleases cooperatively generate RNA ligands for TLR7 activation, Immunity (2024), https://doi.org/10.1016/j.immuni.2024.04.010

activities play a role. It is unlikely that such a scenario is relevant in primary pDC, where PLD4 expression significantly exceeds PLD3 expression, or in myeloid cells, where the reverse scenario applies. Indeed, we observed almost completely attenuated TLR7 responses in the absence of PLD3 in primary human-monocyte-derived macrophages and in J774 mouse macrophages. This indicates that, in myeloid cells, PLD3 is the predominant exonuclease that also operates to generate TLR7 agonistic ligands.

Notably, previous work on the immunological functions of PLDs has established that PLDs can negatively regulate immune responses by limiting nucleic acid ligand availability.[17,18,30] Thus, mice deficient in both PLD3 and PLD4 display a prominent autoinflammatory response that can be rescued by ablating the function of nucleic-acid-sensing TLRs (UNC93B1 deficiency). In this model, lack of both PLD3 and PLD4 was required to unleash the inflammatory response, suggesting redundant functions of these exonucleases in nucleic acid degradation. Moreover, single deficiency of TLR9 was unable to fully rescue the phenotype,[18] suggesting an involvement of the RNA-sensing TLR systems. In support of this notion, mice with a gene dosage increase in TLR7 showed an increased inflammatory response when PLD4 was ablated. *In vitro* experiments with RNA oligonucleotides in part supported the negative regulatory role of PLDs for TLR7 and TLR13 stimulation—but with certain inconsistencies. For example, while TLR13 responses were generally increased, certain TLR7-agonistic RNA oligonucleotides showed increased or unchanged responses in $PLD3^{-/-} \times PLD4^{-/-}$ cells, and some responses were even decreased. Nevertheless, in line with the *in vivo* experiments, it was concluded that PLDs can either negatively regulate TLR7 responses similarly to TLR9 or positively regulate TLR7 responses, depending on the substrate. Our data indicate a requirement for PLD exonuclease activity for TLR7 activation, which seems to contrast the aforementioned work. However, it needs to be considered that our work focuses on the cell-intrinsic role of PLD exonucleases in TLR7 activation and not on the *in vivo* role. This is important because, *in vivo*, additional mechanisms may be involved that are secondary to the defect under study. Consistent with this notion, RNase T2[31] or DNase 2[32] deficiency induces prominent inflammatory responses *in vivo*, whereas these nucleases play a productive role in the production of TLR7/8[12,13] or TLR9[33] ligands at the cell-autonomous level. Another important consideration is that previous studies have focused on murine macrophages, which have a different expression pattern of PLDs and nucleic-acid-sensing TLRs, and that most of the mechanistic studies were conducted with phosphorothioate oligonucleotides that display a clear cell type and cell-type specificity.

Our structural and biochemical studies led to the unexpected finding that both PLD3 and PLD4 form homodimers. Although homodimer formation is well described for several PLD family enzymes, these are enzymes that contain only one HxK motif and require dimerization to form a functional catalytic center.[34] Because PLD3 and PLD4 contain two HxKxxxxD/E motif-containing lobes by internal domain duplication, dimerization should not be necessary to achieve enzymatic activity. However, it appears that dimer formation is needed to create a binding site involving both PLD protomers. These results are also consistent with the notion that nucleic acid molecules below 13 nt do not bind PLD3, a molecular footprint consistent with the requirement of two protomers for binding. While this paper was under review, another structure of PLD3 was reported,[35] supporting the finding that PLD3 forms homodimers. In contrast to our findings, binding of short oligonucleotides (5 nt in length) were reported, yet with significantly lower binding affinities compared with our long substrates. Subsequently, an alternative oligomer binding site was proposed that would not rely on the dimerization of PLD3 to bind to ssDNA, contrasting with our binding model. However, considering that PLD3 is targeted to the acidic lysosomal compartment, we examined the electrostatic surface potential of PLD3 at pH 5. Our analysis revealed two distinct positively charged regions not previously identified, suggesting a potential binding site for long nucleic acids involving both protomers of the dimer, which we could confirm by biochemical studies. Our results would be consistent with a model in which the activity of PLD exonucleases is divided into a distributive and a processive phase, as has been reported for other exonucleases.[36] In the initial distributive phase, the PLDs would show a strong preference for longer RNA sequences, >11 nucleotides in length. During this phase, they would bind to an RNA molecule, cleave a few nucleotides, and then release the RNA before binding to another substrate. This intermittent mode of action would be dictated by the enzyme's higher affinity for longer RNA molecules. As the enzyme progresses to the second phase, it undergoes a change in its mechanism and becomes highly processive. In this phase, once the exonuclease binds to its preferred longer RNA substrates, it stays attached and sequentially cleaves nucleotides, completely processing the RNA in a single binding event. Adverse substrates (e.g., secondary structure and sequence composition) would prevent this switch in activity and remain as shorter RNA fragments. These, in turn, could serve as pocket 2 ligands for TLR7.

In conclusion, our results elucidate the intricate role of nucleases in RNA recognition by TLR7. Interestingly, the dual role of PLD exonucleases, acting both pro-inflammatory (TLR7) and anti-inflammatory (TLR9), suggests a finely tuned balance to orchestrate appropriate immune responses. The simultaneous promotion and inhibition of inflammation by these exonucleases may serve as an essential protective mechanism, shielding the host from potential microbial modulators that would perturb this system. This nuanced modulation may also have important implications for therapeutic strategies aimed at harnessing or recalibrating these immune pathways.

Limitations of the study

Our work indicates that PLD exonucleases are essential for the generation of ligands for the first and second binding pockets of TLR7. Together with RNase T2, PLD enzymes release 2′,3′-cGMP, the proposed ligand for the first binding pocket. Conversely, PLD exonucleases tend to stall at cytidines, leaving fragments suitable for the second binding pocket of TLR7. However, the exact identity of these fragments remains to be determined, indicating the need for further work in this direction. In addition, the possible involvement of other lysosomal endonucleases, such as the RNase A family, in the generation of the ligand for the second binding pocket cannot be ruled out. It is conceivable that RNase A family enzymes may also degrade ssRNAs within the lysosome that are initially too large to bind

Please cite this article in press as: Bérouti et al., Lysosomal endonuclease RNase T2 and PLD exonucleases cooperatively generate RNA ligands for TLR7 activation, Immunity (2024), https://doi.org/10.1016/j.immunu.2024.04.010

TLR7, followed by subsequent trimming by PLD3 and PLD4, rendering them compatible for TLR7 binding.

STAR★METHODS

Detailed methods are provided in the online version of this paper and include the following:

- KEY RESOURCES TABLE
- RESOURCE AVAILABILITY
  - Lead contact
  - Materials availability
  - Data and code availability
- EXPERIMENTAL MODEL AND STUDY PARTICIPANT DETAILS
  - Cell culture
  - Cell stimulation
  - Isolation of PBMCs, primary plasmacytoid dendritic cells and primary human monocytes
  - CRISPR/ Cas9 mediated knockout generation
  - CRISPR/ Cas9 mediated knockout generation in primary human monocytes
  - Lentiviral transduction
- METHOD DETAILS
  - Immunoblotting
  - ELISA
  - Gene expression analysis
  - PLD3 and PLD4 protein purification
  - Coomassie staining of PLD3 and PLD4
  - Cryo-EM sample preparation and data acquisition of PLD3 and PLD4
  - Model building and refinement
  - Mass photometry
  - Nuclease assays
  - Urea gels
  - Affinity measurement by fluorescence anisotropy
  - Fluorescent RNA degradation assay
  - PLD3 and PLD4 quantification and whole proteome analysis
  - Preparation for LC-MS analysis of PLD3 and PLD4 degradation products
  - LC-MS/QQQ analysis of nucleoside-monophosphates
  - LC-HRMS analysis of oligonucleotides
- QUANTIFICATION AND STATISTICAL ANALYSIS

SUPPLEMENTAL INFORMATION

Supplemental information can be found online at https://doi.org/10.1016/j.immuni.2024.04.010.

ACKNOWLEDGMENTS

We kindly thank S. Suppmann and the Protein Production Core Facility (MPI, Munich) for expressing recombinant RNase 1, RNase 2, and RNase 6 and the BioSysM flow cytometry facility for great support. We thank Claudia Ludwig for technical support in isolating primary cells, Bachuki Shashikadze for his help in data analysis, and Zhiqi Sun for helpful discussions (all Gene Center, LMU). This work was supported by grants from the ERC (ERC-2020-ADG–101018672 ENGINES) to V.H., the Deutsche Forschungsgemeinschaft (DFG, German Research Foundation) CRC 237/A27 (Project-ID 369799452) to V.H. and T.C. and CRC 237/A05 (Project-ID 369799452) to K.-P.H., and the BMBF in the framework of the Cluster4future program (CNATM—Cluster for Nucleic Acid Therapeutics Munich) to T.C., K.-P.H., and V.H.

AUTHOR CONTRIBUTIONS

Conceptualization, M.B., K.L., and V.H.; investigation, M.B., K.L., M.H., L.H., S.B., J.S., F.P., I.P., W.G., M.W., C.J., and T.F.; writing – original draft, M.B., K.L., and V.H. with input from all authors; writing – review and editing, M.B. and V.H.; resources, T.C., K.-P.H., and V.H.; funding acquisition, V.H.; supervision, V.H.

DECLARATION OF INTERESTS

The authors declare no competing interests.

Received: October 16, 2023
Revised: March 6, 2024
Accepted: April 12, 2024
Published: May 1, 2024

REFERENCES

1. Diebold, S.S., Kaisho, T., Hemmi, H., Akira, S., and Reis e Sousa, C. (2004). Innate antiviral responses by means of TLR7-mediated recognition of single-stranded RNA. Science *303*, 1529–1531. https://doi.org/10.1126/science.1093616.
2. Heil, F., Hemmi, H., Hochrein, H., Ampenberger, F., Kirschning, C., Akira, S., Lipford, G., Wagner, H., and Bauer, S. (2004). Species-specific recognition of single-stranded RNA via toll-like receptor 7 and 8. Science *303*, 1526–1529. https://doi.org/10.1126/science.1093620.
3. Vinuesa, C.G., Grenov, A., and Kassiotis, G. (2023). Innate virus-sensing pathways in B cell systemic autoimmunity. Science *380*, 478–484. https://doi.org/10.1126/science.adg6427.
4. Fitzgerald, K.A., and Kagan, J.C. (2020). Toll-like Receptors and the Control of Immunity. Cell *180*, 1044–1066. https://doi.org/10.1016/j.cell.2020.02.041.
5. Lind, N.A., Rael, V.E., Pestal, K., Liu, B., and Barton, G.M. (2022). Regulation of the nucleic acid-sensing Toll-like receptors. Nat. Rev. Immunol. *22*, 224–235. https://doi.org/10.1038/s41577-021-00577-0.
6. Majer, O., Liu, B., Woo, B.J., Kreuk, L.S.M., Van Dis, E., and Barton, G.M. (2019). Release from UNC93B1 reinforces the compartmentalized activation of select TLRs. Nature *575*, 371–374. https://doi.org/10.1038/s41586-019-1611-7.
7. Majer, O., Liu, B., Kreuk, L.S.M., Krogan, N., and Barton, G.M. (2019). UNC93B1 recruits syntenin-1 to dampen TLR7 signalling and prevent autoimmunity. Nature *575*, 366–370. https://doi.org/10.1038/s41586-019-1612-6.
8. Swiecki, M., and Colonna, M. (2015). The multifaceted biology of plasmacytoid dendritic cells. Nat. Rev. Immunol. *15*, 471–485. https://doi.org/10.1038/nri3865.
9. Zhang, Z., Ohto, U., Shibata, T., Krayukhina, E., Taoka, M., Yamauchi, Y., Tanji, H., Isobe, T., Uchiyama, S., Miyake, K., and Shimizu, T. (2016). Structural Analysis Reveals that Toll-like Receptor 7 Is a Dual Receptor for Guanosine and Single-Stranded RNA. Immunity *45*, 737–748. https://doi.org/10.1016/j.immuni.2016.09.011.
10. Zhang, Z., Ohto, U., Shibata, T., Taoka, M., Yamauchi, Y., Sato, R., Shukla, N.M., David, S.A., Isobe, T., Miyake, K., and Shimizu, T. (2018). Structural Analyses of Toll-like Receptor 7 Reveal Detailed RNA Sequence Specificity and Recognition Mechanism of Agonistic Ligands. Cell Rep. *25*, 3371–3381.e5. https://doi.org/10.1016/j.celrep.2018.11.081.
11. Tanji, H., Ohto, U., Shibata, T., Taoka, M., Yamauchi, Y., Isobe, T., Miyake, K., and Shimizu, T. (2015). Toll-like receptor 8 senses degradation products of single-stranded RNA. Nat. Struct. Mol. Biol. *22*, 109–115. https://doi.org/10.1038/nsmb.2943.
12. Greulich, W., Wagner, M., Gaidt, M.M., Stafford, C., Cheng, Y., Linder, A., Carell, T., and Hornung, V. (2019). TLR8 Is a Sensor of RNase T2 Degradation Products. Cell *179*, 1264–1275.e13. https://doi.org/10.1016/j.cell.2019.11.001.
13. Ostendorf, T., Zillinger, T., Andryka, K., Schlee-Guimaraes, T.M., Schmitz, S., Marx, S., Bayrak, K., Linke, R., Salgert, S., Wegner, J., et al. (2020). Immune Sensing of Synthetic, Bacterial, and Protozoan RNA by Toll-like Receptor 8 Requires Coordinated Processing by RNase T2 and RNase 2. Immunity *52*, 591–605.e6. https://doi.org/10.1016/j.immuni.2020.03.009.

14. Liu, K., Sato, R., Shibata, T., Hiranuma, R., Reuter, T., Fukui, R., Zhang, Y., Ichinohe, T., Ozawa, M., Yoshida, N., et al. (2021). Skewed endosomal RNA responses from TLR7 to TLR3 in RNase T2-deficient macrophages. Int. Immunol. *33*, 479–490. https://doi.org/10.1093/intimm/dxab033.

15. Maeda, T., Murata, K., Fukushima, T., Sugahara, K., Tsuruda, K., Anami, M., Onimaru, Y., Tsukasaki, K., Tomonaga, M., Moriuchi, R., et al. (2005). A novel plasmacytoid dendritic cell line, CAL-1, established from a patient with blastic natural killer cell lymphoma. Int. J. Hematol. *81*, 148–154. https://doi.org/10.1532/ijh97.04116.

16. Hornung, V., Guenthner-Biller, M., Bourquin, C., Ablasser, A., Schlee, M., Uematsu, S., Noronha, A., Manoharan, M., Akira, S., de Fougerolles, A., et al. (2005). Sequence-specific potent induction of IFN-alpha by short interfering RNA in plasmacytoid dendritic cells through TLR7. Nat. Med. *11*, 263–270. https://doi.org/10.1038/nm1191.

17. Gavin, A.L., Huang, D., Huber, C., Mårtensson, A., Tardif, V., Skog, P.D., Blane, T.R., Thinnes, T.C., Osborn, K., Chong, H.S., et al. (2018). PLD3 and PLD4 are single-stranded acid exonucleases that regulate endosomal nucleic-acid sensing. Nat. Immunol. *19*, 942–953. https://doi.org/10.1038/s41590-018-0179-y.

18. Gavin, A.L., Huang, D., Blane, T.R., Thinnes, T.C., Murakami, Y., Fukui, R., Miyake, K., and Nemazee, D. (2021). Cleavage of DNA and RNA by PLD3 and PLD4 limits autoinflammatory triggering by multiple sensors. Nat. Commun. *12*, 5874. https://doi.org/10.1038/s41467-021-26150-w.

19. Hao, Y., Hao, S., Andersen-Nissen, E., Mauck, W.M., 3rd, Zheng, S., Butler, A., Lee, M.J., Wilk, A.J., Darby, C., Zager, M., et al. (2021). Integrated analysis of multimodal single-cell data. Cell *184*, 3573–3587.e29. https://doi.org/10.1016/j.cell.2021.04.048.

20. Speir, M.L., Bhaduri, A., Markov, N.S., Moreno, P., Nowakowski, T.J., Papatheodorou, I., Pollen, A.A., Raney, B.J., Seninge, L., Kent, W.J., and Haeussler, M. (2021). UCSC Cell Browser: visualize your single-cell data. Bioinformatics *37*, 4578–4580. https://doi.org/10.1093/bioinformatics/btab503.

21. Zhang, S., Hu, Z., Tanji, H., Jiang, S., Das, N., Li, J., Sakaniwa, K., Jin, J., Bian, Y., Ohto, U., et al. (2018). Small-molecule inhibition of TLR8 through stabilization of its resting state. Nat. Chem. Biol. *14*, 58–64. https://doi.org/10.1038/nchembio.2518.

22. Cappel, C., Gonzalez, A.C., and Damme, M. (2021). Quantification and characterization of the 5′ exonuclease activity of the lysosomal nuclease PLD3 by a novel cell-based assay. J. Biol. Chem. *296*, 100152. https://doi.org/10.1074/jbc.RA120.015867.

23. Bowling, F.Z., Salazar, C.M., Bell, J.A., Huq, T.S., Frohman, M.A., and Airola, M.V. (2020). Crystal structure of human PLD1 provides insight into activation by PI(4,5)P(2) and RhoA. Nat. Chem. Biol. *16*, 400–407. https://doi.org/10.1038/s41589-020-0499-8.

24. Gottlin, E.B., Rudolph, A.E., Zhao, Y., Matthews, H.R., and Dixon, J.E. (1998). Catalytic mechanism of the phospholipase D superfamily proceeds via a covalent phosphohistidine intermediate. Proc. Natl. Acad. Sci. USA *95*, 9202–9207. https://doi.org/10.1073/pnas.95.16.9202.

25. Stuckey, J.A., and Dixon, J.E. (1999). Crystal structure of a phospholipase D family member. Nat. Struct. Biol. *6*, 278–284. https://doi.org/10.1038/6716.

26. Jumper, J., Evans, R., Pritzel, A., Green, T., Figurnov, M., Ronneberger, O., Tunyasuvunakool, K., Bates, R., Žídek, A., Potapenko, A., et al. (2021). Highly accurate protein structure prediction with AlphaFold. Nature *596*, 583–589. https://doi.org/10.1038/s41586-021-03819-2.

27. Cruchaga, C., Karch, C.M., Jin, S.C., Benitez, B.A., Cai, Y., Guerreiro, R., Harari, O., Norton, J., Budde, J., Bertelsen, S., et al. (2014). Rare coding variants in the phospholipase D3 gene confer risk for Alzheimer's disease. Nature *505*, 550–554. https://doi.org/10.1038/nature12825.

28. Nibbeling, E.A.R., Duarri, A., Verschuuren-Bemelmans, C.C., Fokkens, M.R., Karjalainen, J.M., Smeets, C.J.L.M., de Boer-Bergsma, J.J., van der Vries, G., Dooijes, D., Bampi, G.B., et al. (2017). Exome sequencing and network analysis identifies shared mechanisms underlying spinocerebellar ataxia. Brain *140*, 2860–2878. https://doi.org/10.1093/brain/awx251.

29. Yan, Y., Tao, H., He, J., and Huang, S.Y. (2020). The HDOCK server for integrated protein-protein docking. Nat. Protoc. *15*, 1829–1852. https://doi.org/10.1038/s41596-020-0312-x.

30. Van Acker, Z.P., Perdok, A., Hellemans, R., North, K., Vorsters, I., Cappel, C., Dehairs, J., Swinnen, J.V., Sannerud, R., Bretou, M., et al. (2023). Phospholipase D3 degrades mitochondrial DNA to regulate nucleotide signaling and APP metabolism. Nat. Commun. *14*, 2847. https://doi.org/10.1038/s41467-023-38501-w.

31. Kettwig, M., Ternka, K., Wendland, K., Krüger, D.M., Zampar, S., Schob, C., Franz, J., Aich, A., Winkler, A., Sakib, M.S., et al. (2021). Interferon-driven brain phenotype in a mouse model of RNaseT2 deficient leukoencephalopathy. Nat. Commun. *12*, 6530. https://doi.org/10.1038/s41467-021-26880-x.

32. Kawane, K., Ohtani, M., Miwa, K., Kizawa, T., Kanbara, Y., Yoshioka, Y., Yoshikawa, H., and Nagata, S. (2006). Chronic polyarthritis caused by mammalian DNA that escapes from degradation in macrophages. Nature *443*, 998–1002. https://doi.org/10.1038/nature05245.

33. Chan, M.P., Onji, M., Fukui, R., Kawane, K., Shibata, T., Saitoh, S., Ohto, U., Shimizu, T., Barber, G.N., and Miyake, K. (2015). DNase II-dependent DNA digestion is required for DNA sensing by TLR9. Nat. Commun. *6*, 5853. https://doi.org/10.1038/ncomms6853.

34. Yang, W. (2011). Nucleases: diversity of structure, function and mechanism. Q. Rev. Biophys. *44*, 1–93. https://doi.org/10.1017/S0033583510000181.

35. Roske, Y., Cappel, C., Cremer, N., Hoffmann, P., Koudelka, T., Tholey, A., Heinemann, U., Daumke, O., and Damme, M. (2024). Structural analysis of PLD3 reveals insights into the mechanism of lysosomal 5′ exonuclease-mediated nucleic acid degradation. Nucleic Acids Res. *52*, 370–384. https://doi.org/10.1093/nar/gkad1114.

36. Ye, X., Axhemi, A., and Jankowsky, E. (2021). Alternative RNA degradation pathways by the exonuclease Pop2p from Saccharomyces cerevisiae. RNA *27*, 465–476. https://doi.org/10.1261/rna.078006.120.

37. Rapino, F., Robles, E.F., Richter-Larrea, J.A., Kallin, E.M., Martinez-Climent, J.A., and Graf, T. (2013). C/EBPalpha induces highly efficient macrophage transdifferentiation of B lymphoma and leukemia cell lines and impairs their tumorigenicity. Cell Rep. *3*, 1153–1163. https://doi.org/10.1016/j.celrep.2013.03.003.

38. Jack, I., Seshadri, R., Garson, M., Michael, P., Callen, D., Zola, H., and Morley, A. (1986). RCH-ACV: a lymphoblastic leukemia cell line with chromosome translocation 1;19 and trisomy 8. Cancer Genet. Cytogenet. *19*, 261–269. https://doi.org/10.1016/0165-4608(86)90055-5.

39. Schmidt, T., Schmid-Burgk, J.L., and Hornung, V. (2015). Synthesis of an arrayed sgRNA library targeting the human genome. Sci. Rep. *5*, 14987. https://doi.org/10.1038/srep14987.

40. Schmid-Burgk, J.L., Schmidt, T., Gaidt, M.M., Pelka, K., Latz, E., Ebert, T.S., and Hornung, V. (2014). OutKnocker: a web tool for rapid and simple genotyping of designer nuclease edited cell lines. Genome Res. *24*, 1719–1723. https://doi.org/10.1101/gr.176701.114.

41. Li, Z., Michael, I.P., Zhou, D., Nagy, A., and Rini, J.M. (2013). Simple piggyBac transposon-based mammalian cell expression system for inducible protein production. Proc. Natl. Acad. Sci. USA *110*, 5004–5009. https://doi.org/10.1073/pnas.1218620110.

42. Punjani, A., Rubinstein, J.L., Fleet, D.J., and Brubaker, M.A. (2017). cryoSPARC: algorithms for rapid unsupervised cryo-EM structure determination. Nat. Methods *14*, 290–296. https://doi.org/10.1038/nmeth.4169.

43. Bepler, T., Morin, A., Rapp, M., Brasch, J., Shapiro, L., Noble, A.J., and Berger, B. (2019). Positive-unlabeled convolutional neural networks for particle picking in cryo-electron micrographs. Nat. Methods *16*, 1153–1160. https://doi.org/10.1038/s41592-019-0575-8.

44. Emsley, P., Lohkamp, B., Scott, W.G., and Cowtan, K. (2010). Features and development of Coot. Acta Crystallogr. D Biol. Crystallogr. *66*, 486–501. https://doi.org/10.1107/S0907444910007493.

45. Croll, T.I. (2018). ISOLDE: a physically realistic environment for model building into low-resolution electron-density maps. Acta Crystallogr. D Struct. Biol. *74*, 519–530. https://doi.org/10.1107/S2059798318002425.

46. Liebschner, D., Afonine, P.V., Baker, M.L., Bunkóczi, G., Chen, V.B., Croll, T.I., Hintze, B., Hung, L.W., Jain, S., McCoy, A.J., et al. (2019). Macromolecular structure determination using X-rays, neutrons and electrons: recent developments in Phenix. Acta Crystallogr. D Struct. Biol. *75*, 861–877. https://doi.org/10.1107/S2059798319011471.

47. Afonine, P.V., Grosse-Kunstleve, R.W., Echols, N., Headd, J.J., Moriarty, N.W., Mustyakimov, M., Terwilliger, T.C., Urzhumtsev, A., Zwart, P.H., and Adams, P.D. (2012). Towards automated crystallographic structure refinement with phenix.refine. Acta Crystallogr. D Biol. Crystallogr. *68*, 352–367. https://doi.org/10.1107/S0907444912001308.

48. Pettersen, E.F., Goddard, T.D., Huang, C.C., Meng, E.C., Couch, G.S., Croll, T.I., Morris, J.H., and Ferrin, T.E. (2021). UCSF ChimeraX: Structure visualization for researchers, educators, and developers. Protein Sci. *30*, 70–82. https://doi.org/10.1002/pro.3943.

49. Jung, C., Bandilla, P., von Reutern, M., Schnepf, M., Rieder, S., Unnerstall, U., and Gaul, U. (2018). True equilibrium measurement of transcription factor-DNA binding affinities using automated polarization microscopy. Nat. Commun. *9*, 1605. https://doi.org/10.1038/s41467-018-03977-4.

50. Shashikadze, B., Valla, L., Lombardo, S.D., Prehn, C., Haid, M., Riols, F., Stöckl, J.B., Elkhateib, R., Renner, S., Rathkolb, B., et al. (2023). Maternal hyperglycemia induces alterations in hepatic amino acid, glucose and lipid metabolism of neonatal offspring: multi-omics insights from a diabetic pig model. Mol. Metab. *75*, 101768. https://doi.org/10.1016/j.molmet.2023.101768.

51. Demichev, V., Messner, C.B., Vernardis, S.I., Lilley, K.S., and Ralser, M. (2020). DIA-NN: neural networks and interference correction enable deep proteome coverage in high throughput. Nat. Methods *17*, 41–44. https://doi.org/10.1038/s41592-019-0638-x.

52. Pino, L.K., Searle, B.C., Bollinger, J.G., Nunn, B., MacLean, B., and MacCoss, M.J. (2020). The Skyline ecosystem: Informatics for quantitative mass spectrometry proteomics. Mass Spectrom. Rev. *39*, 229–244. https://doi.org/10.1002/mas.21540.

Please cite this article in press as: Bérouti et al., Lysosomal endonuclease RNase T2 and PLD exonucleases cooperatively generate RNA ligands for TLR7 activation, Immunity (2024), https://doi.org/10.1016/j.immuni.2024.04.010

STAR★METHODS

KEY RESOURCES TABLE

REAGENT or RESOURCE	SOURCE	IDENTIFIER
Antibodies		
Anti-TLR7	Cell Signaling Technology	Cat#5632 RRID:AB_10692895
Anti-β actin	Santa Cruz Biotechnologies	Cat#47778 RRID:AB_2714189
Direct-Blot HRP anti FLAG tag	BioLegend	Cat#637311 RRID:AB_2566706
Anti-rabbit IgG HRP linked	Cell Signaling Technology	Cat#7074 RRID:AB_2099233
Chemicals, peptides, and recombinant proteins		
Acetonitrile	Carl Roth	Cat# HN40.1
Advanced RPMI 1640 medium	Gibco	Cat# 12633020
Ammonium persulfate	Sigma-Aldrich	Cat# A3678
BioColl	Bio&Sell	Cat# BS.L 6115
Blasticidin	Thermo Scientific	Cat# A1113903
CD14 MircroBeads Human	Miltenyi	Cat# 130-050-201
Coomassie Brilliant Blue R-250 Dye	Thermo Scientific	Cat# 20278
CU-CPT9a	Invivogen	Cat# inh-cc9a
Doxycycline	Sigma-Aldrich	Cat# D9891
Fetal calf serum	Gibco	Cat# 10270106
GlutaMAX	Gibco	Cat# 35050038
HEPES	Sigma-Aldrich	Cat# H0887-100ML
LPS-EB Ultrapure	InvivoGen	Cat#tlrl-3pelps
Lys-C	Wako	Cat# 4548995075888
MEM NEAA	Gibco	Cat# 11140035
Modified porcine trypsin	Promega	Cat# VA9000
NI-NTA agarose beads	Quiagen	Cat# R90115
Nitrocellulose membrane (0.45 μm)	GE Healthcare	Cat#10600002
Opti-MEM™	Gibco	Cat# 31985047
Penicillin/Streptomycin	Gibco	Cat# 15-140-122
PepMap 100 C18 trap column	Thermo Fisher Scientific	Cat#164750
PepMap RSLC C18	Thermo Fisher Scientific	Cat#164540
PLD3 peptides: ALLNVVDNAX (A310 to R319) LFVVPADEAQAX (L397 to R408) SQLEAIFLX (S458 to R466)	JPT Peptide Technologies	N/A
PLD4 peptides: LQQLLGX (L164 to R170) FWVVDGX (F217 to R223)	JPT Peptide Technologies	N/A
Poly-L-arginine	Sigma-Aldrich	Cat#P7762
Puromycin	Carl Roth	Cat# 0240.4
Recombinant Human IL-3	MPI of Biochemistry, Munich	N/A
Recombinant Human IFN-γ	PeproTech	Cat#300-02
Recombinant Human CSF1 (M-CSF)	MPI of Biochemistry, Munich	N/A
Recombinant PreScission Protease	MPI of Biochemistry, Munich	N/A
Recombinant Human PLD3 (and all PLD3 mutants)	This Paper	N/A
Recombinant Human PLD4	This Paper	N/A
Recombinant Human RNase 1	MPI of Biochemistry, Munich	N/A
Recombinant Human RNase 2	MPI of Biochemistry, Munich	N/A
Recombinant Human RNase 6	MPI of Biochemistry, Munich	N/A

(*Continued on next page*)

Please cite this article in press as: Bérouti et al., Lysosomal endonuclease RNase T2 and PLD exonucleases cooperatively generate RNA ligands for TLR7 activation, Immunity (2024), https://doi.org/10.1016/j.immuni.2024.04.010

Continued

REAGENT or RESOURCE	SOURCE	IDENTIFIER
RBC lysis Buffer	BioLegend	Cat# 420301
RPMI 1640 medium	Gibco	Cat# 11875093
R848	InvivoGen	Cat# tlrl-r848
SequaGel Concentrate	National diagnostics	Cat#EC830-1L
SequaGel Buffer	National diagnostics	Cat# EC835-200ml
SequaGel Diluent	National diagnostics	Cat# EC840-1L
Sodium pyruvate	Gibco	Cat# 11360039
Superdex-200 increase 5/50 GL	Sigma-Aldrich	Cat# 28-9909-45
SYBR Gold Nucleic Acid Gel Stain	Thermo Fisher Scientifc	Cat# S33102
TEMED	Carl Roth	Cat# 2367.3
TL8-506	InvivoGen	Cat# tlrl-tl8506
TRIS glycine SDS-PAGE	Thermo Scientific	Cat# XP00125BOX
cOmplete	Roche	Cat# CO-RO
β-Estradiol	Sigma-Aldrich	Cat#E8875
2',3'-cGMP	BIOLOG	Cat# G 025-250
3'-GMP	BIOLOG	Cat# G 021-50
5'-GMP	Sigma Aldrich	Cat # G8377
2x RNA loading dye	Thermo Fisher Scientific	Cat# R0641
Critical commercial assays		
Human IFN-βELISA Set	R&D System	Cat# DY814-05
Human IFN-α2 ELISA Set	R&D System	Cat# DY9345-05
Human IL-6 ELISA Set	BD Biosciences	Cat# 555220
Human TNF ELISA Set	BD Biosciences	Cat# 555212
Mouse IL-6 ELISA Set	BD Biosciences	Cat# 555240
BCA protein assay Kit	Thermo Fisher Scientific	Cat# 23227
CD34 MicroBead Kit UltraPure, human	Miltenyi	Cat# 130-100-453
PAN Monocyte Isolation Kit	Miltenyi	Cat# 130-096-537
SG Cell Line 96-well NucleofectorTM Kit	Lonza	Cat# V4SC-3096
P3 Primary Cell 4D-Nucleofector X Kit S	Lonza	Cat# V4XP-3032
MiSeq Reagent Kit v2, 300 Cycles	Illumina	Cat# MS-102-2002
Deposited data		
Mass spectrometry proteomics	ProteomeXchange Consortium	PXD045912
Experimental models: Cell lines		
CAL-1	Maeda et al.[15]	N/A
BLaER1 human b-cell to monocyte trans-differentiation cell line	Rapino et al.[37]	N/A
RCH-ACV	Jack et al.[38]	N/A
Oligonucleotides		
RNA40S(rG*rC*rC*rC*rG*rU*rC*rU*rG*rU*rU*rG*rU*rG*rU*rG*rA*rC*rU*rC)	Miltenyi	130-104-429
RNA40 (rGrCrCrCrGrUrCrUrGrUrUrGrUrGrUrGrArCrUrC)	IDT	N/A
RNA9.2s (rArGrCrUrUrArArCrCrUrGrUrCrCrUrUrCrArA)	IDT	N/A
CpG^S (T*C*G*T*C*G*T*T*T*T*G*T*C*G*T*T*T*T*G*T*C*G*T*T)	IDT	N/A
CpG^O (TCGTCGTTTTGTCGTTTTGTCGTT)	IDT	N/A
$rCrCrUrUrCrA(AC)_7$	IDT	N/A
$rArArUrUrCrA(AC)_7$	IDT	N/A
$rUrUrUrUrU(AC)_7$	IDT	N/A
rGrUrArGrArGrArGrArGrArGrArGrArGrArG	IDT	N/A
rArGrUrArGrArGrArGrArGrArGrArGrArGrA	IDT	N/A
rGrArGrUrArGrArGrArGrArGrArGrArGrArG	IDT	N/A
rArGrArGrUrArGrArGrArGrArGrArGrArGrA	IDT	N/A

(*Continued on next page*)

Please cite this article in press as: Bérouti et al., Lysosomal endonuclease RNase T2 and PLD exonucleases cooperatively generate RNA ligands for TLR7 activation, Immunity (2024), https://doi.org/10.1016/j.immuni.2024.04.010

Continued

REAGENT or RESOURCE	SOURCE	IDENTIFIER
$(rU*rC*)_{10}$	IDT	N/A
$(A*C*)_{10}$	IDT	N/A
5'-FAM-RNA40-3'-BMNQ530 (rGrCrCrGrUrCrUrGrUrUrGrUrGrUrGrArCrUrC)	Biomers	N/A
RNA9.2s-3'FAM (rArGrCrUrUrArArCrCrUrGrUrCrCrUrUrCrArA-FAM)	Metabion	N/A
rArGrCrUrUrArArCrCrUrGrUrCrCrUrUrC-FAM	Metabion	N/A
rArGrCrUrUrArArCrCrUrGrUrCrCrU-FAM	Metabion	N/A
rArGrCrUrUrArArCrCrUrGrUrC-FAM	Metabion	N/A
rArGrCrUrUrArArCrCrUrG-FAM	Metabion	N/A
rArGrCrUrUrArArCrC-FAM	Metabion	N/A
rArGrCrUrUrArA-FAM	Metabion	N/A
rArGrCrUrU-FAM	Metabion	N/A
DNA9.2s-3'FAM (AGCTTAACCTGTCCTTCAA-FAM)	Metabion	N/A
AGCTTAACCTGTCCTTC-FAM	Metabion	N/A
AGCTTAACCTGTCCT-FAM	Metabion	N/A
AGCTTAACCTGTC-FAM	Metabion	N/A
AGCTTAACCTG-FAM	Metabion	N/A
AGCTTAACC-FAM	Metabion	N/A
Recombinant DNA		
PB_6xHis_hsPLD3 (and all mutants)	This study	N/A
PB_6xHis_hsPLD4	This study	N/A
pFUGW_hsPLD3_Blast	This study	N/A
pCAS9-mCherry-gRNA	Schmidt et al.[39]	N/A
Software and algorithms		
GraphPad Prism10	GraphPad	N/A
Outknocker	Schmid-Burgk et al.[40]	N/A
ChimeraX	UCSF ChimeraX	N/A
AcquireMP	Refeyn	N/A
MassHunter Software	Agilent	N/A
Other		
384W SensoPlate™, Sterile, Flat Bottom, Black/Glass, w/Lid	Greiner Bio-One	Cat# 781892

RESOURCE AVAILABILITY

Lead contact

Further information and requests for resources and reagents should be directed to and will be fulfilled by the lead contact, Veit Hornung (hornung@genzentrum.lmu.de).

Materials availability

All newly generated materials associated with the paper are available upon request from the lead contact.

Data and code availability

- Raw MS data is deposited in PRIDE database under accession number PXD045912.
- The coordinates of the PLD3 apoenzyme structure have been deposited in the Protein Data Bank (PDB) under the accession number 8S86 and the cryo-EM reconstruction is available in the Electron Microscopy Data Bank (EMDB) under the EMBD accession number EMD-19798.
- This paper does not report original code.
- Any additional information required to reanalyze the data reported in this work paper is available from the lead contact upon request.

Please cite this article in press as: Bérouti et al., Lysosomal endonuclease RNase T2 and PLD exonucleases cooperatively generate RNA ligands for TLR7 activation, Immunity (2024), https://doi.org/10.1016/j.immunu.2024.04.010

EXPERIMENTAL MODEL AND STUDY PARTICIPANT DETAILS

Cell culture

CAL-1 cells, which were derived from a male donor (hemizygous for TLR7), were cultured in RPMI 1640 medium supplemented with 10% heat-inactivated fetal calf serum, 100 U/ ml penicillin/streptomycin (PS), 1 mM sodium pyruvate, 2 x GlutaMAX, 10 mM HEPES and 1 x MEM NEAA.

BLaER1 monocytes, which were derived from a female donor, RCH-ACV cells and primary plasmacytoid dendritic cells were cultured in RPMI 1640 medium, supplemented with 10% heat-inactivated fetal calf serum (FCS), 100 U/ ml penicillin/streptomycin (PS) and 1 mM sodium pyruvate. Primary monocytes were cultured in RPMI 1640 medium, supplemented with 10% FCS, 2 mM GlutaMAX and 100 U/ ml penicillin/streptomycin (PS). J774 mouse macrophages were cultured in DMEM medium supplemented with 10% heat-inactivated fetal calf serum (FCS), 100 U/ ml penicillin/streptomycin (PS) and 1 mM sodium pyruvate. All cells were cultured in a humidified incubator at 37 °C with 5% CO_2. For trans-differentiation of BLaER1 monocytes into macrophages, the cytokines M-CSF (10 ng/ml), IL-3 (10 ng/ml) and 100 nM β-estradiol were added to the culture media. Cells were differentiated in a 96-well plate (80,000 cells/well) for 5 days and afterwards used for stimulation experiments. For differentiation of primary monocytes into macrophages, the cytokine M-CSF (100 ng/ml) was added to the culture medium. Cells were differentiated in non-treated 6 well plates ($1x10^6$ cells/well) for 8 days and fresh M-CSF was added every 2 days.

Cell stimulation

CAL-1 cells (if not otherwise indicated: 100,000 cells/well in a 96-well plate) were primed with hIFN-γ (10 ng/ml) for 6 hours prior to stimulation. J774 mouse macrophages (55,000 cells/well in a 96-well plate) were primed with mIFN-γ (20 ng/ml) for 6 hours prior to stimulation. BLaER1 cells (80,000 cells/well in a 96-well plate) as well as monocyte-derived macrophages (70,000 cells/well in a 96-well plate) were stimulated after trans-differentiation. Primary plasmacytoid dendritic cells (20,000 cells/well in a 96-well plate) were incubated with hIL-3 (10ng/ml) for 4 hours before stimulation.

For transfection with RNA9.2s (1.2 μg/well), $RNA40^O$ (1.2 μg/well), $RNA40^S$ (0.6μg/well) and short ORNs (CCUUCA$(dAdC)_7$, AAUUCA$(dAdC)_7$, UUUUUU$(dAdC)_7$) (2.4 μg/well), RNA and poly-L-arginine were incubated separately in a 1:1 ratio for 5 minutes in pre-warmed Opti-MEM (25 μl/well). Subsequently, the two reagents were combined and incubated for additional 20 minutes and afterwards added to the cells. For RNA transfections in the presence of the TLR8 inhibitor, CU-CPT9a was added 30 min prior to the stimulation (final concentration: 10 μM). If not otherwise indicated, cells were further stimulated with 200 ng/ml LPS-EB ultrapure, 1 μg/ml R848, 100 ng/ml TL8-506, 5 μM CpG^S, 5 μM CpG^O DNA or indicated concentrations of 2',3'-cGMP, 3'-GMP and 5'-GMP. Supernatants of CAL-1 cells and primary monocyte-derived macrophages were harvested after 16 hours of incubation at 37 °C and the supernatants of BLaER1 and J774 cells were harvested after 14 hours.

Isolation of PBMCs, primary plasmacytoid dendritic cells and primary human monocytes

Peripheral blood mononuclear cells (PBMCs) were isolated from the leukocyte reduction system chambers left over from platelet donation from healthy donors. Approval from the relevant ethics committee and informed consent from all donors according to the Declaration of Helsinki were obtained (project number: 19-238, Ethics Committee of the Medical Faculty of Ludwig-Maximilians-University Munich). PBMCs were isolated using BioColl and erythrocyte lysis (RBC lysis buffer). Human monocytes were MACS purified from PBMCs using CD14 microbeads and primary plasmacytoid dendritic cells were MACS purified with CD34 microbeads.

CRISPR/ Cas9 mediated knockout generation

Knockouts of CAL-1 cells and J774 macrophages were generated with RNPs. For CAL-1 monoclones the following gRNAs were used: TLR7 gRNA1: 5'-ACTGTGTACCTATTCCACTG-3'; gRNA2: 5'-CAGCTACTAGAGATACCGCA-3', PLD3 gRNA1: 5'-TAGCGGG TGTCATAGAACCG-3'; gRNA2: 5'-CCAGAGCAGGGGTTCCATTG-3', PLD4 gRNA1: 5'-GCAGTGCCAACATGGACTGG-3'; gRNA2: 5'-CCCATGGGGCGGCTCACCAG-3', RNase T2 gRNA1: 5'-ATCCTCACAGGAAGCATGAG-3'; gRNA2: 5'-GTTGAGCGCATCCAC CTGGG-3'. For the PLD3xPLD4 pool knockout of CAL-1 cells the same PLD3 guides were used but the PLD4 gRNAs were exchanged to: gRNA1: 5'-TGGGAGCGCTGGCTGTGCTG-3' and gRNA2: 5'-GACGGGGCACUUGCCACAGG-3'. For the PLD3 pool KO in J774 cells the following three gRNAs were used: gRNA1: 5'-CCACUCCACAGAAAGCCCGC-3', gRNA2: 5'-CACC GAAGCCCACUACCGCC-3' and gRNA3: 5'-CAGCUGUUUCUAUGGGAAUA-3'.

For CRISPR/Cas9 RNP assembly, crRNA and tracrRNA were incubated in a 1:1 molar ratio for 5 min at 95°C followed by incubation at room temperature for 1h. To each gRNA complex (100 pmol) NLS-Cas9 (40 pmol) was added and incubated for 15 minutes at room temperature. gRNA/Cas9 mixtures were once frozen at –80°C before usage. For nucleofection, $1x10^6$ CAL-1 cells or $2x10^5$ J774 macrophages were resuspended in 20 μl of SG Cell Line Nucleofector Solution. Cas9/RNP assembly was added and CAL-1 cells were nucleofected on a 4D-Nucleofector (Lonza) with the following program: DN-100. For J774 the program: CM-139 was used for nucleofection. Cells were transferred into 2 ml of pre-warmed culture medium. CAL-1 cells were rested for 24 hours before subjected to limiting dilution to obtain monoclones.

BLaER1 monocytes were gene targeted with the plasmid based CRISPR system. Here, the following gRNAs were used: PLD3 gRNA: 5'-TGCGGACGTTCACGCCCTT-3', PLD4 gRNA: 5'-GCCACGTGGACGCTCTCCT-3', TLR7 gRNA: 5'-ATGGGGCATTATAA CAACGA-3', TLR8 gRNA: 5'-CAGGAAGTTCCCCAAACGGT-3'. To $2.5x10^6$ cells in 250 μl of warm Opti-Mem medium 5 μg of

Please cite this article in press as: Bérouti et al., Lysosomal endonuclease RNase T2 and PLD exonucleases cooperatively generate RNA ligands for TLR7 activation, Immunity (2024), https://doi.org/10.1016/j.immuni.2024.04.010

DNA (pCAS9-mCherry-gRNA) was added. The mixture was incubated for 15 min at room temperature and afterwards electroporated according to the following protocol: 265 V, 975 μF; 720 Ω using a Gene Pulser (BioRad). Cells were transferred into 2 ml of BLaER1 culture medium and rested for 24 hours. Using FACS analysis, mCherry positive cells were selected and monoclones were generated by limiting dilution. After three to four weeks, monoclones of CAL-1 and BLaER1 cells were picked and analyzed by MiSeq as described before.[40] Pool knockouts of CAL-1 and J774 cells were confirmed with the ICE CRISPR analysis tool from Synthego. For all cell lines, the parental cell line was used as wild-type controls.

CRISPR/ Cas9 mediated knockout generation in primary human monocytes

The same guide RNAs used to generate the *PLD3* x *PLD4* pool knockout in CAL-1 cells were also employed for knockouts in primary human monocytes. TBX21 gRNAs (gRNA1: 5'-CGTCCACAAACATCCTGTAG-3' gRNA2: 5'-GCGGTACCAGAGCGGCAAGT-3') were used as non-targeting controls. Pan monocytes were isolated from PBMCs by negative selection using the PAN Monocyte Isolation Kit. Immediately after isolation, cells were washed twice with PBS and $4x10^6$ cells were resuspended in 20 μl of P3 Nucleofector Solution. Cas9/RNP assembly was added and cells were nucleofected on a 4D-Nucleofector (Lonza) with the following program: EH-100. Immediately after nucleofection, cells were transferred into warm culture medium supplemented with M-CSF for differentiation. After 7 days, cells were counted and re-plated into 96-well plates. Stimulation was conducted on day 8 after nucleofection and knockout efficiencies were confirmed with the ICE CRISPR analysis tool from Synthego.

Lentiviral transduction

PLD3 was amplified from cDNA derived from BLaER1 cell lysate and cloned into a pFUGW_Blasticidin plasmid by Gibson cloning. CAL-1 cells were transduced for 48 h and afterwards selected with blasticidin (10 μg/ml). The polyclonal cell population was used for further experiments.

METHOD DETAILS

Immunoblotting

Samples were lysed in DISC buffer (150 mM NaCl, 50 mM Tris pH 7.5, 10% glycerol, 1% Triton X-100) supplemented with cOmplete protease inhibitor cocktail for 10 minutes on ice and afterwards centrifuged for 10 minutes at 16,000 g. The supernatant was collected, mixed with 6x Laemmli buffer (60 mM Tris pH 6.8, 9.3% DTT (w/v), 12% SDS (w/v), 47% glycerol (v/v), 0.06% bromphenol blue (w/v)) and denatured for 5 minutes at 95 °C. Samples were separated by TRIS glycine SDS-PAGE and transferred onto 0.45 mm nitrocellulose membrane. Next, membranes were blocked in 5% milk for 1 hour at room temperature and afterwards incubated with indicated primary and corresponding secondary antibodies. Chemiluminescent signals were recorded with a CCD camera.

ELISA

hIFN-β, hIFN-α2, hIL-6, hTNF and mIL-6 ELISAs were conducted according to supplier's protocol.

Gene expression analysis

Gene expression data shown in Figure 2A were obtained from the Human Cell Atlas (ImmGen Consortium; GEO: GSE227743). Data represent normalized gene counts of bulk RNA-Seq data from sorted cell populations from two healthy human blood donors.

PLD3 and PLD4 protein purification

Human PLD3 and human PLD4 were amplified from cDNA derived from BLaER1 cell lysates. PLD3 and PLD4 lacking the N-terminal domain and the transmembrane domain were fused to the Igκ leader sequence and a 6x His-tag and cloned into the piggyBac vector system,[41] followed by electroporation into RCH-ACV cells using a Gene Pulser device (BioRad). Stable pools of RCH-ACV cells expressing PLD3, PLD4 or various PLD3 mutants were generated by selection with blasticidin (10μg/ml) and puromycin (2.5 μg/ml).

Selected cells were grown to a density of $4x10^6$ cells/ml and protein expression was induced by exchanging the culture media into advanced RPMI 1640 medium, supplemented with doxycycline (1 μg/ml). Supernatants, containing the secreted proteins, were harvested and sterile filtered when cells viability decreased to 60%.

NI-NTA agarose beads were added to the supernatants and rotated overnight at 4 °C. Beads were washed three times with wash buffer (50 mM NaH_2PO_4, 300 mM NaCl, 10 mM Imidazol, pH=8.0) and eluted (50 mM NaH_2PO_4, 300 mM NaCl, 300 mM Imidazol, pH=8.0). The eluted proteins were concentrated and subjected to size exclusion chromatography (Superdex200) in the following buffer: 30 mM HEPES, 100 mM NaCl, pH=7.2. Fractions containing human PLD3 or human PLD4 were combined, concentrated and flash frozen with liquid nitrogen.

For purification of PLD3 and all PLD3 mutants (except for PLD3(H201N, H416N)), an additional cleavage site was introduced between the His-tag and the protein sequence to get rid of the His-tag before the proteins were subjected to size exclusion chromatography using a PreScission Protease. All protein concentrations were determined by BCA protein assay according to manufacturer's protocol.

Please cite this article in press as: Bérouti et al., Lysosomal endonuclease RNase T2 and PLD exonucleases cooperatively generate RNA ligands for TLR7 activation, Immunity (2024), https://doi.org/10.1016/j.immuni.2024.04.010

Coomassie staining of PLD3 and PLD4

To analyze purity of recombinant PLD3 and PLD4, proteins were separated on a 12% TRIS glycine SDS-PAGE. The gel was afterwards stained with Coomassie (45% Ethanol, 10% acetic acid and 1g/L Coomassie Brilliant Blue R-250 Dye in milliQ water) for 1 h at room temperature and destained (20% Ethanol, 10% acetic acid in milliQ water) overnight.

Cryo-EM sample preparation and data acquisition of PLD3 and PLD4

Cryo EM experiments of active human PLD3 and PLD4 were conducted in a buffer containing 50 mM MES pH 5.5 and 100 mM NaCl (apo structure) or in a buffer containing 50 mM MES pH 5.5 and 50 mM NaCl (Ligand-bound PLD3). The proteins were diluted to a concentration of 0.5 mg/ml prior to grid preparation. For ligand bound sample preparation with RNA $(rU^*rC^*)_{10}$ or DNA $(A^*C^*)_{10}$, RNA or DNA was added to PLD3 in a 1:4 molar ratio (Protein:RNA/DNA) and incubated for 10 seconds at room temperature right before plunge freezing. For vitrification 4.5 μl sample was applied onto a glow discharged QUANTIFOIL® R2/ 1 Cu200 grid. The sample was vitrified in liquid ethane using an EM GP plunge freezer (Leica) at 15 °C and 95% humidity. Cryo-EM data collection was carried out using an FEI Titan Krios G3 transmission electron microscope (300 kV) equipped with either a Gatan energy filter equipped with a GIF quantum energy filter (slit width 20 eV) and a Gatan K2 Summit direct electron detector (software used: EPU 2.12.1.278REL, TEM User interface Titan 2.15.4, Digital Micrograph 3.22.1461.0) or a SelectrisX energy filter (slit width 10 eV) and a Falcon 4 direct electron detector (software used: EPU 3.5.1.6034). For the structure of PLD3 apoenzyme 10.755 movies were collected with the K2 summit setup with a total electron dose of 45 e^- Å^{-2}, fractionated into 40 movie frames. For the structure determination of PLD3 in complex with ssRNA 27.504 movies were collected with a total electron dose of 60 e^- Å^{-2}, fractionated into 60 movie frames. The datasets were collected with defocus values ranging from -0.5 to -2.8 μm and a pixel size of 1.045 Å for apoenzyme PLD3 and 0.727 Å for PLD3 in complex with ssRNA, respectively. Cryo-EM image processing movie frames were motion corrected using the Relion 4 implemented version of MotionCor2. All subsequent cryo-EM data processing steps were carried out using cryoSPARC 4.3.0[42] and the resolutions reported here are calculated based on the gold-standard Fourier shell correlation criterion (FSC = 0.143). The CTF parameters of the datasets were determined using patch CTF estimation. The exact processing schemes are depicted in Figure S4. The data collection and refinement statistics are summarized in Table S2. Particles were initially picked using Blob picker. Reasonable 2D classes were selected and used as input for Topaz train.[43] The resulting Topaz model was used as template for particle picking on all micrographs yielding 4.091.179 particles extracted with a box size of 300 px and a pixel size of 1.045 Å. The particles were subject to 2D classification, ab-initio reconstruction, and the class with clearly defined features was selected. The obtained particles were further sorted by 2D classification. The classes that showed the most defined features of PLD3 were selected (2.823.826 particles) and used for further non-uniform and CTF refinement.[42] The final resolution of the PLD3 reconstruction after non-uniform refinement applying C2 symmetry was 2.82 Å by masking out the flexible density presumably corresponding to glycosylation.

Cryo-EM data processing of PLD3 ssRNA complex was carried out in a similar fashion compared to the PLD3 apoenzyme dataset. In brief, for the complex data set particles were initially picked on 27.619 micrographs using blob picker, 2 classification and subsequent Topaz training and particle extraction. Particles corresponding to ssRNA bound classes were sorted and extracted with a box size of 330 px and a pixel size of 0.727 Å. Particles were further sorted by 2D classification, ab-initio reconstruction, and 3D classification. A total of 891.893 particles were combined and subjected to local Ctf refinement and non-uniform refinement. The final resolution of the PLD3 ssRNA bound reconstruction using C1 symmetry was 3.57 Å.

Model building and refinement

An atomic model was built by rigid body docking of the PLD3 dimer predicted by AlphaFold2[26] multimer into the cryo-EM density. The model was partially rebuilt in Coot 0.9.[44] Missing parts were built de-novo. Atomic models were improved by ISOLDE 1.2.244[45] and real space refinement in PHENIX 1.1745,[46,47] using the map with the highest resolution. All structure figures were prepared using UCSF ChimeraX.[48]

Mass photometry

Mass photometry measurements of PLD3, PLD4 and PLD3 mutants were carried out using a OneMP or TwoMP mass photometer (Refeyn). Proteins were diluted to a final concentration of 50 nM in sterile filtered mass photometry buffer (50 mM NaAC, 100 mM NaCl, pH 4.5) prior to each measurement. Movies were recorded for 60 s and data were analyzed using AcquireMP.

Nuclease assays

If not otherwise indicated 100 ng of RNA or DNA were digested with indicated enzyme concentrations for 20 min at 37°C in assay buffer (50 mM NaAc, 100 mM NaCl, pH 4.5). Afterwards, 2x RNA loading dye was added and samples were incubated for additional 5 min at 95 °C. Fragments were separated and visualized on a urea gel.

Urea gels

Urea gels were casted according to supplier's protocol using SequaGel Concentrate, SequaGel Diluent and SequaGel Bufffer. Gels run at 150 V for 10 min, followed by 250 V for 60 min in 1x TBE (100 mM Tris, 100 mM boric acid, 2 mM EDTA) buffer. Afterwards, gels were stained with SYBR Gold Nucleic Acid Gel Stain for 5 minutes and imaged.

Please cite this article in press as: Bérouti et al., Lysosomal endonuclease RNase T2 and PLD exonucleases cooperatively generate RNA ligands for TLR7 activation, Immunity (2024), https://doi.org/10.1016/j.immuni.2024.04.010

Affinity measurement by fluorescence anisotropy

Fluorescence anisotropy experiments were conducted in a black flat bottom 384 well plate (50 μl total volume). 5 nM of 3'-FAM coupled substrates were incubated with increasing concentrations of indicated PLD3 mutants for 20 minutes at room temperature in assay buffer (50 mM NaAc, 100 mM NaCl, pH=4.5) to ensure equilibrium. Subsequently the change in anisotropy was measured at an excitation wavelength of 490 nm and an emission wavelength of 520 nm using an automated polarization microscope.[49] Each sample was measured at twelve different z-planes to reduce the effect of potential fluorescing protein-DNA aggregates that could lead to erroneous FA values. Data was analyzed by fitting to a one site-specific binding model.

Fluorescent RNA degradation assay

1 pmol/μl of fluorophore/quencher labeled RNA40 (5'-FAM fluorochrome/3'-BMN-Q530, Biomers) was mixed with indicated enzyme concentrations of PLD3 or PLD4 in assay buffer (50 mM NaAc, 100 mM NaCl, pH=4.5) in a black 96-well plate on ice (final reaction volume: 100 μl). FAM fluorescent signal (excitation 485 nm/emission 528 nm) was recorded on a Spark20M (Tecan) reader in 1 min intervals for 2 hours at 37°C.

PLD3 and PLD4 quantification and whole proteome analysis

$1x10^6$ cells (pDCs, $CD14^+$ and CAL-1 WT or KO cells) were washed 5 times with PBS. Cells lysis was performed in 8 M urea/0.4 M NH_4HCO_3 with a Sonopuls HD3200 ultrasonication device (Bandelin, Berlin, Germany). For protein quantification, a Bradford assay was used. Prior to tryptic digestion, 20 μg protein from each sample were reduced with dithiothreitol (final concentration 5 mM) at 37°C for 30 min and alkylated with iodoacetamide (15 mM final concentration) for 30 min at room temperature in the dark. The first digestion step was performed for 4 h with Lys-C (1:100, enzyme:protein -ratio). For additional tryptic digestion, samples were diluted with water to give 1 M Urea and digested overnight at 37°C with modified porcine trypsin (1:50, enzyme:protein-ratio). For absolute quantification of PLD3 and PLD4, 10 fmol of the following stable isotope labeled peptides were added to 1 μg of digested sample: PLD3: ALLNVVDNAX (A310 to R319), LFVVPADEAQAX (L397 to R408) and SQLEAIFLX (S458 to R466); PLD4: LQQLLGX (L164 to R170) and FWVVDGX (F217 to R223), with X being an Arginine labeled with 6 ^{13}C and 4 ^{15}N atoms. Purity of the internal standard peptides was evaluated using mass spectrometry.

For liquid chromatography mass spectrometry analysis, an UltiMate 3000 nano-LC system online coupled to a Q-Exactive HF-X instrument (Thermo Fisher Scientific) was used. As solvent A, 0.1% formic acid in water and as solvent, B 0.1% formic acid in acetonitrile were used. 1 μg of peptides dissolved in solvent A was injected to a PepMap 100 C18 trap column (100 μm × 2 cm, 5 μm particles) and separated on an analytical column (PepMap RSLC C18, 75 μm × 50 cm, 2 μm particles) at 250 nl/min flow-rate. The chromatography method consisted of an 80 min gradient of 5–20% of solvent B followed by a 9-min increase to 40%. After separation, the column was washed with 85% solvent B for 9 min and re-equilibrated for 10 min with 3% solvent B. For mass spectrometry analysis a data-independent acquisition (DIA) method was used as described in Shashikadze et al.[50] Briefly gas phase fractionation-based libraries were constructed using 6 measurements of pooled samples with 6 different scan ranges (i.e. 400.43–502.48, 500.48–602.52, 600.52–702.57, 700.57–802.61, 800.61–902.66, 900.66–1002.70) and staggered 25 × 4 m/z-wide isolation windows. For the analytical runs staggered 50 × 12 m/z-wide isolation windows in the range of 400–1000 *m/z* were used. Every 50 DIA scan was followed by a precursor scan in the range of 390–1010 *m/z*.

For the whole proteome analysis, first a gas phase fractionation spectral library was generated using DIA-NN (v1.8.1)[51] and all human Swiss-Prot entries as database. All raw files of the analytical runs were then searched against this library. For both searches, only tryptic peptides with a maximum of one missed cleavage, a length between 7 and 30 amino acids and charge states of either +2, +3 and +4 were considered. Proteins were grouped in the output based on their gene names. For the quantitative analysis of PLD3 and PLD4, the Skyline ecosystem was used.[52] For each peptide, three product ions were selected and a minimum of rdotp = 0.85 was required of each individual peptide identification. As normalization method, "ratio to heavy" was chosen.

Preparation for LC-MS analysis of PLD3 and PLD4 degradation products

To analyze cleavage products of PLD3 and PLD4 *in vitro*,1 μg of $RNA40^O$ or $RNA9.2s^O$ was incubated with indicated concentrations of PLD3, PLD4, RNase T2, RNase 1, RNase 2 or RNase 6 or combinations thereof at 37°C in assay buffer (50 mM NaAC, 100 mM NaCl, pH 4.5). Next, proteins were precipitated in 80% acetonitrile for 30 min on ice and centrifuged for 10 min at 16,000 g. To detect nucleosides in cells, $3x10^6$ CAL-1 cells were primed with IFN-γ (10 ng/μl) for 6 hours and stimulated with $RNA40^O$ as described above for additional 16 hours. Subsequently, cells were lysed in 80% acetonitrile for 30 min on ice and centrifuged for 10 min at 16,000 g. The supernatants (from *in vitro* and cell studies) were collected, flash frozen in liquid nitrogen and lyophilized overnight. The pellets were dissolved in 50 μl ultrapure water and stored at -20 °C if necessary. Prior to analysis the sample was centrifuged at 10,000 ×g for 1 min and the amount indicated for the respective analysis below was taken from the upper part of the liquid.

LC-MS/QQQ analysis of nucleoside-monophosphates

For semi-quantitative mass spectrometry of nucleoside-monophosphates an Agilent 1290 Infinity HPLC equipped with a variable wavelength detector (VWD) combined with an Agilent Technologies G6490 Triple Quad mass spectrometer with electrospray ionization (ESI-MS, Agilent Jetstream) was used. Operating parameters were as follows: positive-ion mode, cell accelerator voltage of 5 V, N_2 gas temperature of 150 °C and N_2 gas flow of 20 l/min, sheath gas (N_2) temperature of 400 °C with a flow of 12 L/min, capillary voltage of 2400 V, nozzle voltage of 0 V, nebulizer at 60 psi, high-pressure RF at 180 V and low-pressure RF at 80 V. The

Please cite this article in press as: Bérouti et al., Lysosomal endonuclease RNase T2 and PLD exonucleases cooperatively generate RNA ligands for TLR7 activation, Immunity (2024), https://doi.org/10.1016/j.immuni.2024.04.010

instrument was operated in dynamic MRM mode with a cycle time of 700 ms (Table S2). For separation an Interchim Uptisphere 120 Å column (HDO-C18, 3 μm, 2.1 × 150 mm, UP3HDO-150/021) was used. Running conditions were 35 °C and a flow rate of 0.35 ml/min in combination with a binary mobile phase of 5 mM NH_4OAc aqueous buffer A, brought to pH 4.9 with glacial acetic acid (200 μL/L), and an organic buffer B of acetonitrile (Ultra LC-MS grade, purity ≥99.98) acidified with 0.075 % formic acid (187.5 μl per 2.5 l). The used gradient is described below. Of each sample 15 μl were diluted with 15 μl of buffer A and 20 μl of this solution was then co-injected with 1 μl of stable isotope labeled internal standard (ISTD) mix which was aspirated automatically before each injection from the instrument itself and consisted of isotopologues of the 4 canonical nucleosides. The sample data were analyzed by the quantitative MassHunter Software from Agilent using the integrated calibration function. The calibration solutions ranged from 0.01 pmol to 25 pmol for each nucleoside (12 calibration levels, 1:2 dilution). The amount of nucleoside-monophosphates was normalized by the average of the relative amounts of canonical nucleosides. For example, the amount of C in each sample was normalized to the amount of control sample #1. The same was done for U, G and A. Finally, the normalized values for C; U, G and A were averaged and used for normalization of the nucleoside-monophosphates. This normalization method is intended to compensate for fluctuations between the different samples as best as possible while only using highly aberrant nucleoside species.

The gradient was as follows: 0 → 0.75 min, 0% B; 0.75 → 1.50 min, transition to 2.5% B; 1.50 → 3.00 min, 2.5% B; 3.00 → 8.00 min, transition to 15% B; 8.00 → 9.00 min, transition to 80% B; 9.00 → 11.50 min, 80% B; 11.50 → 12.00 min, transition to 0% B; 12.00 → 13.70 min, 0% B.

LC-HRMS analysis of oligonucleotides

A Thermo Scientific Vanquish system coupled to a Thermo Scientific QExactive HF mass spectrometer was used for the high-resolution mass spectrometry (HRMS) analysis of oligonucleotides and their fragments. Ionization was done by a HESI source and ions were scanned in the positive polarity mode over a full-scan range of m/z 200-1600 with a resolution of 120,000, an AGC target of 3e6 and a maximum IT of 200 ms. HESI Tune parameters are: Capillary temperature 320 °C, sheath gas flow rate 20 au, aux gas flow rate 4 au, sweep gas flow rate 0 au, spray voltage 3.5 kV, S-lens RF level 50, aux gas temperature 55 °C. Fragments were separated on a Macherey-Nagel Nucleodur HILIC column (EC125/2, 3 μm, 2 × 125 mm, 760531.20) at 40 °C. Elution buffers were 10 mM NH_4OAc aqueous buffer A, brought to pH 5.3 with glacial acetic acid (65 μL/L) and an organic buffer B of 10 mM NH_4OAc brought to pH 5.3 with glacial acetic acid in 80 % acetonitrile (Ultra LC-MS grade, purity ≥99.98) with a flow rate of 0.30 ml/min. The buffer-gradient is described below. For each measurement 10 μl of sample was spiked with 1 μl of an ISTD-mixture of ^{13}C-labeld C, U, G and A (each of them at a concentration of 10 μM) and diluted with 50 μl of buffer A. Of this solution 20 μl were subjected to HRMS. The ion chromatograms of intact oligonucleotides and their fragments were extracted from the total ion current (TIC) chromatogram. The gradient was as follows: 0.0 → 2.0 min, 100% B; 2.0 → 22.0 min, transition to 60% B; 22.0 → 27.0 min, transition to 25% B; 27.0 → 31.0 min, 25% B; 31.0 → 33.0 min, transition to 100% B; 33.0 → 44.0 min, 100% B.

QUANTIFICATION AND STATISTICAL ANALYSIS

Unless otherwise indicated, statistical significance was determined by either one-way or two-way ANOVA with Dunnett's correction for multiple testing. The exact number of replicates (n) is given in the figure legends. GraphPad Prism 10 was used for data presentation and statistical analysis. When multiple comparisons are displayed with a comparison bar, the longer line on the comparison bar indicates the reference data to which the significance level information relates.

Immunity, Volume *57*

Supplemental information

Lysosomal endonuclease RNase T2 and PLD exonucleases cooperatively generate RNA ligands for TLR7 activation

Marleen Bérouti, Katja Lammens, Matthias Heiss, Larissa Hansbauer, Stefan Bauernfried, Jan Stöckl, Francesca Pinci, Ignazio Piseddu, Wilhelm Greulich, Meiyue Wang, Christophe Jung, Thomas Fröhlich, Thomas Carell, Karl-Peter Hopfner, and Veit Hornung

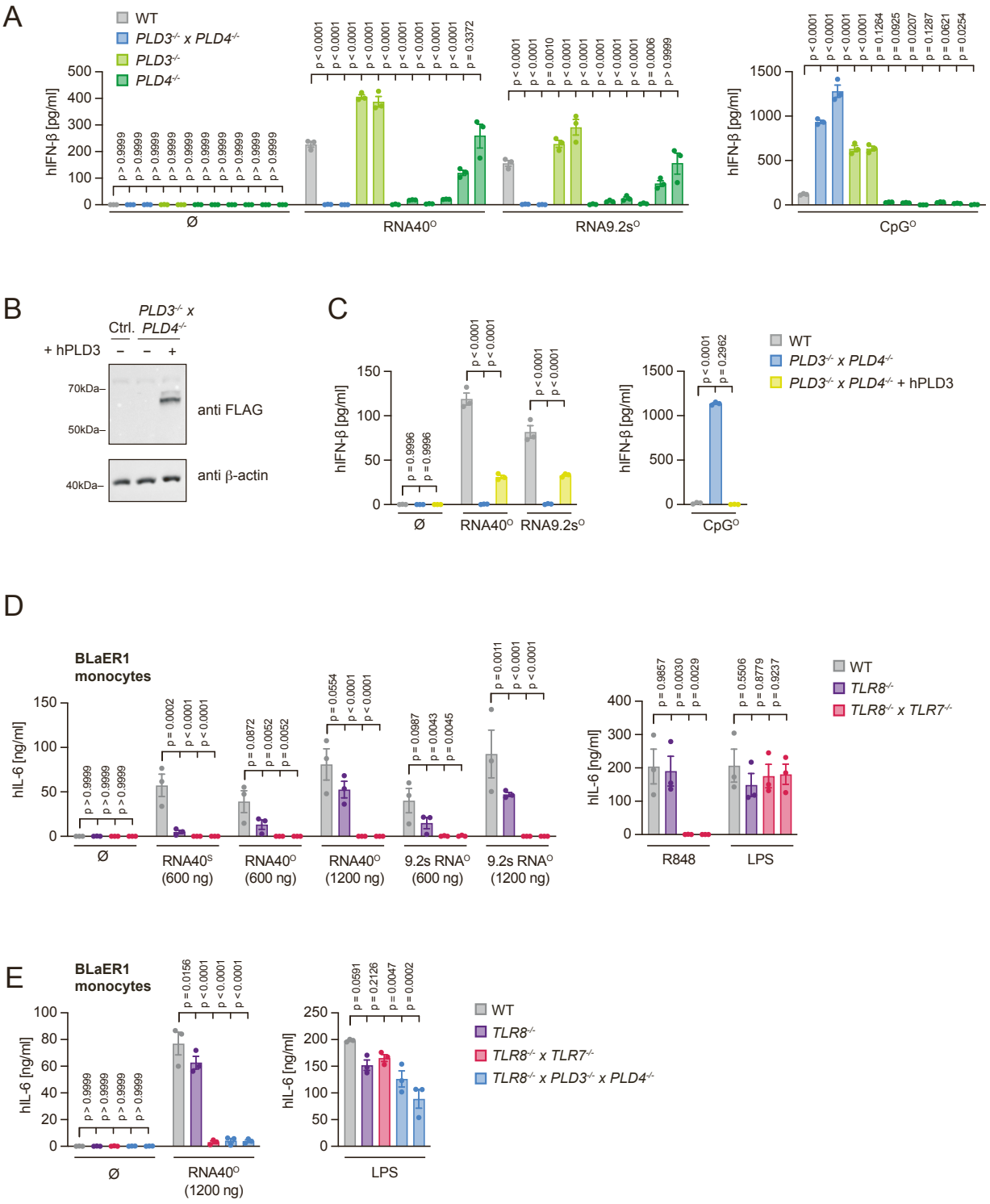
A
WT
PLD3-/- x PLD4-/-
PLD3-/-
PLD4-/-
hIFN-β [pg/ml]
Ø
RNA40O
RNA9.2sO
CpGO
B
PLD3-/- x PLD4-/-
Ctrl.
+ hPLD3
70kDa–
50kDa–
40kDa–
anti FLAG
anti β-actin
C
WT
PLD3-/- x PLD4-/-
PLD3-/- x PLD4-/- + hPLD3
D
BLaER1 monocytes
hIL-6 [ng/ml]
RNA40S (600 ng)
RNA40O (600 ng)
RNA40O (1200 ng)
9.2s RNAO (600 ng)
9.2s RNAO (1200 ng)
R848
LPS
WT
TLR8-/-
TLR8-/- x TLR7-/-
E
BLaER1 monocytes
RNA40O (1200 ng)
LPS
WT
TLR8-/-
TLR8-/- x TLR7-/-
TLR8-/- x PLD3-/- x PLD4-/-

Figure S1

Figure S1, PLD3 exonuclease activity regulates TLR9 responses in CAL-1 cells, related to Figure 2

(A) CAL-1 cells of indicated genotypes were unstimulated or stimulated with RNA40^{O}, RNA9.2s^{O} or CpG^{O}. After 16 h, cytokine release was measured by ELISA. Data are depicted as mean ± SEM of n = 3 independent experiments. Statistical analysis was conducted by two-way ANOVA (left panel) or one-way ANOVA (right panel) with Dunnett´s multiple comparison tests.

(B) Immunoblot of WT and *PLD3*$^{-/-}$ x *PLD4*$^{-/-}$ cells reconstituted with PLD3(3xFlag). One representative blot of three independent experiments is shown.

(C) WT, *PLD3*$^{-/-}$ x *PLD4*$^{-/-}$ cells or *PLD3*$^{-/-}$ x *PLD4*$^{-/-}$ cells reconstituted with PLD3(3xFlag) were stimulated as in (A) and cytokine release was measured by ELISA. Data are depicted as mean ± SEM of n = 3 independent experiments. Statistical analysis was conducted by two-way ANOVA (left panel) or one-way ANOVA (right panel) with Dunnett´s multiple comparison tests.

(D, E) BLaER1 monocytes of indicated genotypes stimulated as indicated. After 14 h, IL-6 release was measured by ELISA. Data are depicted as mean ± SEM of n = 3 independent experiments. Statistical analysis was conducted by two-way ANOVA (D and left panel E) or one-way ANOVA (right panel E) with Dunnett´s multiple comparison tests.

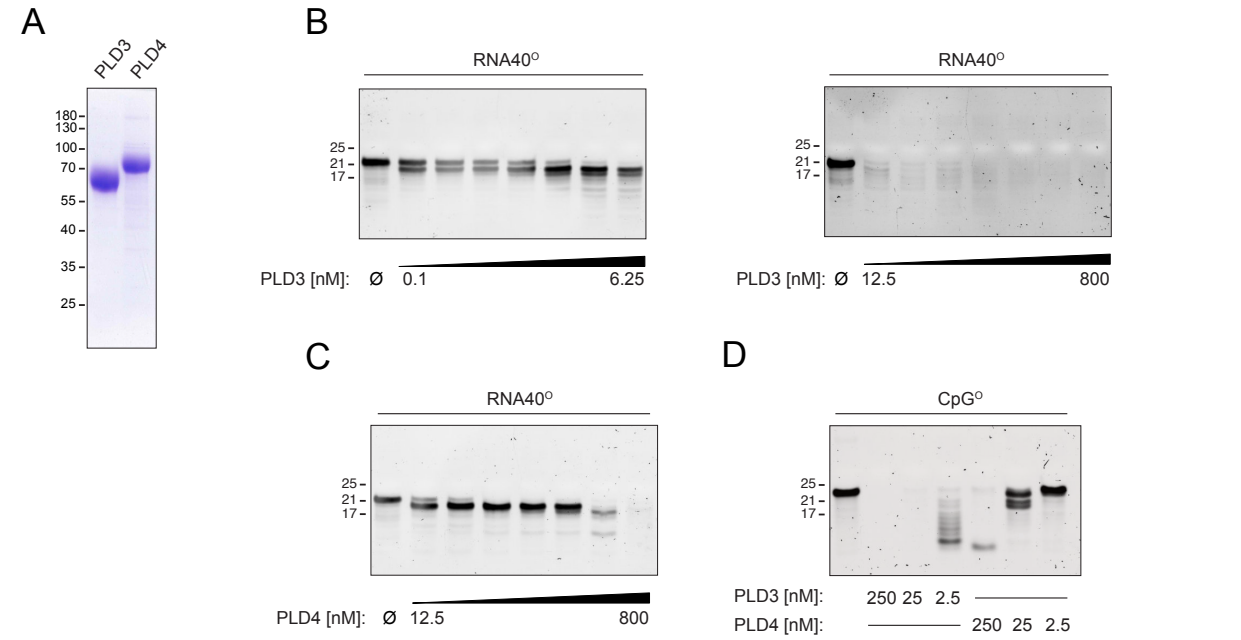
A
PLD3
PLD4
180
130
100
70
55
40
35
25
B
RNA40°
25
21
17
PLD3 [nM]: Ø 0.1 6.25
RNA40°
25
21
17
PLD3 [nM]: Ø 12.5 800
C
RNA40°
25
21
17
PLD4 [nM]: Ø 12.5 800
D
CpG°
25
21
17
PLD3 [nM]: 250 25 2.5
PLD4 [nM]: 250 25 2.5

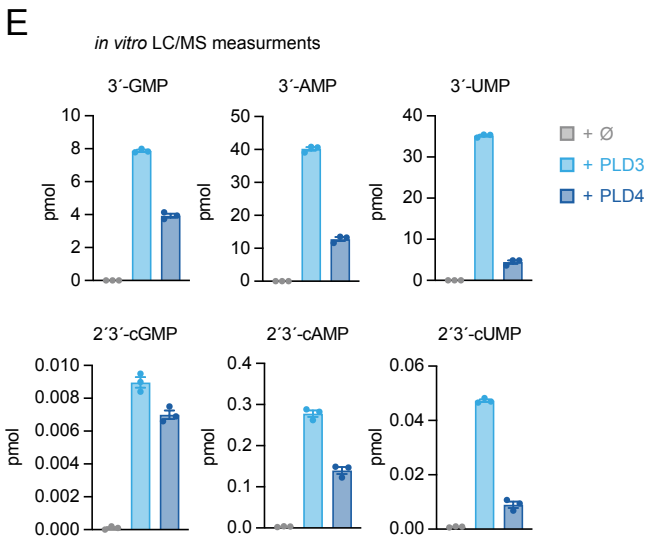
E
in vitro LC/MS measurments
3´-GMP
3´-AMP
3´-UMP
pmol
+ Ø
+ PLD3
+ PLD4
2´3´-cGMP
2´3´-cAMP
2´3´-cUMP

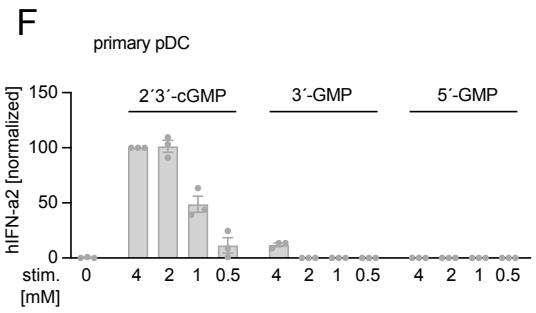
F
primary pDC
hIFN-a2 [normalized]
2´3´-cGMP
3´-GMP
5´-GMP
stim. [mM]
0 4 2 1 0.5 4 2 1 0.5 4 2 1 0.5

Figure S2

Figure S2. PLD3 is more processive towards RNA and DNA substrates compared to PLD4, related to Figure 3

(A) Coomassie of purified recombinant PLD3 and PLD4.

(B, C) Urea gels of RNA40^{O} digested with increasing amounts of (B) PLD3 (0.097 nM, 0.195 nM, 0.39 nM, 0.78 nM, 1.56 nM, 3.13 nM, 6.25 nM, 12.5 nM, 25 nM, 50 nM, 100 nM, 200 nM, 400 nM and 800 nM) or (C) PLD4 (12.5 nM, 25 nM, 50 nM, 100 nM, 200 nM, 400 nM and 800 nM). One representative gel of two independent experiments is shown.

(D) Urea gel of CpG^{O}-DNA digested with indicated concentrations of PLD3 and PLD4. One representative gel of two independent experiments is shown.

(E) RNA9.2s^{O} was incubated at 37 °C for 20 min in assay buffer without (Ø) enzyme, with PLD3 (250 nM) or with PLD4 (250 nM). The release of single nucleotides was subsequently analyzed by LC-MS. Data are depicted as mean ± SEM of n = 3 independent experiments.

(F) Isolated plasmacytoid dendritic cells of three donors were stimulated with indicated decreasing concentrations of 2',3'-cGMP, 3´-GMP and 5´-GMP. After 24 h, IFN-a2 release was determined by ELISA. From each donor were normalized to the 4 mM 2',3'-cGMP condition and are depicted as mean ± SEM of three independent replicates.

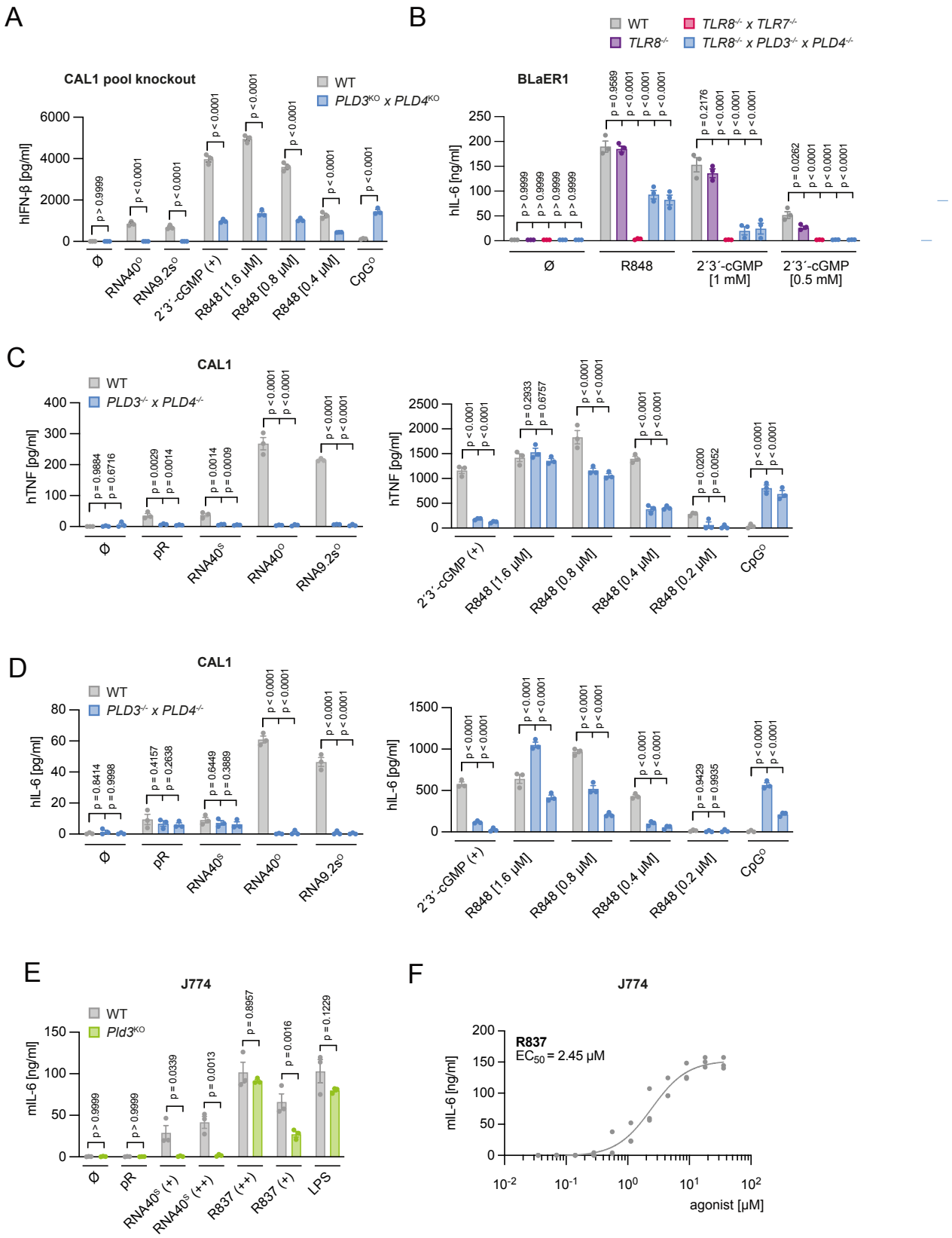
A
CAL1 pool knockout
WT
PLD3KO x PLD4KO
hIFN-β [pg/ml]
6000
4000
2000
0
p > 0.9999
p < 0.0001
p < 0.0001
p < 0.0001
p < 0.0001
p < 0.0001
p < 0.0001
p < 0.0001
Ø
RNA40O
RNA9.2sO
2´3´-cGMP (+)
R848 [1.6 µM]
R848 [0.8 µM]
R848 [0.4 µM]
CpGO
B
WT
TLR8-/-
TLR8-/- x TLR7-/-
TLR8-/- x PLD3-/- x PLD4-/-
BLaER1
hIL-6 [ng/ml]
250
200
150
100
50
0
p > 0.9999
p > 0.9999
p > 0.9999
p > 0.9999
p = 0.9589
p < 0.0001
p < 0.0001
p < 0.0001
p = 0.2176
p < 0.0001
p < 0.0001
p < 0.0001
p = 0.0262
p < 0.0001
p < 0.0001
p < 0.0001
Ø
R848
2´3´-cGMP [1 mM]
2´3´-cGMP [0.5 mM]
C
CAL1
WT
PLD3-/- x PLD4-/-
hTNF [pg/ml]
400
300
200
100
0
p = 0.9884
p = 0.6716
p = 0.0029
p = 0.0014
p = 0.0014
p = 0.0009
p < 0.0001
p < 0.0001
p < 0.0001
p < 0.0001
Ø
pR
RNA40S
RNA40O
RNA9.2sO
hTNF [pg/ml]
2500
2000
1500
1000
500
0
p < 0.0001
p < 0.0001
p = 0.2933
p = 0.6757
p < 0.0001
p < 0.0001
p < 0.0001
p < 0.0001
p = 0.0200
p = 0.0052
p < 0.0001
p < 0.0001
2´3´-cGMP (+)
R848 [1.6 µM]
R848 [0.8 µM]
R848 [0.4 µM]
R848 [0.2 µM]
CpGO
D
CAL1
WT
PLD3-/- x PLD4-/-
hIL-6 [pg/ml]
80
60
40
20
0
p = 0.8414
p = 0.9998
p = 0.4157
p = 0.2638
p = 0.6449
p = 0.3889
p < 0.0001
p < 0.0001
p < 0.0001
p < 0.0001
Ø
pR
RNA40S
RNA40O
RNA9.2sO
hIL-6 [pg/ml]
1500
1000
500
0
p < 0.0001
p < 0.0001
p < 0.0001
p < 0.0001
p < 0.0001
p < 0.0001
p = 0.9429
p = 0.9935
p < 0.0001
p < 0.0001
2´3´-cGMP (+)
R848 [1.6 µM]
R848 [0.8 µM]
R848 [0.4 µM]
R848 [0.2 µM]
CpGO
E
J774
WT
Pld3KO
mIL-6 [ng/ml]
150
100
50
0
p > 0.9999
p > 0.9999
p = 0.0339
p = 0.0013
p = 0.8957
p = 0.0016
p = 0.1229
Ø
pR
RNA40S (+)
RNA40S (++)
R837 (++)
R837 (+)
LPS
F
J774
R837
EC50 = 2.45 µM
mIL-6 [ng/ml]
200
150
100
50
0
10-2
10-1
100
101
102
agonist [µM]

Figure S3

Figure S3. PLD3/PLD4 deficient cells do not respond to TLR7 first binding site ligands, related to Figure 4

(A) Unmodified CAL-1 or PLD3^{KO} x PLD4^{KO} pool knockout CAL-1 cells were unstimulated or stimulated with RNA40^{O}, RNA9.2s^{O}, 2',3'-cGMP (+ = 0.5 mM), CpG^{O} or with indicated concentrations of R848. After 16 h, IFN-β release was measured by ELISA. Data are depicted as mean ± SEM of three independent experiments. Statistical analysis was conducted by two-way ANOVA with Šídák's multiple comparisons test.

(B) BLaER1 monocytes of indicated genotypes were unstimulated or stimulated with R848 or indicated concentrations of 2',3'-cGMP for 14 h. Afterwards, IL-6 release was measured by ELISA. Data are depicted as mean ± SEM of three independent experiments and statistical analysis was conducted by two-way ANOVA with Dunnett's multiple comparisons test.

(C and D) Unmodified CAL-1 cells (WT) or two independent *PLD3*$^{-/-}$ x *PLD4*$^{-/-}$ CAL-1 monoclones were unstimulated or stimulated with pR, RNA40^{S}, RNA40^{O}, RNA9.2s^{O}, R848 and 2',3'-cGMP (++ = 1 mM, + = 0.5 mM), CpG^{O} or with CpG^{S}. After 16 h, TNF (C) or IL-6 (D) release was measured by ELISA. Data are depicted as mean ± SEM of n = 3 independent experiments. Statistical analysis was conducted by two-way ANOVA with Dunnett´s multiple comparison tests.

(E) Unmodified J774 macrophages or PLD3^{KO} pool knockout J774 macrophages were unstimulated or stimulated with RNA40^{S} (+ = 600 ng/well, ++ = 1200 ng/well), R837 (++ = 18 µM, + = 2.25 µM) or with LPS. After 14 h, mIL-6 release was determined by ELISA. Data are depicted as mean ± SEM of three independent experiments. Statistical analysis was conducted by two-way ANOVA with Šídák's multiple comparisons test.

(F) J774 WT cells were stimulated with increasing concentrations of R837. After 14 h, mIL-6 release was determined by ELISA. Each replicate of n = 3 independent experiments is depicted. A four-parameter dose-response curve was fitted to calculate half-maximal effective concentration (EC_{50}).

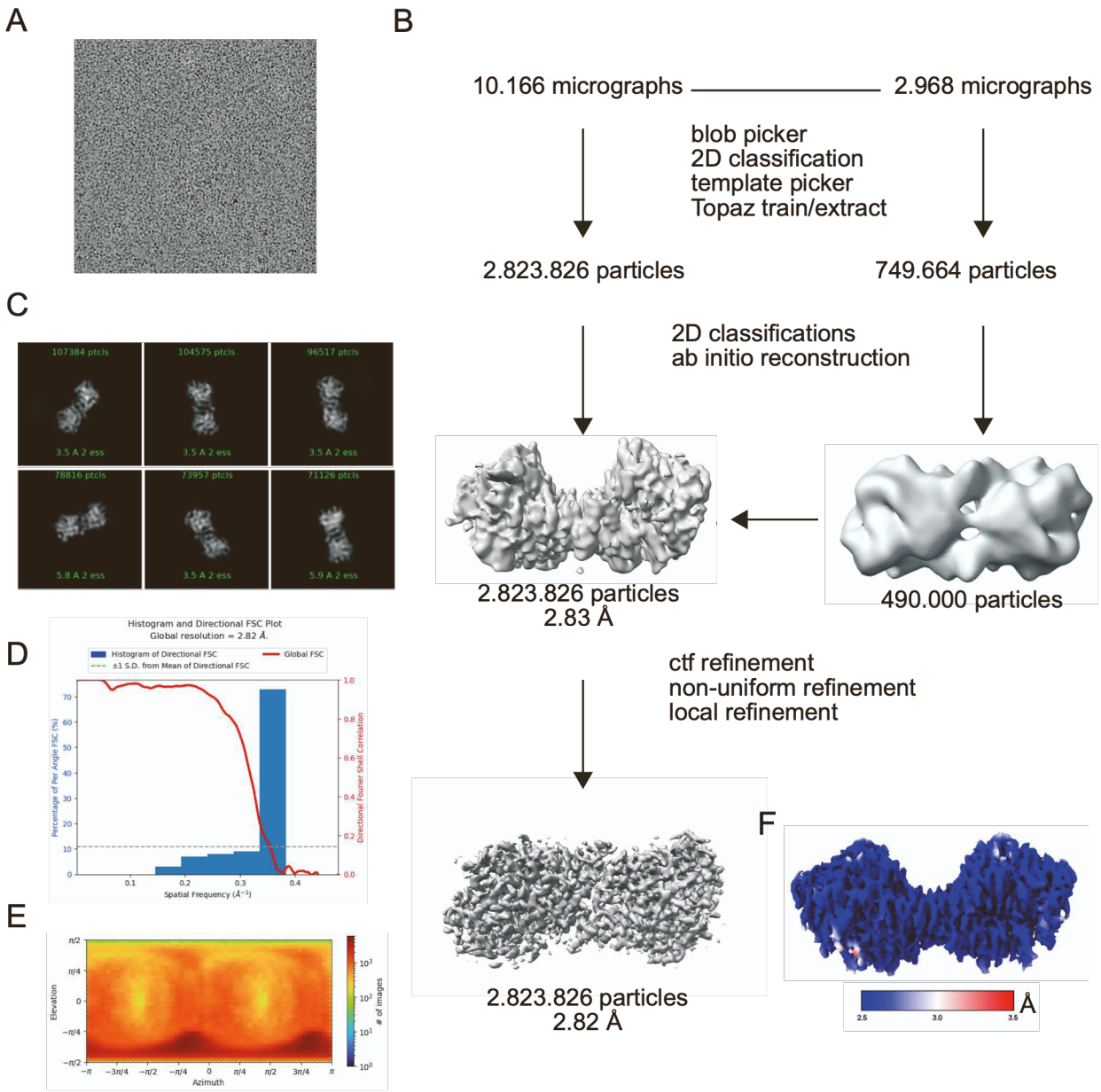
A
B
10.166 micrographs
2.968 micrographs
blob picker
2D classification
template picker
Topaz train/extract
2.823.826 particles
749.664 particles
C
2D classifications
ab initio reconstruction
107384 ptcls
104575 ptcls
96517 ptcls
78816 ptcls
73957 ptcls
71126 ptcls
2.823.826 particles
2.83 Å
490.000 particles
D
ctf refinement
non-uniform refinement
local refinement
Histogram and Directional FSC Plot
Global resolution = 2.82 Å
Histogram of Directional FSC
Global FSC
±1 S.D. from Mean of Directional FSC
Percentage of Per Angle FSC (%)
Directional Fourier Shell Correlation
Spatial Frequency (Å⁻¹)
E
Elevation
Azimuth
# of images
F
2.823.826 particles
2.82 Å
Å

Figure S4

Figure S4. Cryo-EM data analysis of PLD3 apoenzyme, related to Figure 5

(A) Representative micrograph of the PLD3 apoenzyme dataset.

(B) Cryo-EM data processing workflow of PLD3 apoenzyme data using cryoSPARC v4.3.0.

(C) Representative classes of a 2D classification of the particles used for the final PLD3 reconstruction.

(D) Histogram of directional Gold-standard Fourier shell correlation (FSC)[4] (blue) and global FSC curve (red) of the final PLD3 reconstruction. The spread of directional resolution values is defined as ±1σ (dashed green lines). The grey dashed line indicates the 0.143 cut-off criterion, indicating a nominal resolution of 2.82 Å.

(E) Angular distribution of the particles used for the final PLD3 reconstruction.

(F) Visualization of local resolution of PLD3 calculated in cryoSPARC. Blue indicates higher resolution and red indicates lower resolution.

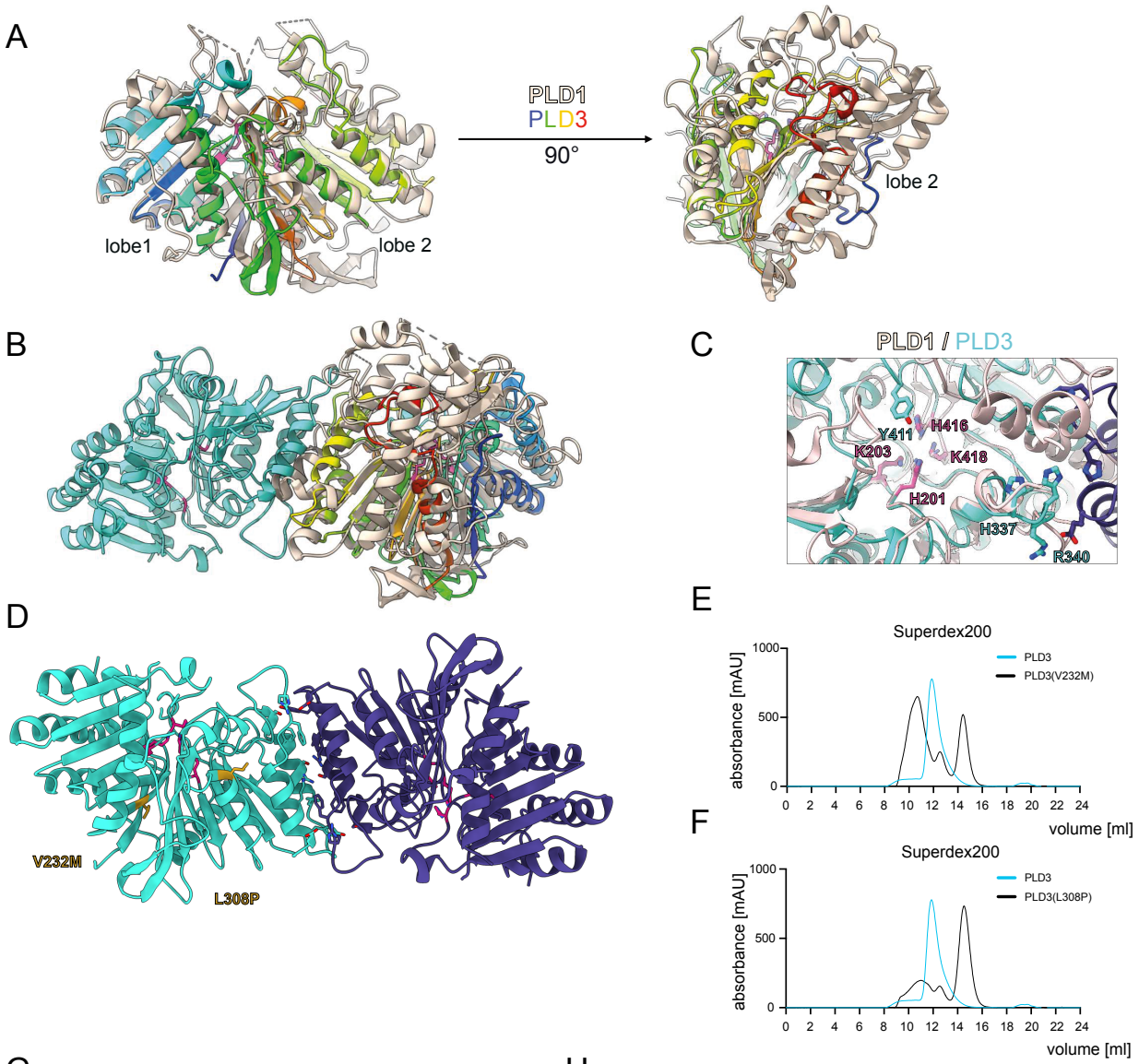
A
PLD1
PLD3
90°
lobe1
lobe 2
lobe 2
B
C
PLD1 / PLD3
Y411
H416
K203
K418
H201
H337
R340
D
V232M
L308P
E
Superdex200
PLD3
PLD3(V232M)
absorbance [mAU]
volume [ml]
F
Superdex200
PLD3
PLD3(L308P)
absorbance [mAU]
volume [ml]
G
PLD3(V232M)
PLD3
counts
mass [kDa]
H
PLD3
PLD3(L308P)
counts
mass [kDa]
I
PLD3
PLD3(V232M)
PLD3(L308P)
RNA9.2s
nM 25 2.5 0.25
K
PLD3
PLD3(V232M)
PLD3(L308P)
CpG
nM 25 2.5 0.25

Figure S5

Figure S5. PLD3 mutants V232M and L308P fail to form stable homodimers *in vitro*, related to Figure 5

(A) Structural comparison between human PLD1 in beige and one PLD3 protomer with rainbow colors from the N- (blue) to the C-termini (red) illustrates the conserved overall fold and similarities in lobe 1. The 90° rotation highlights the structural differences in the C-terminal lobe 2.

(B) Superposition of hPLD1 with the PLD3 dimer, color coded as in (A), showing the structural differences in the dimer interface area.

(C) Superposition of the active site cleft of human PLD1 in beige and the PLD3 dimer presenting the structural conservation of the HxK motif and the differences in the substrate binding area.

(D) Ribbon representation of the PLD3 dimer colored in turquoise and dark blue, with the HxK motif in pink, the dimer interface shown as sticks, and disease-related mutations V232 and L308 represented as golden sticks.

(E, F) Size exclusion chromatography (SEC) run of PLD3 superimposed with the SEC run of (E) PLD3(V232M) or (F) PLD3(L308P). Note that the SEC run of PLD3 is identical to Fig. 5A.

(G, H) Mass distribution of PLD3 and (G) PLD3(V232M) or (H) PLD3(L308P) observed by mass photometry. Note that the mass distribution control of PLD3 is identical to Fig. 5B.

(I, K) Urea gels of (I) RNA9.2s^{O} and (K) CpG^{O} digested with decreasing concentrations PLD3, PLD3(V232M) and PLD3(L308P). For both urea gels, one representative gel of two independent experiments is shown.

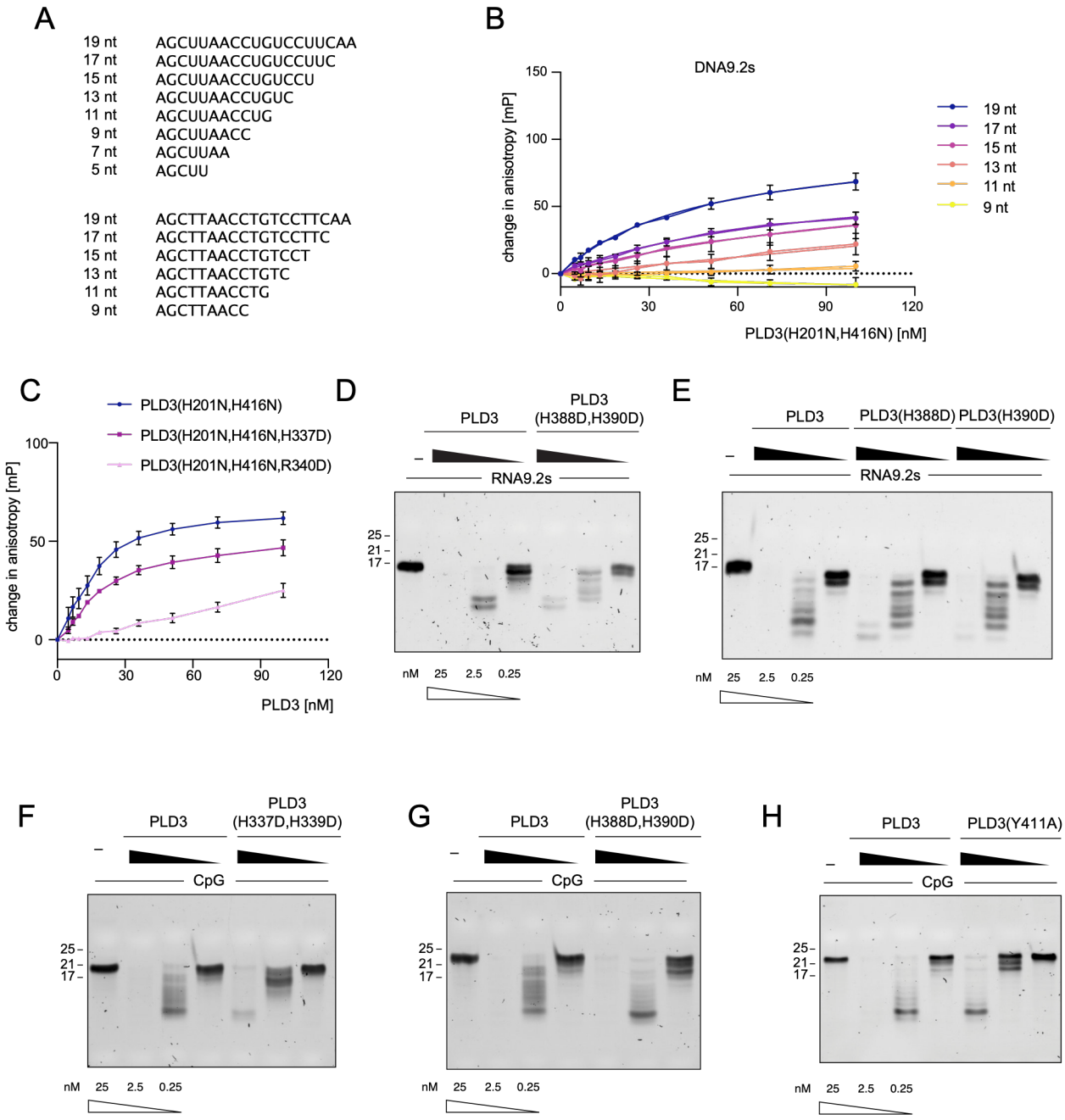
A
19 nt AGCUUAACCUGUCCUUCAA
17 nt AGCUUAACCUGUCCUUC
15 nt AGCUUAACCUGUCCU
13 nt AGCUUAACCUGUC
11 nt AGCUUAACCUG
9 nt AGCUUAACC
7 nt AGCUUAA
5 nt AGCUU
19 nt AGCTTAACCTGTCCTTCAA
17 nt AGCTTAACCTGTCCTTC
15 nt AGCTTAACCTGTCCT
13 nt AGCTTAACCTGTC
11 nt AGCTTAACCTG
9 nt AGCTTAACC
B
DNA9.2s
change in anisotropy [mP]
PLD3(H201N,H416N) [nM]
19 nt
17 nt
15 nt
13 nt
11 nt
9 nt
C
PLD3(H201N,H416N)
PLD3(H201N,H416N,H337D)
PLD3(H201N,H416N,R340D)
change in anisotropy [mP]
PLD3 [nM]
D
PLD3
PLD3 (H388D,H390D)
RNA9.2s
nM 25 2.5 0.25
E
PLD3
PLD3(H388D)
PLD3(H390D)
RNA9.2s
nM 25 2.5 0.25
F
PLD3
PLD3 (H337D,H339D)
CpG
nM 25 2.5 0.25
G
PLD3
PLD3 (H388D,H390D)
CpG
nM 25 2.5 0.25
H
PLD3
PLD3(Y411A)
CpG
nM 25 2.5 0.25

Figure S6

Figure S6. A minimal DNA binding motif for PLD3, related to Figure 6

(A) RNA and DNA sequences used in anisotropy experiments.

(B) Fluorescence anisotropy assay depicting the binding of PLD3(H201N, H416N) at increasing concentrations to DNA of various lengths. Data are depicted as mean ± SEM of n = 3 independent experiments. Please note that the 19 nt DNA9.2s binding data are identical to Fig. 6B.

(C) Fluorescence anisotropy assay comparing the binding of PLD3(H201N, H416N, H337D) and PLD3(H201N, H416N, R340D) to PLD3(H201N, H416N) at increasing concentrations to the 19 nt RNA9.2s substrates. Data are shown as mean ± SEM of n = 5 independent experiments.

(D-H) Urea gels of (D and E) RNA9.2s^{O} or (F, G and H) CpG^{O} digested with decreasing concentrations of PLD3 and decreasing concentrations of indicated PLD3 mutants. For every urea gel, one representative gel of two independent experiments is shown.

Table S2: Cryo-EM data collection, refinement and validation statistics, related to Figure 5

	PLD3 apoenzyme	PLD3 ssRNA complex
Data collection and processing		
Magnification	130,000	165,000
Voltage (kV)	300	300
Electron exposure (e^{-}/Å^2)	45	40.0
Defocus range (μm)	-1.0 to -2.9	-0.5 to -2.8
Pixel size (Å)	1.045	0.727
Symmetry imposed	C2	C1
Initial particle images (no.)	2.823.826	1.342.490
Final particle images (no.)	2.823.826	891.893
Map resolution (Å)	2.82	3.6
FSC threshold	0.143	0.143
Refinement		
Initial model used	AlphaFold	
Map sharpening *B* factor (Å^2)	110	
Model composition		
Non-hydrogen atom	6247	
Protein residues	793	
B factors (Å^2)		
Protein	69.79	
R.m.s. deviations		
Bond lengths (Å)	0.005	
Bond angles (°)	0.96	
Validation		
Clashscore	7.3	
Poor rotamers (%)	0.00	
Ramachandran plot		
Favored (%)	95.2	
Allowed (%)	4.8	
Disallowed (%)	0.00	

4.2 Pseudouridine RNA avoids immune detection through impaired endolysosomal processing and TLR engagement

The following research article was published in *Cell*, 2025:

Marleen Bérouti,[1,7] Mirko Wagner,[2,7] Wilhelm Greulich,[1] Ignazio Piseddu,[1,3,4] Jan Gärtig,[4] Larissa Hansbauer,[1] Christoph Müller-Hermes,[5,6] Matthias Heiss,[2] Alexander Pichler,[2] Annika J. Tölke,[2] Gregor Witte,[1] Karl-Peter Hopfner,[1] David Anz,[3,4] Michael Sattler,[5,6] Thomas Carell,[2,*] and Veit Hornung,[1,8,*]

[1]Gene Center and Department of Biochemistry, Ludwig-Maximilians-Universität, Munich, Germany
[2]Department of Chemistry, Ludwig-Maximilians-Universität, Munich, Germany
[3]Department of Medicine II, LMU University Hospital, Ludwig-Maximilians-Universität, Munich, Germany
[4]Division of Clinical Pharmacology, LMU University Hospital, Ludwig-Maximilians-Universität, Munich, Germany
[5] Institute of Structural Biology, Helmholtz Munich, Neuherberg, Germany
[6] TUM School of Natural Sciences, Bavarian NMR Center and Department of Bioscience, Technical University of Munich, Garching, Germany
[7]These authors contributed equally
[8]Lead contact
*Correspondence: thomas.carell@cup.uni-muenchen.de (T.C.),veit.hornung@lmu.de (V.H.)
https://doi.org/10.1016/j.cell.2025.05.032

Cell

Article

Pseudouridine RNA avoids immune detection through impaired endolysosomal processing and TLR engagement

Graphical abstract

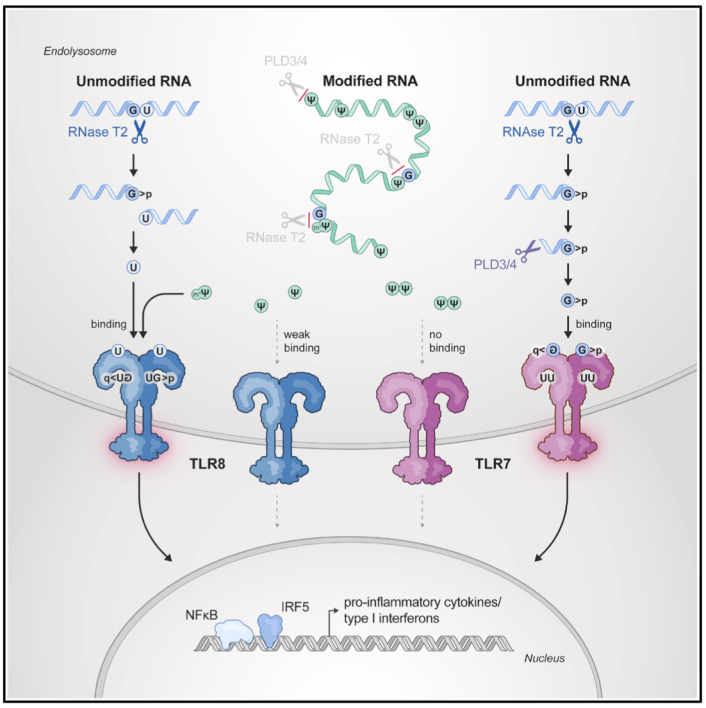

Highlights

- The non-immunogenicity of Ψ-RNA results from poor processing by lysosomal nucleases
- RNase T2 and PLDs fail to generate TLR7 and TLR8 ligands from Ψ-modified RNA
- Ψ and Ψ-RNA poorly engage distinct ligand-binding pockets of TLR8 and TLR7
- $m^1\Psi$ evades nuclease cleavage but could activate TLR8 if released from RNA

Authors

Marleen Bérouti, Mirko Wagner, Wilhelm Greulich, ..., Michael Sattler, Thomas Carell, Veit Hornung

Correspondence

thomas.carell@cup.uni-muenchen.de (T.C.), veit.hornung@lmu.de (V.H.)

In brief

Toll-like receptors (TLRs) 7 and 8 detect RNA degradation products to sense infection. However, modified nucleosides common in self-RNA—most notably pseudouridine—evade recognition. This study finds that poor nuclease processing and selective TLR avoidance drive this evasion, offering insight into the molecular basis of immune tolerance to pseudouridine-containing RNA.

Bérouti et al., 2025, Cell *188*, 1–16
September 4, 2025
https://doi.org/10.1016/j.cell.2025.05.032

CellPress

Please cite this article in press as: Bérouti et al., Pseudouridine RNA avoids immune detection through impaired endolysosomal processing and TLR engagement, Cell (2025), https://doi.org/10.1016/j.cell.2025.05.032

Cell

CellPress
OPEN ACCESS

Article

Pseudouridine RNA avoids immune detection through impaired endolysosomal processing and TLR engagement

Marleen Bérouti,[1,7] Mirko Wagner,[2,7] Wilhelm Greulich,[1] Ignazio Piseddu,[1,3,4] Jan Gärtig,[4] Larissa Hansbauer,[1] Christoph Müller-Hermes,[5,6] Matthias Heiss,[2] Alexander Pichler,[2] Annika J. Tölke,[2] Gregor Witte,[1] Karl-Peter Hopfner,[1] David Anz,[3,4] Michael Sattler,[5,6] Thomas Carell,[2,*] and Veit Hornung[1,8,*]

[1]Gene Center and Department of Biochemistry, Ludwig-Maximilians-Universität, Munich, Germany
[2]Department of Chemistry, Ludwig-Maximilians-Universität, Munich, Germany
[3]Department of Medicine II, LMU University Hospital, Ludwig-Maximilians-Universität, Munich, Germany
[4]Division of Clinical Pharmacology, LMU University Hospital, Ludwig-Maximilians-Universität, Munich, Germany
[5]Institute of Structural Biology, Helmholtz Munich, Neuherberg, Germany
[6]TUM School of Natural Sciences, Bavarian NMR Center and Department of Bioscience, Technical University of Munich, Garching, Germany
[7]These authors contributed equally
[8]Lead contact
*Correspondence: thomas.carell@cup.uni-muenchen.de (T.C.), veit.hornung@lmu.de (V.H.)
https://doi.org/10.1016/j.cell.2025.05.032

SUMMARY

Recognition of exogenous RNA by Toll-like receptors (TLRs) is central to pathogen defense. Using two distinct binding pockets, TLR7 and TLR8 recognize RNA degradation products generated by endolysosomal nucleases. RNA modifications present in endogenous RNA prevent TLR activation; notably, pseudouridine-containing RNA lacks immunostimulatory activity. Indeed, this property has been critical to the successful implementation of mRNA technology for medical purposes. However, the molecular mechanism for this immune evasion has remained elusive. Here, we report that RNase T2 and PLD exonucleases do not adequately process pseudouridine-containing RNA to generate TLR-agonistic ligands. As a second safety mechanism, TLR8 neglects pseudouridine as a ligand for its first binding pocket and TLR7 neglects pseudouridine-containing RNA as a ligand for its second pocket. Interestingly, the medically used N1-methylpseudouridine also evades RNase T2, PLD3, and PLD4 processing but is able to directly activate TLR8. Taken together, our findings provide a molecular basis for self-avoidance by RNA-sensing TLRs.

INTRODUCTION

Pattern recognition receptors (PRRs) are integral to the innate immune system's ability to recognize and respond to infectious agents. Among various receptor families, Toll-like receptors (TLRs) belong to the best characterized PRRs. TLRs are expressed as transmembrane receptors with their LRR (leucine rich repeat) ligand-binding domain either facing the extracellular space or the luminal compartment. A distinct evolutionary subgroup of TLRs, located in the endolysosomal compartment, is specialized in sensing nucleic acids, which constitutes a critical function in defense against viral and bacterial pathogens.[1] In the human system this group includes TLR7 and TLR8 that have evolved to recognize RNA degradation products[2] and TLR9 that senses single-stranded DNA with unmethylated cytosine and guanine (CG) motifs.[3] TLR7 and TLR8 are characterized by two distinct binding sites that function in a cooperative manner. The presence of a single-stranded RNA (ssRNA) fragment in binding pocket 2 allosterically regulates the affinity of the first binding pocket for its respective nucleoside or nucleotide ligand: TLR8 recognizes uridine (U) in combination with short purine (R)-terminated ssRNA fragments,[4] while TLR7 binds guanosine (G) or a 2′,3′-cyclophosphate-guanosine (2′,3′-cGMP or G>p) together with short pyrimidine-rich fragments.[5,6]

The production of the relevant RNA ligands for TLR7 and TLR8 is a regulated process in which the lysosomal endonuclease RNase T2 is non-redundantly involved. Human RNase T2 cleaves ssRNA, preferring R-U motifs (5′-N_nR↓UN_n-3′), thus generating fragments with a 2′,3′-cyclophosphate-R at one end (5′-N_nR>p) and a 5′-hydroxyl-U at the other end (UN_n-3′).[7] The former fragment binds to the second pocket of TLR8, while the UN_n-3′ fragment undergoes exonucleolytic degradation, potentially via PLD3 or PLD4 exonucleases, thereby increasing the lysosomal U concentration required for the engagement of pocket 1. The reverse scenario is true for TLR7: here, the RNase T2 generated 2′,3′-cyclophosphate-guanosine terminated RNA fragments constitute substrate for the exonucleases PLD3 and PLD4 that degrade the RNA to release the terminal 2′,3′-cyclic

Please cite this article in press as: Bérouti et al., Pseudouridine RNA avoids immune detection through impaired endolysosomal processing and TLR engagement, Cell (2025), https://doi.org/10.1016/j.cell.2025.05.032

GMP to engage pocket 1. In addition, PLD3 and PLD4 activity also contributes to generate short RNA fragments that occupy the second binding pocket.[8]

Pseudouridine (Ψ), first identified in the early 1950s, is the most abundant naturally occurring modification within RNA, making up to 9% of the U pool of total RNA.[9] Chemically, Ψ is a U isomer characterized as a C-glycoside in which the β-D-ribose is attached to the C5 atom rather than the N1 atom of uracil. This small but significant structural change confers distinctive biophysical and biochemical properties on RNA molecules, notably enhanced base stacking and pairing capabilities. Ψ is ubiquitously present in various endogenous RNAs, including tRNA, rRNA, mRNA, and small nuclear RNA, where it plays a pivotal role in enhancing RNA structural stability and modulating its protein interactions.[9]

The integration of Ψ into therapeutic RNA molecules has significantly advanced the field of RNA-based therapeutics. As such, a landmark 2005 study by Karikó et al. showed that replacing U with Ψ in *in vitro*-transcribed mRNA completely suppressed the pro-inflammatory response from RNA-sensing TLRs.[10] This discovery represented a significant leap forward, especially considering earlier findings that unmodified mRNAs elicited strong immunostimulatory effects, thereby limiting the practicality of mRNA-based transgene expression.[11] Follow-up studies confirmed these findings and demonstrated the superior translation efficiency of Ψ-modified RNA *in vivo*, which was inversely correlated to its immune-stimulatory capacity.[12,13] Further studies in cells devoid of functional TLR signaling documented enhanced translation of Ψ-modified mRNA. This could be attributed to the fact that pseudouridinylated RNA did not trigger PKR activation and thus translational arrest, which was readily observed when using unmodified RNA.[14] Further, Ψ-RNA's failure to activate the OAS RNase L system—an antiviral pathway triggered by unmodified RNA that shuts down translation—also enhanced mRNA translation.[15]

Subsequent studies showed that N1-methylpseudouridine ($m^1\Psi$) enhances translation compared with Ψ-modified mRNA *in vitro* and *in vivo*, partly due to reduced TLR3 stimulation.[16] Unlike Ψ, $m^1\Psi$ is extremely rare in eukaryotes, with only one known site in human 18S rRNA.[17,18] $m^1\Psi$-modified mRNA also showed improved translation in cell-free systems,[19] attributed to suppression of immune/PKR-mediated translation inhibition and alterations in translation dynamics, including increased ribosome pausing and density. These effects were linked to enhanced mRNA stability via secondary structure stabilization.[20] Although extensive direct comparisons between Ψ and $m^1\Psi$ were not made, $m^1\Psi$ was rapidly adopted to suppress innate immune activation and boost mRNA translation.

Given the profound effects of both Ψ and $m^1\Psi$ on RNA stability, translation efficiency, and immunogenicity, it remains challenging to disentangle the individual contributions of these factors. However, there is substantial evidence that TLR7-dependent recognition of unmodified RNA predominantly dictates the pro-inflammatory activity and immunogenicity of mRNA-based vaccines in mice *in vivo*.[21–23] In this context, it has to be noted that TLR8 is not functional in mice and hence not accounted for in such studies. At the same time, it has also been shown that the antiviral responses induced by mRNA therapeutics can adversely affect RNA-driven transgene expression.[24,25]

Interestingly, despite their widespread implementation in mRNA vaccine technologies and other RNA-based therapeutics, the exact mechanisms by which Ψ or $m^1\Psi$ evade immune recognition by the endolysosomal TLR system are unclear. Therefore, we wanted to revisit this unresolved issue, also in light of the recently discovered importance of nuclease activity upstream of TLR7 and TLR8.

RESULTS

A quantitative, mass spectrometry-based approach to analyze RNase T2 cleavage fragments

In previous work, we had employed MALDI-TOF mass spectrometry (MS) as a qualitative MS technology to characterize the cleavage products of RNase T2 using various RNA oligo substrates. Doing so, we had inferred that RNase T2 preferentially cleaves between R and U bases to render fragments that are terminated with a 3′ R and initiated with a 5′ U. Opposed to our initial finding that ssRNA, but not double-stranded RNA (dsRNA), served as a good substrate for RNase T2 (see Greulich et al.[7] and Figure S1A), it was reported that RNase T2 can also degrade dsRNA.[26] Therefore, we wished to revisit this topic and designed 4 oligonucleotides, all of which enable the formation of a hairpin secondary structure (Figures S1B–S1E). While RNase T2 was largely unable to cut hairpin 1, which lacks Us (Figure S1B), and hairpin 2, which contains a GU cleavage site within the stem region (Figure S1C), it efficiently cleaved the RNA when a GU cleavage site was positioned directly in the single-stranded loop region of the hairpin (Figure S1D). Interestingly, when the U in the stem loop was additionally paired with G, forming a non-canonical wobble base pair adjacent to the GU cleavage site, RNase T2 efficiently cut the RNA at the two highest concentrations tested (Figure S1E). RNase 1 on the other side, a member of the RNase A family, was able to cut all 4 hairpin RNAs equally well (Figures S1B–S1E). This data indicates that RNase T2 preferentially cuts non-base-paired RNA. To analyze RNase T2 cleavage products using a more quantitative approach, we digested the previously established model substrate RNA40 under undercutting conditions with RNase T2 (Figure 1A) and analyzed the so-obtained cleavage products using liquid chromatography-MS (LC-MS). We detected 17 distinct RNA fragments (Figure 1B). Due to the presence of well distinguishable, non-overlapping high-performance liquid chromatography (HPLC) peaks in the UV chromatogram, we could determine the abundance of these fragments based on their UV absorbance and extinction coefficient. Relating the amount of the individual fragments to their position in the RNA oligo educt strand showed that we were able to accurately reconstruct all fragments with a decisive abundance. Indeed, when we quantified the abundance of all nucleotides of the educt RNA40 and compared the values with the quantities determined in the identified fragments, we observed an even representation with only a small underrepresentation of position 10–20 of the educt oligo RNA40 (Figure 1C). Based on these data, we could identify three major cut sites, all consisting of a GU dinucleotide. At these sites, 64% (position 5/6), 43% (position 9/10), or 37% (position 12/13) of the RNA40 starting material was cleaved. Only two minor non-GU cleavage events were detected, with 2% at the CU

Please cite this article in press as: Bérouti et al., Pseudouridine RNA avoids immune detection through impaired endolysosomal processing and TLR engagement, Cell (2025), https://doi.org/10.1016/j.cell.2025.05.032

CellPress
OPEN ACCESS

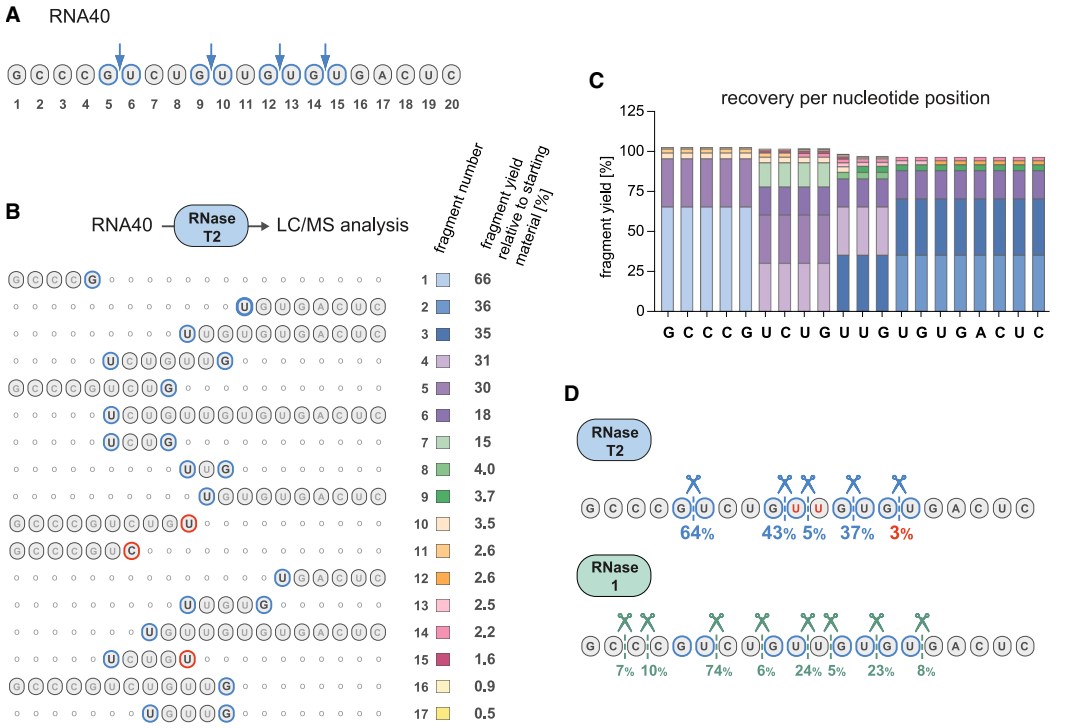

E coverage of dinucleotide sequence motivs as potential cleavage sites

RNA40	BASE2 C	U	G	A
BASE1 C	2	2	1	0
U	1	1	4	0
G	0	4	0	1
A	1	0	0	0

F average cleavage by RNase T2 [%]

RNA40	BASE2 C	U	G	A
C	0 < 0.1	1 +/- 1.3	0 —	
U	0 —	5 —	0 < 0.1	
G		37 +/- 22		0 —
A	0 —			

average cleavage by RNase 1 [%]

RNA40	BASE2 C	U	G	A
C	9 +/- 1.4	1 +/- 0.7	2 —	
U	74 —	24 —	10 +/- 7	
G		0 < 0.1		0 —
A	0 —			

G combined coverage of dinucleotide sequence motifs as potential cleavage sites in RNA40, RNA40i and RNA9.2s

RNA40 RNA40i RNA9.2s	BASE2 C	U	G	A
BASE1 C	6	7	1	2
U	4	4	5	5
G	2	5	0	1
A	2	4	1	1

H average cleavage by RNase T2 [%]

RNA40 RNA40i RNA9.2s	BASE2 C	U	G	A
C	0 +/- 0.2	6 +/- 12	0 —	0 +/- 0.1
U	0 < 0.1	5 +/- 5	0 +/- 0.6	1 +/- 0.9
G	0 < 0.1	39 +/- 20		0 —
A	0 +/- 0.5	36 +/- 19	0 —	2 —

average cleavage by RNase 1 [%]

RNA40 RNA40i RNA9.2s	BASE2 C	U	G	A
C	11 +/- 12	1 +/- 2	2 —	22 +/- 18
U	31 +/- 28	6 +/- 10	9 +/- 7	47 +/- 14
G	0 < 0.1	0 < 0.1		0 —
A	0 < 0.1	1 +/- 0.6	0 —	0 —

(legend on next page)

Please cite this article in press as: Bérouti et al., Pseudouridine RNA avoids immune detection through impaired endolysosomal processing and TLR engagement, Cell (2025), https://doi.org/10.1016/j.cell.2025.05.032

position 7/8% and 5% at the UU position 10/11 (Figures 1D, blue color, 1E and 1F, blue color). Using recombinant RNase 1 resulted in a different outcome: now all cleavage sites consisted of a pyrimidine followed by a random nucleotide (YN) (Figures 1D, green color, 1E and 1F, green color). To extend the targeting space of these enzymes we continued our study with the oligonucleotide RNA40i, in which all R bases of RNA40 were inverted (Figure S2A). Subjecting this oligonucleotide to RNase T2 digestion allowed us to identify four major cleavage sites that were all within an AU sequence (Figures S2B–S2D). Interestingly, for this oligonucleotide, the observed cleavage frequencies at the different positions were slightly different, with the second RU site now being the most frequently processed site. Also, no cuts beyond AU were recorded with a frequency higher than 3%. As for RNA40, digestion of RNA40i with RNase 1 resulted in fragments that were all terminated by a pyrimidine (Figures S2B–S2D). Finally, we studied the cleavage of RNA9.2s, another RNA oligo that is commonly used to activate TLR7 or TLR8 (Figure S2E). While the predominant RNase T2 cleavage site within RNA9.2s was again the central GU motif (position 11/12) with 50% processing at this side, also two additional non-RU cleavage sites were found with 14% cleavage at UU (position 4/5) and 34% at CU (position 9/10). RNase 1 dependent processing of RNA9.2s again provided only pyrimidine-terminated fragments (Figures S2E–S2G). Combining the processing data of all three oligonucleotides confirmed that RU dinucleotides are the optimal cleavage site for RNase T2. RNase 1, on the other hand, cleaves atYN with a preference for either YC or YA (Figures 1G and 1H).

RNase T2 substrate specificity for complex RNA molecules

In light of the notion that we observed the cleavage of non-RU substrates by RNase T2 under certain conditions, we wished to explore the substrate specificity of RNase T2 and RNase 1 on a complex RNA molecule, hence mimicking a physiological substrate. To do so, we *in vitro* transcribed a 2,500-nt ssRNA molecule and subjected this RNA to RNase T2 and RNase 1 digestion. Using LC-MS, we detected masses in the analyzed LC elution window, which encompassed dimers and trimers (Figure 2A). As expected, the UV chromatograms as well as the MS signal intensities were clearly distinct for these two treatments. Due to the complexity of the UV chromatograms with several peaks overlapping, we could not quantify the abundance of individual fragments by UV absorption. However, we could use the MS signal intensities of the fragments obtained by RNase T2 and RNase 1 digestion to calculate a ratio for a given fragment between the two samples, using the condition with the higher abundance as the reference (Figures 2B and 2C). Conducting this analysis revealed that dinucleotides UA and UG were exclusively seen for RNase T2, whereas their isomers AU and GU were only seen when digesting the RNA with RNase 1. Also, the other pyrimidine-terminated dinucleotides such as CU, UC, GC, AC, and CC as well as UU were either exclusively or predominantly observed when digesting the RNA molecule with RNase 1. Consistent with their substrate specificity, R-terminated dinucleotides that were not initiated by U (CG, CA, GA, AG, GG, and AA) were only detected at low abundance or trace amounts for both RNase T2 and RNase 1 digestion. Extending this analysis to certain trinucleotides confirmed this picture. U-initiated, R-terminated trinucleotides such as UUG or UUA were exclusively seen in RNase T2 digested samples, whereas their isomers were either confined to the RNase 1-treated sample (UGU, GUU, or AUU) or only detected at low abundance (UAU). Altogether, in a setting in which all possible dinucleotide substrates are available, RNase T2 preferentially cleaves substrates at RU, whereas RNase 1 cleaves after pyrimidine. Thus, it can be concluded that cleavage of non-RU substrates by RNase T2 is only observed under conditions of a restricted target range.

RNase T2 shows strongly reduced activity toward Ψ RNA

Next, we wanted to investigate whether modifications that occur naturally in RNA molecules affect the activity of RNase T2. To do this in a more reductionist setting, we used a previously established oligonucleotide containing a defined RNase T2 cleavage site. The used substrate consists of a stretch of 14 deoxynucleotides followed by a 6-nt RNA motif (UUGUCU) with a central GU dinucleotide (Figure 3A). Transferase-type ribonucleases, such as RNase T2 and RNase 1, cleave their substrates by catalyzing a 2′-O-transphosphorylation step that yields a cyclic 2′,3′-phosphodiester product of the fragment 5′ of the scissile bond and the concomitant release of a 5′OH fragment 3′ of the

Figure 1. Characterization of ssRNA digested with RNase T2 or RNase 1

(A) Scheme of RNA40 and its major RNase T2 cut sites.

(B) RNA40 (1 μg) was digested with RNase T2 (35 nM) in IDTE buffer and analyzed by HPLC-HESI-MS. The molecular identity and the fragment yields of the 17 identified fragments generated by RNase T2 digestion of RNA40 are shown. Fragment yields (percent product of educt) from three independent experiments were summarized.

(C) The yield of the fragments identified in (B) is shown for each nucleotide position.

(D) The percentage of cleavage at a given site for RNA40 processed by RNase T2 (35 nM) or RNase 1 (3 nM) is indicated. All sites with >3% cleavage are shown; RNase T2 cleavage percentage for the fourth GU motif is also depicted. Data from three independent experiments were summarized.

(E) The coverage of dinucleotide motifs as potential cleavage sites in RNA40 is shown. Note that only internal sites are considered, as RNase T2 and RNase 1 do not have exonuclease activity.

(F) Average cleavage percentages for all possible dinucleotide motifs of RNA40 digested with RNase T2 (35 nM) or RNase 1 (3 nM). Data from three independent experiments were summarized and cleavage percentages are depicted as mean values (large letters) ± SD (small letters, below).

(G) The coverage of dinucleotide motifs as potential cleavage sites in RNA40, RNA40i, and RNA9.2s are shown (only internal sites considered).

(H) Average cleavage percentages for all possible dinucleotide motifs of RNA40, RNA40i, and RNA9.2s digested with RNase T2 or RNase 1 were calculated from (F) and Figures S2D and S2G by summing the individual cleavage percentages of a given dinucleotide motif divided by the number of occurrences of that cleavage site in all three oligonucleotides. Data are depicted as mean values ± SD.

See also Figures S1 and S2.

Please cite this article in press as: Bérouti et al., Pseudouridine RNA avoids immune detection through impaired endolysosomal processing and TLR engagement, Cell (2025), https://doi.org/10.1016/j.cell.2025.05.032

CellPress
OPEN ACCESS

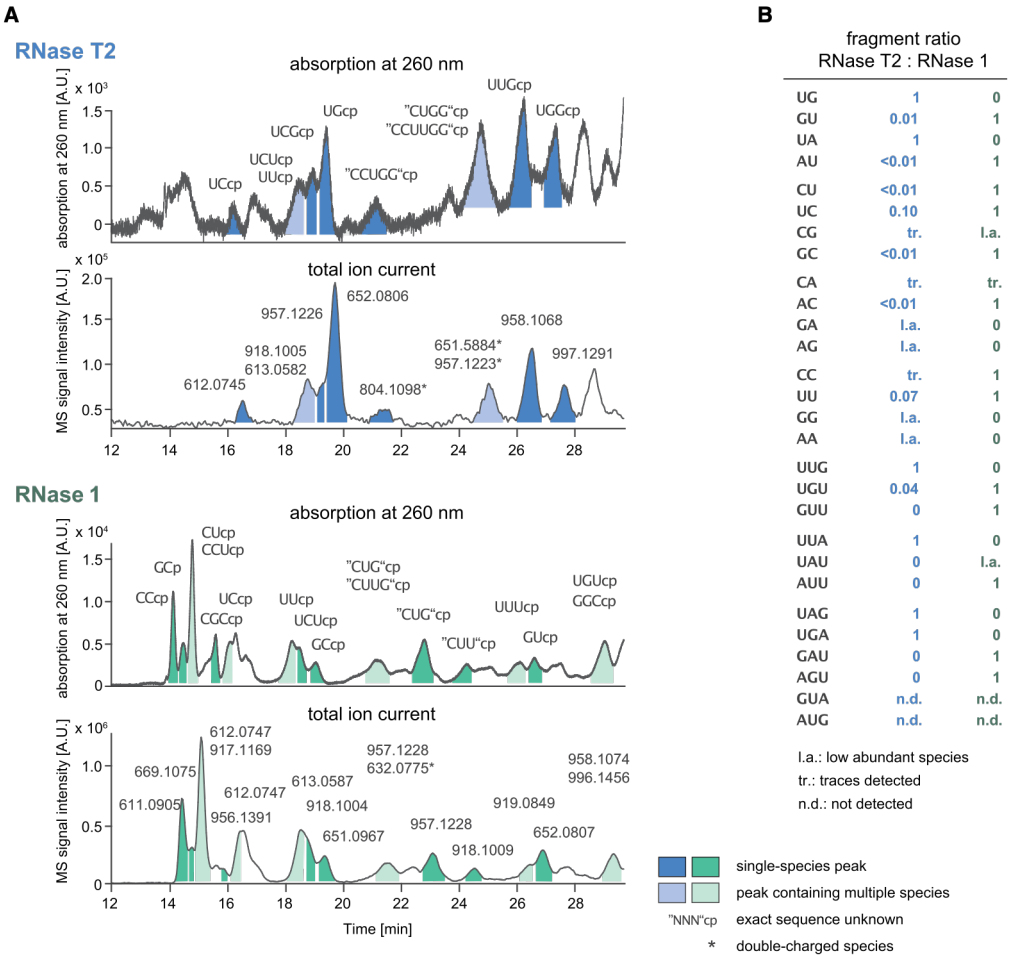

(legend on next page)

Please cite this article in press as: Bérouti et al., Pseudouridine RNA avoids immune detection through impaired endolysosomal processing and TLR engagement, Cell (2025), https://doi.org/10.1016/j.cell.2025.05.032

scissile bond. This step requires a free 2′OH group of the nucleotide at the B1 position (Figure 3B). Consistent with this notion, replacement of the G of UUGUCU with a 2′-O-methylguanosine (UUGmUCU) indeed largely abolished RNase T2-dependent cleavage of this oligonucleotide (Figures 3C and 3D). In contrast, 2′-O-methylation of the U in this motif (UUGUmCU) had no effect on RNase T2-dependent cleavage of this oligo, consistent with its cleavage mechanism (Figures 3C and 3D). Mass spectrometric analysis of the cleaved fragments confirmed these results (Figure 3E, left). While the GU-containing oligonucleotide was cleaved preferentially between G and U by RNase T2, this activity was fully abolished by the introduction of a 2′-O-methylguanosine. Of note, RNase 1 cleaved this oligo preferentially after the U at position 1 and position 4 of the 6-nt RNA motif (Figure 3E, right), whereas the introduction of a 2′-O-methylguanosine had no effect on this selectivity.

Next, we investigated whether Ψ or $m^1Ψ$ instead of U would affect RNase T2 activity (Figure 3C). We introduced Ψ or $m^1Ψ$ into the B2 position of the RNase T2 dinucleotide motif. Interestingly, neither GΨ nor $Gm^1Ψ$ were cleaved by RNase T2 as shown by PAGE and LC-MS analysis (Figures 3F and 3G, left). Since Ψ or $m^1Ψ$ was also part of the second cleavage site of the oligo preferentially cleaved by RNase 1, we could also assess the effect of this modification on RNase 1 activity. This revealed that RNase 1 in contrast to RNase T2 processed Ψ or $m^1Ψ$ just like U (Figure 3G, right). Since RNase 2 and RNase 6 have also been reported to act upstream of TLR8,[26,27] we included these RNase A family members in our analysis. As shown above, RNase T2 was largely unable to cleave between GΨ, while RNase 2 and RNase 6, similar to RNase 1, processed Ψ to a comparable extent as U (Figure 3H). Building on these findings, we also tested RNase T2 activity on a long, complex ssRNA substrate by transcribing the previously used 2,500-nt template *in vitro*, incorporating either U, Ψ, or $m^1Ψ$. Incubation of these RNAs with RNase T2 revealed that Ψ- and $m^1Ψ$-containing RNAs remained largely intact at low enzyme concentrations (Figure 3I, +), whereas U-containing RNA was completely digested. At higher enzyme concentrations (Figure 3I, ++), modified RNA substrates were also degraded by RNase T2 but to a lesser extent than unmodified RNA. These results suggest that RNase T2 cannot accommodate 2′-O-methylated Rs in its B1 pocket, as it requires a free hydroxyl group at this position. Furthermore, the B2 pocket of RNase T2 disfavors Ψ and $m^1Ψ$. In contrast, RNase A family members process Ψ and $m^1Ψ$ similarly to U.

Ψ RNA does not activate TLR8

In the next step, we evaluated the immune-stimulatory potential of these long ssRNA substrates in primary human monocytes in the presence of the TLR8-specific inhibitor CU-CPT9a. As expected, Ψ- or $m^1Ψ$-containing *in vitro* transcripts (IVTs) failed to stimulate TLR8 in primary human monocytes, while the unmodified IVT clearly triggered a TLR8-dependent interleukin-6 (IL-6), interferon gamma-induced protein 10 (IP-10), and tumor necrosis factor (TNF) response (Figures 4A–4C). Similar results were obtained in primary human peripheral blood mononuclear cells (PBMCs) (Figure S3A) and the monocytic cell line THP-1 (Figure S3B). We further utilized the BLaER1 monocyte model as these cells have been shown to respond to ssRNA when delivered with the cationic polypeptide poly-L-arginine (pR) in a TLR8- and RNase T2-dependent manner.[7] Like for primary human cells, the unmodified IVT induced a TLR8- and RNase T2-dependent IL-6 response in BLaER1 monocytes, while Ψ- or $m^1Ψ$-containing IVTs failed to stimulate TLR8 (Figure 4D). To exclude the possibility that uptake accounts for the differences observed, we transfected BLaER1 monocytes with fluorescently labeled RNAs and monitored their uptake by fluorescence-activated cell sorting (FACS). These data indicate that the RNA is equally taken up by cells independent of the RNA modification present (Figure S3C). At the same time, varying the oligonucleotide length did not affect the immune-stimulatory activity of IVT-U RNA, while Ψ-containing IVTs of any length failed to induce TLR-dependent interferon (IFN) release in PBMCs (Figure S3D). To study the impact of pseudouridylation in a setting in which a single RNase T2 motif is affected, we also tested the different UUGUCU-containing oligonucleotides (Figure 3) for their biological activity (Figure 4E). At the concentrations tested, the unmodified $(dAdC)_7$-UUGUCU oligonucleotide induced similar levels of IL-6 as RNA40. This activity was dependent on both RNase T2 and TLR8. All other oligonucleotides tested showed no TLR8 agonistic activity. These results are fully consistent with the observation that the GmU-, GΨ-, and $Gm^1Ψ$-containing oligonucleotides are no longer cleaved by RNase T2 (Figures 3D and 3F). Interestingly, the GUm-containing oligonucleotide was no longer stimulatory despite being cleaved by RNase T2 (Figure 3D). We speculate that this is due to reduced lysosomal U release, consistent with previous findings showing that the 3′-terminal fragment UCU is critical for this effect.[7] To further investigate this, we tested whether RNase A enzymes can cleave 2′-O-methyl Us, as RNase 2—a member of this family—has been implicated in U release for pocket 1.[26] As expected, based on their mode of action, none of these enzymes were able to cleave 2′-O-methyl Us (Figures S3E–S3G). Similarly, the lysosomal exonucleases PLD3 and PLD4 exhibited reduced activity but were not entirely inactive toward 2′-O-methyluridine-containing substrates (Figures S3H and S3I). In summary, these results indicate that Ψ-containing RNA fails to activate TLR8 across a wide range

Figure 2. Characterization of RNase T2 or RNase 1 digestion of a complex RNA substrate

(A) A 2,500 nt IVT (1 μg) was digested with RNase T2 (3.5 μM) or RNase 1 (3 nM). Representative LC-UV and LC-MS chromatograms of the two digests are shown (only the elution window from 12–30 min is shown). Annotated are fragment sequences with their corresponding masses (i.e., *m/z* values) as identified by LC-MS. The chromatograms are representative for two (RNase T2) or three (RNase 1) independent experiments.

(B) Ratios of different fragments (all with 2′,3′-cyclic monophosphate moiety at the 3′ end) present in the RNase T2 and/or RNase 1 digest as found by LC-MS. The fragment ratios are representative for two or three independent measurements. Note that the nonbinary results can only be considered as estimates, since no internal standards were available.

(C) Comparison of exemplary fragments of a specific mass/overall nucleotide composition as found by LC-MS in digests with the two enzymes. The resulting MS peaks correspond to specific fragment sequences. Data represent two or three independent experiments.

Please cite this article in press as: Bérouti et al., Pseudouridine RNA avoids immune detection through impaired endolysosomal processing and TLR engagement, Cell (2025), https://doi.org/10.1016/j.cell.2025.05.032

CellPress
OPEN ACCESS

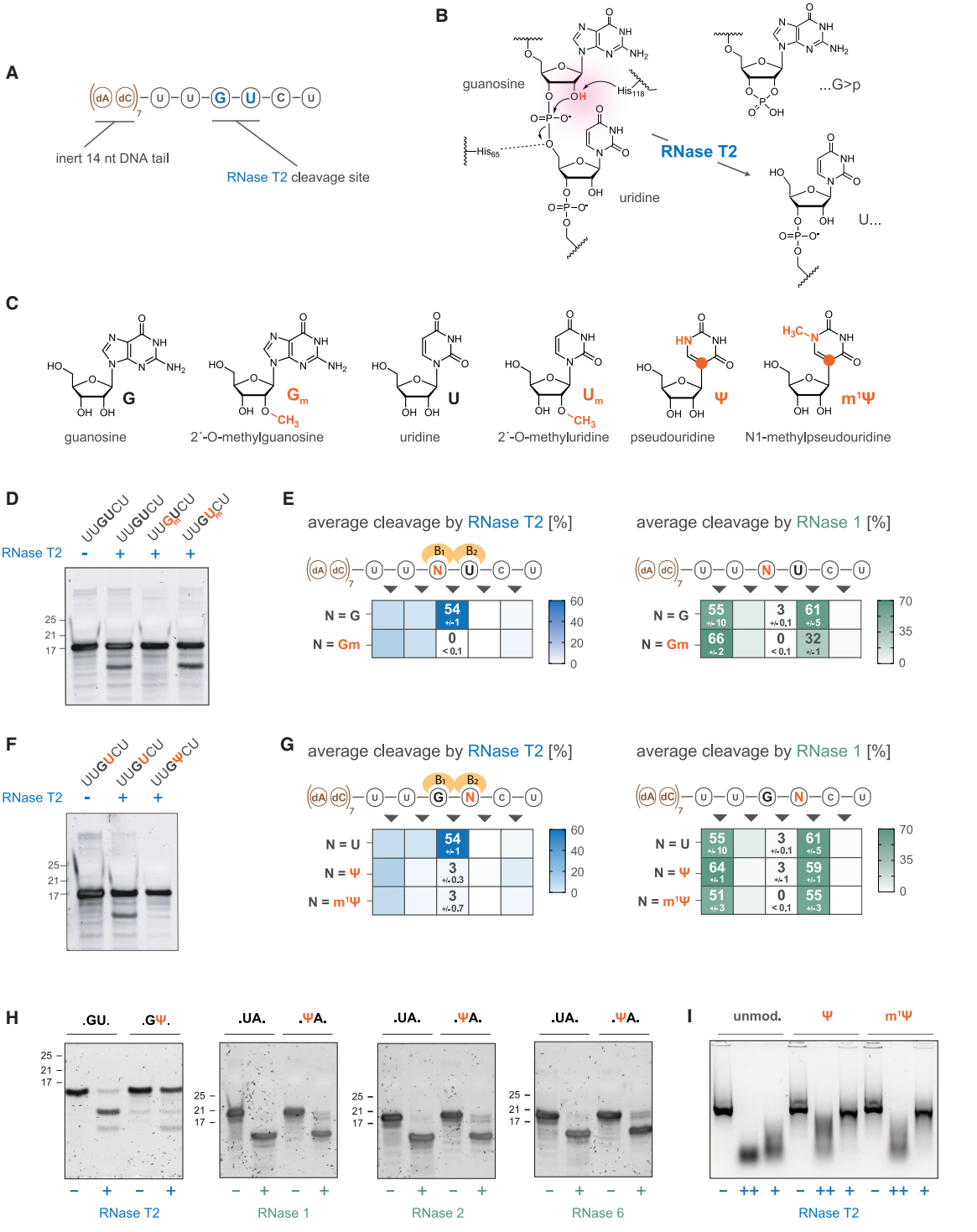

(legend on next page)

Please cite this article in press as: Bérouti et al., Pseudouridine RNA avoids immune detection through impaired endolysosomal processing and TLR engagement, Cell (2025), https://doi.org/10.1016/j.cell.2025.05.032

of cell types. In a reductionist setting, this lack of immunogenicity can be attributed to the modification affecting a single RNase T2 cleavage site.

Ψ is not a ligand for TLR8

Our results suggested that RNase T2 no longer generates RNA fragments from Ψ- or $m^1Ψ$-modified RNA, which was previously identified as a critical upstream requirement for TLR8 activation. However, these results could not exclude that Ψ or $m^1Ψ$ single nucleosides are still released from ssRNA, e.g., by RNase A enzymes in cells, and that the observed lack of immune stimulation is primarily due to these molecules not acting as agonists for TLR8. Under physiological conditions, RNA fragments engage the second binding pocket to allosterically regulate U binding in the first pocket, whereas small-molecule agonists such as R848 or TL8 bypass this requirement.[4] Binding studies indicate that TLR8 can bind U independently of the second pocket, albeit with a >50-fold reduction in affinity. Based on these considerations, we hypothesized that it should be possible to stimulate TLR8 in cells by hyperphysiological concentrations of U alone (Figure 5A). Indeed, at up to 32 mM, U elicited an IL-6 response of similar efficacy as TL8 but with greatly reduced potency (EC_{50} for TL8, 128 nM[28]; EC_{50} for U, 10.7 mM) (Figures S3J and S3K). Comparing U, Ψ, or $m^1Ψ$ as a pocket one agonist in cell culture, we again determined a high TLR8 agonistic efficacy for U (top IL-6 levels at 167.2 ng/ml) with an EC_{50} of 9.3 mM. Ψ, however, was completely inactive in stimulating TLR8 in the range tested (4–32 mM). Interestingly, $m^1Ψ$ induced a significant IL-6 response, albeit with reduced efficacy compared with U (IL-6 levels at 72.1 ng/ml), yet with a comparable EC_{50} (9.9 mM) (Figure 5B). Analogous results were obtained using primary monocytes (Figure S3L). Since 2′-O-methylation only partially inhibits PLD exonucleases, we tested whether 2′-O-methyluridine could activate TLR8. Here, like Ψ, 2′-O-methyluridine was unable to activate TLR8 in cells (Figure S3M). Next, we investigated whether U, Ψ, and $m^1Ψ$, when co-delivered with ssRNA, could enhance the TLR8-dependent RNA response. Therefore, we stimulated BLaER1 monocytes with $ssRNA40^S$ and the three single nucleosides (1.25–5 mM). U increased the RNA response by ~3-fold, with a similar effect observed for $m^1Ψ$ (Figures 5C and 5D). Surprisingly, Ψ, despite not inducing TLR8 activation alone (Figure 5B), enhanced the RNA response ~2-fold (Figure 5D), suggesting potential TLR8 binding. A similar effect was observed for 2′-O-methyluridine with $ssRNA40^S$ (Figure S3N).

Our results suggested that Ψ and $m^1Ψ$ can bind TLR8 when released from ssRNA, though Ψ is a weaker substrate than U and $m^1Ψ$. Despite their similar uptake, we aimed to investigate direct TLR8 stimulation through a biochemical assay that measures ligand-induced dimerization (Figure 5E). Unlike binding assays, this method distinguishes agonists from competitive antagonists. We expressed and purified human TLR8 ectodomain (ECD), confirming its autoprocessing at the Z-loop (Figure S4A) and its 110 kDa size at pH 5.0 via mass photometry (Figure S4B). Incubation with U (0.625–5 mM) revealed a dose-dependent ECD dimerization, reaching ~60% at 5 mM U (Figure 5F, left). Ψ showed minimal dimerization, even at the highest concentration (Figure 5F, middle), while $m^1Ψ$ mirrored U's activity (Figure 5F, right). In contrast, 2′-O-methyluridine failed to induce dimerization (Figure S4C). We further co-incubated the single nucleosides with $ssRNA40^O$ to introduce a second binding pocket ligand (Figures 5E and 5F, bottom row). While $ssRNA40^O$ alone failed to induce TLR8 ECD dimerization *in vitro* (Figure S4D), its combination with U or $m^1Ψ$ further enhanced dimer formation compared with the nucleosides alone (Figure 5F, bottom left and right). Notably, although $ssRNA40^O$ and Ψ individually showed little to no dimerization, their combination triggered robust dimerization, albeit weaker than U + ssRNA or $m^1Ψ$ + ssRNA (Figure 5F, bottom middle), aligning with stimulation results. In contrast, ssRNA with 2′-O-methyluridine induced the weakest dimerization (Figure S4E), suggesting the lowest TLR8 binding affinity among the tested nucleosides. Last, to rule out the competitive binding of Ψ to TLR8, we stimulated BLaER1 monocytes with U alone or combined with increasing Ψ concentrations. Co-stimulation did not reduce the U-dependent TLR8 response (Figure S4F). Taken together, these results indicate that Ψ as well as Um are much weaker substrates for TLR8 compared with U, however binding is not completely prohibited. Surprisingly, $m^1Ψ$ exhibits similar TLR8 activation to U.

Ψ inhibits the release of 2′,3′-cGMP for TLR7 activation

Beyond its lack of TLR8 stimulation, Ψ RNA also strongly dampens the TLR7 response.[10] In line with this notion, IVT-Ψ and IVT-$m^1Ψ$

Figure 3. Ψ and $m^1Ψ$ impair RNA cleavage by RNase T2 but not RNase A enzymes

(A) Chimeric DNA-RNA oligonucleotides used as test substrate for cleavage experiments with RNase T2 and RNase 1.

(B) RNA cleavage mechanism of a transferase-type endoribonuclease exemplified on a GU dinucleotide site.

(C) Structures of guanosine, 2′-O-methylguanosine, uridine, 2′-O-methyluridine, Ψ, and $m^1Ψ$.

(D) Indicated oligonucleotides (1 μg each) were subjected to RNase T2 (9 μM) cleavage in IDTE buffer and analyzed on a denaturing urea gel. Data represent two independent experiments.

(E) HPLC-HESI-MS analysis of cleavage by RNase T2 (3.5 μM) and RNase 1 (6 nM) in IDTE buffer using oligonucleotides (1 μg each) with either guanosine or 2′-O-methylguanosine. Mean cleavage percentages ± SD from three independent experiments.

(F) Unmodified or modified oligonucleotides (1 μg each) were subjected to RNase T2 (9 μM) cleavage in IDTE buffer and analyzed on a denaturing urea gel. Data represent two independent experiments.

(G) Cleavage by RNase T2 (3.5 μM) and RNase 1 (6 nM) on oligonucleotides (1 μg) with U, Ψ, or $m^1Ψ$, analyzed by HPLC-HESI-MS. Mean cleavage percentage ± SD from three independent experiments.

(H) Urea gel of $(dAdC)_7$UUGUCU and $(dAdC)_7$UUGΨCU digested with RNase T2 (10 nM) in assay buffer. One representative blot of three independent experiments is shown. Urea gels of $(dAdC)_7$GAGUAGA and $(dAdC)_7$GAGΨAGA digested with RNase 1 (60 nM), RNase 2 (55 nM), or RNase 6 (60 nM) in assay buffer. One representative blot of two independent experiments.

(I) IVTs containing U, Ψ, or $m^1Ψ$ were digested with RNase T2 (+ = 0.37 μM) and (++ = 3.7 μM) for 20 min and analyzed on a non-denaturing agarose gel. Data represent two independent experiments.

Please cite this article in press as: Bérouti et al., Pseudouridine RNA avoids immune detection through impaired endolysosomal processing and TLR engagement, Cell (2025), https://doi.org/10.1016/j.cell.2025.05.032

CellPress
OPEN ACCESS

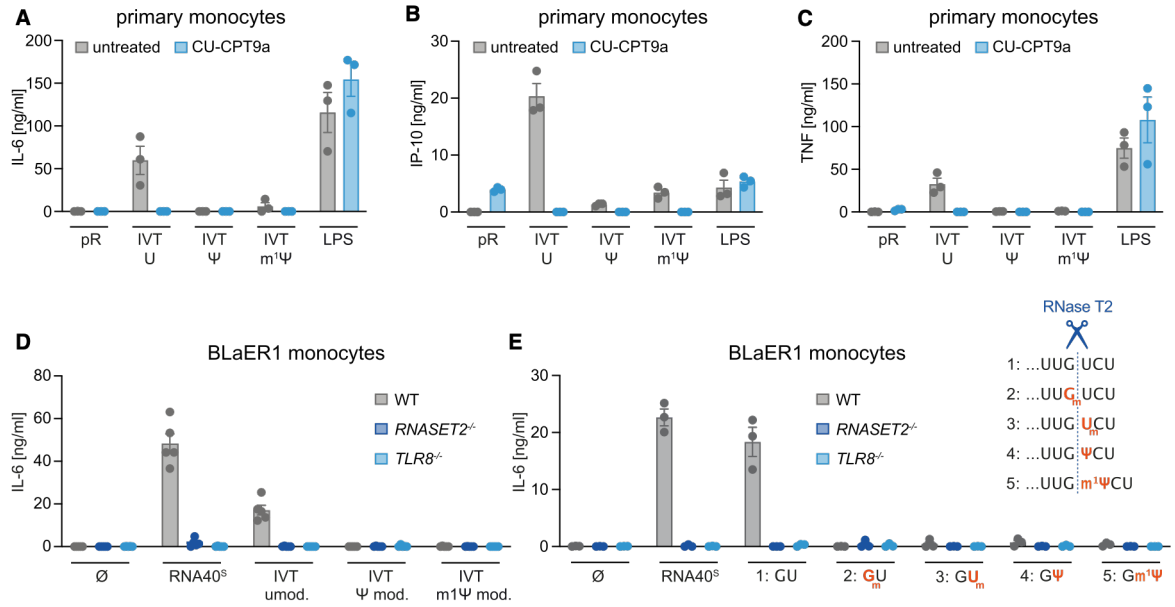

Figure 4. Ψ RNA does not activate TLR8

(A–C) CD14$^+$ monocytes were stimulated with pR, OVA IVT-U, OVA IVT-Ψ, OVA IVT-m^{1}Ψ, and LPS in the presence or absence of CU-CPT9a. After 24 h, (A) IL-6, (B) IP-10, and (C) TNF release was measured. Data are depicted as mean ± SEM of n = 3 independent donors.

(D) BLaER1 monocytes of indicated genotypes were unstimulated or stimulated with ssRNA40^S, Cas9 IVT-U, Cas9 IVT-Ψ, and Cas9 IVT-m^{1}Ψ. After 14 h, IL-6 release was measured. Mean ± SEM of n = 5 independent experiments.

(E) BLaER1 monocytes of indicated genotypes were stimulated as indicated. After 14 h, IL-6 release was measured. Mean ± SEM of n = 3 independent experiments.

See also Figure S3.

RNA failed to activate TLR7 in primary plasmacytoid dendritic cells (pDCs), whereas IVT-U RNA induced TLR7-dependent IFNα release upon transfection (Figure 6A). Similar but weaker effects were observed when using lipofectamine instead of pR for delivery (Figure S5A). We recently found that RNase T2 and PLD exonucleases are essential for generating stimulatory ssRNA fragments for TLR7. Accordingly, IVT-U mRNA triggered a TLR7-dependent response in CAL-1 cells, which was entirely reliant on these nucleases, whereas Ψ-modified IVTs failed to induce any response (Figure 6B). Specifically, RNase T2 and PLD collaboratively process RNA to generate 2′,3′-cGMP, the endogenous TLR7 pocket 1 ligand. RNase T2 first cleaves ssRNA between G and U, producing 2′,3′-cGMP-terminated fragments, which PLD exonucleases further degrade into single nucleotides, releasing 2′,3′-cGMP (see Bérouti et al.[8]; Figure 6C). Since RNase T2 poorly processes Ψ- and m^{1}Ψ-containing RNAs (Figures 3F and 3G, left), and cleavage at GΨ is crucial for 2′,3′-cGMP release, we hypothesized that Ψ and m^{1}Ψ impair its production. To test this, we digested the IVT constructs with RNase T2, PLD3, or both, and analyzed 2′,3′-cGMP release via LC-MS. As expected, only the RNase T2 + PLD3 combination efficiently released 2′,3′-cGMP from IVT-U RNA, while substitution with Ψ or m^{1}Ψ (IVT-Ψ, IVT-m^{1}Ψ) completely abolished its release (Figure 6D). Consistent with this, we observed 2′,3′-cGMP production in primary pDCs stimulated with IVT-U RNA, whereas IVT-Ψ RNA led to a markedly reduced release (Figures 6E and 6F). We further stimulated CAL-1 cells with RNA40^O, RNA9.2s, and modified RNA9.2s variants. RNA9.2s is ideal for studying RNase T2's impact, as it contains a single GU cleavage site, which should be essential for generating 2′,3′-cGMP. Indeed, blocking RNase T2 cleavage by adding a 2′-O-methylation to G at this site (Figure 3D) completely abolished RNA9.2s's immune-stimulatory effect (Figures 6G and S5B). Similarly, substituting U with Ψ at the cleavage site strongly reduced but did not fully eliminate TLR7 responses. However, adding three additional Ψs upstream of the GU site completely abrogated RNA9.2s's immune-stimulatory potential (Figures 6G and S5B). Intriguingly, these effects correlated with 2′,3′-cGMP release by RNase T2 and PLD3 *in vitro* (Figure 6H). Notably, all oligonucleotides retained a U-containing motif (CCUUC) necessary for TLR7 pocket 2,[6] indicating that the blunted or reduced TLR7 response resulted primarily from impaired 2′,3′-cGMP release. These findings indirectly suggest that PLD exonucleases, like RNase T2, do not efficiently process Ψ as a substrate. Since PLD exonucleases must degrade RNase T2-processed RNA to the single nucleotide level to release 2′,3′-cGMP, we examined whether PLD3 and PLD4 can degrade Ψ and m^{1}Ψ when encountered at the 5′ end. To formally address this, we incubated PLD3 and PLD4 with oligonucleotides starting with three consecutive U, Ψ, or m^{1}Ψ. As expected, both enzymes efficiently degraded U-RNA but failed to effectively digest Ψ- or m^{1}Ψ-RNA (Figures S5C and S5D). Further analysis using PLD3^{H201N,H416N}, a catalytically inactive mutant that retains substrate binding,[8] showed a ∼4-fold reduction in

Please cite this article in press as: Bérouti et al., Pseudouridine RNA avoids immune detection through impaired endolysosomal processing and TLR engagement, Cell (2025), https://doi.org/10.1016/j.cell.2025.05.032

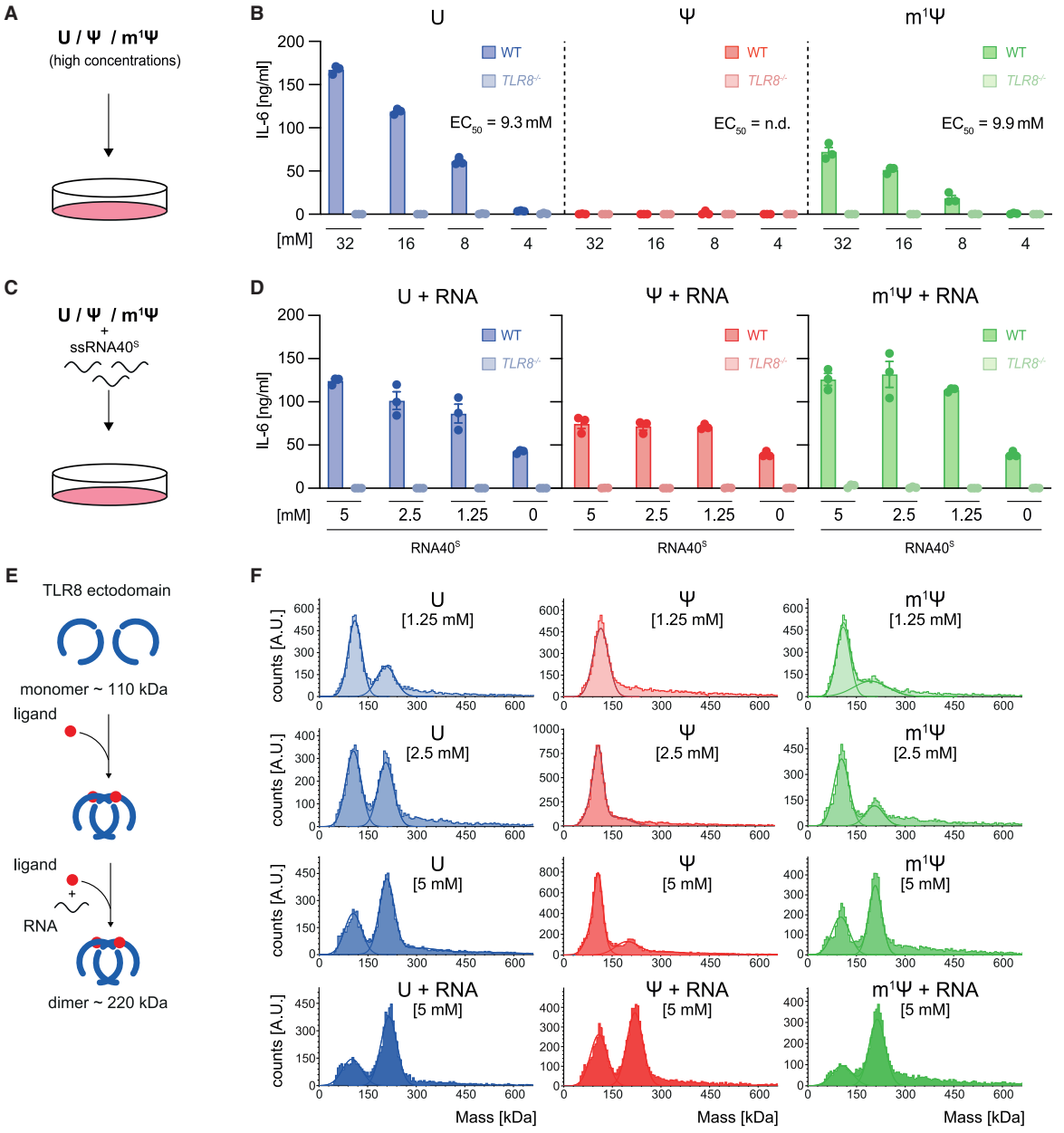

Figure 5. Ψ is a poor ligand for TLR8

(A) Scheme of cell stimulation with high concentration of single nucleosides.

(B) Wild-type and TLR8$^{-/-}$ BLaER1 monocytes were stimulated with indicated concentrations of U, Ψ, or m^{1}Ψ. After 14 h, IL-6 release was detected. Data are depicted as mean ± SEM of $n = 3$ independent experiments. A four-parameter dose-response curve was fitted to calculate half-maximal effective concentration (EC_{50}).

(C) Scheme of cell stimulation with high concentration of single nucleosides in combination with ssRNA40^S.

(D) Wild-type and TLR8$^{-/-}$ BLaER1 monocytes were stimulated with ssRNA40^S or with ssRNA40^S in combination with U (left), Ψ (middle), or m^{1}Ψ (right). After 14 h, IL-6 release was detected. Mean ± SEM of $n = 3$ independent experiments. Please note that the ssRNA40^S-only control data for Ψ and m^{1}Ψ are identical and that one of the U control replicates is also shared with the Ψ/m^{1}Ψ control.

(E) Scheme of the TLR8 ECD dimerization assay.

(F) Mass distribution of hsTLR8 (AA27-827) observed by mass photometry after incubation with increasing concentrations of single nucleosides and in combination with ssRNA40^O.

See also Figures S3 and S4.

Please cite this article in press as: Bérouti et al., Pseudouridine RNA avoids immune detection through impaired endolysosomal processing and TLR engagement, Cell (2025), https://doi.org/10.1016/j.cell.2025.05.032

CellPress
OPEN ACCESS

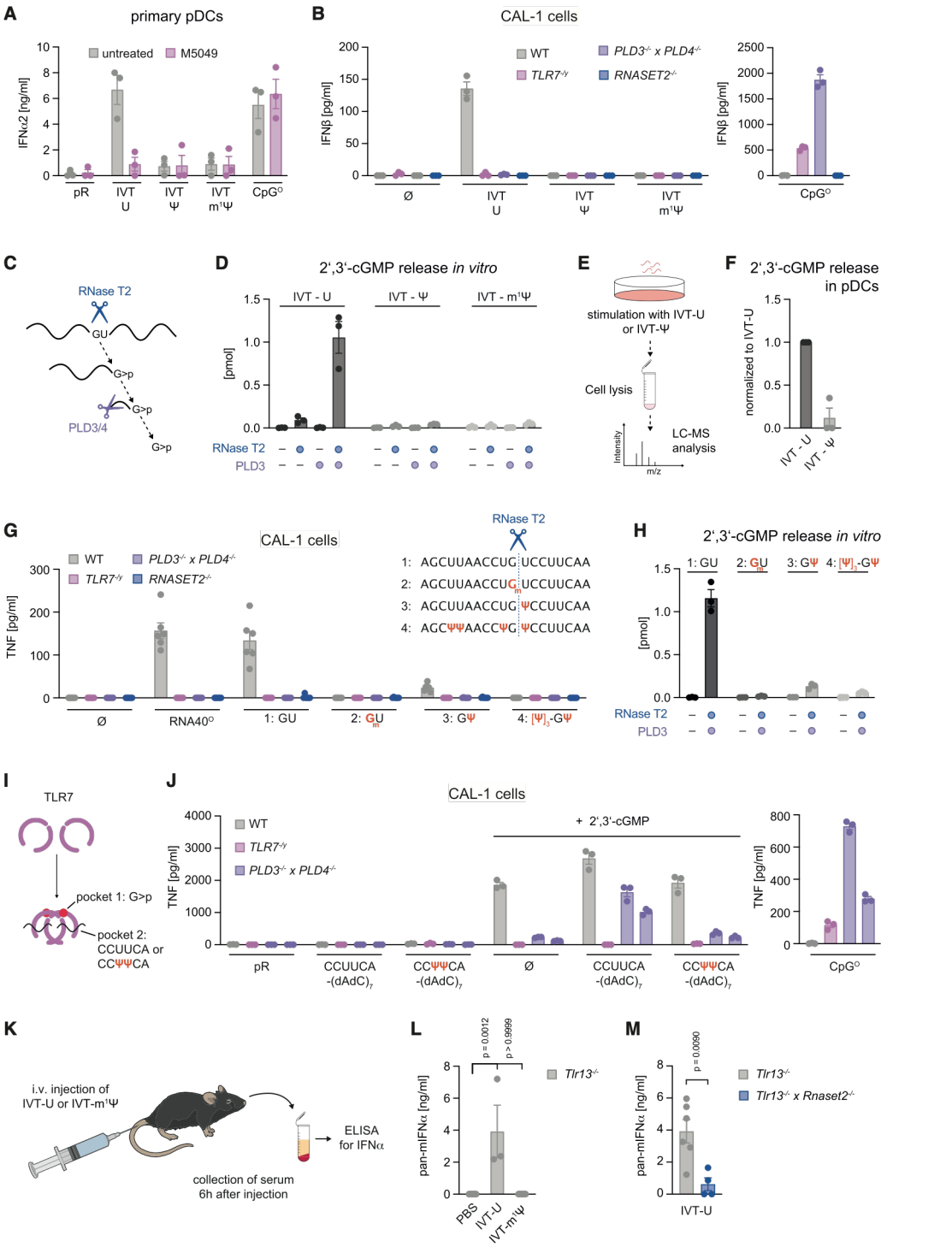

(legend on next page)

Please cite this article in press as: Bérouti et al., Pseudouridine RNA avoids immune detection through impaired endolysosomal processing and TLR engagement, Cell (2025), https://doi.org/10.1016/j.cell.2025.05.032

binding affinity, from 71.38 nM (U-RNA) to 266.3 nM (Ψ-RNA) (Figure S5E). Consistent with previous work,[29] we found that Ψ-containing RNA favors an A-form helical conformation by analyzing Ψ-RNA using NMR. These data indicate additional intramolecular interactions of the Ψ base with the phosphate backbone and Ψ-mediated base stacking between Ψ and the 3′ neighboring base leading to a preferential conformation of the RNA from B into A helical form (Figures S6A–S6D). These structural changes could explain why Ψ is a poor substrate for RNase T2 and PLD exonucleases.

In addition to 2′,3′-cGMP for pocket 1, TLR7 requires a short oligoribonucleotide (ORN) in the second binding pocket, preferably with two consecutive Us for activation.[5] To determine whether Ψ-containing ORNs engage TLR7 pocket 2, we stimulated PLD3xPLD4-deficient CAL-1 cells with 2′,3′-cGMP and a short U- or Ψ-rich oligonucleotide. These cells serve as a model for studying pocket 2 ligands, as they do not respond to the pocket 1 ligand alone (see Bérouti et al.[8]; Figures 6I and 6J), indicating the lack of a pocket 2 ligand under steady state. As expected, co-stimulation with 2′,3′-cGMP and a U-containing oligonucleotide induced TLR7-dependent TNF release. However, when U was replaced with Ψ, no TNF release was observed, suggesting that Ψ cannot allosterically activate TLR7 via the second pocket (Figure 6J). A major challenge of mRNA delivery via LNPs *in vivo* is the low efficiency of endosomal escape, limiting the amount of RNA that reaches the cytosol.[30] As a result, mRNA vaccination triggers a strong TLR7-dependent immune response.[21–23] Since TLR7 drives this response, we hypothesized that it would also depend on RNase T2. However, as RNase T2-deficient mice develop TLR13-driven autoinflammation,[31,32] we investigated mRNA vaccination effects in *Tlr13*$^{-/-}$ × *Rnaset2*$^{-/-}$ double-deficient mice. First, we injected *Tlr13*$^{-/-}$ control mice with IVT-U or IVT-m^{1}Ψ mRNA (Figure 6K). As expected, IVT-U mRNA induced high IFNα levels in the serum, whereas IVT-m^{1}Ψ mRNA did not (Figure 6L). We then compared responses in *Tlr13*$^{-/-}$ and *Tlr13*$^{-/-}$ × *Rnaset2*$^{-/-}$ mice after IVT-U mRNA injection. While *Tlr13*$^{-/-}$ mice showed elevated IFNα levels, IFNα production was significantly reduced in *Tlr13*$^{-/-}$ × *Rnaset2*$^{-/-}$ mice (Figure 6M), demonstrating that RNase T2 is crucial for mRNA recognition *in vivo*. In summary, these results not only show that Ψ as well as m^{1}Ψ impair the release of 2′,3′-cGMP required for TLR7 pocket 1 by inhibiting efficient degradation by RNase T2 and PLD exonucleases, but also that Ψ does not serve as a ligand for the second binding pocket of TLR7.

DISCUSSION

In this study, we investigated how Ψ, the most abundant modification in endogenous RNA, and m^{1}Ψ, the U analog used in prophylactic COVID-19 vaccines, evade recognition by the endolysosomal TLR system. We began by revisiting RNase T2 substrate specificity, as prior reports suggested it was more relaxed, with limited B1 site selectivity for Rs.[26,33] Using quantitative MS, we confirmed our earlier findings that RNase T2 strongly prefers RU motifs. While YU cuts also occurred in a model substrate, they were less frequent. As expected, RNase 1, an enzyme of the RNase A family, cleaved substrates following pyrimidines. Extending these studies to complex RNA substrates—long *in vitro* transcripts—we found that R-terminated fragments were almost exclusively generated by RNase T2. Thus, in a setting with diverse potential substrates, RNase T2 favors RU motifs, whereas in limited substrate contexts, it may act more broadly. Given RNase T2's critical role in processing RNA upstream of TLR7 and TLR8, we reasoned that modifications within RU motifs might regulate TLR activation. Consistent with its catalytic mechanism involving 2′-O-transphosphorylation of the first nucleotide, we found that 2′-O-methylation of G—but not U as the second nucleotide—completely blocked GU cleavage by RNase T2.[33] Turning to Ψ, the most abundant nucleoside modification in mammalian RNA and relevant medically, we observed that RNase T2 processing of Ψ-containing RNA was strongly impaired. A similar result was seen with m^{1}Ψ. These findings were

Figure 6. Ψ inhibits the release of 2′,3′-cGMP for TLR7 activation

(A) pDCs were stimulated as indicated in the presence or absence of M5049. After 24 h, hIFNα2 release was detected. Data are depicted as mean ± SEM of $n = 3$ independent donors.

(B) CAL-1 cells of indicated genotypes were unstimulated or stimulated with OVA IVT-U, OVA IVT-Ψ, OVA IVT-m^{1}Ψ, and CpG^O. After 16 h, hIFN-β release was determined. Mean ± SEM of $n = 3$ independent experiments.

(C) Scheme of 2′,3′-cGMP release from ssRNA by RNase T2 and PLD exonucleases.

(D) IVT-U, IVT- Ψ, and IVT-m^{1}Ψ were digested with RNase T2 (0.5 nM), PLD3 (25 nM), or a combination of RNase T2 (0.5 nM) and PLD3 (25 nM) for 1 h and the release of 2′,3′-cGMP was analyzed by LC-MS. Mean ± SEM of $n = 3$ independent experiments.

(E) Scheme of the workflow for detecting single nucleotides in cells after transfection.

(F) 2′,3′-cGMP release in pDCs detected by LC-MS after transfection with OVA IVT-U or OVA IVT-Ψ. From each donor data were normalized to stimulation with OVA IVT-U and are depicted as mean ± SEM of $n = 3$ independent donors.

(G) CAL-1 cells of indicated genotypes were stimulated as indicated. After 16 h, TNF release was determined. Mean ± SEM of $n = 6$ independent experiments.

(H) RNA9.2s oligonucleotides from (G) were incubated in assay buffer or were digested with a combination of RNase T2 (10 nM) and PLD3 (25 nM) for 30 min and the release of 2′,3′-cGMP was analyzed by LC-MS. Mean ± SEM of $n = 3$ independent experiments.

(I) Scheme of ligand binding to TLR7 ectodomain.

(J) CAL-1 cells of indicated genotypes were unstimulated or stimulated with 2′,3′-cGMP (0.5 mM), short ORNs, or ORNs in combination with 2′,3′-cGMP (0.5 mM). Mean ± SEM of $n = 3$ independent experiments.

(K) Scheme of mouse injection followed by serum IFNα measurement.

(L) Pan-mIFNα release detected in the serum of Tlr13$^{-/-}$ mice injected with PBS, OVA IVT-U, or OVA IVT-m^{1}Ψ. Data are depicted as mean ± SEM of $n = 6$ (PBS), $n = 3$ (IVT-U), and $n = 6$ (IVT-m^{1}Ψ) Tlr13$^{-/-}$ mice. Statistical analysis was conducted by one-way ANOVA with Tukey's multiple comparison tests.

(M) Pan-mIFNα release detected in the serum of Tlr13$^{-/-}$ or Tlr13$^{-/-}$ × Rnaset2$^{-/-}$ mice injected with OVA IVT-U. Data are depicted as mean ± SEM of $n = 6$ (Tlr13$^{-/-}$) and $n = 4$ (*Tlr13*$^{-/-}$ × *Rnaset2*$^{-/-}$) mice. Statistical analysis was conducted by an unpaired t test.

See also Figures S5 and S6.

Please cite this article in press as: Bérouti et al., Pseudouridine RNA avoids immune detection through impaired endolysosomal processing and TLR engagement, Cell (2025), https://doi.org/10.1016/j.cell.2025.05.032

confirmed in long, complex RNA molecules, including those in the size range of mRNA vaccines. Reflecting its non-redundant role upstream of TLR7 and TLR8, the lack of cleavage of Ψ- and $m^1Ψ$-containing RNAs correlated with absent immunostimulatory activity. Indeed, introducing a single Ψ into an RNA oligonucleotide containing an RNase T2 motif substantially reduced both cleavage and the TLR7/8 response in cells. Tracking the fate of RNA in primary cells, we observed that Ψ-modified RNA no longer yielded the TLR7 agonist 2′,3′-cGMP. In this context, we also found that PLD exonucleases, which are essential upstream of TLR7 to release 2′,3′-cGMP from RNase T2-cleaved RNA, were similarly unable to degrade Ψ- and $m^1Ψ$-containing RNA, further contributing to the immune evasion of these modifications. Supporting these cellular observations, unmodified mRNA elicited a strong type I IFN response in mice, which was largely blunted in RNase T2-deficient animals.

Our results indicate that Ψ-modified RNA loses its stimulatory activity because it is not properly processed by RNase T2 and PLD exonucleases to generate TLR7 and TLR8 agonistic molecules. However, this does not rule out the possibility that Ψ-modified RNA may also fail to act as a ligand at the level of TLR7 and TLR8. To investigate this, we directly stimulated human monocytes with high concentrations of U, Ψ, or $m^1Ψ$ as potential agonists for the first binding pocket of TLR8. While these stimulatory conditions may not fully reflect the physiological engagement of TLR8 by incoming RNA and its degradation products, they provided an experimental setup to assess the activatability of TLR8 in a cellular context. Although U exhibited significantly lower potency compared with synthetic pocket 1 agonists, it still produced similar efficacies, making this an informative experiment. Using this setup, we found that Ψ was completely inactive in activating TLR8 compared with U, whereas, unexpectedly, $m^1Ψ$ displayed comparable activity. Interestingly, while Ψ alone failed to activate TLR8, it could enhance the TLR8-dependent RNA response, suggesting that Ψ may bind to TLR8 pocket 1 when released from ssRNA. A biochemical assay examining TLR8 dimerization in response to these nucleosides confirmed these findings: U and $m^1Ψ$ induced comparable TLR8 dimerization across a range of ligand concentrations, whereas Ψ alone exhibited little to no receptor dimerization activity. However, in combination with ssRNA, Ψ was still able to induce TLR8 dimerization *in vitro*. On the other hand, Ψ-containing RNA failed to activate TLR7 in PLD-deficient CAL-1 cells when stimulated with 2′,3′-cGMP, suggesting that Ψ-oligos do not bind to the second binding pocket of TLR7. Taken together, these findings suggest that Ψ-modified RNA is immune stealth for at least two reasons: first, its processing by RNase T2 and PLD exonucleases is significantly impaired, and second, Ψ itself is a weak agonist for the first binding pocket of TLR8, while Ψ-containing RNA does not serve as an agonist for the second binding pocket of TLR7. Interestingly, and somewhat unexpectedly, while the therapeutically relevant $m^1Ψ$ modification also resists RNase T2 and PLD exonuclease cleavage, it nonetheless functions as a TLR8 pocket 1 agonist.

In the absence of substrate-bound structures, it remains unclear how RNase T2 or PLD exonucleases distinguish U from Ψ. Ψ's N1 acts as an additional hydrogen bond donor, altering hydration and promoting intramolecular interactions with the RNA phosphate backbone. We and others[29] also observed Ψ-mediated base stacking with the 3′ neighboring nucleotide. These changes favor an A-form helical conformation, possibly explaining Ψ-RNA's poor substrate compatibility with PLD enzymes. For RNase T2, we further hypothesize that Ψ-induced conformational changes disrupt base coordination in the B2 pocket. Similar structural effects have been shown to inhibit RNase E cleavage,[34] where Ψ substitution adjacent to the cleavage site constrains the backbone and impairs catalytic site binding. A parallel mechanism may apply to PLDs and RNase T2, where Ψ-RNA adopts an unfavorable conformation for substrate binding. Interestingly, RNase A enzymes are unaffected by Ψ, suggesting that these structural alterations do not broadly impair lysosomal nuclease activity. Whether $m^1Ψ$ induces stacking or conformational changes like Ψ remains underexplored, though some evidence suggests similar effects.[35] The N1 methyl group in $m^1Ψ$ introduces steric bulk, potentially influencing its fit in RNase T2's B2 pocket. Notably, TLR8's responsiveness to $m^1Ψ$ but not Ψ is structurally unexpected. In the TLR8-U complex,[4] U adopts a syn conformation. This would position Ψ's N1 (or the methyl group of $m^1Ψ$) near Tyr353, which π stacks with the pyrimidine ring. Why this allows binding of $m^1Ψ$ but not Ψ remains unresolved, warranting further structural studies.

In conclusion, our study provides the first molecular insights into how Ψ evades immune recognition by RNA-sensing TLRs. We show that lysosomal nucleases fail to adequately process Ψ-containing RNA into TLR-agonistic ligands, highlighting their critical upstream role in non-self-RNA detection. Additionally, TLR8 bypasses Ψ in its first binding pocket, while TLR7 neglects Ψ-containing fragments in its second pocket, providing a secondary safeguard. Notably, $m^1Ψ$ also evades processing by these nucleases, yet retains the ability to activate TLR8. Taken together, these findings define the molecular basis for selective RNA recognition by TLRs and support the rational design of immunostealth mRNAs by avoiding RNase T2-dependent processing.

Limitations of the study

It is tempting to speculate that Ψ modification of endogenous RNA contributes to the non-responsiveness of TLR7 and TLR8 to self-RNA. Supporting this idea, pseudouridylation follows specific sequence motifs that may underlie self-non-self-discrimination. In eukaryotes, Ψ is introduced either by box H/ACA ribonucleoproteins or by sequence-specific Ψ synthases (PUS enzymes),[9] such as Pus1 targeting RU motifs[36] or Pus7 targeting UGUA motifs.[37] Although these patterns may aid self-recognition, their contribution is difficult to test due to the redundancy and essentiality of the pseudouridylation machinery. Indeed, additional modifications, like 2′-O-methylation, may also help render self-RNA non-immunogenic. Future studies will be needed to dissect the relative contributions of Ψ and other modifications to TLR7/8 evasion. Another important limitation to note is that, while our study reveals why Ψ-RNA fails to activate TLR7 and TLR8, it was not designed to assess RNase T2's role *in vivo* during responses to unmodified mRNA vaccines. Thus, we cannot infer its impact on adaptive responses, such as antibody or T cell induction. Nonetheless, elucidating RNase T2 function in this context may inform strategies to optimize mRNA vaccine efficacy.

Please cite this article in press as: Bérouti et al., Pseudouridine RNA avoids immune detection through impaired endolysosomal processing and TLR engagement, Cell (2025), https://doi.org/10.1016/j.cell.2025.05.032

RESOURCE AVAILABILITY

Lead contact

Further information and requests for resources and reagents should be directed to and will be fulfilled by the lead contact, Veit Hornung (hornung@genzentrum.lmu.de).

Materials availability

All newly generated materials associated with the paper are available upon request from the lead contact.

Data and code availability

This paper does not report any original code. Any additional information required to reanalyze the data reported in this work is available from the lead contact upon request.

ACKNOWLEDGMENTS

We thank Claudia Ludwig for technical support in isolating primary cells and Tobias Komar for his help in purifying TLR8 ECD (both Gene Center, LMU). This work was supported by grants from the Deutsche Forschungsgemeinschaft (DFG, German Research Foundation) CRC 237/A27 (project-ID 369799452) to V.H. and T.C., CRC 237/A05 (project-ID 369799452) to K.-P.H, CRC 1309/A02 (project-ID 325871075) to M.S., CRC 1309/A04 (project-ID 325871075) to T.C., and CRC 1361/P2 (project-ID 393547839) to T.C., grants from the ERC (ERC-2016-ADG-741912 EpiR) to T.C. and (ERC-2020-ADG–101018672 ENGINES) to V.H., and grants from the Federal Ministry of Education and Research (BMBF) in the framework of the Cluster4future program (CNATM – Cluster for Nucleic Acid Therapeutics Munich) (grant-ID 03ZU1201AA) to T.C., K.-P.H., and V.H.

AUTHOR CONTRIBUTIONS

Conceptualization, M.B., M.W., W.G., and V.H.; investigation, M.B., M.W., W.G., I.P., J.G., L.H., C.M.-H., M.H., A.P., A.J.T., G.W., and V.H.; writing, M.B. and V.H. with input from all authors; resources, K.-P.H., M.S., D.A., T.C., and V.H.; funding acquisition, V.H.; supervision, V.H.

DECLARATION OF INTERESTS

The authors declare no competing interests.

DECLARATION OF GENERATIVE AI AND AI-ASSISTED TECHNOLOGIES IN THE WRITING PROCESS

Portions of this manuscript were edited for clarity and conciseness using OpenAI's ChatGPT. The AI-assisted modifications were restricted to improving readability and conciseness, with all scientific content and conclusions remaining the sole responsibility of the authors.

STAR★METHODS

Detailed methods are provided in the online version of this paper and include the following:

Received: July 7, 2024
Revised: March 15, 2025
Accepted: May 22, 2025

REFERENCES

1. Fitzgerald, K.A., and Kagan, J.C. (2020). Toll-like Receptors and the Control of Immunity. Cell *180*, 1044–1066. https://doi.org/10.1016/j.cell.2020.02.041.
2. Heil, F., Hemmi, H., Hochrein, H., Ampenberger, F., Kirschning, C., Akira, S., Lipford, G., Wagner, H., and Bauer, S. (2004). Species-specific recognition of single-stranded RNA via toll-like receptor 7 and 8. Science *303*, 1526–1529. https://doi.org/10.1126/science.1093620.
3. Hemmi, H., Takeuchi, O., Kawai, T., Kaisho, T., Sato, S., Sanjo, H., Matsumoto, M., Hoshino, K., Wagner, H., Takeda, K., et al. (2000). A Toll-like receptor recognizes bacterial DNA. Nature *408*, 740–745. https://doi.org/10.1038/35047123.
4. Tanji, H., Ohto, U., Shibata, T., Taoka, M., Yamauchi, Y., Isobe, T., Miyake, K., and Shimizu, T. (2015). Toll-like receptor 8 senses degradation products of single-stranded RNA. Nat. Struct. Mol. Biol. *22*, 109–115. https://doi.org/10.1038/nsmb.2943.
5. Zhang, Z., Ohto, U., Shibata, T., Krayukhina, E., Taoka, M., Yamauchi, Y., Tanji, H., Isobe, T., Uchiyama, S., Miyake, K., et al. (2016). Structural Analysis Reveals that Toll-like Receptor 7 Is a Dual Receptor for Guanosine and Single-Stranded RNA. Immunity *45*, 737–748. https://doi.org/10.1016/j.immuni.2016.09.011.
6. Zhang, Z., Ohto, U., Shibata, T., Taoka, M., Yamauchi, Y., Sato, R., Shukla, N.M., David, S.A., Isobe, T., Miyake, K., et al. (2018). Structural Analyses of Toll-like Receptor 7 Reveal Detailed RNA Sequence Specificity and Recognition Mechanism of Agonistic Ligands. Cell Rep. *25*, 3371–3381. https://doi.org/10.1016/j.celrep.2018.11.081.
7. Greulich, W., Wagner, M., Gaidt, M.M., Stafford, C., Cheng, Y., Linder, A., Carell, T., and Hornung, V. (2019). TLR8 Is a Sensor of RNase T2 Degradation Products. Cell *179*, 1264–1275. https://doi.org/10.1016/j.cell.2019.11.001.
8. Bérouti, M., Lammens, K., Heiss, M., Hansbauer, L., Bauernfried, S., Stöckl, J., Pinci, F., Piseddu, I., Greulich, W., Wang, M., et al. (2024). Lysosomal endonuclease RNase T2 and PLD exonucleases cooperatively generate RNA ligands for TLR7 activation. Immunity *57*, 1482–1496. https://doi.org/10.1016/j.immuni.2024.04.010.
9. Borchardt, E.K., Martinez, N.M., and Gilbert, W.V. (2020). Regulation and Function of RNA Pseudouridylation in Human Cells. Annu. Rev. Genet. *54*, 309–336. https://doi.org/10.1146/annurev-genet-112618-043830.

10. Karikó, K., Buckstein, M., Ni, H., and Weissman, D. (2005). Suppression of RNA recognition by Toll-like receptors: the impact of nucleoside modification and the evolutionary origin of RNA. Immunity *23*, 165–175. https://doi.org/10.1016/j.immuni.2005.06.008.

11. Weissman, D., Ni, H., Scales, D., Dude, A., Capodici, J., McGibney, K., Abdool, A., Isaacs, S.N., Cannon, G., and Karikó, K. (2000). HIV gag mRNA transfection of dendritic cells (DC) delivers encoded antigen to MHC class I and II molecules, causes DC maturation, and induces a potent human in vitro primary immune response. J. Immunol. *165*, 4710–4717. https://doi.org/10.4049/jimmunol.165.8.4710.

12. Karikó, K., Muramatsu, H., Welsh, F.A., Ludwig, J., Kato, H., Akira, S., and Weissman, D. (2008). Incorporation of pseudouridine into mRNA yields superior nonimmunogenic vector with increased translational capacity and biological stability. Mol. Ther. *16*, 1833–1840. https://doi.org/10.1038/mt.2008.200.

13. Kormann, M.S., Hasenpusch, G., Aneja, M.K., Nica, G., Flemmer, A.W., Herber-Jonat, S., Huppmann, M., Mays, L.E., Illenyi, M., Schams, A., et al. (2011). Expression of therapeutic proteins after delivery of chemically modified mRNA in mice. Nat. Biotechnol. *29*, 154–157. https://doi.org/10.1038/nbt.1733.

14. Anderson, B.R., Muramatsu, H., Nallagatla, S.R., Bevilacqua, P.C., Sansing, L.H., Weissman, D., and Karikó, K. (2010). Incorporation of pseudouridine into mRNA enhances translation by diminishing PKR activation. Nucleic Acids Res. *38*, 5884–5892. https://doi.org/10.1093/nar/gkq347.

15. Anderson, B.R., Muramatsu, H., Jha, B.K., Silverman, R.H., Weissman, D., and Karikó, K. (2011). Nucleoside modifications in RNA limit activation of 2′-5′-oligoadenylate synthetase and increase resistance to cleavage by RNase L. Nucleic Acids Res. *39*, 9329–9338. https://doi.org/10.1093/nar/gkr586.

16. Andries, O., Mc Cafferty, S., De Smedt, S.C., Weiss, R., Sanders, N.N., and Kitada, T. (2015). N(1)-methylpseudouridine-incorporated mRNA outperforms pseudouridine-incorporated mRNA by providing enhanced protein expression and reduced immunogenicity in mammalian cell lines and mice. J. Control. Release *217*, 337–344. https://doi.org/10.1016/j.jconrel.2015.08.051.

17. Cappannini, A., Ray, A., Purta, E., Mukherjee, S., Boccaletto, P., Moafinejad, S.N., Lechner, A., Barchet, C., Klaholz, B.P., Stefaniak, F., et al. (2024). MODOMICS: a database of RNA modifications and related information. 2023 update. Nucleic Acids Res. *52*, D239–D244. https://doi.org/10.1093/nar/gkad1083.

18. Taoka, M., Nobe, Y., Yamaki, Y., Sato, K., Ishikawa, H., Izumikawa, K., Yamauchi, Y., Hirota, K., Nakayama, H., Takahashi, N., et al. (2018). Landscape of the complete RNA chemical modifications in the human 80S ribosome. Nucleic Acids Res. *46*, 9289–9298. https://doi.org/10.1093/nar/gky811.

19. Svitkin, Y.V., Cheng, Y.M., Chakraborty, T., Presnyak, V., John, M., and Sonenberg, N. (2017). N1-methyl-pseudouridine in mRNA enhances translation through eIF2alpha-dependent and independent mechanisms by increasing ribosome density. Nucleic Acids Res. *45*, 6023–6036. https://doi.org/10.1093/nar/gkx135.

20. Mauger, D.M., Cabral, B.J., Presnyak, V., Su, S.V., Reid, D.W., Goodman, B., Link, K., Khatwani, N., Reynders, J., Moore, M.J., et al. (2019). mRNA structure regulates protein expression through changes in functional half-life. Proc. Natl. Acad. Sci. USA *116*, 24075–24083. https://doi.org/10.1073/pnas.1908052116.

21. Fotin-Mleczek, M., Duchardt, K.M., Lorenz, C., Pfeiffer, R., Ojkić-Zrna, S., Probst, J., and Kallen, K.J. (2011). Messenger RNA-based vaccines with dual activity induce balanced TLR-7 dependent adaptive immune responses and provide antitumor activity. J. Immunother. *34*, 1–15. https://doi.org/10.1097/CJI.0b013e3181f7dbe8.

22. Kallen, K.J., Heidenreich, R., Schnee, M., Petsch, B., Schlake, T., Thess, A., Baumhof, P., Scheel, B., Koch, S.D., and Fotin-Mleczek, M. (2013). A novel, disruptive vaccination technology: self-adjuvanted RNActive((R)) vaccines. Hum. Vaccin. Immunother. *9*, 2263–2276. https://doi.org/10.4161/hv.25181.

23. Kranz, L.M., Diken, M., Haas, H., Kreiter, S., Loquai, C., Reuter, K.C., Meng, M., Fritz, D., Vascotto, F., Hefesha, H., et al. (2016). Systemic RNA delivery to dendritic cells exploits antiviral defence for cancer immunotherapy. Nature *534*, 396–401. https://doi.org/10.1038/nature18300.

24. Pollard, C., Rejman, J., De Haes, W., Verrier, B., Van Gulck, E., Naessens, T., De Smedt, S., Bogaert, P., Grooten, J., Vanham, G., et al. (2013). Type I IFN counteracts the induction of antigen-specific immune responses by lipid-based delivery of mRNA vaccines. Mol. Ther. *21*, 251–259. https://doi.org/10.1038/mt.2012.202.

25. Pepini, T., Pulichino, A.M., Carsillo, T., Carlson, A.L., Sari-Sarraf, F., Ramsauer, K., Debasitis, J.C., Maruggi, G., Otten, G.R., Geall, A.J., et al. (2017). Induction of an IFN-Mediated Antiviral Response by a Self-Amplifying RNA Vaccine: Implications for Vaccine Design. J. Immunol. *198*, 4012–4024. https://doi.org/10.4049/jimmunol.1601877.

26. Ostendorf, T., Zillinger, T., Andryka, K., Schlee-Guimaraes, T.M., Schmitz, S., Marx, S., Bayrak, K., Linke, R., Salgert, S., Wegner, J., et al. (2020). Immune Sensing of Synthetic, Bacterial, and Protozoan RNA by Toll-like Receptor 8 Requires Coordinated Processing by RNase T2 and RNase 2. Immunity *52*, 591–605.e6. https://doi.org/10.1016/j.immuni.2020.03.009.

27. Nunes, I.V., Breitenbach, L., Pawusch, S., Eigenbrod, T., Ananth, S., Schad, P., Fackler, O.T., Butter, F., Dalpke, A.H., and Chen, L.S. (2024). Bacterial RNA sensing by TLR8 requires RNase 6 processing and is inhibited by RNA 2′O-methylation. EMBO Rep. *25*, 4674–4692. https://doi.org/10.1038/s44319-024-00281-9.

28. Lu, H., Dietsch, G.N., Matthews, M.A.H., Yang, Y., Ghanekar, S., Inokuma, M., SUni, M., Maino, V.C., Henderson, K.E., Howbert, J.J., et al. (2012). VTX-2337 is a novel TLR8 agonist that activates NK cells and augments ADCC. Clin. Cancer Res. *18*, 499–509. https://doi.org/10.1158/1078-0432.CCR-11-1625.

29. Davis, D.R. (1995). Stabilization of RNA stacking by pseudouridine. Nucleic Acids Res. *23*, 5020–5026. https://doi.org/10.1093/nar/23.24.5020.

30. Chatterjee, S., Kon, E., Sharma, P., and Peer, D. (2024). Endosomal escape: A bottleneck for LNP-mediated therapeutics. Proc. Natl. Acad. Sci. USA *121*, e2307800120. https://doi.org/10.1073/pnas.2307800120.

31. Gomez-Diaz, C., Greulich, W., Wefers, B., Wang, M., Bolsega, S., Effern, M., Varga, D.P., Han, Z., Chen, M., Bérouti, M., et al. (2025). RNase T2 restricts TLR13-mediated autoinflammation in vivo. J. Exp. Med. *222*, e20241424. https://doi.org/10.1084/jem.20241424.

32. Sato, R., Liu, K., Shibata, T., Hoshino, K., Yamaguchi, K., Miyazaki, T., Hiranuma, R., Fukui, R., Motoi, Y., Fukuda-Ohta, Y., et al. (2025). RNase T2 deficiency promotes TLR13-dependent replenishment of tissue-protective Kupffer cells. J. Exp. Med. *222*, e20230647. https://doi.org/10.1084/jem.20230647.

33. Tong, A.J., Leylek, R., Herzner, A.M., Rigas, D., Wichner, S., Blanchette, C., Tahtinen, S., Kemball, C.C., Mellman, I., Haley, B., et al. (2024). Nucleotide modifications enable rational design of TLR7-selective ligands by blocking RNase cleavage. J. Exp. Med. *221*, e20230341. https://doi.org/10.1084/jem.20230341.

34. Islam, M.S., Bandyra, K.J., Chao, Y., Vogel, J., and Luisi, B.F. (2021). Impact of pseudouridylation, substrate fold, and degradosome organization on the endonuclease activity of RNase E. RNA *27*, 1339–1352. https://doi.org/10.1261/rna.078840.121.

35. Nivedita, D., Indrajit, D., Joanna, S., and Ansuman, L. (2023). Structural and thermodynamic consequences of base pairs containing pseudouridine and N1-methylpseudouridine in RNA duplexes. Preprint at bioRxiv. https://doi.org/10.1101/2023.03.19.533340.

36. Carlile, T.M., Martinez, N.M., Schaening, C., Su, A., Bell, T.A., Zinshteyn, B., and Gilbert, W.V. (2019). mRNA structure determines modification by pseudouridine synthase 1. Nat. Chem. Biol. *15*, 966–974. https://doi.org/10.1038/s41589-019-0353-z.

37. Carlile, T.M., Rojas-Duran, M.F., Zinshteyn, B., Shin, H., Bartoli, K.M., and Gilbert, W.V. (2014). Pseudouridine profiling reveals regulated mRNA pseudouridylation in yeast and human cells. Nature *515*, 143–146. https://doi.org/10.1038/nature13802.

Please cite this article in press as: Bérouti et al., Pseudouridine RNA avoids immune detection through impaired endolysosomal processing and TLR engagement, Cell (2025), https://doi.org/10.1016/j.cell.2025.05.032

38. Rapino, F., Robles, E.F., Richter-Larrea, J.A., Kallin, E.M., Martinez-Climent, J.A., and Graf, T. (2013). C/EBPalpha induces highly efficient macrophage transdifferentiation of B lymphoma and leukemia cell lines and impairs their tumorigenicity. Cell Rep. *3*, 1153–1163. https://doi.org/10.1016/j.celrep.2013.03.003.

39. Maeda, T., Murata, K., Fukushima, T., Sugahara, K., Tsuruda, K., Anami, M., Onimaru, Y., Tsukasaki, K., Tomonaga, M., Moriuchi, R., et al. (2005). A novel plasmacytoid dendritic cell line, CAL-1, established from a patient with blastic natural killer cell lymphoma. Int. J. Hematol. *81*, 148–154. https://doi.org/10.1532/ijh97.04116.

40. Schmid-Burgk, J.L., Schmidt, T., Gaidt, M.M., Pelka, K., Latz, E., Ebert, T. S., and Hornung, V. (2014). OutKnocker: a web tool for rapid and simple genotyping of designer nuclease edited cell lines. Genome Res. *24*, 1719–1723. https://doi.org/10.1101/gr.176701.114.

41. Baiersdörfer, M., Boros, G., Muramatsu, H., Mahiny, A., Vlatkovic, I., Sahin, U., and Karikó, K. (2019). A Facile Method for the Removal of dsRNA Contaminant from In Vitro-Transcribed mRNA. Mol. Ther. Nucleic Acids *15*, 26–35. https://doi.org/10.1016/j.omtn.2019.02.018.

42. Li, X.D., and Chen, Z.J. (2012). Sequence specific detection of bacterial 23S ribosomal RNA by TLR13. eLife *1*, e00102. https://doi.org/10.7554/eLife.00102.

Please cite this article in press as: Bérouti et al., Pseudouridine RNA avoids immune detection through impaired endolysosomal processing and TLR engagement, Cell (2025), https://doi.org/10.1016/j.cell.2025.05.032

CellPress
OPEN ACCESS

STAR★METHODS

KEY RESOURCES TABLE

REAGENT or RESOURCE	SOURCE	IDENTIFIER
Antibodies		
Anti dsRNA Antibody, clone rJ2	Sigma-Aldrich	Cat# MABE1134-25UL; RRID: AB_2819101
Anti mouse IgG, HRP linked antibody	Cell Signaling Technology	Cat# #7076; RRID: AB_330924
Chemicals, peptides, and recombinant proteins		
Acetonitrile	Carl Roth	Cat# HN40.1
Advanced RPMI 1640 medium	Gibco	Cat# 12633020
Ammonium persulfate	Sigma-Aldrich	Cat# A3678
BioColl	Bio&Sell	Cat# BS.L 6115
Blasticidin	Thermo Scientific	Cat# A1113903
CaptureSelect™ C-tagXL Affinity Matrix	Thermo Scientific	Cat# 2943072010
CD14 MircroBeads Human	Miltenyi	Cat# 130-050-201
Cellulose fibers	Merck	Cat#C6288-100G
Coomassie Brilliant Blue R-250 Dye	Thermo Scientific	Cat# 20278
CU-CPT9a	Invivogen	Cat# inh-cc9a
Express Five® SFM (1x)	Gibco	Cat# 10486025
Fetal calf serum	Gibco	Cat# 10270106
FuGene® Transfection Reagent	Promega	Cat# E2691
GlutaMAX	Gibco	Cat# 10270106
HEPES	Sigma-Aldrich	Cat# H0887-100ml
vivo-jetRNA®	VWR	Cat#76579-662
LPS-EB Ultrapure	InvivoGen	Cat#tlrl-3pelps
MEM NEAA	Gibco	Cat# 11140035
M5049	Invivogen	Cat# inh-m5049
N1-Methylpseudouridine	Sigma-Aldrich	Cat# SMB01360
N1-Methylpseudo UTP	Jena Bioscience	Cat#NU-890S
Opti-MEMTM	Gibco	Cat# 31985047
Penicillin/Streptomycin	Gibco	Cat# 15-140-122
Poly-L-arginine	Sigma-Aldrich	Cat#P7762
Pseudouridine	Sigma-Aldrich	Cat# SMB00912
Pseudo-UTP solution 100 mM	Jena Bioscience	Cat#NU-1139S
Recombinant Human IL-3	MPI of Biochemistry, Munich	N/A
Recombinant Human CSF1 (M-CSF)	MPI of Biochemistry, Munich	N/A
Recombinant Human RNase 1	MPI of Biochemistry, Munich	N/A
Recombinant Human RNase 2	MPI of Biochemistry, Munich	N/A
Recombinant Human RNase 6	MPI of Biochemistry, Munich	N/A
Recombinant Human TLR8 (AA27-827)	This study	N/A
RBC lysis Buffer	BioLegend	Cat# 420301
RPMI 1640 medium	Gibco	Cat# 11875093
R848	InvivoGen	Cat# tlrl-r848
SequaGel Concentrate	National diagnostics	Cat#EC830-1l
SequaGel Buffer	National diagnostics	Cat# EC835-200ml
SequaGel Diluent	National diagnostics	Cat# EC840-1l
Sf-900TM III SFM	Gibco	Cat# 12658019
Sodium pyruvate	Gibco	Cat# 11360039
SYBR Gold Nucleic Acid Gel Stain	Thermo Fisher Scientifc	Cat# S33102

(*Continued on next page*)

Please cite this article in press as: Bérouti et al., Pseudouridine RNA avoids immune detection through impaired endolysosomal processing and TLR engagement, Cell (2025), https://doi.org/10.1016/j.cell.2025.05.032

Continued

REAGENT or RESOURCE	SOURCE	IDENTIFIER
TEMED	Carl Roth	Cat# 2367.3
TL8-506	InvivoGen	Cat# tlrl-tl8506
TRIS glycine SDS-PAGE	Thermo Scientific	Cat# XP00125BOX
Uridine	Sigma-Aldrich	Cat# U3750
β-Estradiol	Sigma-Aldrich	Cat#E8875
2x RNA loading dye	Thermo Fisher Scientific	Cat# R0641
5-Propargylamino-CTP-PEG5-AZDye488	Jena Bioscience	Cat# NU-831-PEG5-AZ488
6x DNA loading dye	Thermo Fisher Scienctific	Cat#R1161
2′,3′-cGMP	BIOLOG	Cat# G 025-250
Critical commercial assays		
Ampliscribe-T7-flash-transcription kit	Lucigen	Cat# ASF3507
Faustovirus Capping Enzyme	New England Biolabs	Cat# M2081I
E. coli Poly(A) Polymerase	New England Biolabs	Cat# M0276I
Human IFN-β ELISA Set	R&D System	Cat# DY814-05
Human IFN-α2 ELISA Set	R&D System	Cat# DY9345-05
Human IL-6 ELISA Set	BD Biosciences	Cat# 555220
Human TNF ELISA Set	BD Biosciences	Cat# 555212
Human IP10 ELISA Set	BD Biosciences	Cat# 550926
BCA protein assay Kit	Thermo Fisher Scientific	Cat# 23227
Mouse IFN-alpha ELISA Kit	R&D Systems	Cat# 42120-1
CD34 MicroBead Kit UltraPure, human	Miltenyi	Cat# 130-100-453
Monarch RNA Cleanup Kit	New England Biolabs	Cat# T2050I
Experimental models: Cell lines		
BLaER1 human B-cell to monocyte trans-differentiation cell line	Rapino et al[3,8]	N/A
CAL-1	Maeda et al.[39]	N/A
SF21	Thermo Fisher Scientific	Cat#12682019
High Five™ Cells in Express Five™ Medium	Thermo Scientific	Cat# B85502
Oligonucleotides		
RNA40^{S}(rG*rC*rC*rC*rG*rU*rC*rU*rG* rU*rU*rG*rU*rG*rU*rG*rA*rC*rU*rC)	Miltenyi	130-104-429
RNA40^{O}(rGrCrCrCrGrUrCrUrGr UrUrGrUrGrUrGrArCrUrC)	IDT	N/A
RNA40i(rArCrCrCrArUrCrUrArUrUr ArUrArUrArGrCrUrC)	IDT	N/A
RNA9.2s(rArGrCrUrUrArArCrCrUrGr UrCrCrUrUrCrArA)	IDT	N/A
rArGrCrUrUrArArCrCrUrGrm UrCrCrUrUrCrArA	IDT	N/A
rArGrCrUrUrArArCrCrUrGrΨrCr CrUrUrCrArA	This study	N/A
rArGrCrΨrΨrArArCrCrΨrGrΨr CrCrUrUrCrArA	This study	N/A
rCrCrUrUrCrA(dAdC)$_7$	This study	N/A
rCrCrΨrΨrCrA(dAdC)$_7$	This study	N/A
(dAdC)$_7$rUrUrGrUrCrU	Ella Biotech	N/A
(dAdC)$_7$rUrUrGrmUrCrU	Ella Biotech	N/A
(dAdC)$_7$rUrUrGrUrmCrU	Ella Biotech	N/A
(dAdC)$_7$rUrUrGrΨrCrU	Ella Biotech	N/A

(*Continued on next page*)

Please cite this article in press as: Bérouti et al., Pseudouridine RNA avoids immune detection through impaired endolysosomal processing and TLR engagement, Cell (2025), https://doi.org/10.1016/j.cell.2025.05.032

Continued

REAGENT or RESOURCE	SOURCE	IDENTIFIER
(dAdC)$_7$rUrUrGrm^{1}ΨrCrU	Ella Biotech	N/A
rΨrΨrΨrArGrC	This study	N/A
rUrUrUrArGrC	This study	N/A
rUrUrUrArGrCrUrUrArAr CrCrUrGrUrCrCrUrU	IDT	N/A
rΨrΨrΨrArGrCrUrUrAr ArCrCrUrGrUrCrCrUrU	This study	N/A
m^{1}Ψm^{1}Ψm^{1}ΨrArGrCrUr UrArArCrCrUrGrUrCrCrUrU	This study	N/A
(dAdC)$_7$rGrArGrUrArGrA	IDT	N/A
(dAdC)$_7$rGrArGrΨrArGrA	This study	N/A
rUrUrUrArGrCrUrUrAr ArCrCrUrGrUrCrCrUrU-FAM	Biomers	N/A
rΨrΨrΨrArGrCrUrUrArArCrCrUrGrUrCrCrUrU-FAM	Biomers	N/A
CpG O (TCGTCGTTTTGTCGTTTTGTCGTT	IDT	N/A
Recombinant DNA		
pACEBac1_IgK_hsTLR8(AA27-827)_EPEA	This study	N/A
Software and algorithms		
GraphPad Prism10	GraphPad	N/A
Outknocker	Schmid-Burgk et al.[40]	N/A
AcquireMP	Refeyn	N/A
FlowJo	BD Biosciences	N/A
Other		
Ultrafiltration spin columns, 0.45 μm cutoff	Merck	Cat# 20-218

METHOD DETAILS

Cell culture

BLaER1, THP-1, primary PBMCs, CD14$^+$ and pDCs were cultured in RPMI 1640 medium supplemented with 10% heat-inactivated fetal calf serum (FCS), 100 U/ml penicillin/streptomycin (PS), and 1 mM sodium pyruvate. CAL-1 cells were cultured in RPMI 1640 medium supplemented with 10% heat-inactivated fetal calf serum, 100 U/ ml penicillin/streptomycin (PS), 1 mM sodium pyruvate, 2x GlutaMAX, 10 mM HEPES and 1x MEM NEAA. The cells were maintained in a 37°C humidified incubator with a 5% CO_2 atmosphere. To induce the transformation of BLaER1 monocytes into macrophages, a cytokine cocktail - M-CSF (10 ng/ml), IL-3 (10 ng/ml) and 100 nM β-estradiol - was added to the culture for a period of 5 days. THP-1 cells were differentiated with PMA (100 ng/ml) for 16 h and rested for 2 days prior to stimulation. The differentiation process for both cell lines was carried out in a 96-well plate, with each well containing 80,000 cells. Afterwards, cells were used for various stimulation experiments.

SF21 insect cells were cultured in Sf-900™ III SFM (1x) medium supplemented with 100 U/ml penicillin/streptomycin (PS) and High5 insect cells were cultured in Express Five SFM (1x) medium supplemented with L-Glutamine (18 mM) and 100 U/ml penicillin/streptomycin (PS). Both cell lines were maintained in a shaking incubator (95 rpm) without CO_2.

Isolation of PBMCs, primary human monocytes and primary human pDCs

As previously described, peripheral blood mononuclear cells (PBMCs) were isolated from the leukocyte reduction system chambers left over from platelet donation from healthy donors. Approval from the relevant ethics committee and informed consent from all donors according to the Declaration of Helsinki were obtained (project number: 19-238, Ethics Committee of the Medical Faculty of Ludwig-Maximilians-University Munich). PBMCs were isolated using BioColl and erythrocyte lysis (RBC lysis buffer). Human monocytes purified by MACS from PBMCs using CD14 microbeads and human primary pDCs were MACS purified from PBMCs using CD304 microbeads.

Cell stimulation

CAL-1 cells (100,000 cells/well) and THP-1 cells were primed with IFN-γ (10 ng/ml) for 6 hours prior to stimulation. BLaER1 cells were stimulated after trans-differentiation and primary human PBMCs (400,000 cells/well), CD14$^+$ monocytes (100,000 cells/well) and pDCs (20,000 cells/well) were rested for 4 hours after isolation prior to stimulation. Primary pDCs were additionally treated with

Please cite this article in press as: Bérouti et al., Pseudouridine RNA avoids immune detection through impaired endolysosomal processing and TLR engagement, Cell (2025), https://doi.org/10.1016/j.cell.2025.05.032

IL-3 (10 ng/ml). For transfection with RNA40^{S} (0.6 μg/well), RNA40^{O} (1.2 μg/well), RNA9.2s and modified version of RNA9.2s (1.2 μg/well), short ORNs ((dAdC)$_7$UUGUCU, (dAdC)$_7$UUGmUCU, (dAdC)$_7$UUGUmCU, (dAdC)$_7$UUGΨCU, (dAdC)$_7$UUGm^{1}ΨCU, CCUUCA(dAdC)$_7$ and CCΨΨCA(dAdC)$_7$) (2.4 μg/well) and indicated Cas9 IVT (each 1.2 μg/well) or OVA IVT (each 0.6 μg/well) constructs, RNA and poly-L-arginine were incubated separately in a 1:1 ratio for 5 minutes in pre-warmed Opti-MEM (25 μl/well). After combining, the two reagents were incubated for additional 20 minutes before being added to the cells. To stimulate primary pDCs with OVA-IVT constructs using Lipofectamine instead of poly-L-arginine as transfection reagent, Lipofectamine2000 (0.5 μl/well) and OVA-IVTs (each 0.6 μg/well) were mixed and incubated in pre-warmed Opti-MEM (50 μl/well) for 20 min and afterwards added to the cells. For RNA transfections in the presence of the TLR specific inhibitors, CU-CPTa (final concentration: 10 μM) or M5049 (final concentration: 1 μM) was added to the cells 30 min prior to stimulation. Furthermore, cells were stimulated with 200 ng/ml LPS-EB ultrapure (Lipopolysaccharide from Escherichia coli 0111:B4), 0.5 mM 2′,3′-cGMP, 5 μM CpG^{O} and indicated concentrations of uridine, pseudourdine (Ψ), N1-methylpseudouridine (m^{1}Ψ) and 2′-O-methyluridine (Um). To calculate EC$_{50}$ values (Figure 5B), BLaER1 monocytes were stimulated with the different nucleosides at concentrations ranging from 64 mM to 4 mM. Supernatants of CD14$^+$ monocytes were harvested after 24 hours of stimulation at 37 °C, the supernatants of BLaER1 cells were harvested after 14 hours and the supernatants of CAL-1 cells were harvested after 16 hours.

Baculovirus production

A codon optimized version of the Igκ leader sequence fused to the ectodomain of human TLR8 encompassing AA27-827 was obtained from Max Planck Institute (Munich) and cloned into pACEBac1 vector for bacmid preparation. Production of TLR8 baculovirus was conducted in SF21 insect cells. For transfection, 200 μl SF21 medium, 3 μl FuGene® and 2 μg of bacmid were combined and incubated for 45 min at room temperature. Next, the transfection mix was added dropwise to SF21 cells (0.4x10^6 cells/2 ml) and incubated at 27 °C. After three days, the supernatant (P0) was harvested, added to a cell suspension of SF21 cells (1x10^6 cells/ml, 10 ml in total) and shaken for three days at 27 °C at 95 rpm. Subsequently, the virus containing supernatant (P1) was collected and filtered. Next, P1 virus (0.5 ml) was added to 50 ml of SF21 suspension cells (0.4x10^6 cells/ml), which were shaken (95 rpm) for 3 days at 27 °C. The supernatant (P2) was collected, filtered and stored at 4°C.

Protein expression and purification

Expression of recombinant TLR8 ectodomain was induced for three days by adding P2 baculovirus (Dilution of virus: 1:200) to High5 cells (1x10^6 cells/m). Subsequently, the supernatant containing secreted TLR8 ectodomain was harvested and filtered. EPEA agarose beads were added to the supernatant and rotated for 2 hours at 4°C. The beads were washed three times with wash buffer (20 mM Tris pH=7.5, 150 mM NaCl) and the protein was eluted (20 mM Tris pH=7.5, 150 mM NaCl, 2M $MgCl_2$). Eluted TLR8 was dialyzed overnight (50 mM $NaHPO_4$, 100 mM NaCl pH=5.0) and concentrated to 10 μM. TLR8 was stored at 4°C prior to mass photometry measurements.

Coomassie staining of hsTLR8 (AA27-827)

To assess the purity of recombinant hsTLR8 (AA27-827), the protein was separated on a 12% TRIS glycine SDS-PAGE. The gel was subsequently stained with Coomassie (45% Ethanol, 10% acetic acid and 1g/L Coomassie Brilliant Blue R-250 Dye in milliQ water) for 1 hour at room temperature and destained again (20% Ethanol, 10% acetic acid in milliQ water) overnight.

Mass photometry

Mass photometric assays for hsTLR8 (AA27-827) ectodomain dimerization were performed using a Refeyn TwoMP mass photometer. Prior to each measurement, hsTLR8 (AA27-827) (10 μM) was incubated with indicated concentrations of uridine, pseudouridine, N1-methylpseudouridine or 2′-O-methyluridine or in combination with ssRNA40 (30 μM) for 10 min at room temperature. Prior to each measurement, the different samples were diluted to a final concentration of 50 nM hsTLR8 (AA27-827) in sterile filtered mass photometry buffer (50 mM $NaHPO_4$, 100 mM NaCl, pH=5.0). The measurements were recorded as 60-second movies and the resulting data were processed using AcquireMP software. All incubations and measurements were performed in triplicates, except for the incubation of single nucleosides in combination with ssRNA40 (Figure 5F, lower panel), which was performed in duplicates.

RNase assays

Unless otherwise stated, 100 ng of RNA was treated with indicated amounts of enzyme in assay buffer (50 mM NaAc, 100 mM NaCl, pH=4.5) or in IDTE buffer (10 mM Tris, 0.1 mM EDTA, pH=8) for 20 minutes at 37°C. Subsequently, 2x RNA loading dye was added to the mixture, which was then heated at 95°C for 5 additional minutes. The resulting fragments were separated and detected on a urea gel. For agarose gels, 1 μg of different Cas9 IVT constructs were incubated with indicated amounts of RNase T2 for 20 min at 37 °C. Afterwards 6x DNA loading dye was added, and 0.5 μg of RNA was loaded onto the agarose gel.

ELISA

hIL-6, hTNF, hIP-10, hIFNα2, hIFNβ and mIFNα ELISAs were conducted according to supplier's protocol. For TLR7 and TLR8 stimulation assays, we primarily used IFNα or IFNβ as readouts for TLR7 activation in plasmacytoid cell models and IL-6 for TLR8 activation in myeloid cells. These cytokines were selected as proximal indicators of pathway activation and have been shown to be robust readouts based on extensive prior experience.

Please cite this article in press as: Bérouti et al., Pseudouridine RNA avoids immune detection through impaired endolysosomal processing and TLR engagement, Cell (2025), https://doi.org/10.1016/j.cell.2025.05.032

Urea and agarose gels

Urea gels were prepared according to the manufacturer's instructions using SequaGel Concentrate, SequaGel Diluent, and SequaGel buffer. The gels were first run at 150 V for 10 minutes, followed by a 60-minute run at 250 V in 1x TBE buffer (containing 100 mM Tris, 100 mM boric acid, and 2 mM EDTA). The gels were then stained with SYBR Gold Nucleic Acid Gel Stain for 5 minutes, followed by imaging. 1% agarose gels were run for 40 min at 120 V prior to imaging.

Affinity measurement by fluorescence anisotropy

The Fluorescence anisotropy assay was carried out in a black 384-well flat-bottom plate with a total reaction volume of 50 μl. 3′-FAM-labeled substrates (10 nM) were incubated for 20 minutes at room temperature with increasing concentrations of PLD3(H201N, H416N) in assay buffer (50 mM sodium acetate, 100 mM NaCl, pH 4.5). After incubation, the change in anisotropy was measured at an excitation wavelength of 490 nm and an emission wavelength of 520 nm using an automated polarization microscope. Data was analyzed by fitting to a one site-specific binding model.

In vitro transcription

In vitro transcription of a ~2,500 bp Cas9 amplicon (forward primer: GACAAGAAGTACAGCAT-CGGCCTGG; reverse primer: CCACCCGAAATTAATACGACTCACTATAGGGAGACCAC-AACTGCAGGTAGTACAGGTACAGCTTC) was conducted according to supplier's protocol (Lucigen, #ASF3507), followed by DNase I treatment to remove the DNA template from the IVT. For IVT Ψ, IVT $m^1\Psi$, Pseudo-UTP and N^1-Methylpseudo-UTP was added to the reaction mix instead of UTP. For the fluorescently labeled IVT, the reaction mix contained 2.5 mM ATP, GTP, and UTP, along with 0.2 mM CTP and 0.1 mM 5-Propargylamino-CTP-PEG5-AZDye488. The fluorescently labeled RNA was purified using the Monarch RNA Cleanup Kit after DNase I treatment.

Sodium acetate precipitation of Cas9 IVT constructs

After IVT, glycogen (final concentration: 0.5 mg/ml), 3 M sodium acetate (1:10 volume) and 100% ethanol (4 volumes) were added to the nucleic acid solution. The reaction was mixed thoroughly after each addition of the three components and incubated for 16 hours at –20 °C. The precipitated RNA was centrifuged for 30 min at 4000 rpm at 4 °C. Subsequently, the supernatant was carefully discarded, and the pellet was washed twice by adding 500 μl of 80% cold ethanol. Lastly, the pellet was air dried and resuspended in water to a final concentration of 1 μg/μl. Prior to use it was confirmed that the RNA is fully intact by an agarose gel.

Purification of IVT mRNA using cellulose

To remove dsRNA contaminants from OVA-IVT RNAs, OVA-IVTs were purified by cellulose chromatography as previously described.[41] In brief, cellulose fibers were initially resuspended in RNase-free chromatography buffer (10 mM HEPES, pH 7.2, 0.1 mM EDTA, 125 mM NaCl, and 16% (v/v) ethanol) to a final concentration of 0.2 g/ml. Next, 700 μl of cellulose slurry was transferred to an ultrafiltration spin-column (0.45 μm cutoff) and centrifuged for 1 min at 14,000 x g. The flowthrough was discarded, the cellulose washed with 500 μl of chromatography buffer and centrifuged again for 1 min at 14,000 x g. Next, 200 μg of OVA-IVT RNA in 500 μl chromatography buffer was added to the washed cellulose into the spin column. The column was rotated on a spinning wheel for 30 min at room temperature and afterwards centrifuged for 1 min at 14,000 x g. The flowthrough, containing the purified RNA, was collected, and subjected to two more rounds of cellulose purification.

Finally, the RNA was precipitated by adding 50 μl of 3 M NaOAc (pH 5.5) and 500 μl of isopropanol and subsequent centrifugation at 16,000 x g for 2 hours at 4 °C. The recovered purified RNA was resuspended in nuclease free water. The removal of dsRNA contaminations was confirmed by RNA dot blot using an anti-dsRNA antibody.

Capping and Tailing of IVT mRNA

An m^7G cap (Cap-0) structure was added to the purified OVA IVT RNAs using the Faustovirus capping enzyme, following the supplier's protocol (NEB #M2081). Subsequently, IVTs were poly(A)-tailed using E. coli Poly(A) Polymerase, also following the supplier's protocol (NEB# M0276). RNA was purified after each step using the Monarch RNA Cleanup Kit.

Cellular RNA uptake assay

To determine the uptake of RNA upon transfection, GFP-negative BLaER1 monocyte-derived macrophages (80,000 cells/well) were stimulated with AZDye488-labeled RNAs (1.2 μg/well) using poly-L-arginine as a transfection reagent as described above. At 2 h post transfection, cells were detached and resuspended in FACS buffer (PBS+2% FCS). Subsequently, AZDye488-positive cells were analyzed using a BD FACS Melody™ flow cytometer. Data was analyzed using FlowJo software (BD Biosciences).

Mouse lines

Mice in this study were housed under specific pathogen-free (SPF) conditions at 21 ± 1°C, with a 12-hour light/dark cycle and an average humidity of 55%. Breeding and maintenance followed the regulations of the animal welfare authorities of the government of Upper Bavaria (application number: 55.2-2532.Vet_02-21-97). The mouse lines used were previously established, including $Tlr13^{-/-}$[42] and $Rnaset2^{-/-}$.[31] Experimental mice were between 40 and 80 weeks old.

Please cite this article in press as: Bérouti et al., Pseudouridine RNA avoids immune detection through impaired endolysosomal processing and TLR engagement, Cell (2025), https://doi.org/10.1016/j.cell.2025.05.032

In vivo injection of mRNA

OVA-mRNA for in vivo injections was complexed using in vivo-jet PEI® according to the manufacturer's protocol. Mice were then intravenously injected with 10 μg of mRNA per mouse. As a negative control, PBS was injected. Tlr13$^{-/-}$ mice that received PBS injections (Figure 6L) were later injected with U-IVT following a 7-day washout period. Six hours post-injection, blood was collected and left at room temperature for 45 to 60 minutes to allow natural clotting. The samples were then centrifuged at 1,000 × g for 10 minutes, and the serum was transferred to a clean tube for PAN-IFNα analysis via ELISA. All animal experiments were approved by the local regulatory agency (Regierung von Oberbayern, #55.2-2532-02-20-109).

RNase assays for LC-MS

RNA (1 μg) was digested with indicated concentrations of RNase T2 or RNase 1 for 20 min at 37°C in IDTE buffer (10 mM Tris, 0.1 mM EDTA, pH=8.0).

RNA isolation

All RNA isolation steps were performed at room temperature. Enzyme reactions (vol. of reaction mixture < 350 μl) were quenched by addition of 350 μl *Roti-Phenol* (phenol / chloroform / isoamyl alcohol; 25/24/1; *Roth*). milliQ water was added until a total sample volume of 700 μl was reached (aqueous phase / *Roti-Phenol*; 1/1; v/v). After vigorous vortexing (2 min) and centrifugation (10,000 x g; 1 min), the upper, aqueous phase was transferred to a new tube. 350 μl of milliQ water were added to the phenol/chloroform phase, again followed by vortexing (2 min) and centrifugation (10,000 x g; 1 min). The aqueous phases were combined, and 700 μl of chloroform were added (H_2O / chloroform; 1/1; v/v). The samples were vortexed (2 min), centrifuged (10,000 x g; 1 min), and the upper, aqueous layer was transferred to a new tube. This chloroform extraction step was repeated two more times. The resulting, clean aqueous phase was lyophilized overnight (*Alpha 2-4 LSCbasic, Christ*). The remaining residue was re-dissolved in 200 μl of milliQ water and again lyophilized overnight. Samples were then re-dissolved in 100 μl of milliQ water and stored at -78 °C until submission to LC-MS analysis (see below).

Liquid chromatography – mass spectrometry (LC-MS): general procedure

All samples were filtrated before measurement using an AcroPrep Advance 96 filter plate 0.2 μm Supor from Pall Life Sciences and were kept on ice during handling. HPLC-HESI-MS analyses were performed on a Dionex Ultimate 3000 HPLC system coupled to a Thermo Fisher LTQ Orbitrap XL mass spectrometer. Compounds of interest (injection volume: 85 μl) were separated with an Interchim Uptisphere120-3HDO C18 column whose temperature was maintained at 30 °C. Elution buffers were buffer X (2 mM NH_4HCOO in H_2O; pH 5.5) and buffer Y (2 mM NH_4HCOO in H_2O/MeCN 20/80 v/v; pH 5.5). Different and optimized HPLC gradients and flow rates were used for experiments involving 20mer RNA digests, 2,500 bp RNA digests, or chimeric DNA-RNA species (see below). Chromatograms were recorded at 260 nm with a Dionex Ultimate 3000 Diode Array Detector with a data collection rate of 20 Hz and a response time 0.10 s. The chromatographic eluent was directly injected into the ion source of the mass spectrometer without prior splitting. Ions were scanned in the positive polarity mode over a full-scan range of m/z = 225-2000 with a resolution of 100,000. Parameters of the mass spectrometer were tuned with a freshly mixed solution of inosine (5 μM) in buffer X. Source-dependent parameters were set as follows: Capillary temperature 275 °C; APCI vaporizer temperature 100 °C; sheath gas flow 5.00; auxiliary gas flow 21.0; sweep gas flow 1.00; source voltage 4.80 kV; capillary voltage 0 V; tube lens voltage 45.00 V. Data analysis was performed using the program Xcalibur from Thermo Scientific: Ion chromatograms of the compounds of interest were extracted from the total ion current (TIC) chromatogram with a mass range set to +/- 0.0100 u (Δm<3ppm) around m/z = [M+nH]/n (z =n; corresponding to the fragment $[M+nH]^{n+}$) of the compound's most abundant isotopologue (the isotopologue distribution of a compound was calculated with ChemDraw).

LC-MS analysis of RNA40/RNA40i/RNA9.2s and their cleavage products

This section outlines the LC-MS analysis methods used to generate the data shown in Figure 1. In this case, the HPLC gradient was as follows: 0→3 min, 0 % Y, 150 μl/min; 3→4 min, 0→0.1 % Y, 150 μl/min; 4→8 min, 0.1 % Y, 150 μl/min; 8→63 min, 0.1→6 % Y, 150 μl/min; 63→73 min, 6→15 % Y, 150 μl/min; 73→80 min, 15→75 % Y, 150→200 μl/min; 80→88 min, 75 % Y, 200 μl/min.

Two obstacles had to be overcome to identify and quantify the fragments: First, all isomers of a given base composition have the same mass. Second, although an optimized HPLC gradient was used, some fragments have similar retention times, so their UV absorption peaks overlap. Nevertheless, to identify and quantify all fragments, we first identified fragments with unique nucleotide composition (and mass) and with non-overlapping UV absorption peaks. Each of these fragments was quantified by integrating its UV absorption peak and dividing this value by its extinction coefficient (the extinction coefficients themselves were calculated using IDT's OligoAnalyzer). The value thus obtained is directly proportional to the absolute amount of the fragment in the sample. In addition, the total base compositions (but not the sequence) of all other fragments present were identified via their mass, and non-overlapping UV absorption peaks were integrated. The identity/sequence and the absolute amounts of all fragments present were then determined by applying the following logical principles: For any given cleavage site, the total amount of fragments with a 3′-end at this position must equal the total amount of fragments possessing the matching 5′-end. Furthermore, for each of the 20 nucleotide positions of the reactant strand, the total amount of all fragments containing a given nucleotide must add up to the same value (this value is the total amount/fraction of educt oligomer processed by RNase T2 or RNase 1, respectively). The same value should be obtained

Please cite this article in press as: Bérouti et al., Pseudouridine RNA avoids immune detection through impaired endolysosomal processing and TLR engagement, Cell (2025), https://doi.org/10.1016/j.cell.2025.05.032

at any cleavage site when adding up the amounts of fragments bearing a 3′-end (or a 5′-end, respectively) at this position and the amounts of all fragments not being cleaved at this site but instead containing both nucleotides of the cleavage site. Following these rules, all fragments present in the samples could unequivocally be identified, and their absolute amounts could be determined. The cleavage percentage at a given site was then calculated by dividing the total amount of fragments with a 3′-end at this position (or a 5′-end, respectively) by the total amount of educt oligomer processed by RNase T2 or RNase 1, respectively (i.e. sum of all 3′ fragments ending at a particular cleavage site divided by the sum of these 3′ fragments and of the fragments covering this cleavage site).

LC-MS analysis of a 2,500 nt RNA digested either by RNase T2 or RNase 1

This section outlines the LC-MS analysis methods used to generate the data shown in Figure 2. In this case, the HPLC gradient was as follows: 0→3 min, 0 % Y, 150→100 µl/min; 3→4 min, 0→0.1 % Y, 100 µl/min; 4→8 min, 0.1 % Y, 100 µl/min; 8→63 min, 0.1→6 % Y, 100 µl/min; 63→73 min, 6→15 % Y, 100 µl/min; 73→80 min, 15→75 % Y, 100→150 µl/min; 80→88 min, 75 % Y, 150→200 µl/min.

In these experiments, a plethora of cleavage products with similar retention times were generated. Since their UV-peaks were overlapping in most cases, an UV-based absolute quantification of fragments was not possible. We therefore decided to go for relative quantification. For di- and trimer identification, we designed 9 different RNA 5mers (UGUUU; UAUUU; UUGUU; GUCCC; AUCCC; UCGUU; UCAUU; UAGUU; UGAUU) and subjected them to digestion either by RNase T2 or RNase 1. The resulting cleavage products were dimers and trimers of a defined sequence (and mass). These were analyzed by LC-MS using the same HPLC gradient as for the 2,500 bp RNA analysis. This way, we obtained a data set correlating particular 2/3mer sequences (and masses) with their HPLC retention time. Based on this data set, the ratios of 16 dimers and 12 trimers in the samples (RNase T2 vs. RNase 1) were determined. Incidentally, in most cases, fragments of interest were either only present in the RNase T2 digest sample or in the RNase 1 digest sample. The resulting fragment ratio of 1:0 is the same as it would be based on absolute fragment amounts.

LC-MS analysis of chimeric DNA/RNA probes and their cleavage products

This section outlines the LC-MS analysis methods used to generate the data shown in Figure 3. In this case, the HPLC gradient was as follows: 0→3 min, 0 % Y, 150 µl/min; 3→4 min, 0→0.1 % Y, 150 µl/min; 4→8 min, 0.1 % Y, 150 µl/min; 8→53 min, 0.1→5 % Y, 150 µl/min; 53→70 min, 5→15 % Y, 150 µl/min; 70→73 min, 15→100 % Y, 150→200 µl/min; 73→77 min, 100 % Y, 200 µl/min. Identity /sequence of fragments and their absolute amounts were determined as in the case of the RNA40/RNA40i/RNA9.2s samples (see above). Here, and in contrast to the calculations done for RNA40/RNA40i/RNA9.2s, cleavage percentages were calculated considering the amount of non-processed chimeric educt oligomer, too: The cleavage percentage at a given site was calculated by dividing the total amount of fragments with a 3′-end at this position (or a 5′-end, respectively) by the sum of the total amount of educt oligomer processed by RNase T2 (or RNase 1, respectively) AND the amount of remaining/non-cleaved educt oligomer (otherwise, when calculated as for RNA40/RNA40i/RNA9.2s, a minimal cleaving at a single position would lead to a calculated cutting percentage of 100 %).

LC-MS/QQQ analysis of nucleoside-monophosphates)

This section outlines the LC-MS analysis methods used to generate the data shown in Figures 6D, 6F, and 6H. The preparation for LC-MS analysis to measure 2′,3′-cGMP *in vitro* released by PLD3 and RNase T2 and the subsequent analysis of the nucleoside-monophosphate by LC-MS/QQQ was conducted as previously described.[8]

Synthesis and purification of oligonucleotides

Phosphoramidites of canonical ribonucleosides (Bz-A-CE, Dmf-G-CE, Ac-C-CE and U-CE) were purchased from LinkTech and Sigma-Aldrich. Phosphoramidites of Ψ and $m^1Ψ$ were synthesized respectively. Oligonucleotides were synthesized on a 1 µmol scale using High Load Glen UnySupport™ as solid supports for strands employing an RNA automated synthesizer (Applied Biosystems 394 DNA/RNA Synthesizer) utilizing standard phosphoramidite chemistry. ONs were synthesized in DMT-OFF mode using DCA as a deblocking agent in CH_2Cl_2, BTT or Activator 42® as activator in MeCN, Ac_2O as capping reagent in pyridine/THF and I_2 as oxidizer in pyridine/H_2O.

The solid support beads were suspended in a 1:1 aqueous solution mixture (0.6 ml) of 30% NH_4OH and 40% $MeNH_2$. The suspension was heated at 65 °C for 60 min for High Load Glen UnySupport™. Subsequently, the supernatant was collected, and the beads were washed with water (2×0.3 ml). The combined aqueous solutions were concentrated under reduced pressure using a SpeedVac concentrator. The crude was dissolved in DMSO (100 µl) and triethylamine trihydrofluoride (125 µl) was added. The solution was heated at 65 °C for 1.5 h. Finally, the ON was precipitated by adding 3 M NaOAc in water (25 µl) and n-butanol (1 ml). The mixture was kept at -80 °C for 2 h and centrifuged at 4°C for 1 h. The supernatant was removed, and the white precipitate was lyophilized.

The crude was purified by semi-preparative HPLC (1260 Infinity II Manual Preparative LC System from Agilent equipped with a G7114A detector) using a reverse-phase (RP) VP 250/10 Nucleodur 100-5 C18ec column from Macherey-Nagel. Buffers: A) 0.1 M AcOH/Et_3N in H_2O at pH 7 and B) 0.1 M AcOH/Et_3N in 80% (v/v) MeCN in H_2O. Gradient: 0-25% of B in 45 min. Flow rate = 5 ml·min^{-1}. The purified ON was analyzed by RP-HPLC (1260 Infinity II LC System from Agilent equipped with a G7165A detector) using an EC 250/4 Nucleodur 100-3 C18ec from Macherey-Nagel. Gradient: 0-25% or 0-30% of B in 45 min. Flow rate = 1 ml·min^{-1}. Finally, the purified ON was desalted using a C18 RP-cartridge from Waters.

Please cite this article in press as: Bérouti et al., Pseudouridine RNA avoids immune detection through impaired endolysosomal processing and TLR engagement, Cell (2025), https://doi.org/10.1016/j.cell.2025.05.032

The absorbance of the synthesized ON in H_2O solution was measured using an IMPLEN NanoPhotometer® N60/N50 at 260 nm. The extinction coefficient of the single stranded ONs was calculated using the OligoAnalyzer Version 3.0 from Integrated DNA Technologies. For ONs incorporating non-canonical bases, the extinction coefficients were assumed to be identical to those containing only canonical counterparts. The synthesized ON (2-3 μl) was desalted on a 0.025 μm VSWP filter (Millipore), co-crystallized in a 3- hydroxypicolinic acid matrix (HPA, 1 μl) and analyzed by MALDI-TOF mass spectrometry (negative mode).

NMR analysis of ΨΨΨAGC and UUUAGC

Samples of ΨΨΨAGC and UUUAGC were purified by an NaOAc/EtOH precipitation with subsequent desalting by a NAP-5 Sephadex column (Cytiva). Purified oligonucleotides were lyophilized and dissolved in 25 mM sodium phosphate pH 6.4, 25 mM NaCl, 10% D_2O. NMR experiments were recorded on 600 and 1200 MHz Bruker NMR spectrometers equipped with cryogenic probes. 1D ^1H experiments were recorded at 282 K using a WATERGATE flip-back pulse sequence for water suppression. For investigation of non-exchangeable resonances, samples were dissolved in 25 mM sodium phosphate pH 6.4, 25 mM NaCl, 100% D_2O. 1D ^1H experiments were recorded, as well as homonuclear ^1H,^1H-NOESY (mixing time 300 ms) and ^1H,^1H-TOCSY (mixing time 60 ms) experiments. The residual water signal was suppressed using an excitation sculpting sequence. Spectra were processed in TopSpin v.3.5pl7 and analyzed in CCPNMR 2.4.2.

QUANTIFICATION AND STATISTICAL ANALYSIS

Statistical analyses were conducted using Prism 10. The sample sizes (n) and statistical methods, where applicable, are detailed in the respective figure legends.

Supplemental figures

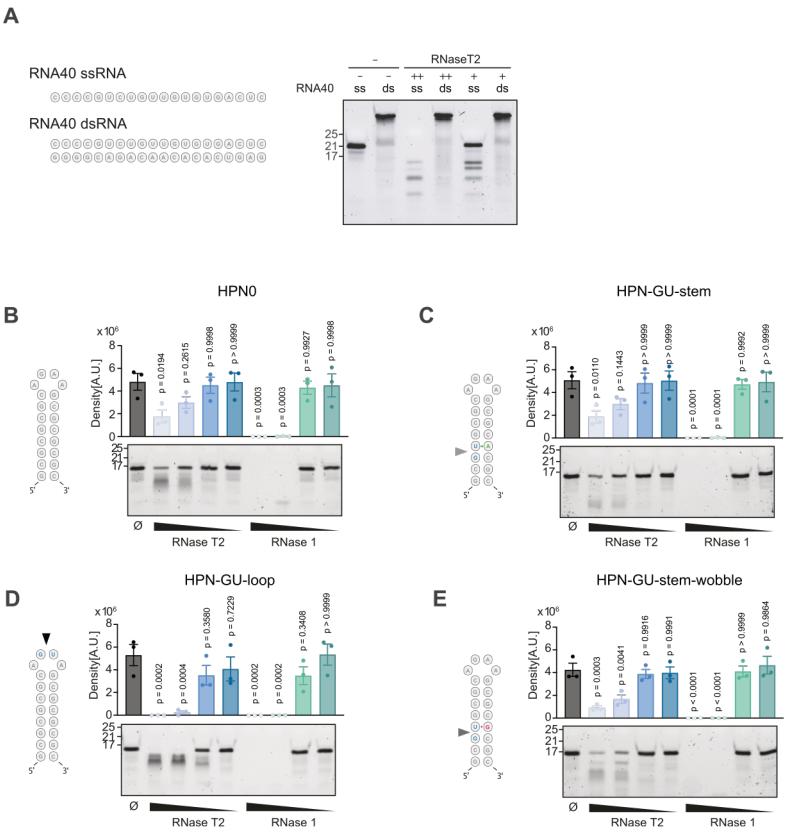

Figure S1. RNase T2 does not cleave dsRNA40, related to Figure 1

(A) Urea gel of ssRNA40 and dsRNA40 digested with RNase T2 (++ = 37 nM, + = 3.7 nM) in IDTE buffer. Data represent two independent experiments.

(B–E) Urea gels of depicted hairpin RNAs digested with RNase T2 (3.7 μM, 0.37 μM, 37 nM, and 0.37 nM) or RNase 1 (0.6 μM, 60 nM, 6 nM, and 0.6 nM) in IDTE buffer. One representative gel of three independent experiments is shown. Top, the quantification of the densitometry analysis of the uncut RNA oligonucleotide for each condition. Data are presented as mean ± SEM from $n = 3$ independent experiments. Statistical analysis was performed using a one-way ANOVA, comparing the untreated RNA to other conditions with Dunnett's multiple comparisons test.

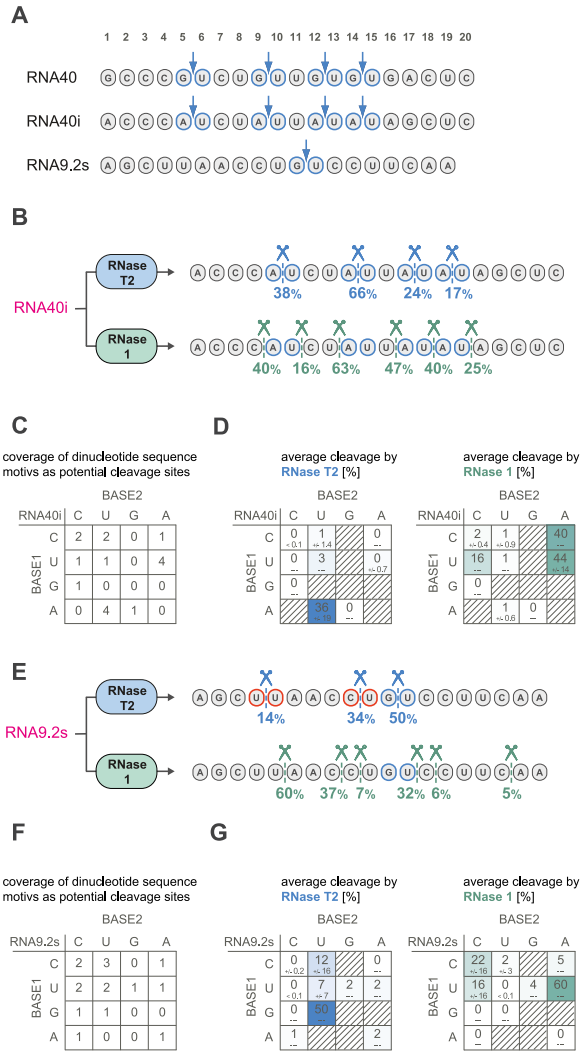

Figure S2. Characterization of RNA40i and RNA9.2s digested with RNase T2 or RNase 1, related to Figure 1

(A) Scheme of RNA40, RNA40i, and RNA9.2s and their major RNase T2 cut sites.

(B) RNA40i (1 μg) was digested with RNase T2 (35 nM) or RNase 1 (3 nM) in IDTE buffer and analyzed by HPLC-HESI-MS. The percentage of cleavage at a given site for RNA40i processed by RNase T2 or RNase 1 is indicated. All sites with >3% cleavage are shown. Data from three independent experiments were summarized.

(C) The coverage of dinucleotide motifs as potential cleavage sites in RNA40i is shown with only internal sites being considered.

(D) Average cleavage percentages for all possible dinucleotide motifs of RNA40i digested with RNase T2 (35 nM) or RNase 1 (3 nM). Data from three independent experiments were summarized and cleavage percentages are depicted as mean values (large letters) + SD (small letters, below).

(E) RNA9.2s (1 μg) was digested with RNase T2 (35 nM) or RNase 1 (3 nM) in IDTE buffer and analyzed by HPLC-HESI-MS. The percentage of cleavage at a given site for RNA9.2s processed by RNase T2 or RNase 1 is indicated. All sites with >4 % cleavage are shown. Data from three independent experiments were summarized.

(F) The coverage of dinucleotide motifs as potential cleavage sites in RNA9.2s is shown with only internal sites being considered.

(G) Average cleavage percentages for all possible dinucleotide motifs of RNA9.2s digested with RNase T2 (35 nM) or RNase 1 (3 nM). Data from three independent experiments were summarized and cleavage percentages are depicted as mean values (large letters) + SD (small letters, below).

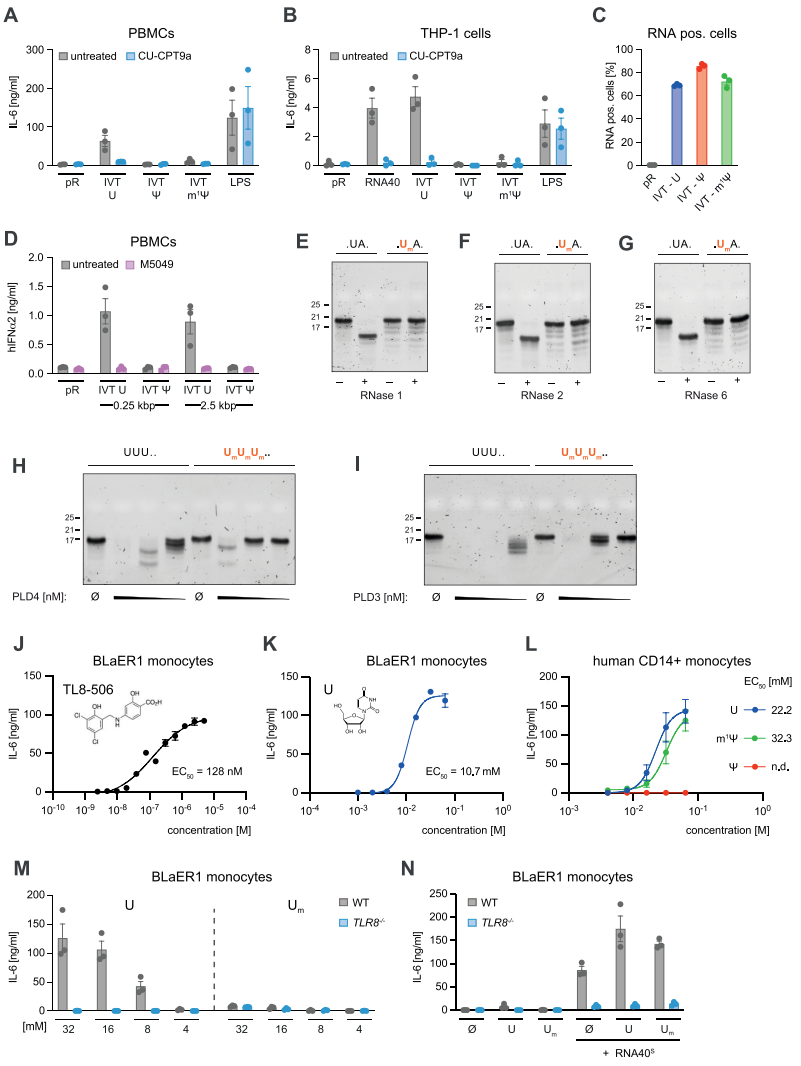

Figure S3. 2′-O-methyluridine is not a substrate for TLR8, related to Figures 4 and 5

(A) PBMCs were stimulated with pR, OVA-U, OVA-Ψ, OVA-m^{1}Ψ, and LPS with or without CU-CPT9a. After 24 h, IL-6 release was measured. Data are depicted as mean ± SEM of *n* = 3 independent donors.

(B) THP-1 cells were stimulated with pR, ssRNA40^S, OVA-U, OVA-Ψ, OVA-m^{1}Ψ, and LPS in the presence or absence of CU-CPT9a. After 14 h, IL-6 release was measured. Data are depicted as mean ± SEM of *n* = 3 independent experiments.

(C) Percentage of AZDye488 percentage-positive BLaER1 monocytes after transfection with pR alone or pR complexed with OVA IVT-U, OVA IVT-Ψ, or OVA IVT-m^{1}Ψ analyzed by FACS. Data are depicted as mean ± SEM of *n* = 3 independent experiments.

(D) PBMCs were stimulated with indicated Cas9 IVT constructs with or without M5049. After 24 h, IFNα2 release was measured. Data are depicted as mean ± SEM of *n* = 3 independent donors.

(E–G) Urea gels of $(dAdC)_7$GAGUAGA and $(dAdC)_7$GAGUmAGA digested with (E) RNase 1 (60 nM), (F) RNase 2 (55 nM), or (G) RNase 6 (60 nM) in assay buffer. One representative blot of two independent experiments is shown.

(H and I) Urea gels of UUUGCUUAACCUGUCCUU and UmUmUmGCUUAACCUGUCCUU digested with (H) PLD4 (250, 25, and 2.5 nM) or (I) PLD3 (25, 2.5, and 0.25 nM) in assay buffer. One out of two independent experiments is shown.

(J and K) BLaER1 monocytes were stimulated with increasing concentrations of (J) TL8-506 or (K) U. After 14 h, IL-6 release was measured. Each replicate of *n* = 3 independent experiments is depicted. A four-parameter dose-response curve was fitted to calculate half-maximal effective concentration (EC_{50}).

(L) CD14$^+$ monocytes were stimulated with increasing concentrations of U, Ψ, or m^{1}Ψ for 24 h. Afterward, IL-6 release was detected. Data are depicted as mean ± SEM of *n* = 3 independent donors. A four-parameter dose-response curve was fitted to calculate half-maximal effective concentration (EC_{50}).

(legend continued on next page)

(M) Wild-type and TLR8$^{-/-}$ BLaER1 monocytes were stimulated with decreasing concentrations of U or 2′-O-methyluridine as indicated. After 14 h, IL-6 release was detected. Data are depicted as mean ± SEM of $n = 3$ independent experiments.
(N) BLaER1 cells of indicated genotypes were stimulated with U, 2′-O-methyluridine or in combination with ssRNA40^{S} for 14 h. IL-6 release was subsequently analyzed. Data are depicted as mean ± SEM of $n = 3$ independent experiments.

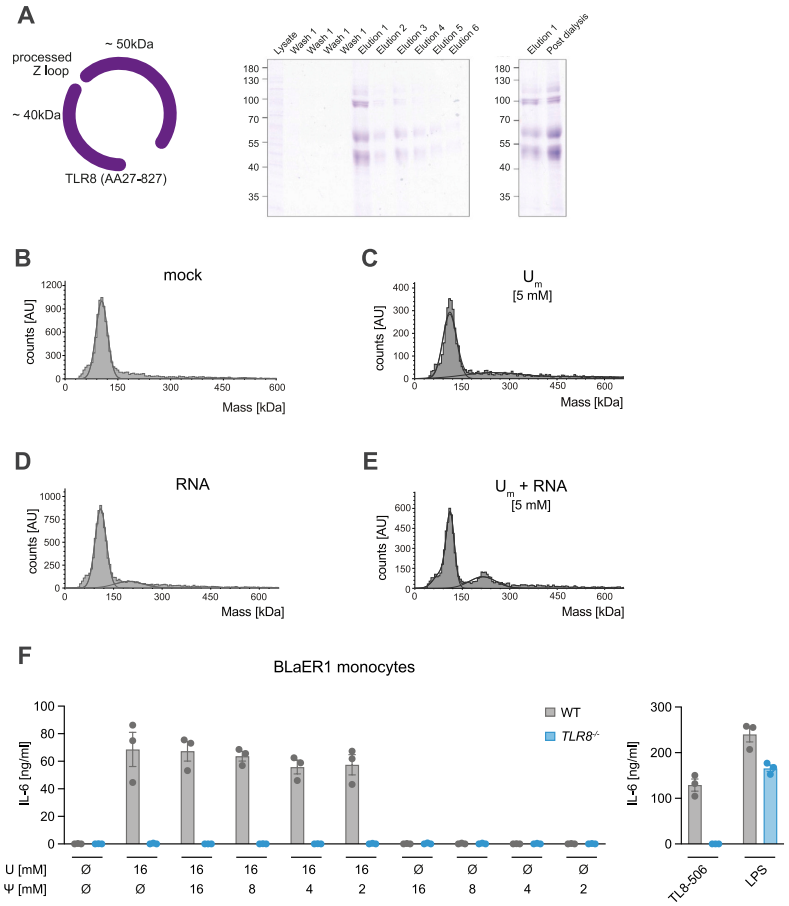

Figure S4. Ψ does not inhibit U binding to TLR8, related to Figure 5

(A) Scheme of hsTLR8 (AA27-827) after cleavage of the Z-loop and Coomassie gels of the EPEA bead purification of hsTLR8 (aa27–827) and of hsTLR8 (aa27–827) after buffer exchange by dialysis.

(B) Mass distribution of hsTLR8 (aa27–827) observed by mass photometry.

(C) Mass photometry analysis of hsTLR8 (aa27–827) incubated with ssRNA40^{O}.

(D) Mass photometry analysis of hsTLR8 (aa27–827) incubated with 5 mM Um.

(E) Mass photometry analysis of hsTLR8 (aa27–827) incubated with 5 mM Um and ssRNA40^{O}.

(F) Wild-type and TLR8$^{-/-}$ BLaER1 monocytes were unstimulated or stimulated with U, a combination of U and Ψ, TL8-506, or LPS. After 14 h, IL-6 release was measured. Data are depicted as mean ± SEM of *n* = 3 independent experiments.

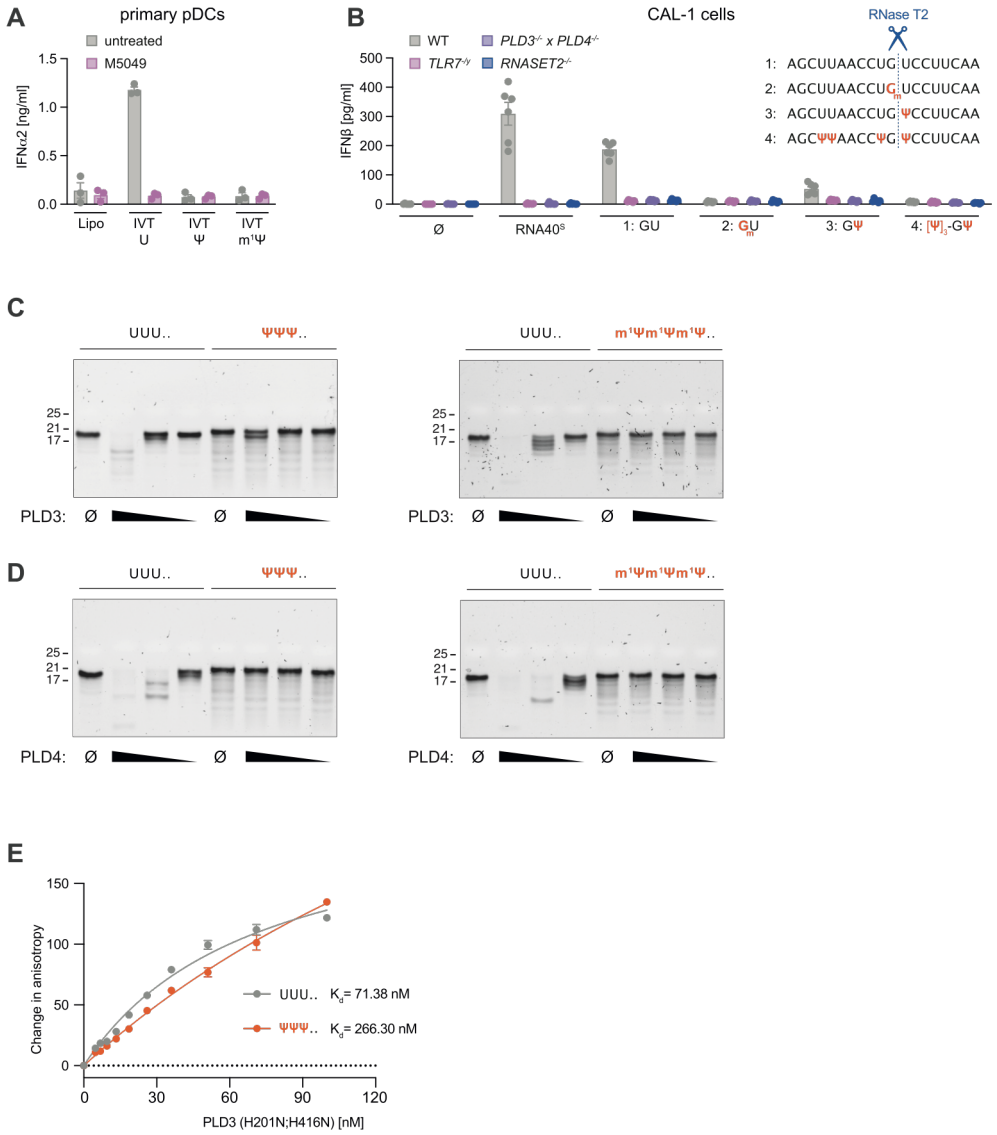

Figure S5. Ψ inhibits cleavage by PLD exonucleases, related to Figure 6

(A) pDCs were stimulated with lipofectamine only or with OVA-U, OVA-Ψ, and OVA-m^{1}Ψ with or without M5049. After 24 h, IFNα2 release was measured. Data are depicted as mean ± SEM of *n* = 3 independent donors.

(B) CAL-1 cells of indicated genotypes were stimulated as indicated. After 16 h, IFN-β release was determined. Data are depicted as mean ± SEM of *n* = 6 independent experiments.

(C) Urea gels of UUUGCUUAACCUGUCCUU, ΨΨΨGCUUAACCUGUCCUU, and m^{1}Ψm^{1}Ψm^{1}ΨGCU-UAACCUGUCCUU digested with PLD3 (2.5, 0.25, and 0.025 nM) in assay buffer. One out of two independent experiments is shown.

(D) Urea gels of UUUGCUUAACCUGUCCUU, ΨΨΨGCUUAACCUGUCCUU, and m^{1}Ψm^{1}Ψm^{1}ΨGCU-UAACCUGUCCUU digested with PLD4 (250, 25, and 2.5 nM) in assay buffer. One out of two independent experiments is shown.

(E) Fluorescence anisotropy assay assessing the binding of PLD3$^{H201N,\ H416N}$ at increasing concentrations to UUUGCUUAACCUGUCCUU and ΨΨΨGCUUAACCUGUCCUU. Data are shown as mean ± SEM of *n* = 3 independent experiments.

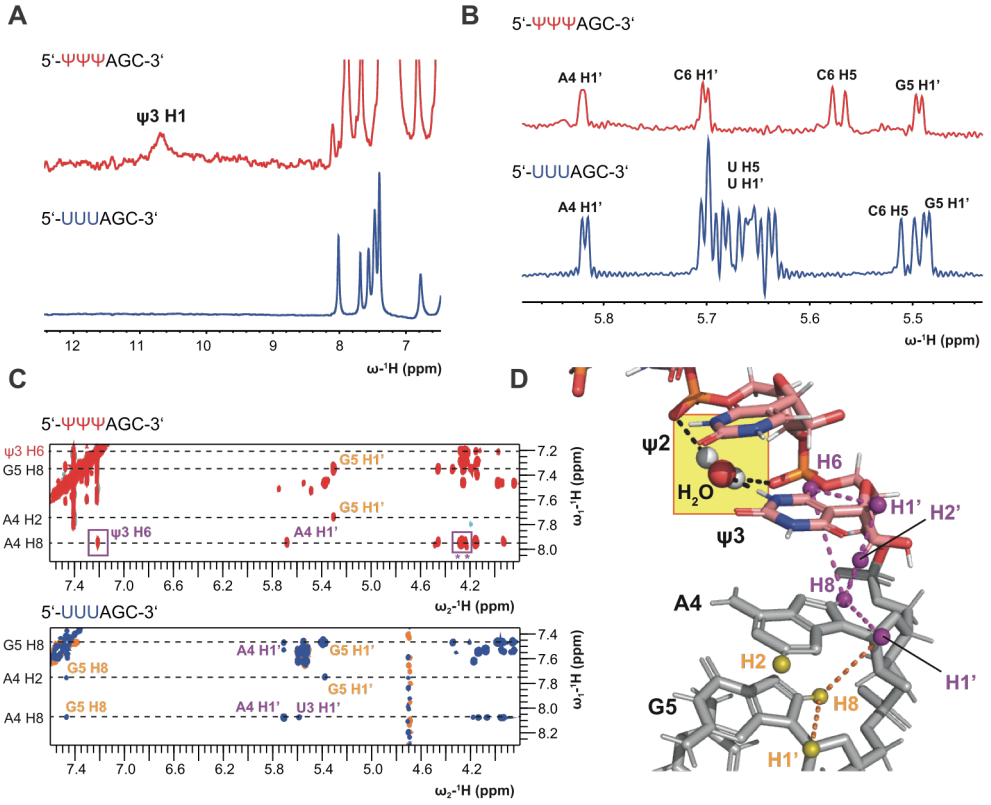

Figure S6. Ψ-RNA adopts an A-form conformation, related to Figure 6

(A) 1D ^{1}H NMR spectra of the imino region of ΨΨΨAGC (highlighted in red) and UUUAGC (highlighted in blue) revealing an additional H1 signal in ΨΨΨAGC most likely corresponding to Ψ3. Spectra were recorded at 600 MHz, 282 K.

(B) 1D ^{1}H NMR spectra of the H1′ region of the ribose's of ΨΨΨAGC and UUUAGC indicating a smaller splitting due to the 3J(H1′, H2′) coupling of the A4 and G5 signals (≈1–2 Hz) compared with the spectrum of the UUU-oligo (≈3 Hz). The smaller coupling in ΨΨΨAGC suggests a higher population of C3′endo conformation for the ribose of A4. Spectra were recorded at 600 MHz, 282 K for UUUAGC and 293 K for ΨΨΨAGC.

(C) Anomeric-aromatic region of ^{1}H,^{1}H NOESY spectra recorded at 600 MHz for UUUAGC and 1,200 MHz for ΨΨΨAGC. Both NMR spectra were recorded at 282 K with a mixing time of 300 ms. NOEs of A4 to U3/Ψ3 are annotated in purple, NOEs to G5 in yellow. An NOE from A4H8 to Ψ3H6 indicates base stacking. A corresponding NOE could not be observed in UUUAGC, suggesting a higher structural stabilization in ΨΨΨAGC. Two NOEs to the Ψ3 ribose were observed (marked by asterisks), which could not be further assigned.

(D) The NOEs are shown in a structural model of ΨΨΨAGC with A-form geometry. The model was generated using RNA composer. The imino H1 proton of Ψ3 is stabilized by a water-mediated H-bond to its own phosphate and the phosphate of the 5′ nucleotide (yellow box).

5 Publication list

(1) L. Hoffmann, E.-M. Eckl, **M. Bérouti**, M. Pries, A. Koller, C. Guhl, U. A. Hellmich, V. Hornung, W. Xiang, L. T. Jae, P. Kielkowski, AMPylation regulates 5'-3' exonuclease PLD3 processing, ***Molecular & Cellular Proteomics***, **2025**, https://doi.org/10.1016/j.mcpro.2025.101051

(2) **M. Bérouti**, M. Wagner, W. Greulich, I. Piseddu, J. Gärtig, L. Hansbauer, C. Müller-Hermes, M. Heiss, A. Pichler, A. J. Tölke, G. Witte, K.-P. Hopfner, D. Anz, M. Sattler, T. Carell, V. Hornung, Pseudouridine RNA avoids immune detection through impaired endolysosomal processing and TLR engagement, ***Cell***, **2025**, 188, 1-16, https://doi.org/10.1016/j.cell.2025.05.032.

(3) C. Gomez-Diaz, W. Greulich, B. Wefers, M. Wang, S. Bolsega, M. Effern, D. P. Varga, Z. Han, M. Chen, **M. Bérouti**, N. Leonardi, U. Schillinger, B. Holzmann, A. Liesz, A. Roers, M. Hölzel, M. Basic, W. Wurst, V. Hornung, RNase T2 restricts TLR13-mediated autoinflammation in vivo, ***JEM***, **2025**, 222 (3), e20241424, https://doi.org/10.1084/jem.20241424.

(4) M. Wang, H. Flaswinkel, A. Joshi, M. Napoli, S. Masgrau-Alsina, J. M. Kamper, A. Henne, A. Heinz, **M. Bérouti**, N. A. Schmacke, K. Hiller, E. Kremmer, B. Wefer, W. Wurst, M. Sperandio, J. Ruland, T. Fröhlich, V. Hornung, Phosphorylation of PFKL regulates metabolic reprogramming in macrophages following pattern recognition receptor activation, ***Nat Commun***, **2024**, 15, 6438, https://doi.org/10.1038/s41467-024-50104-7.

(5) **M. Bérouti**, K. Lammens, M. Heiss, L. Hansbauer, S. Bauernfried, J. Stöckl, F. Pinci, I. Piseddu, W. Greulich, M. Wang, C. Jung, T. Fröhlich, T. Carell, K.-P. Hopfner, V. Hornung, Lysosomal endonuclease RNase T2 and PLD exonucleases cooperatively generate RNA ligands for TLR7 activation, ***Immunity***, **2024**, 57 (7), 1482-1496, https://doi.org/10.1016/j.immuni.2024.04.010.

(6) N. A. Schmacke, S. C. Mädler, G. Wallmann, A. Metousis, **M. Bérouti**, H. Hartz, H. Leonhardt, M. Mann, V. Hornung, SPARCS, a platform for genome-scale CRISPR screening for spatial cellular phenotypes, ***bioRXiv***, **2023**, https://doi.org/10.1101/2023.06.01.542416.

(7) M. Reynders, B. S. Matsuura, **M. Bérouti**, D. Simoneschi, A. Marzio, M. Pagano, D. Trauner, PHOTACs Enable Optical Control of Protein Degradation, ***Sci. Adv.***, **2020**, 6 (8), eaay5064, https://doi.org/10.1126/sciadv.aay5064.

(8) M. Reynders, B. Matsuura, **M. Bérouti**, M. Pagano, D. Trauner, Photoswitchable PROTACs and synthesis and uses thereof, U.S. Pat. WO2020172655, **2020**.

6 List of Abbreviations

2’,3’-cGMP	2’,3’-cyclic guanosine monophosphate
AP-1	Activator protein 1
AP-2	Adaptor Protein 2
ATP	Adenosine triphosphate
BMP	Bis(monoacylglycerol)phosphate
cGAMP	cyclic GMP-AMP
cGAS	cyclic GMP-AMP synthase
CLR	C-type lectin receptor
CMP	Common myeloid progenitor
COPII	Coat Protein Complex II
CpG	cytosine-phosphate-guanine
CRISPR	Clustered Regularly Interspaced Short Palindromic Repeats
CRP	C-reactive protein
CTLR	C-type lectin-like receptor
CXCL8	C-X-C motif chemokine ligand 8
CXCL10	C-X-C motif chemokine ligand 10
DAMP	damage-associated molecular pattern
DC	dendritic cell
DC	dendritic cell
DKC	Dyskerin
DNA	Deoxyribonucleic acid
DNase	Deoxyribonuclease
ds	double-stranded
eiF2	eukaryotic initiation factor 2
ER	endoplasmatic reticulum
ERGIC	endoplasmic reticulum-Golgi intermediate compartment
ERK	Extracellular signal-related kinase
ETI	Effector-triggered immunity
GMP	Guanosine monophosphate

gp41	glycoprotein 41
gp96	glycoprotein 96
GTP	Guanosine triphosphate
H	Histidine
HIV	Human Immunodeficiency Virus
HKD	Histidine Lysine Aspartic acid
HSC	hematopoietic stem cells
HSV-1	Herpes simplex virus 1
IFN	Interferons
IFNB1	Interferon beta 1
IKKε	IκB kinase-ε
IL	Interleukin
IRAK	Interleukin-1 Receptor-Associated Kinase
IRF	Interferon regulatory factor
ISG	interferon-stimulated genes
ITAM	immune-receptor tyrosine-based activation motif
ITC	Isothermal Titration Calorimetry
ITIM	immune-receptor tyrosine-based inhibition motif
JNK	Jun N-terminal kinase
K	Lysine
LGP2	laboratory of genetics and physiology 2
LRR	Leucine-rich repeat
m1Ψ	N1-methylpseudouridine
m5C	5-methylcytosine
m5U	5-methyluridine
m6A	N6-methyladenosine
MAL	MyD88 Adaptor-like
MAPK	mitogen-activated protein kinase
MAVS	mitochondrial antiviral-signaling protein
MD-2	Myeloid Differentiation Factor 2

MDA5	melanoma differentiation-associated protein 5
mDC	monocyte-derived dendritic cell
MHC	Major Histocompatibility Complex
MORC3	Microrchidia family CW-type zinc finger 3
MyD88	myeloid differentiation primary response 88
m1Ψ	N1-Methylpseudouridine
NF-κB	Nuclear Factor kappa-light-chain-enhancer of activated B cells
NK	natural killer
NLR	Nucleotide-binding domain and leucine-rich repeat-containing receptor
NO	nitric oxygen
NOD	nucleotide-binding oligomerization domain
OAS	oligoadenylate synthase
PAMP	pathogen-associated molecular pattern
pDC	Plasmacytoid dendritic cell
PKR	Protein kinase R
PLD	Phospholipase D
PRAT4A	Protein Associated with Toll-like receptor 4A
PRR	pattern recognition receptor
PTI	Pattern-triggered immunity
PUS	Pseudouridine synthase
Q	Glutamine
RAF-1	rapidly accelerated fibrosarcoma
RIG	Retinoic acid-inducible gene
RIPK-1	Receptor-interacting serine/threonine-protein kinase 1
RLR	RIG-I-like receptor

RNA	Ribonucleic acid
RNase	Ribonuclease
ROS	reactive oxygen species
S2U	2-thiouridine
SAA	Serum amyloid A
scaRNA	small Cajal body-specific RNA
SLC15A4	Solute Carrier Family 15 Member 4
SLE	Systemic lupus erythematosus
snoRNA	small nucleolar RNA
SnRNA	Small nuclear RNA
ss	single-stranded
STING	Stimulator of interferon genes
SYK	spleen tyrosine kinase
TAB	TAK1-binding protein
TAK1	Transforming growth factor-β (TGF-β)-activated kinase 1
TASL	TLR adaptor interacting with SLC15A4 on the lysosome
TBK1	TANK binding kinase 1
TGF-β	Transforming growth factor β
TIR	Toll/interleukin-1
TIRAP	TIR domain-containing adaptor protein
TLR	Toll-like receptor
TNF	Tumor necrosis factor
TRAF6	TNF receptor-associated factor 6
TRAM	TRIF-related adaptor molecule
TRIF	TIR-domain-containing adapter-inducing interferon
UBC13	Ubiquitin-Conjugating enzyme 13
UEV1A	Ubiquitin-conjugating Enzyme E2 Variant 1A
Unc31B1	Unc-93 homolog B1
Ψ	Pseudouridine

7 References

Ablasser, A., Goldeck, M., Cavlar, T., Deimling, T., Witte, G., Röhl, I., Hopfner, K.-P., Ludwig, J., and Hornung, V. (2013). cGAS produces a 2′-5′-linked cyclic dinucleotide second messenger that activates STING. Nature *498*, 380-384. 10.1038/nature12306.

Akizuki, S., Ishigaki, K., Kochi, Y., Law, S.-M., Matsuo, K., Ohmura, K., Suzuki, A., Nakayama, M., Iizuka, Y., Koseki, H., et al. (2019). PLD4 is a genetic determinant to systemic lupus erythematosus and involved in murine autoimmune phenotypes. Annals of the Rheumatic Diseases *78*, 509-518. 10.1136/annrheumdis-2018-214116.

Alexopoulou, L., Holt, A.C., Medzhitov, R., and Flavell, R.A. (2001). Recognition of double-stranded RNA and activation of NF-κB by Toll-like receptor 3. Nature *413*, 732-738. 10.1038/35099560.

Alharbi, A.S., Sapkota, S., Zhang, Z., Jin, R., Jayasekara, W.S.N., Rupasinghe, E., Speir, M., Wilkinson-White, L., Gamsjaeger, R., Cubeddu, L., et al. (2024). 10.1101/2024.07.25.605091.

Almskog, L.M., and Ågren, A. (2025). Thromboinflammation vs. immunothrombosis: strategies for overcoming anticoagulant resistance in COVID-19 and other hyperinflammatory diseases. Is ROTEM helpful or not? Front Immunol *16*, 1599639. 10.3389/fimmu.2025.1599639.

Anderson, B.R., Muramatsu, H., Jha, B.K., Silverman, R.H., Weissman, D., and Karikó, K. (2011). Nucleoside modifications in RNA limit activation of 2'-5'-oligoadenylate synthetase and increase resistance to cleavage by RNase L. Nucleic Acids Res *39*, 9329-9338. 10.1093/nar/gkr586.

Anderson, B.R., Muramatsu, H., Nallagatla, S.R., Bevilacqua, P.C., Sansing, L.H., Weissman, D., and Karikó, K. (2010). Incorporation of pseudouridine into mRNA enhances translation by diminishing PKR activation. Nucleic Acids Research *38*, 5884-5892. 10.1093/nar/gkq347.

Andries, O., Mc Cafferty, S., De Smedt, S.C., Weiss, R., Sanders, N.N., and Kitada, T. (2015). N1-methylpseudouridine-incorporated mRNA outperforms pseudouridine-incorporated mRNA by providing enhanced protein expression and reduced immunogenicity in mammalian cell lines and mice. Journal of Controlled Release *217*, 337-344. https://doi.org/10.1016/j.jconrel.2015.08.051.

Balachandran, S., Kim, C.N., Yeh, W.C., Mak, T.W., Bhalla, K., and Barber, G.N. (1998). Activation of the dsRNA-dependent protein kinase, PKR, induces apoptosis through FADD-mediated death signaling. The EMBO Journal *17*, 6888-6902-6902. https://doi.org/10.1093/emboj/17.23.6888.

Balka, K.R., Louis, C., Saunders, T.L., Smith, A.M., Calleja, D.J., D'Silva, D.B., Moghaddas, F., Tailler, M., Lawlor, K.E., Zhan, Y., et al. (2020). TBK1 and IKKε Act

Redundantly to Mediate STING-Induced NF-κB Responses in Myeloid Cells. Cell Rep *31*, 107492. 10.1016/j.celrep.2020.03.056.

Barrangou, R., and Marraffini, L.A. (2014). CRISPR-Cas systems: Prokaryotes upgrade to adaptive immunity. Mol Cell *54*, 234-244. 10.1016/j.molcel.2014.03.011.

Barton, G.M., Kagan, J.C., and Medzhitov, R. (2006). Intracellular localization of Toll-like receptor 9 prevents recognition of self DNA but facilitates access to viral DNA. Nat Immunol *7*, 49-56. 10.1038/ni1280.

Belizário, J.E., Neyra, J.M., and Setúbal Destro Rodrigues, M.F. (2018). When and how NK cell-induced programmed cell death benefits immunological protection against intracellular pathogen infection. Innate Immun *24*, 452-465. 10.1177/1753425918800200.

Berg, J.M., Held, A., Stryer, L., Lange, C., Mahlke, K., Maxam, G., Seidler, L., Zellerhoff, N., Häcker, B., and Jarosch, B. (2012). Stryer Biochemie (Springer Berlin Heidelberg).

Berouti, M., Lammens, K., Heiss, M., Hansbauer, L., Bauernfried, S., Stockl, J., Pinci, F., Piseddu, I., Greulich, W., Wang, M., et al. (2024). Lysosomal endonuclease RNase T2 and PLD exonucleases cooperatively generate RNA ligands for TLR7 activation. Immunity *57*, 1482-1496 e1488. 10.1016/j.immuni.2024.04.010.

Bonham, Kevin S., Orzalli, Megan H., Hayashi, K., Wolf, Amaya I., Glanemann, C., Weninger, W., Iwasaki, A., Knipe, David M., and Kagan, Jonathan C. (2014). A Promiscuous Lipid-Binding Protein Diversifies the Subcellular Sites of Toll-like Receptor Signal Transduction. Cell *156*, 705-716. 10.1016/j.cell.2014.01.019.

Borchardt, E.K., Martinez, N.M., and Gilbert, W.V. (2020). Regulation and Function of RNA Pseudouridylation in Human Cells. Annu Rev Genet *54*, 309-336. 10.1146/annurev-genet-112618-043830.

Bruns, A.M., Leser, G.P., Lamb, R.A., and Horvath, C.M. (2014). The innate immune sensor LGP2 activates antiviral signaling by regulating MDA5-RNA interaction and filament assembly. Mol Cell *55*, 771-781. 10.1016/j.molcel.2014.07.003.

Cabeza-Cabrerizo, M., Cardoso, A., Minutti, C.M., Pereira da Costa, M., and Reis e Sousa, C. (2021). Dendritic Cells Revisited. Annu Rev Immunol *39*, 131-166. 10.1146/annurev-immunol-061020-053707.

Cambier, S., Gouwy, M., and Proost, P. (2023). The chemokines CXCL8 and CXCL12: molecular and functional properties, role in disease and efforts towards pharmacological intervention. Cellular & Molecular Immunology *20*, 217-251. 10.1038/s41423-023-00974-6.

Cao, Z., Henzel, W.J., and Gao, X. (1996a). IRAK: a kinase associated with the interleukin-1 receptor. Science *271*, 1128-1131. 10.1126/science.271.5252.1128.

Cao, Z., Xiong, J., Takeuchi, M., Kurama, T., and Goeddel, D.V. (1996b). TRAF6 is a signal transducer for interleukin-1. Nature *383*, 443-446. 10.1038/383443a0.

Cappannini, A., Ray, A., Purta, E., Mukherjee, S., Boccaletto, P., Moafinejad, S.N., Lechner, A., Barchet, C., Klaholz, B.P., Stefaniak, F., and Bujnicki, J.M. (2024). MODOMICS: a database of RNA modifications and related information. 2023 update. Nucleic Acids Res *52*, D239-d244. 10.1093/nar/gkad1083.

Carlile, T.M., Rojas-Duran, M.F., Zinshteyn, B., Shin, H., Bartoli, K.M., and Gilbert, W.V. (2014). Pseudouridine profiling reveals regulated mRNA pseudouridylation in yeast and human cells. Nature *515*, 143-146. 10.1038/nature13802.

Celhar, T., Magalhães, R., and Fairhurst, A.M. (2012). TLR7 and TLR9 in SLE: when sensing self goes wrong. Immunol Res *53*, 58-77. 10.1007/s12026-012-8270-1.

Cerneckis, J., Cui, Q., He, C., Yi, C., and Shi, Y. (2022). Decoding pseudouridine: an emerging target for therapeutic development. Trends in Pharmacological Sciences *43*, 522-535. 10.1016/j.tips.2022.03.008.

Chan, M.P., Onji, M., Fukui, R., Kawane, K., Shibata, T., Saitoh, S., Ohto, U., Shimizu, T., Barber, G.N., and Miyake, K. (2015). DNase II-dependent DNA digestion is required for DNA sensing by TLR9. Nat Commun *6*, 5853. 10.1038/ncomms6853.

Chaplin, D.D. (2010). Overview of the immune response. J Allergy Clin Immunol *125*, S3-23. 10.1016/j.jaci.2009.12.980.

Chen, W.C., Wang, W.C., Okada, Y., Chang, W.P., Chou, Y.H., Chang, H.H., Huang, J.D., Chen, D.Y., and Chang, W.C. (2017). rs2841277 (PLD4) is associated with susceptibility and rs4672495 is associated with disease activity in rheumatoid arthritis. Oncotarget *8*, 64180-64190. 10.18632/oncotarget.19419.

Cheung, P.C., Nebreda, A.R., and Cohen, P. (2004). TAB3, a new binding partner of the protein kinase TAK1. Biochem J *378*, 27-34. 10.1042/bj20031794.

Chiffoleau, E. (2018). C-Type Lectin-Like Receptors As Emerging Orchestrators of Sterile Inflammation Represent Potential Therapeutic Targets. Front Immunol *9*, 227. 10.3389/fimmu.2018.00227.

Cho, S., Beintema, J.J., and Zhang, J. (2005). The ribonuclease A superfamily of mammals and birds: identifying new members and tracing evolutionary histories. Genomics *85*, 208-220. https://doi.org/10.1016/j.ygeno.2004.10.008.

Christensen, S.R., Shupe, J., Nickerson, K., Kashgarian, M., Flavell, R.A., and Shlomchik, M.J. (2006). Toll-like receptor 7 and TLR9 dictate autoantibody specificity and have opposing inflammatory and regulatory roles in a murine model of lupus. Immunity *25*, 417-428. 10.1016/j.immuni.2006.07.013.

Cohn, W.E., and Volkin, E. (1951). Nucleoside-5′-Phosphates from Ribonucleic Acid. Nature *167*, 483-484. 10.1038/167483a0.

Cruchaga, C., Karch, C.M., Jin, S.C., Benitez, B.A., Cai, Y., Guerreiro, R., Harari, O., Norton, J., Budde, J., Bertelsen, S., et al. (2014). Rare coding variants in the phospholipase D3 gene confer risk for Alzheimer's disease. Nature *505*, 550-554. 10.1038/nature12825.

Cuthbert, B.J., Burley, K.H., and Goulding, C.W. (2018). Introducing the new bacterial branch of the RNase A superfamily. RNA Biol *15*, 9-12. 10.1080/15476286.2017.1387710.

Deane, J.A., Pisitkun, P., Barrett, R.S., Feigenbaum, L., Town, T., Ward, J.M., Flavell, R.A., and Bolland, S. (2007). Control of toll-like receptor 7 expression is essential to restrict autoimmunity and dendritic cell proliferation. Immunity *27*, 801-810. 10.1016/j.immuni.2007.09.009.

del Toro Duany, Y., Wu, B., and Hur, S. (2015). MDA5—filament, dynamics and disease. Current Opinion in Virology *12*, 20-25. https://doi.org/10.1016/j.coviro.2015.01.011.

Deng, L., Wang, C., Spencer, E., Yang, L., Braun, A., You, J., Slaughter, C., Pickart, C., and Chen, Z.J. (2000). Activation of the IkappaB kinase complex by TRAF6 requires a dimeric ubiquitin-conjugating enzyme complex and a unique polyubiquitin chain. Cell *103*, 351-361. 10.1016/s0092-8674(00)00126-4.

Diebold, S.S., Kaisho, T., Hemmi, H., Akira, S., and Reis e Sousa, C. (2004). Innate antiviral responses by means of TLR7-mediated recognition of single-stranded RNA. Science *303*, 1529-1531. 10.1126/science.1093616.

Diner, E.J., Burdette, D.L., Wilson, S.C., Monroe, K.M., Kellenberger, C.A., Hyodo, M., Hayakawa, Y., Hammond, M.C., and Vance, R.E. (2013). The innate immune DNA sensor cGAS produces a noncanonical cyclic dinucleotide that activates human STING. Cell Rep *3*, 1355-1361. 10.1016/j.celrep.2013.05.009.

Drappier, M., and Michiels, T. (2015). Inhibition of the OAS/RNase L pathway by viruses. Current Opinion in Virology *15*, 19-26. https://doi.org/10.1016/j.coviro.2015.07.002.

Durbin, A.F., Wang, C., Marcotrigiano, J., and Gehrke, L. (2016). RNAs Containing Modified Nucleotides Fail To Trigger RIG-I Conformational Changes for Innate Immune Signaling. mBio *7*. 10.1128/mBio.00833-16.

Eklund, K.K., Niemi, K., and Kovanen, P.T. (2012). Immune functions of serum amyloid A. Crit Rev Immunol *32*, 335-348. 10.1615/critrevimmunol.v32.i4.40.

Ewald, S.E., Engel, A., Lee, J., Wang, M., Bogyo, M., and Barton, G.M. (2011). Nucleic acid recognition by Toll-like receptors is coupled to stepwise processing by cathepsins and asparagine endopeptidase. J Exp Med *208*, 643-651. 10.1084/jem.20100682.

Fang, F.C. (2004). Antimicrobial reactive oxygen and nitrogen species: concepts and controversies. Nat Rev Microbiol *2*, 820-832. 10.1038/nrmicro1004.

Farhat, K., Riekenberg, S., Heine, H., Debarry, J., Lang, R., Mages, J., Buwitt-Beckmann, U., Röschmann, K., Jung, G., Wiesmüller, K.H., and Ulmer, A.J. (2008). Heterodimerization of TLR2 with TLR1 or TLR6 expands the ligand spectrum but does not lead to differential signaling. J Leukoc Biol *83*, 692-701. 10.1189/jlb.0807586.

Fitzgerald, K.A., and Kagan, J.C. (2020). Toll-like Receptors and the Control of Immunity. Cell *180*, 1044-1066. 10.1016/j.cell.2020.02.041.

Fitzgerald, K.A., McWhirter, S.M., Faia, K.L., Rowe, D.C., Latz, E., Golenbock, D.T., Coyle, A.J., Liao, S.M., and Maniatis, T. (2003a). IKKepsilon and TBK1 are essential components of the IRF3 signaling pathway. Nat Immunol *4*, 491-496. 10.1038/ni921.

Fitzgerald, K.A., Palsson-McDermott, E.M., Bowie, A.G., Jefferies, C.A., Mansell, A.S., Brady, G., Brint, E., Dunne, A., Gray, P., Harte, M.T., et al. (2001). Mal (MyD88-adapter-like) is required for Toll-like receptor-4 signal transduction. Nature *413*, 78-83. 10.1038/35092578.

Fitzgerald, K.A., Rowe, D.C., Barnes, B.J., Caffrey, D.R., Visintin, A., Latz, E., Monks, B., Pitha, P.M., and Golenbock, D.T. (2003b). LPS-TLR4 signaling to IRF-3/7 and NF-kappaB involves the toll adapters TRAM and TRIF. J Exp Med *198*, 1043-1055. 10.1084/jem.20031023.

Fukui, R., Saitoh, S., Matsumoto, F., Kozuka-Hata, H., Oyama, M., Tabeta, K., Beutler, B., and Miyake, K. (2009). Unc93B1 biases Toll-like receptor responses to nucleic acid in dendritic cells toward DNA- but against RNA-sensing. J Exp Med *206*, 1339-1350. 10.1084/jem.20082316.

Gaidt, M.M., and Hornung, V. (2018). The NLRP3 Inflammasome Renders Cell Death Pro-inflammatory. Journal of Molecular Biology *430*, 133-141. https://doi.org/10.1016/j.jmb.2017.11.013.

Gaidt, M.M., Morrow, A., Fairgrieve, M.R., Karr, J.P., Yosef, N., and Vance, R.E. (2021). Self-guarding of MORC3 enables virulence factor-triggered immunity. Nature *600*, 138-142. 10.1038/s41586-021-04054-5.

Gavin, A.L., Huang, D., Blane, T.R., Thinnes, T.C., Murakami, Y., Fukui, R., Miyake, K., and Nemazee, D. (2021). Cleavage of DNA and RNA by PLD3 and PLD4 limits autoinflammatory triggering by multiple sensors. Nat Commun *12*, 5874. 10.1038/s41467-021-26150-w.

Gavin, A.L., Huang, D., Huber, C., Martensson, A., Tardif, V., Skog, P.D., Blane, T.R., Thinnes, T.C., Osborn, K., Chong, H.S., et al. (2018). PLD3 and PLD4 are single-stranded acid exonucleases that regulate endosomal nucleic-acid sensing. Nat Immunol *19*, 942-953. 10.1038/s41590-018-0179-y.

Girardin, S.E., Boneca, I.G., Viala, J., Chamaillard, M., Labigne, A., Thomas, G., Philpott, D.J., and Sansonetti, P.J. (2003). Nod2 Is a General Sensor of Peptidoglycan through Muramyl Dipeptide (MDP) Detection *. Journal of Biological Chemistry *278*, 8869-8872. 10.1074/jbc.C200651200.

Gonzalez, A.C., Schweizer, M., Jagdmann, S., Bernreuther, C., Reinheckel, T., Saftig, P., and Damme, M. (2018). Unconventional Trafficking of Mammalian Phospholipase D3 to Lysosomes. Cell Reports *22*, 1040-1053. 10.1016/j.celrep.2017.12.100.

Greulich, W., Wagner, M., Gaidt, M.M., Stafford, C., Cheng, Y., Linder, A., Carell, T., and Hornung, V. (2019). TLR8 Is a Sensor of RNase T2 Degradation Products. Cell *179*, 1264-1275 e1213. 10.1016/j.cell.2019.11.001.

Guiducci, C., Gong, M., Cepika, A.M., Xu, Z., Tripodo, C., Bennett, L., Crain, C., Quartier, P., Cush, J.J., Pascual, V., et al. (2013). RNA recognition by human TLR8 can lead to autoimmune inflammation. J Exp Med *210*, 2903-2919. 10.1084/jem.20131044.

Hayashi, F., Smith, K.D., Ozinsky, A., Hawn, T.R., Yi, E.C., Goodlett, D.R., Eng, J.K., Akira, S., Underhill, D.M., and Aderem, A. (2001). The innate immune response to bacterial flagellin is mediated by Toll-like receptor 5. Nature *410*, 1099-1103. 10.1038/35074106.

Heil, F., Hemmi, H., Hochrein, H., Ampenberger, F., Kirschning, C., Akira, S., Lipford, G., Wagner, H., and Bauer, S. (2004). Species-specific recognition of single-stranded RNA via toll-like receptor 7 and 8. Science *303*, 1526-1529. 10.1126/science.1093620.

Heim, V.J., Stafford, C.A., and Nachbur, U. (2019). NOD Signaling and Cell Death. Frontiers in Cell and Developmental Biology *Volume 7 - 2019*. 10.3389/fcell.2019.00208.

Heinz, L.X., Lee, J., Kapoor, U., Kartnig, F., Sedlyarov, V., Papakostas, K., Cesar-Razquin, A., Essletzbichler, P., Goldmann, U., Stefanovic, A., et al. (2020). TASL is the SLC15A4-associated adaptor for IRF5 activation by TLR7-9. Nature *581*, 316-322. 10.1038/s41586-020-2282-0.

Hemmi, H., Takeuchi, O., Kawai, T., Kaisho, T., Sato, S., Sanjo, H., Matsumoto, M., Hoshino, K., Wagner, H., Takeda, K., and Akira, S. (2000). A Toll-like receptor recognizes bacterial DNA. Nature *408*, 740-745. 10.1038/35047123.

Horng, T., Barton, G.M., and Medzhitov, R. (2001). TIRAP: an adapter molecule in the Toll signaling pathway. Nature Immunology *2*, 835-841. 10.1038/ni0901-835.

Hornung, V., Ellegast, J., Kim, S., Brzózka, K., Jung, A., Kato, H., Poeck, H., Akira, S., Conzelmann, K.-K., Schlee, M., et al. (2006). 5'-Triphosphate RNA Is the Ligand for RIG-I. Science *314*, 994-997. doi:10.1126/science.1132505.

Hornung, V., and Gaidt, M.M. (2024). Friendly fire: recognition of self by the innate immune system. Current Opinion in Immunology *90*, 102457. https://doi.org/10.1016/j.coi.2024.102457.

Hornung, V., Rothenfusser, S., Britsch, S., Krug, A., Jahrsdorfer, B., Giese, T., Endres, S., and Hartmann, G. (2002). Quantitative expression of toll-like receptor 1-10 mRNA

in cellular subsets of human peripheral blood mononuclear cells and sensitivity to CpG oligodeoxynucleotides. J Immunol *168*, 4531-4537. 10.4049/jimmunol.168.9.4531.

Huang, H., Gao, Q., Peng, X., Choi, S.-Y., Sarma, K., Ren, H., Morris, Andrew J., and Frohman, Michael A. (2011). piRNA-Associated Germline Nuage Formation and Spermatogenesis Require MitoPLD Profusogenic Mitochondrial-Surface Lipid Signaling. Developmental Cell *20*, 376-387. 10.1016/j.devcel.2011.01.004.

Huh, J.W., Shibata, T., Hwang, M., Kwon, E.H., Jang, M.S., Fukui, R., Kanno, A., Jung, D.J., Jang, M.H., Miyake, K., and Kim, Y.M. (2014). UNC93B1 is essential for the plasma membrane localization and signaling of Toll-like receptor 5. Proc Natl Acad Sci U S A *111*, 7072-7077. 10.1073/pnas.1322838111.

Huysamen, C., and Brown, G.D. (2009). The fungal pattern recognition receptor, Dectin-1, and the associated cluster of C-type lectin-like receptors. FEMS Microbiol Lett *290*, 121-128. 10.1111/j.1574-6968.2008.01418.x.

Ipsaro, J.J., Haase, A.D., Knott, S.R., Joshua-Tor, L., and Hannon, G.J. (2012). The structural biochemistry of Zucchini implicates it as a nuclease in piRNA biogenesis. Nature *491*, 279-283. 10.1038/nature11502.

Jang, D.I., Lee, A.H., Shin, H.Y., Song, H.R., Park, J.H., Kang, T.B., Lee, S.R., and Yang, S.H. (2021). The Role of Tumor Necrosis Factor Alpha (TNF-α) in Autoimmune Disease and Current TNF-α Inhibitors in Therapeutics. Int J Mol Sci *22*. 10.3390/ijms22052719.

Kang, J.Y., Nan, X., Jin, M.S., Youn, S.J., Ryu, Y.H., Mah, S., Han, S.H., Lee, H., Paik, S.G., and Lee, J.O. (2009). Recognition of lipopeptide patterns by Toll-like receptor 2-Toll-like receptor 6 heterodimer. Immunity *31*, 873-884. 10.1016/j.immuni.2009.09.018.

Kariko, K., Buckstein, M., Ni, H., and Weissman, D. (2005). Suppression of RNA recognition by Toll-like receptors: the impact of nucleoside modification and the evolutionary origin of RNA. Immunity *23*, 165-175. 10.1016/j.immuni.2005.06.008.

Karikó, K., Muramatsu, H., Welsh, F.A., Ludwig, J., Kato, H., Akira, S., and Weissman, D. (2008). Incorporation of Pseudouridine Into mRNA Yields Superior Nonimmunogenic Vector With Increased Translational Capacity and Biological Stability. Molecular Therapy *16*, 1833-1840. https://doi.org/10.1038/mt.2008.200.

Kawai, T., and Akira, S. (2006). TLR signaling. Cell Death & Differentiation *13*, 816-825. 10.1038/sj.cdd.4401850.

Kawasaki, T., and Kawai, T. (2014). Toll-like receptor signaling pathways. Front Immunol *5*, 461. 10.3389/fimmu.2014.00461.

Kawata, Y., Sakiyama, F., Hayashi, F., and Kyogoku, Y. (1990). Identification of two essential histidine residues of ribonuclease T2 from Aspergillus oryzae. Eur J Biochem *187*, 255-262. 10.1111/j.1432-1033.1990.tb15303.x.

Kelemen, B.R., Schultz, L.W., Sweeney, R.Y., and Raines, R.T. (2000). Excavating an active site: the nucleobase specificity of ribonuclease A. Biochemistry *39*, 14487-14494. 10.1021/bi001862f.

Kierzek, E., Malgowska, M., Lisowiec, J., Turner, D.H., Gdaniec, Z., and Kierzek, R. (2014). The contribution of pseudouridine to stabilities and structure of RNAs. Nucleic Acids Res *42*, 3492-3501. 10.1093/nar/gkt1330.

Kim, Y.M., Brinkmann, M.M., Paquet, M.E., and Ploegh, H.L. (2008). UNC93B1 delivers nucleotide-sensing toll-like receptors to endolysosomes. Nature *452*, 234-238. 10.1038/nature06726.

Labbé, K., and Saleh, M. (2008). Cell death in the host response to infection. Cell Death & Differentiation *15*, 1339-1349. 10.1038/cdd.2008.91.

Lamphier, M.S., Sirois, C.M., Verma, A., Golenbock, D.T., and Latz, E. (2006). TLR9 and the recognition of self and non-self nucleic acids. Ann N Y Acad Sci *1082*, 31-43. 10.1196/annals.1348.005.

Laroui, H., Yan, Y., Narui, Y., Ingersoll, S.A., Ayyadurai, S., Charania, M.A., Zhou, F., Wang, B., Salaita, K., Sitaraman, S.V., and Merlin, D. (2011). l-Ala-γ-d-Glu-meso-diaminopimelic Acid (DAP) Interacts Directly with Leucine-rich Region Domain of Nucleotide-binding Oligomerization Domain 1, Increasing Phosphorylation Activity of Receptor-interacting Serine/Threonine-protein Kinase 2 and Its Interaction with Nucleotide-binding Oligomerization Domain 1*. Journal of Biological Chemistry *286*, 31003-31013. https://doi.org/10.1074/jbc.M111.257501.

Lee, B.L., Moon, J.E., Shu, J.H., Yuan, L., Newman, Z.R., Schekman, R., and Barton, G.M. (2013). UNC93B1 mediates differential trafficking of endosomal TLRs. Elife *2*, e00291. 10.7554/eLife.00291.

Lemaitre, B., Nicolas, E., Michaut, L., Reichhart, J.M., and Hoffmann, J.A. (1996). The dorsoventral regulatory gene cassette spätzle/Toll/cactus controls the potent antifungal response in Drosophila adults. Cell *86*, 973-983. 10.1016/s0092-8674(00)80172-5.
Lin, S.C., Lo, Y.C., and Wu, H. (2010). Helical assembly in the MyD88-IRAK4-IRAK2 complex in TLR/IL-1R signalling. Nature *465*, 885-890. 10.1038/nature09121.

Liu, K., Sato, R., Shibata, T., Hiranuma, R., Reuter, T., Fukui, R., Zhang, Y., Ichinohe, T., Ozawa, M., Yoshida, N., et al. (2021). Skewed endosomal RNA responses from TLR7 to TLR3 in RNase T2-deficient macrophages. Int Immunol *33*, 479-490. 10.1093/intimm/dxab033.

Liu, S., Cai, X., Wu, J., Cong, Q., Chen, X., Li, T., Du, F., Ren, J., Wu, Y.-T., Grishin, N.V., and Chen, Z.J. (2015a). Phosphorylation of innate immune adaptor proteins MAVS, STING, and TRIF induces IRF3 activation. Science *347*, aaa2630. doi:10.1126/science.aaa2630.

Liu, S., Cai, X., Wu, J., Cong, Q., Chen, X., Li, T., Du, F., Ren, J., Wu, Y.T., Grishin, N.V., and Chen, Z.J. (2015b). Phosphorylation of innate immune adaptor proteins MAVS, STING, and TRIF induces IRF3 activation. Science *347*, aaa2630. 10.1126/science.aaa2630.

Liu, T., Zhang, L., Joo, D., and Sun, S.-C. (2017). NF-κB signaling in inflammation. Signal Transduction and Targeted Therapy *2*, 17023. 10.1038/sigtrans.2017.23.

Lodoen, M.B., and Lanier, L.L. (2006). Natural killer cells as an initial defense against pathogens. Curr Opin Immunol *18*, 391-398. 10.1016/j.coi.2006.05.002.

Lübke, T., Lobel, P., and Sleat, D.E. (2009). Proteomics of the lysosome. Biochim Biophys Acta *1793*, 625-635. 10.1016/j.bbamcr.2008.09.018.

MacIntosh, G.C. (2011). RNase T2 Family: Enzymatic Properties, Functional Diversity, and Evolution of Ancient Ribonucleases. In Ribonucleases, pp. 89-114. 10.1007/978-3-642-21078-5_4.

Maeda, K., and Akira, S. (2016). TLR7 Structure: Cut in Z-Loop. Immunity *45*, 705-707. https://doi.org/10.1016/j.immuni.2016.10.003.

McDermott, M.I., Wang, Y., Wakelam, M.J.O., and Bankaitis, V.A. (2020). Mammalian phospholipase D: Function, and therapeutics. Progress in Lipid Research *78*, 101018. https://doi.org/10.1016/j.plipres.2019.101018.

Medzhitov, R., Preston-Hurlburt, P., and Janeway, C.A. (1997). A human homologue of the Drosophila Toll protein signals activation of adaptive immunity. Nature *388*, 394-397. 10.1038/41131.

Mogensen, T.H. (2009). Pathogen recognition and inflammatory signaling in innate immune defenses. Clin Microbiol Rev *22*, 240-273, Table of Contents. 10.1128/cmr.00046-08.

Mold, C., Gewurz, H., and Du Clos, T.W. (1999). Regulation of complement activation by C-reactive protein. Immunopharmacology *42*, 23-30. 10.1016/s0162-3109(99)00007-7.

Motshwene, P.G., Moncrieffe, M.C., Grossmann, J.G., Kao, C., Ayaluru, M., Sandercock, A.M., Robinson, C.V., Latz, E., and Gay, N.J. (2009). An oligomeric signaling platform formed by the Toll-like receptor signal transducers MyD88 and IRAK-4. J Biol Chem *284*, 25404-25411. 10.1074/jbc.M109.022392.

Murphy, K.M., and Weaver, C. (2017). Janeway's Immunobiology (Garland Science/Taylor & Francis Group, LLC).

Murthy, A.M.V., Robinson, N., and Kumar, S. (2020). Crosstalk between cGAS–STING signaling and cell death. Cell Death & Differentiation *27*, 2989-3003. 10.1038/s41418-020-00624-8.

Nagpal, K., Plantinga, T.S., Wong, J., Monks, B.G., Gay, N.J., Netea, M.G., Fitzgerald, K.A., and Golenbock, D.T. (2009). A TIR domain variant of MyD88 adapter-like (Mal)/TIRAP results in loss of MyD88 binding and reduced TLR2/TLR4 signaling. J Biol Chem *284*, 25742-25748. 10.1074/jbc.M109.014886.

Nance, K.D., and Meier, J.L. (2021). Modifications in an Emergency: The Role of N1-Methylpseudouridine in COVID-19 Vaccines. ACS Central Science *7*, 748-756. 10.1021/acscentsci.1c00197.

Ngo, C., Garrec, C., Tomasello, E., and Dalod, M. (2024). The role of plasmacytoid dendritic cells (pDCs) in immunity during viral infections and beyond. Cellular & Molecular Immunology *21*, 1008-1035. 10.1038/s41423-024-01167-5.

Ninomiya-Tsuji, J., Kishimoto, K., Hiyama, A., Inoue, J., Cao, Z., and Matsumoto, K. (1999). The kinase TAK1 can activate the NIK-I kappaB as well as the MAP kinase cascade in the IL-1 signalling pathway. Nature *398*, 252-256. 10.1038/18465.

Nishimasu, H., Ishizu, H., Saito, K., Fukuhara, S., Kamatani, M.K., Bonnefond, L., Matsumoto, N., Nishizawa, T., Nakanaga, K., Aoki, J., et al. (2012). Structure and function of Zucchini endoribonuclease in piRNA biogenesis. Nature *491*, 284-287. 10.1038/nature11509.

Nishino, T., and Morikawa, K. (2002). Structure and function of nucleases in DNA repair: shape, grip and blade of the DNA scissors. Oncogene *21*, 9022-9032. 10.1038/sj.onc.1206135.

Nunes, I.V., Breitenbach, L., Pawusch, S., Eigenbrod, T., Ananth, S., Schad, P., Fackler, O.T., Butter, F., Dalpke, A.H., and Chen, L.S. (2024). Bacterial RNA sensing by TLR8 requires RNase 6 processing and is inhibited by RNA 2'O-methylation. EMBO Rep *25*, 4674-4692. 10.1038/s44319-024-00281-9.

Ofengand, J. (2002). Ribosomal RNA pseudouridines and pseudouridine synthases. FEBS Letters *514*, 17-25. https://doi.org/10.1016/S0014-5793(02)02305-0.

Ohgi, K., Horiuchi, H., Watanabe, H., Iwama, M., Takagi, M., and Irie, M. (1992). Evidence that three histidine residues of a base non-specific and adenylic acid preferential ribonuclease from Rhizopus niveus are involved in the catalytic function. J Biochem *112*, 132-138. 10.1093/oxfordjournals.jbchem.a123852.

Ohto, U., Ishida, H., Shibata, T., Sato, R., Miyake, K., and Shimizu, T. (2018). Toll-like Receptor 9 Contains Two DNA Binding Sites that Function Cooperatively to Promote Receptor Dimerization and Activation. Immunity *48*, 649-658 e644. 10.1016/j.immuni.2018.03.013.

Ohto, U., Shibata, T., Tanji, H., Ishida, H., Krayukhina, E., Uchiyama, S., Miyake, K., and Shimizu, T. (2015). Structural basis of CpG and inhibitory DNA recognition by Toll-like receptor 9. Nature *520*, 702-705. 10.1038/nature14138.

Ohyama, H., Sakai, T., Agari, Y., Fukui, K., Nakagawa, N., Shinkai, A., Masui, R., and Kuramitsu, S. (2014). The role of ribonucleases in regulating global mRNA levels in the model organism Thermus thermophilus HB8. BMC Genomics *15*, 386. 10.1186/1471-2164-15-386.

Ostendorf, T., Zillinger, T., Andryka, K., Schlee-Guimaraes, T.M., Schmitz, S., Marx, S., Bayrak, K., Linke, R., Salgert, S., Wegner, J., et al. (2020). Immune Sensing of Synthetic, Bacterial, and Protozoan RNA by Toll-like Receptor 8 Requires Coordinated Processing by RNase T2 and RNase 2. Immunity *52*, 591-605 e596. 10.1016/j.immuni.2020.03.009.

Otani, Y., Yamaguchi, Y., Sato, Y., Furuichi, T., Ikenaka, K., Kitani, H., and Baba, H. (2011). PLD4 Is Involved in Phagocytosis of Microglia: Expression and Localization Changes of PLD4 Are Correlated with Activation State of Microglia. PLOS ONE *6*, e27544. 10.1371/journal.pone.0027544.

Parry, S., Newbigin, E., Currie, G., Bacic, A., and Oxley, D. (1997). Identification of active-site histidine residues of a self-incompatibility ribonuclease from a wild tomato. Plant Physiol *115*, 1421-1429. 10.1104/pp.115.4.1421.

Pelka, K., Bertheloot, D., Reimer, E., Phulphagar, K., Schmidt, S.V., Christ, A., Stahl, R., Watson, N., Miyake, K., Hacohen, N., et al. (2018). The Chaperone UNC93B1 Regulates Toll-like Receptor Stability Independently of Endosomal TLR Transport. Immunity *48*, 911-922.e917. 10.1016/j.immuni.2018.04.011.

Pelka, K., Shibata, T., Miyake, K., and Latz, E. (2016). Nucleic acid-sensing TLRs and autoimmunity: novel insights from structural and cell biology. Immunological Reviews *269*, 60-75. https://doi.org/10.1111/imr.12375.

Piao, W., Shirey, Kari A., Ru, Lisa W., Lai, W., Szmacinski, H., Snyder, Greg A., Sundberg, Eric J., Lakowicz, Joseph R., Vogel, Stefanie N., and Toshchakov, Vladimir Y. (2015). A Decoy Peptide that Disrupts TIRAP Recruitment to TLRs Is Protective in a Murine Model of Influenza. Cell Reports *11*, 1941-1952. 10.1016/j.celrep.2015.05.035.

Pichlmair, A., Schulz, O., Tan, C.P., Näslund, T.I., Liljeström, P., Weber, F., and Reis e Sousa, C. (2006). RIG-I-mediated antiviral responses to single-stranded RNA bearing 5'-phosphates. Science *314*, 997-1001. 10.1126/science.1132998.

Poltorak, A., He, X., Smirnova, I., Liu, M.Y., Van Huffel, C., Du, X., Birdwell, D., Alejos, E., Silva, M., Galanos, C., et al. (1998). Defective LPS signaling in C3H/HeJ and C57BL/10ScCr mice: mutations in Tlr4 gene. Science *282*, 2085-2088. 10.1126/science.282.5396.2085.

Primo, E.D., Otero, L.H., Ruiz, F., Klinke, S., and Giordano, W. (2018). The disruptive effect of lysozyme on the bacterial cell wall explored by an in-silico structural outlook. Biochemistry and Molecular Biology Education *46*, 83-90. https://doi.org/10.1002/bmb.21092.

Raines, R.T. (1998). Ribonuclease a. Chemical reviews *98*, 1045-1066.
Randow, F., and Seed, B. (2001). Endoplasmic reticulum chaperone gp96 is required for innate immunity but not cell viability. Nature Cell Biology *3*, 891-896. 10.1038/ncb1001-891.

Rehwinkel, J., and Gack, M.U. (2020). RIG-I-like receptors: their regulation and roles in RNA sensing. Nature Reviews Immunology *20*, 537-551. 10.1038/s41577-020-0288-3.

Remick, B.C., Gaidt, M.M., and Vance, R.E. (2023). Effector-Triggered Immunity. Annual Review of Immunology *41*, 453-481. https://doi.org/10.1146/annurev-immunol-101721-031732.

Rintala-Dempsey, A.C., and Kothe, U. (2017). Eukaryotic stand-alone pseudouridine synthases - RNA modifying enzymes and emerging regulators of gene expression? RNA Biol *14*, 1185-1196. 10.1080/15476286.2016.1276150.

Roers, A., Hiller, B., and Hornung, V. (2016). Recognition of Endogenous Nucleic Acids by the Innate Immune System. Immunity *44*, 739-754. 10.1016/j.immuni.2016.04.002.

Roske, Y., Cappel, C., Cremer, N., Hoffmann, P., Koudelka, T., Tholey, A., Heinemann, U., Daumke, O., and Damme, M. (2023). Structural analysis of PLD3 reveals insights into the mechanism of lysosomal 5′ exonuclease-mediated nucleic acid degradation. Nucleic Acids Research *52*, 370-384. 10.1093/nar/gkad1114.

Rothenfusser, S., Goutagny, N., DiPerna, G., Gong, M., Monks, B.G., Schoenemeyer, A., Yamamoto, M., Akira, S., and Fitzgerald, K.A. (2005). The RNA helicase Lgp2 inhibits TLR-independent sensing of viral replication by retinoic acid-inducible gene-I. J Immunol *175*, 5260-5268. 10.4049/jimmunol.175.8.5260.

Rozenski, J., Crain, P.F., and McCloskey, J.A. (1999). The RNA Modification Database: 1999 update. Nucleic Acids Res *27*, 196-197. 10.1093/nar/27.1.196.

Saelens, X., Kalai, M., and Vandenabeele, P. (2001). Translation inhibition in apoptosis: caspase-dependent PKR activation and eIF2-alpha phosphorylation. J Biol Chem *276*, 41620-41628. 10.1074/jbc.M103674200.

Sarma, J.V., and Ward, P.A. (2011). The complement system. Cell and Tissue Research *343*, 227-235. 10.1007/s00441-010-1034-0.

Shi, J., Zhao, Y., Wang, K., Shi, X., Wang, Y., Huang, H., Zhuang, Y., Cai, T., Wang, F., and Shao, F. (2015). Cleavage of GSDMD by inflammatory caspases determines pyroptotic cell death. Nature *526*, 660-665. 10.1038/nature15514.

Shibuya, H., Yamaguchi, K., Shirakabe, K., Tonegawa, A., Gotoh, Y., Ueno, N., Irie, K., Nishida, E., and Matsumoto, K. (1996). TAB1: An Activator of the TAK1 MAPKKK in TGF-β Signal Transduction. Science *272*, 1179-1182. doi:10.1126/science.272.5265.1179.

Shimazu, R., Akashi, S., Ogata, H., Nagai, Y., Fukudome, K., Miyake, K., and Kimoto, M. (1999). MD-2, a molecule that confers lipopolysaccharide responsiveness on Toll-like receptor 4. J Exp Med *189*, 1777-1782. 10.1084/jem.189.11.1777.

Singh, S., Dransfeld, U.E., Ambaw, Y.A., Lopez-Scarim, J., Farese, R.V., Jr., and Walther, T.C. (2024). PLD3 and PLD4 synthesize S,S-BMP, a key phospholipid enabling lipid degradation in lysosomes. Cell *187*, 6820-6834.e6824. 10.1016/j.cell.2024.09.036.

Sozmen, E.G., and Akassoglou, K. (2021). Coagulation and immunity: Caught in the fibrin web. Immunity *54*, 2439-2441. https://doi.org/10.1016/j.immuni.2021.10.016.

Stuckey, J.A., and Dixon, J.E. (1999). Crystal structure of a phospholipase D family member. Nature Structural Biology *6*, 278-284. 10.1038/6716.

Sun, L., Su, Y., Jiao, A., Wang, X., and Zhang, B. (2023). T cells in health and disease. Signal Transduction and Targeted Therapy *8*, 235. 10.1038/s41392-023-01471-y.

Sundaram, B., Tweedell, R.E., Prasanth Kumar, S., and Kanneganti, T.-D. (2024). The NLR family of innate immune and cell death sensors. Immunity *57*, 674-699. 10.1016/j.immuni.2024.03.012.

Suzuki, A., Yao, M., Tanaka, I., Numata, T., Kikukawa, S., Yamasaki, N., and Kimura, M. (2000). Crystal structures of the ribonuclease MC1 from bitter gourd seeds, complexed with 2'-UMP or 3'-UMP, reveal structural basis for uridine specificity. Biochem Biophys Res Commun *275*, 572-576. 10.1006/bbrc.2000.3318.

Svitkin, Y.V., Cheng, Y.M., Chakraborty, T., Presnyak, V., John, M., and Sonenberg, N. (2017). N1-methyl-pseudouridine in mRNA enhances translation through eIF2α-dependent and independent mechanisms by increasing ribosome density. Nucleic Acids Res *45*, 6023-6036. 10.1093/nar/gkx135.

Takaesu, G., Kishida, S., Hiyama, A., Yamaguchi, K., Shibuya, H., Irie, K., Ninomiya-Tsuji, J., and Matsumoto, K. (2000). TAB2, a Novel Adaptor Protein, Mediates Activation of TAK1 MAPKKK by Linking TAK1 to TRAF6 in the IL-1 Signal Transduction Pathway. Molecular Cell *5*, 649-658. 10.1016/S1097-2765(00)80244-0.

Takahashi , K., Shibata , T., Akashi-Takamura , S., Kiyokawa , T., Wakabayashi , Y., Tanimura , N., Kobayashi , T., Matsumoto , F., Fukui , R., Kouro , T., et al. (2007). A protein associated with Toll-like receptor (TLR) 4 (PRAT4A) is required for TLR-dependent immune responses. Journal of Experimental Medicine *204*, 2963-2976. 10.1084/jem.20071132.

Takeuchi, O., and Akira, S. (2010). Pattern Recognition Receptors and Inflammation. Cell *140*, 805-820. 10.1016/j.cell.2010.01.022.

Tanaka, T., Narazaki, M., and Kishimoto, T. (2014). IL-6 in inflammation, immunity, and disease. Cold Spring Harb Perspect Biol *6*, a016295. 10.1101/cshperspect.a016295.

Tanji, H., Ohto, U., Motoi, Y., Shibata, T., Miyake, K., and Shimizu, T. (2016). Autoinhibition and relief mechanism by the proteolytic processing of Toll-like receptor 8. Proc Natl Acad Sci U S A *113*, 3012-3017. 10.1073/pnas.1516000113.

Tanji, H., Ohto, U., Shibata, T., Miyake, K., and Shimizu, T. (2013). Structural Reorganization of the Toll-Like Receptor 8 Dimer Induced by Agonistic Ligands. Science *339*, 1426-1429. doi:10.1126/science.1229159.

Tanji, H., Ohto, U., Shibata, T., Taoka, M., Yamauchi, Y., Isobe, T., Miyake, K., and Shimizu, T. (2015). Toll-like receptor 8 senses degradation products of single-stranded RNA. Nature Structural & Molecular Biology *22*, 109-115. 10.1038/nsmb.2943.

Taoka, M., Nobe, Y., Yamaki, Y., Sato, K., Ishikawa, H., Izumikawa, K., Yamauchi, Y., Hirota, K., Nakayama, H., Takahashi, N., and Isobe, T. (2018). Landscape of the complete RNA chemical modifications in the human 80S ribosome. Nucleic Acids Res *46*, 9289-9298. 10.1093/nar/gky811.

Terao, C., Ohmura, K., Kawaguchi, Y., Nishimoto, T., Kawasaki, A., Takehara, K., Furukawa, H., Kochi, Y., Ota, Y., Ikari, K., et al. (2013). PLD4 as a novel susceptibility gene for systemic sclerosis in a Japanese population. Arthritis & Rheumatism *65*, 472-480. https://doi.org/10.1002/art.37777.

Thorn, A., Steinfeld, R., Ziegenbein, M., Grapp, M., Hsiao, H.H., Urlaub, H., Sheldrick, G.M., Gartner, J., and Kratzner, R. (2012). Structure and activity of the only human RNase T2. Nucleic Acids Res *40*, 8733-8742. 10.1093/nar/gks614.

Tighe, R.M., Liang, J., Liu, N., Jung, Y., Jiang, D., Gunn, M.D., and Noble, P.W. (2011). Recruited exudative macrophages selectively produce CXCL10 after noninfectious lung injury. Am J Respir Cell Mol Biol *45*, 781-788. 10.1165/rcmb.2010-0471OC.

Tong, A.J., Leylek, R., Herzner, A.M., Rigas, D., Wichner, S., Blanchette, C., Tahtinen, S., Kemball, C.C., Mellman, I., Haley, B., et al. (2024). Nucleotide modifications enable rational design of TLR7-selective ligands by blocking RNase cleavage. J Exp Med *221*. 10.1084/jem.20230341.

Van Acker, Z.P., Perdok, A., Hellemans, R., North, K., Vorsters, I., Cappel, C., Dehairs, J., Swinnen, J.V., Sannerud, R., Bretou, M., et al. (2023). Phospholipase D3 degrades mitochondrial DNA to regulate nucleotide signaling and APP metabolism. Nature Communications *14*, 2847. 10.1038/s41467-023-38501-w.

Veerareddygari, G.R., Singh, S.K., and Mueller, E.G. (2016). The Pseudouridine Synthases Proceed through a Glycal Intermediate. J Am Chem Soc *138*, 7852-7855. 10.1021/jacs.6b04491.

Vignali, D.A.A., Collison, L.W., and Workman, C.J. (2008). How regulatory T cells work. Nature Reviews Immunology *8*, 523-532. 10.1038/nri2343.

Wakabayashi, Y., Kobayashi, M., Akashi-Takamura, S., Tanimura, N., Konno, K., Takahashi, K., Ishii, T., Mizutani, T., Iba, H., Kouro, T., et al. (2006). A Protein

Associated with Toll-Like Receptor 4 (PRAT4A) Regulates Cell Surface Expression of TLR41. The Journal of Immunology *177*, 1772-1779. 10.4049/jimmunol.177.3.1772.

Wang, C., Deng, L., Hong, M., Akkaraju, G.R., Inoue, J., and Chen, Z.J. (2001a). TAK1 is a ubiquitin-dependent kinase of MKK and IKK. Nature *412*, 346-351. 10.1038/35085597.

Wang, C., Deng, L., Hong, M., Akkaraju, G.R., Inoue, J.-i., and Chen, Z.J. (2001b). TAK1 is a ubiquitin-dependent kinase of MKK and IKK. Nature *412*, 346-351. 10.1038/35085597.

Wang, J.P., Bowen, G.N., Padden, C., Cerny, A., Finberg, R.W., Newburger, P.E., and Kurt-Jones, E.A. (2008). Toll-like receptor-mediated activation of neutrophils by influenza A virus. Blood *112*, 2028-2034. 10.1182/blood-2008-01-132860.

Yamamoto, M., Sato, S., Hemmi, H., Uematsu, S., Hoshino, K., Kaisho, T., Takeuchi, O., Takeda, K., and Akira, S. (2003). TRAM is specifically involved in the Toll-like receptor 4-mediated MyD88-independent signaling pathway. Nat Immunol *4*, 1144-1150. 10.1038/ni986.

Yang, E., and Li, M.M.H. (2020). All About the RNA: Interferon-Stimulated Genes That Interfere With Viral RNA Processes. Front Immunol *11*, 605024. 10.3389/fimmu.2020.605024.

Yang, Y., Liu, B., Dai, J., Srivastava, P.K., Zammit, D.J., Lefrançois, L., and Li, Z. (2007). Heat shock protein gp96 is a master chaperone for toll-like receptors and is important in the innate function of macrophages. Immunity *26*, 215-226. 10.1016/j.immuni.2006.12.005.

Yuan, M., Peng, L., Huang, D., Gavin, A., Luan, F., Tran, J., Feng, Z., Zhu, X., Matteson, J., Wilson, I.A., and Nemazee, D. (2024). Structural and mechanistic insights into disease-associated endolysosomal exonucleases PLD3 and PLD4. Structure *32*, 766-779.e767. 10.1016/j.str.2024.02.019.

Zhang, X., Bai, X.C., and Chen, Z.J. (2020). Structures and Mechanisms in the cGAS-STING Innate Immunity Pathway. Immunity *53*, 43-53. 10.1016/j.immuni.2020.05.013.

Zhang, Z., Ohto, U., Shibata, T., Krayukhina, E., Taoka, M., Yamauchi, Y., Tanji, H., Isobe, T., Uchiyama, S., Miyake, K., and Shimizu, T. (2016). Structural Analysis Reveals that Toll-like Receptor 7 Is a Dual Receptor for Guanosine and Single-Stranded RNA. Immunity *45*, 737-748. 10.1016/j.immuni.2016.09.011.

Zhang, Z., Ohto, U., Shibata, T., Taoka, M., Yamauchi, Y., Sato, R., Shukla, N.M., David, S.A., Isobe, T., Miyake, K., and Shimizu, T. (2018). Structural Analyses of Toll-like Receptor 7 Reveal Detailed RNA Sequence Specificity and Recognition Mechanism of Agonistic Ligands. Cell Rep *25*, 3371-3381 e3375. 10.1016/j.celrep.2018.11.081.

8 Acknowledgements

Above all, I want to thank my supervisor, Prof. Veit Hornung, for welcoming me into his group, suggesting a research topic I was truly passionate about, and for his guidance throughout my doctoral studies. I really enjoyed our many discussions on project progress and the exchange of ideas on what to try next. I will miss you (and working on TLRs) a lot.

I would also like to sincerely thank my TAC committee members, Prof. Karl-Peter Hopfner and Prof. Andreas Pichlmair, for their valuable input during my PhD and their commitment to being part of the doctoral examination committee.

Next, I would like to express my gratitude to all my collaborators who contributed to the publications. In particular, thanks to Dr. Katja Lammens for solving the structure of PLD3 and to Dr. Matthias Heiss and Dr. Mirko Wagner for measuring RNA degradation products using LC-MS. Thank you to Dr. med. Ignazio Piseddu for his support during the revisions of both manuscripts, and to Dr. Jan Gärtig for his help with mouse experiments. Without their contributions, I would not have been able to complete both projects.

Further, I would like to thank all my colleagues from the Hornung lab for a great working atmosphere and for their helpful suggestions. Thanks to Dr. Wilhelm Greulich, Dr. Francesca Pinci, and Dr. Dennis Nagl for teaching me many techniques during my Master's Thesis and at the start of my PhD. A special thank you also to Meiyue, Julia, Janina, Varvara, Tobias and Larissa, who have become friends. You made coming to the lab every day a pleasure. I will miss you deeply as colleagues when I move on to the next chapter of my life.

A heartfelt thank you to my parents, Daniela and Christian, my siblings Aline and René, my grandmothers Barbara and Gabriele, and to my grandfather Emile for their unconditional support.

Last but not least, I want to thank my boyfriend Martin for the past nine years. Thank you for always being there for me and supporting me every step of the way. I could not have done this without you.